THE JOURNAL OF

PHYSICAL

CHEMISTRY

THE JOURNAL OF
PHYSICAL CHEMISTRY

THE JOURNAL OF
PHYSICAL CHEMISTRY

■ Supplementary and/or miniprint material for this paper is available separately, in
photocopy or microfiche form. Ordering information is given in the paper.

* In papers with more than one author, the asterisk indicates the name of the author to
whom inquiries about the paper should be addressed.

AUTHOR INDEX

Ring Opening of Chemically Activated Cyclopentyl and Methylcyclobutyl Radicals[1]

W. P. L. Carter and D. C. Tardy*

Department of Chemistry, University of Iowa, Iowa City, Iowa 52242   (Received December 21, 1973)

The endothermic ring opening of vibrationally excited cyclopentyl radicals generated in the gas phase by adding H to cyclopentene has been studied. The results obtained were combined with literature results to test activated complex models for the ring-opening reaction, and the data were fit by a model which gives a thermal A factor of $10^{14.0 \pm 0.4}$ sec^{-1}, and a critical energy of 34.6 ± 0.6 kcal/mol. The exothermic ring opening of vibrationally excited methylcyclobut-1-yl generated by adding H to methylenecyclobutane in the gas phase was also studied. Assuming a model for the ring-opening activated complex which corresponds to a thermal A factor of $10^{14.1 \pm 0.4}$ sec^{-1}, the critical energy is calculated to be 31.7 ± 0.7 kcal/mol. These results suggest that the critical energies for ring openings of cycloalkyl radicals may be relatively insensitive to ring strain.

Introduction

An interesting class of free-radical isomerizations is the ring opening of cycloalkyl radicals and their reverse, the internal addition of radical centers to a double bond on the same molecule. In addition to being of interest to organic chemists,[2a] these reactions are also of theoretical interest.[2b] An incompletely resolved question, for example, is how does the critical energy for the ring opening (or the internal addition) depend on the ring size, and how does it compare with analogous reactions in a cyclic systems. It has been suggested[2b] that if the transition state has about the same strain as the cyclic radical, then the ring-opening critical energy should be independent of ring strain. In that case it is reasonable to expect that this critical energy should be about the same as that for the β scission decomposition of acyclic radicals, which is 31–33 kcal/mol.[3] However, it is conceivable that the strain of the transition state could be less than in the cyclic radical because the ring is opening and thus strain is being relieved; it is also conceivable that the strain in the transition state is more because examination of models suggests that the ring has to be quite puckered for significant overlap in the forming π bond.

Some quantitative gas-phase studies of ring opening or internal addition reactions have been reported.[2b,4–7] Thermal work gives cyclopropyl a ring-opening activation energy of about 22 kcal/mol[4] and cyclobutyl about 18 kcal/mol[5] and indicates that cyclopentyl has a ring opening en- ergy of less than about 38 kcal/mol.[6] From chemical activation work, a critical energy for cyclopentyl opening of about 33 ± 3 kcal/mol has been calculated.[7] However, despite this work, more work is needed. The activation energy of 18 kcal/mol for the ring opening of cyclobutyl[5] is unreasonably low, and that work[5] has been suggested as unreliable.[2b,6] Corrections have been suggested which increase the ring opening energy of cyclobutyl to a more reasonable 35 ± 5 kcal/mol.[2] In addition, in the chemical activation study of the internal addition forming cyclopentyl,[7] only an average rate constant is experimentally measured. In order to obtain an estimate of the critical energy, the rate constant must be calculated using RRKM[8] theory; this requires a vibrational frequency model for the isomerization activated complex as well as the critical energy and at present no reliably tested way to obtain frequency assignments for cyclic activated complexes is available.

The gas-phase chemical activation studies reported here are aimed at solving these problems. The ring opening of cyclopentyl was studied by forming vibrationally excited cyclopentyl by the addition of H atoms to cyclopentene. The reactions believed important in this system are shown in Figure 1. The radicals formed are at a much lower energy than those in the previously reported chemical activation study of this reaction.[9] With an idea of the isomerization rate constant at two different energies, RRKM theory can then be used to test the activated complex models, and thus a more reliable critical energy can be
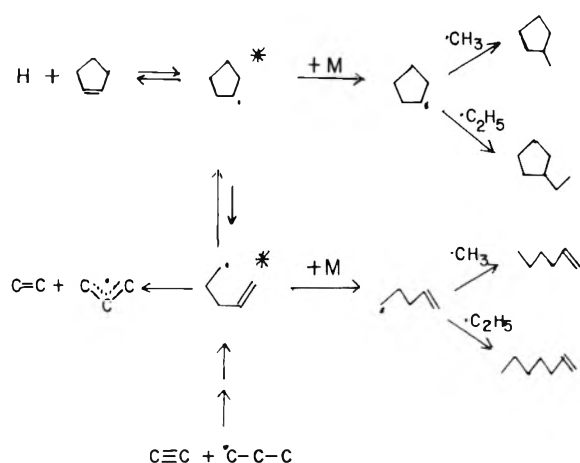
Figure 1. Reaction scheme for H + cyclopentene. For the studies made by Watkins[7] the minimum energies for cyclopentyl and 1-penten-5-yl radicals were 57.3 and 42.7 kcal/mol, while in this work the energies were 36.3 and 21.6 kcal/mol, respectively. M depicts any molecules which will stabilize the excited radicals.

obtained. Such a test is possible because essentially two parameters determine RRKM calculated rate constants: the critical energy and the activated complex model. With two different rate constants, these two quantities can be unambiguously determined. Indeed, the nature of the activated complex model which best fits the data should also be of interest.

The ring opening of cyclobutyl was studied in this work by forming virbrationaly excited methylcyclobutyl-1 by the addition of H to methylenecyclobutane (Figure 2). As this is studied at only one energy, an activated complex model for this reaction could not be tested. However, the nature of the model which fits best for the cyclopentyl system should give some clues as to the best model for the methylcyclobutyl-1 system, so a fair estimate of its critical energy should be possible.

Experimental Section

Hydrogen atoms were generated by the mercury($^3P_1$) photosensitized decomposition of hydrogen molecules[9] resulting from irradiation (through a 90–99% opaque filter) by a G8T5 germicidal lamp. The lamp was in a quartz well in a 20-l. Pyrex reaction vessel attached to a standard, mercury-saturated, Pyrex vacuum system with grease-free stopcocks and a Barocel electronic manometer. Photolyses were done at room temperature with the following mixtures: (1) cyclopentene and cis-2-butene in hydrogen; (2) cyclopentene and ethylene in hydrogen; (3) methylenecyclobutane and ethylene in hydrogen. The mixture ratios for the qualitative runs are shown in Tables I and II. Hydrogen gas was purified through a liquid nitrogen cooled silica gel trap before use. Ethylene and cis-2-butene (Matheson, CP) were taken from their tanks and not further purified except by being pumped on while condensed in a liquid nitrogen trap. The samples of cyclopentene (Chemical Samples Co., 99.9%) and methylenecyclobutane (Chemical Samples Co., 98%) were found to have no impurities interfering with the products of interest and were not further purified.

After each run, the condensable gases were trapped by pumping out the reaction vessel through a glass-wool filled trap cooled with liquid nitrogen, and trapped again in a similar way for the vapor-phase chromatography
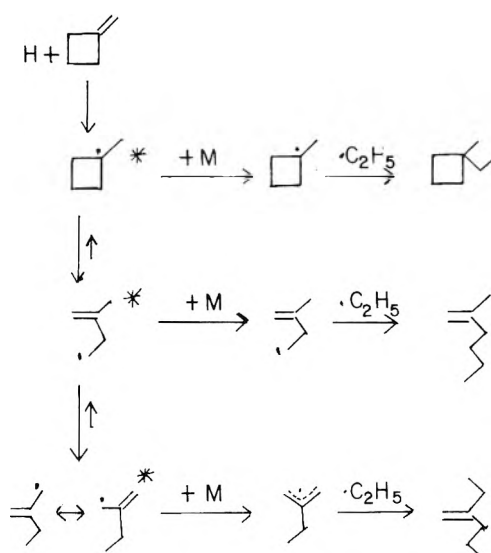
Figure 2. Reaction scheme for H + methylenecyclobutane. The methylcyclobutyl-1 radical has a minimum energy of 42.3 kcal/mol. M dipicts any molecule which will stabilize the excited radicals.

TABLE I: Experimental Data for the H + Cyclopentene System

Pressure, Torr	S/DC[a]	% reactants[b]			
		H	Et	Bu	C$_5$
0.038	9.1[c]	99.0	0.4		0.6
0.0548	11.7	99.0	0.4		0.6
0.075	11.9	99.0	0.4		0.6
0.113	15.0	99.0	0.4		0.6
0.140	16.4	99.0	0.4		0.6
0.156	16.3	99.0	0.4		0.6
0.156	16.3	99.0	0.4		0.6
0.157	17.0	99.0	0.4		0.6
0.215	16.3	99.0	0.4		0.6
0.300	17.3	99.0	0.4		0.6
0.353	21.7	99.0	0.4		0.6
0.689	30.5	99.0	0.4		0.6
0.785	30.0	99.0	0.4		0.6
1.60	35.3	99.0	0.4		0.6
1.44	48.0[d]	99.0		1.2	0.8
3.39	88.8	97.8		1.4	0.8
4.09	85.1	97.7		1.4	0.9
5.99	126.4	97.7		1.4	0.9
11.1	234.0	97.3		1.4	0.9

[a] Stabilization/decyclization. [b] Reactants: H = hydrogen, Et = ethylene, Bu = cis-2-butene, C$_5$ = cyclopentene. [c] Methylcyclopentane/1-hexene, corrected for disproportionation. [d] Ethylcyclopentane/1-heptene, corrected for disproportionation.

(vpc) injection system. Noncondensable products were not analyzed. All analysis were done by vpc. 1-Hexene, methylcyclopentane, 1-heptene, ethylcyclopentane, 2-methyl-1-hexene, and 2-ethyl-1-pentene were identified by comparison of vpc retention times of reaction products with authentic samples. The cyclopentene runs were analyzed using a squalane column, while the methylenecyclobutane runs were analyzed with both squalane and hexamethylphosphoramide columns. Products retained longer than heptenes were not analyzed.

Results and Discussion

The presence of cis-2-butene or ethylene in the reaction mixtures was to produce methyl or ethyl radicals to trap

TABLE II: Experimental Data for the H + Methylenecyclobutane System

Pressure, Torr	S/DC[a]	% reactants[b]		
		H	Et	C₅
2.14	0.309[c]	99.0	0.62	0.40
3.0	0.421	97.5	1.6	0.9
5.03	0.693	97.5	1.6	0.9
9.80	1.45	97.0	2.0	1.0
9.83	1.37	96.9	2.0	1.1
9.95	1.37	96.0	2.9	1.1
14.9	2.20	97.5	1.6	0.9
20.0	2.87	99.0	0.6	0.4
42.3	5.44	96.7	2.2	1.1
79.0	9.32	97.6	1.6	0.8
99.9	11.96	97.7	1.6	0.8

[a] See Table I, footnote a. [b] Reactants: H = hydrogen, Et = ethylene, C₅ = methylenecyclobutane. [c] 1,1-Methylethylcyclobutane/(2-methyl-1-hexene + 2-ethyl-1-pentene), corrected for disproportionation.

the C₅ radicals. Methyl radicals were generated after the addition of H to cis-2-butene by the following reactions

$$H + C—C{=}C—C \longrightarrow C—C—C\!\cdot\!—C^* \quad (1)$$

$$C—C—C\!\cdot\!—C^* \longrightarrow C—C{=}C + C\!\cdot \quad (2)$$

$$C—C—C\!\cdot\!—C^* + M \longrightarrow C—C—C\!\cdot\!—C \longrightarrow \longrightarrow$$
$$\text{other products} \quad (3)$$
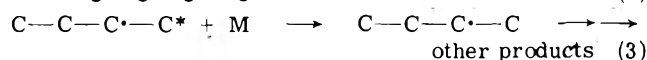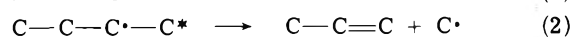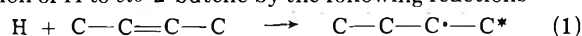
As the rate of reaction 2 is approximately 2×10^7 sec^{-1},[3] this method of producing methyl radicals is only useful at pressures at or below about 0.5–1.0 mm, where reaction 3 does not predominate over 2. Ethyl radicals are generated when ethylene is present by the following reactions

$$H + C{=}C \longrightarrow C—C\!\cdot\!^* \quad (4)$$

$$C—C\!\cdot\!^* \longrightarrow C{=}C + H \quad (5)$$

$$C—C\!\cdot\!^* + M \longrightarrow C—C\!\cdot + M \quad (6)$$
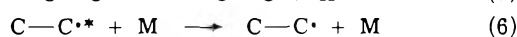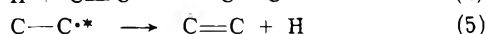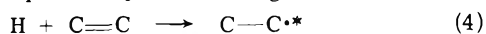
As the rate of reaction 5 is about 4×10^7 sec^{-1},[3] this technique is useful for producing ethyl radicals at pressures above 1–2 mm, where decomposition of excited ethyl is not important.

Cyclopentene Runs. Cyclopentene + hydrogen mixtures gave, upon photolysis, a number of C₅ products, including a large yield of a compound whose vpc retention time is appropriate to cyclopentane. There were no major C₆ or C₇ products observed. Three new peaks on the vpc were observed when the reaction mixtures contained cis-2-butene in addition to cyclopentene and hydrogen. One was identified as 1-hexene, considered to result from the methyl trapping of 1-penten-4-yl, and another product was identified as methylcyclopentane, from methyl + cyclopentyl. Table I gives the cyclopentyl/1-penten-5-yl concentrations calculated from the yields of their trapping products. Corrections were made for disproportionation assuming disproportionation/combination ratios of 0.10 for methyl + 1-penten-5-yl and 0.31 for methyl + cyclopentyl.[10] The third C₆ product, whose yield varied from ¹⁄₁₀ that of methylcyclopentane at 1.6 mm pressure to about ⅕ at 0.038 mm, was not identified, but is believed to be a result of methyl adding directly to cyclopentene. Other new products in the runs with cis-2-butene were those expected to result from the H + cis-2-butene reactions.

When ethylene was present in the reaction mixture instead of cis-2-butene, the C₆ products were not observed, and were replaced by four vpc peaks appropriate to C₇ hydrocarbons. One product was identified as 1-heptene from the combination of ethyl and 1-penten-5-yl, and another was identified as ethylcyclopentane, from ethyl + cyclo-
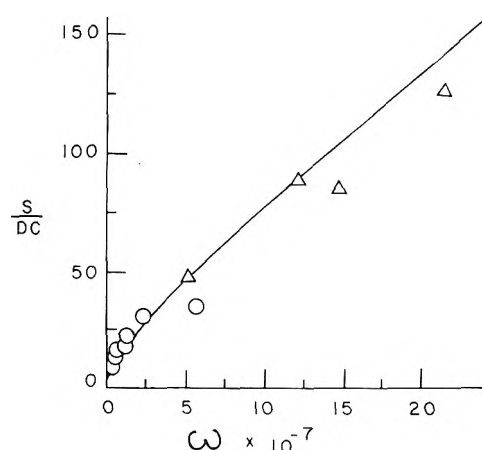
Figure 3. Plot of stabilization/decyclization, S/DC (cyclopentyl/ 1-penten-5-yl), as monitored by methyl (○) or ethyl (△) trapping vs. ω, the collision frequency in the H + cyclopentene system. The line corresponds to the optimized calculation.

pentyl. The cyclopentyl/1-penten-5-yl ratios calculated from the yields of these products are shown in Table I. Correction for disproportionation assumed disproportionation/combination ratios of 0.08 for ethyl + 1-penten-5-yl and 0.27 for ethyl + cyclopentyl.[10] A known ratio mixture of ethylcyclopentane and 1-heptene was injected into the vpc and it was verified that the vpc area ratios corresponded to the actual mole ratios of these compounds. The two other C₇ products were not identified; they occured at about ¹⁄₁₀ the yield of ethylcyclopentane and are presumed to result from the direct addition of ethyl to cyclopentene.

A plot of stabilization/decyclization (the cyclopentyl/ 1-penten-5-yl radical concentrations obtained by both methyl and ethyl trapping) vs. collision rate is shown in Figure 3. The low pressure ethyl trapping run can be considered unreliable because it was done at a pressure low enough so that a significant amount of the excited ethyl radicals formed decompose before they can be stabilized. If this run is ignored, the ethyl trapping and the methyl trapping runs agree moderately well.

Methylenecyclobutane Runs. Methylenecyclobutane/ hydrogen mixtures gave several C₅ hydrocarbons upon photolysis, two of these occur in large yields and have retention times appropriate for 2-methyl-1,3-butadiene and methylcyclobutane; though none of these C₅ products were unambiguously identified. When ethylene was present in the reaction mixture, three additional products corresponding to C₇ hydrocarbons were observed. Two of these were poorly resolved but were identified as 2-methyl-1-hexene and 2-ethyl-1-pentene believed to result from the ethyl trapping of the radicals formed when methylcyclobutyl-1 opens (see Figure 2). The other peak is believed to be 1-methyl-1-ethylcyclobutane, resulting from the ethyl trapping of methylcyclobutyl-1. Though no authentic sample of that compound could be obtained, this belief is supported by several observations. (1) A plot of the yield of this product/(2-methyl-1-hexene + 2-ethyl-1-pentene) vs. pressure is linear with a zero pressure intercept near zero. The slope is identical when using two different types of vpc columns. This pressure dependence is consistent with the assumption that this product results from the trapping of an initially formed radical which is thermodynamically less favored than its isomers. (2) The vpc retention time of this product on a boiling point column is what would be reasonably expected for 1-methyl-
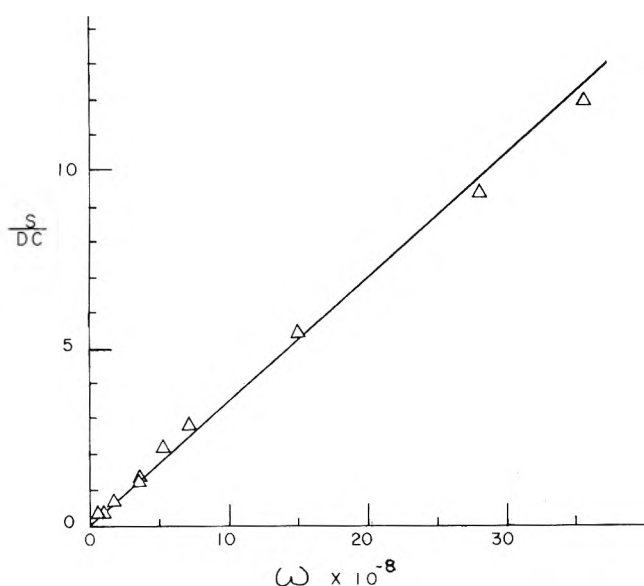
Figure 4. Plot of stabilization/decyclization, S/DC (methycyclo-butyl-1-2-methyl-1-buten-4-yl + 2-ethyallyl), as monitored by ethyl trapping vs. ω in the H + methylenecyclobutane system. The line corresponds to the optimized calculation.

1-ethylcyclobutane. (3) Relative to the C_7 olefins, this compound is retained for a significantly shorter time on a vpc column with double bond characteristics (hexamethylphosphoramide) than on a boiling point column (squalane). This suggests that this product is not an olefin. The only C_7 nonolefin product other than 1-methyl-1-ethylcyclobutane expected in this system is ethylcyclopentane, however, it has a retention time too long to be identified with the observed peak.

Table II gives the methylcyclobutyl-1/(2-methyl-1-buten-4-yl + 2-ethylallyl) ratio calculated from the observed C_7 products. Corrections for disproportionation were estimated from disproportionation/combination ratios of 0.31 for ethyl + methylcyclobutyl-1 and 0.08 for ethyl + either of the ring-opened radicals.[10] A plot of this ratio (stabilization/decyclization) vs. collision rate is shown in Figure 4.

Calculations

In order to obtain estimates of the energy parameters from observed stabilization yields, steady-state RRKM[8] calculations were done on these systems. The principles of calculating decomposition and stabilization yields in systems with decompositions, isomerizations, and inefficient stabilizations are described elsewhere.[11,12] Required for these calculations are the following.

(1) The heats of formation at 0°K of the radicals and the activated complexes is required. Heats of formation of radicals were obtained using C–H bond dissociation energies of 96.2 kcal/mol for propane and 1-pentene,[13] of 93.4 kcal/mol for cyclopentene,[14] and of 87.1 kcal/mol for allyl-H.[15] Except for the cyclobutanes, the 0°K heats of formation of H· and the hydrocarbons are obtained in the API tables.[16] The 0°K heat of formation of methylcyclobutyl-1 of 44.6 kcal/mol is calculated using a 298°K heat of formation of methylcyclobutane of −0.6 kcal/mol,[17] a C–H bond dissociation energy of 93.6 kcal/mol (96.8 kcal/mol for cyclobutane,[18] corrected to tertiary by subtracting 3.2 kcal/mol[13]), and a 298°K heat content of 3.2 kcal/mol.[19] The heats of formation of the formation complexes

in the cyclopentyl system are obtained from a H + cyclopentyl critical energy of 2.0 kcal/mol,[13] and a n-propyl + acetylene critical energy of 9.0 kcal/mol.[7] The 0°K heat of formation of the H + methylenecyclobutane addition complex is obtained using a 298°K heat of formation of methylenecyclobutane of 30.0 kcal/mol,[17] a H addition critical energy of 2.0 kcal/mol,[13] and a 298°K heat content of 4.1 kcal/mol. The heats of formation of the isomerization complexes were treated as adjustable parameters. The appropriate energies are presented in Appendix I.

(2) The sum of states of the activated complexes and the density of states of the radicals are also required for RRKM calculations.[8] These are obtained from the vibrational frequencies. Methods of frequency assignments[19,20] and frequency lists[19] are given elsewhere. The cyclopentyl radical frequencies are based on those of cyclopentane,[21] and the methylcyclobutyl frequencies are based on those of cyclobutane[22] and methylenecyclobutane.[23] Several different vibrational assignments of the ring-opening activated complexes were obtained using normal mode calculations described elsewhere.[24] Calculated frequencies are related to bond numbers associated with the forming or breaking bonds through bond order-force constant correlations.[24,25] The frequencies used are listed in Appendix II.

(3) The rate constants are proportional to the reaction path degeneracies. Both ring opening and internal addition reactions have path degeneracies of 2; all others considered here have a degeneracy of 1.

(4) An energy transfer model for the collisional stabilization of the excited radicals is needed to perform the steady-state calculation. In the experiments reported here, hydrogen was used as the bath gas so these radicals are stabilized by collisions with hydrogen. Collision numbers (in sec^{-1}) are obtained by multiplying the pressure (in Torr) by 3.56×10^7 sec^{-1} Torr^{-1}. This is calculated using a Lennard-Jones potential[26,27] with cross sections of 2.97 and 5.70 Å, and ϵ/k values of 33.3 and 310°K for hydrogen[26] and all C_5 hydrocarbons,[28] respectively. Hydrogen is not a strong collider;[12,29] one collision with hydrogen in general will not remove enough vibrational energy to quench the unimolecular reaction. Energy transfer models of weak colliders are given by probabilities of the excited species going from one energy state to another upon collision. In these calculations, a step ladder model with step size of 400 cm^{-1} (1.144 kcal/mol) was assumed for hydrogen, i.e., one collision with hydrogen causes a change in internal energy of 1.144 kcal/mol. Details on obtaining the detailed probabilities for step ladder and other models are given elsewhere.[30]

The calculated stabilization yield ratios are compared with experiment; the adjustable energy parameters are varied until an optimum set is obtained. With an optimum set of energy parameters any change in an adjustable energy causes the square of the per cent deviation of the calculated yield ratios relative to the experimental yield ratios to increase. Although the energy levels used in the calculation are spaced at 400 cm^{-1} (1.144 kcal/mol), the energy parameters could be changed in increments of 100 cm^{-1} (0.29 kcal/mol).

Cyclopentene System. Shown in Figure 1 are the reactions believed to be important. The critical energies of the isomerization of I to II and of the decomposition of II are considered to be unknown energy parameters. In addition, it is necessary to consider the vibrational assignment of

the ring-opening activated complex to be another unknown "parameter," as there is much uncertainty as how to assign the vibrational frequencies of cyclic activated complexes. Clearly, the data obtained in this study, the ratios of stabilization yields of cyclopentyl to 1-penten-5-yl, are not enough to test all these unknowns. However, such a test is possible if we make use of the earlier chemical activation study of this system done by Watkins and Olsen (WO),[7] where vibrationally excited 1-penten-5-yl was produced with a minimum excitation of 42.7 kcal/mol by the exothermic addition of n-propyl to acetylene forming 1-penten-1-yl which undergoes a rapid 1,5 H shift to II. This excitation contrasts with the much lower minimum excitation of 21.7 kcal/mol for 1-penten-5-yl obtained in the H + cyclopentene system. A knowledge of the rate constant for a reaction at two energies gives us an ability to test the activated complex model not possible with just one chemical activation study. With a more reliable activated complex model, a better estimate of the critical energy is possible. WO did their experiments using acetylene as the bath gas; acetylene is probably not a strong collider, but is probably more efficient than nitrogen, which was found to have an efficiency of 0.55[12] in chemical activation systems. An efficiency of 0.75 for acetylene was assumed, as suggested by some thermal energy transfer studies;[31] the correction was made by multiplying WO's collision rates by the assumed efficiency.

Optimization calculations were done on both the H + cyclopentene system and WO's n-propyl + acetylene system. The calculations on the H + cyclopentene system were done assuming the mechanism of Figure 1, where back isomerization and decompositions to form cyclopentene and ethylene were allowed. In WO's system, back isomerization could be neglected because of thermodynamic considerations and because of the high pressures they employed. The optimized isomerization critical energies for the two systems would agree only when an ring-opening activated complex model corresponding to partial single bond and partial double bond numbers of 0.2 and 1.8 was used.[24] In that case, the ring-opening critical energy was 34.6 kcal/mol and the internal addition was 19.7 kcal/mol. WO also measured the decomposition of II; and we use their data to calculate its critical energy to be 26.3 kcal/mol. This corresponds to a critical energy for the addition of allyl to ethylene of 13.7 kcal/mol, about 6 kcal/mol higher than the usual radical + olefin additions,[32] indicating that about 6 kcal/mol. though not all, of the allylic stabilization of allyl[15] must be destroyed in the activated complex.

If a collisonal efficiency for acetylene of 1.0 is assumed (instead of 0.75), the data are fit by a ring-opening complex with bond numbers of 0.1 and 1.9, a ring-opening critical energy of 34.9 kcal/mol, and an allyl + ethylene addition critical energy of 13.2 kcal/mol. If the efficiency of acetylene is assumed to be 0.5, then the data are fit by bond numbers of 0.35 and 1.65, a ring-opening energy of 34.0 kcal/mol, and an allyl + ethylene energy of 14.3 kcal/mol. These models bracket the A factor by a factor of 2.5.

Methylenecyclobutane System. The scheme of expected reactions in the H + methylenecyclobutane system are shown in Figure 2. From energetic considerations, decompositions are not believed to be important in this system. The stabilization yields of IV and V had to be measured together, so their interconversion rate was not a consideration. Because of the thermodynamics of the isomeriza-

TABLE III: Ring-Opening Critical Energies[a]

	Thermal E_{act}	Chemical activation E_{crit}
Cyclopropyl	22[b]	
Cyclobutyl	18[c]	
	35 ± 5[d]	
Methylcyclobutyl-1		31.7 ± 0.7[f]
Cyclopentyl	≤37.7[e]	34.6 ± 0.6[f]
C-C-C-C → C=C-C + C·	33.9[e]	33.0[g]

[a] All energies in kcal/mol. [b] Reference 4. [c] Reference 5. [d] Reference 2. [e] Reference 6. [f] This work. [g] Reference 3.

tion of III to IV, the reverse reaction can be ignored, and the system can be treated as a simple stabilization-decomposition competition,[12] where "decomposition" corresponds to eventual formation of the stabilization products of IV and V. The activated complex for the ring opening could not be tested, so it was assumed to have partial bond numbers[24] of 0.2 and 1.8, as this is what the cyclopentene data indicate. With that, the ring-opening critical energy is calculated to be 31.7 kcal/mol. An activated complex model with bond numbers of 0.1 and 1.9 gives a ring opening critical energy of 32.6 kcal/mol, while bond numbers of 0.35 and 1.65 give a ring-opening critical energy of 31.2 kcal/mol.

Conclusion

Table III gives the critical energies for the various strained ring-opening reactions compared with an analogous acyclic decomposition process using data obtained in this work and in the literature. Note that all except cyclopropyl have about the same critical energy, indicating that even in the very strained cyclobutyl system the ring strain does not have a dramatic effect on the C-C rupture reaction. In view of the problems in the thermal studies of the cyclobutyl ring opening,[2b,6] it is not clear how reliable the reported 22 kcal/mol activation energy for the opening of cyclopropyl is. Clearly, the cyclopropyl system should also be restudied to see if it really constitutes a major break in the trend found in the cyclopentyl and cyclobutyl systems; work along these lines is currently underway in this laboratory.

Note Added in Proof. After this manuscript was submitted it was learned that Professor B. S. Rabinovitch had completed a similar study; his results, which will be submitted for publication, are in agreement with ours.
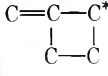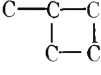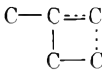
Appendix I. Energy Values

The minimum energy of excitation which the formed radical contains (E_{min}) and the critical energy for reaction of the radical (E_0) can be calculated from the equations

$$E_{min} = E_{form}^* - E_R$$

$$E_0 = E_{react}^* - E_R$$

where the asterisk designates an activated complex and the following heats of formation

H + [cyclopentene]* ΔH_f° = 67.29 kcal/mol

C—C—C· + C≡C*   88.45

[cyclopentyl radical]   30.97

C=C—C—C—C·   45.84

[cyclobutane ring]*   65.57[33]

C≡C···C≡C···C   72.15[33]

H + C=C—C*
     | | 88.90
     C—C

C—C·—C
| | 46.58
C—C

C—C≡C
| :   78.32[33]
C—C

Appendix II. Vibrational Frequency Models

A. Complexes

I. H + Cyclopentene Complex

2950 (8)	1300	1118	965	906 (2)
631	417	200	115	1496
1479	1471	1338	1322	1305
1300	1290	1222	1040	829
720	1423	1214	1102	786
150 (2)				

Adapted from frequencies of cyclopentene.[34]

II. Cyclopentyl Ring Opening

2950 (9), 1513, 1487, 1449, 1441, 1319, 892, 1268, 1257, 1215, 1193, 1187, 1064, 1035, 944, 843, 796, 620, 480, 1573, 1013, 926, 921, 534, 375, 252, 157

III. H + Methylenecyclobutane

2950 (8)	1340	1490	1415	1395
1197	954	944	895	1130
1061	890	836	1425	1385
1248	1167	728	526	373
1070	879	870	800	354
130	150 (2)			

Adapted from frequencies of methylenecyclobutane.[23]

IV. Methylcyclobutyl-1 Ring Opening

2950 (9), 1595, 1473, 1467, 1460, 1458, 1367, 1312, 1295, 1098, 1080, 961, 918, 842, 673, 484, 1042, 1028, 1611, 992, 903, 777, 197, 502, 395, 340, 168

B. Radicals

I. Cyclopentyl Radical

2950 (9)	1465	1447	1431 (2)	1350 (2)
1330	1302	1293	1285 (2)	1210 (2)
1021 (2)	720 (2)	575	1043 (2)	890 (2)
871	624 (2)	282 (2)		

Adapted from frequencies of cyclopentane.[35]

II. Methylcyclobutyl Radical

2950 (9)	1465	1462	(2)	1447		1444
1374	1265	1260		1223	(2)	1205
1168	1148	1146		1104		1011
950 (2)	943	918		901		745
651 (2)	373	354		130		

References and Notes

(1) Taken in part from the doctoral thesis of W. P. L. Carter, University of Iowa, 1973.
(2) (a) M. Julia, Pure Appl. Chem., 15, 167 (1967); J. W. Wilt in "Free Radicals," Wiley-Interscience, New York, N. Y., 1973, pp 333–502; (b) R. Walsh, Int. J. Chem. Kinet., 2, 71 (1970).
(3) M. J. Pearson and B. S. Rabinovitch, J. Chem. Phys., 42, 1624 (1965).
(4) G. Greig and J. C. J. Thyne, Trans. Faraday Soc., 62, 3338 (1966); J. A. Kerr, A. Smith, and A. F. Trotman-Dickenson, J. Chem. Soc. A, 1400 (1969).
(5) A. S. Gordon, S. R. Smith, and C. M. Drew, J. Chem. Phys., 36, 824 (1962); A. S. Gordon, Int. J. Chem. Kinet., 2, 75 (1970).
(6) S. W. Benson and H. E. O'Neal, Nat. Stand. Ref. Data Ser., Nat. Bur. Stand., No. 21 (1970).
(7) K. W. Watkins and D. K. Olsen, J. Phys. Chem., 76, 1089 (1972).
(8) R. A. Marcus and O. K. Rice, J. Phys. Colloid. Chem., 55, 894 (1951); R. A. Marcus, J. Chem. Phys., 20, 359 (1952).
(9) R. J. Cvetanovic, Progr. React. Kinet., 2, 39 (1964).
(10) A. F. Trotman-Dickenson and G. S. Milne, Nat. Stand. Ref. Data Ser., Nat. Bur. Stand., No. 9 (1967).
(11) W. P. L. Carter and D. C. Tardy, J. Phys. Chem., submitted for publication.
(12) D. C. Tardy and B. S. Rabinovitch, J. Chem. Phys., 48, 5194 (1968).
(13) C. W. Larson and B. S. Rabinovitch, J. Chem. Phys., 50, 871 (1969).
(14) S. Furuyama, D. M. Golden, and S. W. Benson, Int. J. Chem. Kinet., 2, 83 (1970).
(15) D. M. Golden and S. W. Benson, Chem Rev., 69, 125 (1969).
(16) F. D. Rossini, "Selected Values of Physical and Thermodynamic Properties of Hydrocarbons and Related Compounds," Carnagie Press, Pittsburgh, Pa., 1953.
(17) S. W. Benson, F. R. Cruickshank, D. M. Golden, G. R. Haugen, H E. O'Neal, A. S. Rodgers, R. Shaw, and R. Walsh, Chem. Rev. 69, 279 (1969).
(18) D. F. McMillen, D. M. Golden, and S. W. Benson, Int. J. Chem. Kinet., 4, 487 (1972).
(19) W. P. L. Carter, Ph.D. Thesis, University of Iowa, Iowa City, Iowa, 1973.
(20) W. P. L. Carter and D. C. Tardy, manuscript in preparation.
(21) L. M. Sverdlov and N. I. Prokofeva, Opt Spektrosk., 7, 363 (1959).
(22) E. P. Krainov, N. I. Prokofeva, and L. M. Sverdlov, Opt. Spektrosk., 16, 309 (1964).
(23) W. J. Engelbrecht, M. J. De Vries, and J. S. Afric, Chem. Inst., 23, 191 (1970).
(24) W. P. L. Carter and D. C. Tardy, J. Phys. Chem., submitted for publication
(25) H. S. Johnston, "Gas Phase Reaction Rate Theory," Ronald Press, New York, N. Y., 1966, pp 80–83.
(26) J. O. Hirschfelder, C. F. Curtis, and R. B. Bird, "Molecular Theory of Gases and Liquids," Wiley, New York, N. Y., 1954.
(27) F. J. Fletcher, B. S. Rabinovitch, K. W. Watkins, and D. J. Locker, J. Phys. Chem., 70, 2823 (1966).
(28) Y. N. Lin, S. C. Chan, and B. S. Rabinovitch, J. Phys. Chem., 72, 1932 (1968).
(29) Y. N. Lin and B. S. Rabinovitch, J. Phys. Chem., 74, 3151 (1968).
(30) D. C. Tardy and B. S. Rabinovitch, J. Chem. Phys., 45, 3720 (1966).
(31) S. P. Pavlou and B. S. Rabinovitch, J. Phys. Chem., 75, 3037 (1971).
(32) R. J. Cvetanovic and R. S. Irwin, J. Chem. Phys., 46, 1694 (1967).
(33) These values were calculated in the present experiments
(34) L. M. Sverdlov and E. N. Krainov, Opt. Spektrosk., 6, 214 (1959).
(35) L. M. Sverdlov and N. V. Tarsova, Opt. Spektrosk., 9, 159 (1960).

Analysis of External Activation Systems with Multiple Isomerizations and Decompositions[1]

W. P. L. Carter and D. C. Tardy*

University of Iowa, Department of Chemistry, Iowa City, Iowa 52242 (Received November 21, 1973)

A general method for the steady-state analysis of complex external activation systems with multiple isomerization and decompositions is developed. This method is used for both "strong" and "weak" collisions. The algorithm for such an analysis is discussed.

Introduction

Unimolecular isomerization of vibrationally excited species produced in the gas phase by external activation has recently been receiving attention.[2-5] In some cases, such as chemically activated free radicals,[3-5] quite complicated networks of interacting isomers are possible. In such systems, it is desired to obtain methods of calculating the observed product yields. Steady-state calculations of product yields at various pressures using rate constants calculated by RRKM theory[6] and various energy transfer models[7,8] have been found to be very useful in systems where isomerization is not important.[8,9] Such comparisons of theory with experiment can be used to obtain critical energies, test activated complex models, or test energy transfer models. However, especially in the case of systems with more than two interconverting isomers, such calculations are usually not done with the same degree of accuracy because of the lack of simple expressions for use in obtaining the steady-state populations. This is especially true in systems where the strong collision approximation is not valid; the iterative technique that has been used in nonisomerizing systems[7,9] has been found by us to be generally unsatisfactory in studying isomerizations, especially when isomerization is fast compared to decomposition and stabilization. Even for strong collisions, solving by hand the algebra of the steady-state equations for a system with isomerizations is usually tedious and error-prone. A method is described here where the pressure dependence of product yields can be computer calculated without the need for first manipulating the steady-state equations by hand. This is useful for systems with weak as well as strong collisions.

Theory

Consider a system of interconverting isomers at various levels of excitation. The state of that system is specified by both its energy level and its isomeric form. Although in general there is an extremely large number of energy levels in a given range, it is necessary to use a structure of equally spaced levels, each level characterized by a statistical weight reflecting the actual number of quantum levels in its neighborhood. It is useful to distinguish between activated and stabilized energy levels. A stabilized level corresponds to an energy low enough so that once the species is in that level there is no significant probability of a unimolecular reaction even after a number of collisions. Clearly, such a state can exist only if the temperature is low enough so that thermalized species have little probability of reacting. This is assumed to be the case in the external activation systems under discussion here.

For each state i, the energy is given by E_i and the iso-

meric form is given by r_i and the following steady-state relation is assumed (input = output)

$$f_i + \sum_j k_{ij} n_j + \omega \sum_j P_{ij} n_j = \left(\sum_d k_i{}^d + \sum_j k_{ji} + \omega \right) n_i \quad (1)$$

(where all summations are over only activated states). n_i = the concentration of species with form r_i and energy E_i. If $r_i \neq r_j$ but $E_i = E_j$ then k_{ij} is the rate constant for isomerization of isomer r_j to r_i at energy E_i; otherwise, k_{ij} = 0. $k_i{}^d$ is the rate constant for decomposition from state i via path d. In general, there may be more than one way a species can decompose. $k_i{}^d = 0$ if path d is not a decomposition undergone by isomer r_i. f_i is the input flux into state i due to the external activation reaction. If $r_i = r_j$, then P_{ij} is the probability of isomer r_i going from energy E_j to energy E_i upon collision with a bath gas molecule; otherwise, P_{ij} is zero. Such collisions occur with the pseudounimolecular rate constant ω, proportional to the gas pressure. It is useful to define a quantity s_i

$$s_i = 1 - \sum_j P_{ji} \quad (2)$$

This is the probability of going from state i to a stabilized state upon collision.

The quantities that are actually measured are the total amount of decomposition via path d

$$D^d = \sum_i k_i{}^d n_i \quad (3)$$

or the amount of isomer p that is stabilized

$$S^p = \sum_{\{i:r_i = p\}} s_i n_i \quad (4)$$

(to calculate stabilization, one sums only over levels of the isomer under consideration). It may also be of interest to determine the isomerization flux of isomer p going to isomer q

$$\text{flux } (p \longrightarrow q) = \sum_{\{(i,j):r_i = p, r_j = q\}} k_{ji} n_i$$

These quantities must be calculated since they are related to the measured quantities of an experiment. From RRKM theory,[6] k_{ij} and $k_i{}^d$ can be calculated from any E_i. We will assume that f_i is also known since it can be calculated[10] in most chemical activation systems. The probabilities P_{ij} depend on the energy transfer model chosen; calculations of these probabilities are discussed elsewhere.[7] Thus, it remains to determine, from eq 1, the steady-state populations n_i. Once these populations have been calculated, the pressure dependence of any function of the decomposition or stabilization yields of isomeriza-

tion fluxes can be calculated and compared with experiment.

The populations can be found by a matrix inversion technique. Although the energy levels can go up arbitrarily high, sufficiently high levels will not be significantly populated, so one need only consider a finite number of states. Then (1) can be recast into matrix notation

$$\mathbf{f} = \mathbf{J}_w(\omega)\mathbf{n} \tag{5}$$

$\mathbf{J}_w(\omega)$ can be partitioned such that its submatrices are

$$J_{ij}(\omega) =$$

$$(\sum_j k_{ji} + \omega + \sum_d k_i{}^d) - P_{ij} \qquad \text{if } r_i = r_j \tag{6}$$

$$J_{ij} = - k_{ij} \qquad \text{if } r_i \neq r_j; E_i = E_j$$

$$J_{ij} = 0 \qquad \text{if } r_i \neq r_j; E_i \neq E_j$$

Therefore

$$\mathbf{n} = \mathbf{J}_w{}^{-1}(\omega)\mathbf{f} \tag{7}$$

Since $\mathbf{J}_w(\omega)$ can be inverted by standard numerical techniques, the problem has in theory been solved. Due to the size of $\mathbf{J}_w(\omega)$, number of energy level times the number of isomers, more efficient ways than brute-force inversion must be used.

It is useful to treat the strong collision case separately. Under the strong collision assumption, all collisions stabilize, i.e., all $P_{ij} \equiv 0$ and $s_i \equiv 1$. Thus each energy level is independent of the others. For each energy E, eq 8 gives the steady-state relation for isomer p. (Here, p and q index isomeric form only.) The symbols are analogous to those in eq 1

$$f_p(E) + \sum_q k_{pq}(E)n_q(E) =$$

$$(\sum_d k_p{}^d(E) + \sum_q k_{qp}(E) + \omega)n_p(E) \tag{8}$$

Therefore, for each energy level the steady-state populations of the various isomers are given

$$\mathbf{n}(E) = \mathbf{J}_s{}^{-1}(E, \omega)\mathbf{f}(E) \tag{9}$$

where the submatrices of $\mathbf{J}_s(E,\omega)$ are

$$J_{pp}(E, \omega) = \sum_q k_{qp}(E) + \omega + \sum_d k_p{}^d(E)$$

$$J_{pq}(E) = - k_{pq}(E) \qquad \text{for } p \neq q$$

In this case, the arrays have their dimension equal to the number of isomers, r, rather than ϵ times r. Thus one solves ϵ $r \times r$ matrix inversions rather than one $\epsilon r \times \epsilon r$ matrix inversion. In the weak collision case, where different energy levels interact, such a simplification can not be made; it is still necessary to invert the full $\mathbf{J}_w(\omega)$. However, there is a similarity in the form of $\mathbf{J}_w(\omega)$ and $\mathbf{J}_s(E,\omega)$ as shown by eq 10 and 11.

$$\mathbf{J}_s(E, \omega) = \begin{bmatrix} k_1{}^*(E) + \omega & - k_{12}(E) & \cdot & \cdot \\ - k_{21}(E) & k_2{}^*(E) + \omega & \cdot & \cdot \\ \cdot & & \cdot & \cdot \\ \cdot & & \cdot & \cdot \end{bmatrix} \tag{10}$$

$$\mathbf{J}_w(\omega) =$$

$$\begin{bmatrix} \mathbf{k}_1{}^* + \omega(\mathbf{I} - \mathbf{P}_1) & - \mathbf{k}_{12} & \cdot & \cdot \\ - \mathbf{k}_{21} & \mathbf{k}_2{}^* + \omega(\mathbf{I} - \mathbf{P}_2) & \cdot & \cdot \\ \cdot & \cdot & \cdot & \cdot \\ \cdot & \cdot & & \cdot \end{bmatrix}$$

$$\tag{11}$$

where

$$k_p{}^*(E) = \sum_q k_{pq}(E) + \sum_d k_p{}^d(E) \tag{12}$$

Physically, $k_p{}^*(E)$ refers to the total rate of unimolecular reaction out of a given state of isomer p. The subarrays of $\mathbf{J}_w(\omega)$ are arrays over the activated energy levels of a single isomer.

Steady-State Populations. Strong Collision

Although the strong collider steady states can be calculated evaluating the elements of $\mathbf{J}_s(E,\omega)$ at each energy level for each pressure and numerically inverting it for each energy level, clearly such a calculational technique would be less efficient than it could be if a general formula were involved. Thus one wants to be able to invert $\mathbf{J}$ symbolically and obtain, if not one simple equation, at least a series of assignment statements for computing $\mathbf{n}$ from $\mathbf{J}$ and $\mathbf{f}$. However, solving the linear equations by hand for an isomerization network of even moderate complexity is usually prohibitively tedious. Described is a method by which a computer program is used to obtain the assignment statements that the steady-state program would use to obtain $\mathbf{n}$, and thus the decomposition and stabilization yields, from $\mathbf{J}$ and $\mathbf{f}$.

This method is most easily explained by means of two examples. First consider a system of two interconverting isomers, where each isomer can be formed by an external activation mechanism and either decompose or be stabilized with rate constants k_i and ω, respectively

$$\xleftarrow{k_1 + \omega} (1) \underset{k_{21}}{\overset{k_{12}}{\rightleftharpoons}} (2) \xrightarrow{k_2 + \omega}$$
$$f_1 \uparrow \qquad f_2 \uparrow$$
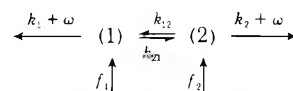
Let $J_{11} = k_{21} + k_1 + \omega$, etc. The steady-state relation is

$$\begin{bmatrix} f_1 \\ f_2 \end{bmatrix} = \begin{bmatrix} J_{11} & - k_{12} \\ - k_{21} & J_{22} \end{bmatrix} \begin{bmatrix} n_1 \\ n_2 \end{bmatrix} \tag{13}$$

or solving for the steady-state populations

$$\begin{bmatrix} n_1 \\ n_2 \end{bmatrix} = \begin{bmatrix} J_{11} & - k_{12} \\ - k_{21} & J_{22} \end{bmatrix}^{-1} \begin{bmatrix} f_1 \\ f_2 \end{bmatrix}$$

Any matrix may be partitioned such that[11] its inverse is also subdivided, i.e.

$$\begin{bmatrix} \mathbf{a}_{11} & \mathbf{a}_{12} \\ \mathbf{a}_{21} & \mathbf{a}_{22} \end{bmatrix}^{-1} = \begin{bmatrix} \mathbf{b}_{11} & \mathbf{b}_{12} \\ \mathbf{b}_{21} & \mathbf{b}_{22} \end{bmatrix}$$

The a's and b's can be either scalars or matrices and are related by the following relations.[11]

$$\mathbf{b}_{11} = \mathbf{a}_{11}{}^{-1} + \mathbf{a}_{11}{}^{-1}\mathbf{a}_{12}(\mathbf{a}_{22}')^{-1}\mathbf{a}_{21}\mathbf{a}_{11}{}^{-1}$$

$$\mathbf{b}_{21} = -(\mathbf{a}_{22}')^{-1}\mathbf{a}_{21}\mathbf{a}_{11}{}^{-1}$$

$$\mathbf{b}_{12} = -\mathbf{a}_{11}{}^{-1}\mathbf{a}_{12}(\mathbf{a}_{22}')^{-1}$$

$$\mathbf{b}_{22} = (\mathbf{a}_{22}')^{-1}$$

where

$$\mathbf{a}_{22}' = \mathbf{a}_{22} - \mathbf{a}_{21}\mathbf{a}_{11}^{-1}\mathbf{a}_{12}$$

Equations 14 and 15 result for the solution to $\mathbf{n}_1$ and $\mathbf{n}_2$.

$$\mathbf{n}_1 = \mathbf{a}_{11}^{-1}\mathbf{f}_1 +$$

$$\mathbf{a}_{11}^{-1}\mathbf{a}_{12}(\mathbf{a}_{22}')^{-1}\mathbf{a}_{21}\mathbf{a}_{11}^{-1}\mathbf{f}_1 - \mathbf{a}_{11}^{-1}\mathbf{a}_{12}(\mathbf{a}_{22}')^{-1}\mathbf{f}_2 \quad (14)$$

$$\mathbf{n}_2 = -(\mathbf{a}_{22}')^{-1}\mathbf{a}_{21}\mathbf{a}_{11}^{-1}\mathbf{f}_1 + (\mathbf{a}_{22}')^{-1}\mathbf{f}_2 \quad (15)$$

Instead of expressing equivalence, eq 14 and 15 can be thought of as assignment statements used by a computer program. In that case, the same values in n_1 and n_2 are obtained by the following

$$\mathbf{n}_1 \longleftarrow \mathbf{a}_{11}^{-1}\mathbf{f}_1 \quad (16)$$

$$\mathbf{n}_2 \longleftarrow -\mathbf{a}_{21}\mathbf{n}_1 + \mathbf{f}_2 \quad (17)$$

$$\mathbf{n}_2 \longleftarrow (\mathbf{a}_{22}')^{-1}\mathbf{n}_2 \quad (18)$$

$$\mathbf{n}_1 \longleftarrow \mathbf{n}_1 + \mathbf{a}_{11}^{-1}\mathbf{a}_{12}\mathbf{n}_2 \quad (19)$$

Thus eq (statements) 16–19 provide a scheme for arriving at n_1 and n_2 from the matrix in eq 13 where

$$a_{11} = J_{11}$$

$$a_{22} = J_{22}$$

$$a_{12} = -k_{12}$$

$$a_{21} = -k_{21}$$

Now consider a more complex system consisting of three interconverting isomers. Using the terminology developed for two isomers the scheme is shown below.
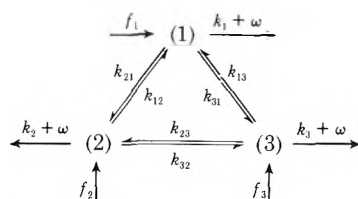
Let $J_{11} = k_{21} + k_{31} + k_1 + \omega$, etc. The steady-state relation is

$$\begin{bmatrix} f_1 \\ \cdot\cdot \\ f_2 \\ f_3 \end{bmatrix} = \begin{bmatrix} J_{11} & \cdot & -k_{12} & -k_{13} \\ \cdot\cdot & \cdot & \cdot\cdot\cdot\cdot\cdot & \cdot\cdot\cdot\cdot\cdot \\ -k_{21} & \cdot & J_{22} & -k_{23} \\ -k_{31} & \cdot & -k_{32} & J_{33} \end{bmatrix} \begin{bmatrix} n_1 \\ \cdot\cdot \\ n_2 \\ n_3 \end{bmatrix} \quad (20)$$

Equation 20 involving three simultaneous equations can be partitioned, as shown by the dotted lines, into one eq 21 involving two simultaneous equations.

$$\begin{bmatrix} f_1 \\ \mathbf{f}_2'' \end{bmatrix} = \begin{bmatrix} J_{11} & -\mathbf{k}_{12}'' \\ -\mathbf{k}_{21}'' & \mathbf{J}_{22}'' \end{bmatrix} \begin{bmatrix} n_1 \\ \mathbf{n}_2'' \end{bmatrix} \quad (21)$$

where

$$\mathbf{f}_2'' = \begin{bmatrix} f_2 \\ f_3 \end{bmatrix}; \quad \mathbf{n}_2'' = \begin{bmatrix} n_2 \\ n_3 \end{bmatrix}; \quad \mathbf{k}_{21}'' = \begin{bmatrix} k_{21} \\ k_{31} \end{bmatrix}$$

$$\mathbf{k}_{12}'' = \begin{bmatrix} k_{12} & k_{13} \end{bmatrix}; \quad \mathbf{J}_{22}'' = \begin{bmatrix} J_{22} & -k_{23} \\ -k_{32} & J_{33} \end{bmatrix}$$

n_1 and n_2'' are obtained using statements analogous to statements 16–19, respectively

$$n_1 \longleftarrow (1/J_{11})f_1 \quad (16')$$

$$\mathbf{n}_2'' \longleftarrow \mathbf{k}_{21}''n_1 + \mathbf{f}_2'' \quad (17')$$

i.e.

$$n_2 \longleftarrow k_{21}n_1 + f_2 \quad (17.1')$$

and

$$n_3 \longleftarrow k_{31}n_1 + f_3 \quad (17.2')$$

$$\mathbf{n}_2'' \longleftarrow (\mathbf{J}_{22}''')^{-1}\mathbf{n}_2'' \quad (18')$$

$$n_1 \longleftarrow n_1 + (1/J_{11})\mathbf{k}_{12}''\mathbf{n}_2'' \quad (19')$$

i.e.

$$n_1 \longleftarrow n_1 + (1/J_{11})(k_{12}n_2 + k_{13}n_3) \quad (19.1')$$

where $\mathbf{J}_{22}''' = \mathbf{J}_{22}'' - \mathbf{k}_{21}''(1/J_{11})\mathbf{k}_{12}''$. Equation (statement) 18' requires the inversion of $\mathbf{J}_{22}'''$. If we let

$$\mathbf{J}_{22}''' = \begin{bmatrix} a_{22} & a_{23} \\ a_{32} & a_{33} \end{bmatrix}$$

and use the relations between the a's and b's used earlier, statement 18' can be replaced by

$$n_2 \longleftarrow (1/a_{22})n_2 \quad (18.1')$$

$$n_3 \longleftarrow a_{32}n_2 + f_3 \quad (18.2')$$

$$n_3 \longleftarrow (1/a_{33}')n_3 \quad (18.3')$$

where

$$a_{33}' = a_{33} - a_{32}(1/a_{22})a_{23}$$

$$n_2 \longleftarrow n_2 + (1/a_{22})a_{23}n_3 \quad (18.4')$$

Note that if this system had more than three species, b_{33}' would not be a scalar, and additional inversion statements would replace (22.3). But in this case, the statements 20–23 above constitute a complete algorithm for obtaining $\mathbf{n}$ from $\mathbf{J}_s(E,\omega)$ and $\mathbf{f}$. Clearly this scheme can be generalized to any number of interconverting species, particularly the more specific case when some of the k's and f's are zero.

A computer program producing the assignment statements for the solution of any specific isomerization network using these general principles is not complicated. A pseudo-Fortran "program" to perform these operations is given in the Appendix.

Steady-State Populations. Weak Collision

Recognizing the similarity of $\mathbf{J}_w(\omega)$ to $\mathbf{J}_s(E,\omega)$ shown by eq 10 and 11, the inversion of $\mathbf{J}_w$ can be considered analogous to the inversion of $\mathbf{J}_s$; where the elements of $\mathbf{J}_w$ are square matrices rather than scalars. However, each of the operations on the scalars in eq 20–21 have corresponding valid matrix-vector operations, where $\mathbf{J}_{11}$, $\mathbf{k}_{12}$, etc. are considered to be square matrices and $\mathbf{f}_1$, $\mathbf{n}_2$, etc. are vectors whose dimension is the number of energy levels. (Note that commutivity of scalars has not been used in the strong collision example.) Therefore, this method can be applied to solving the weak collision steady state, where (for example) $\mathbf{J}_{11}$, $\mathbf{J}_{22}'$ are inverted by standard

matrix inversion techniques. This method is much more efficient than the brute-force inversion of $\mathbf{J}_w(\omega)$, especially considering that the off-diagonal submatrices (such as $\mathbf{k}_{12}$) are themselves diagonal, so multiplication operations are rapid and much less storage space is required than if all of $\mathbf{J}_w(\omega)$ had to be stored at once, as would be required for a standard inversion procedure.

The assignment statements obtained for the strong collision problem readily indicate how to code calls to matrix-vector operation routines for obtaining the weak collision populations, as the operations in both cases are analogous.

Conclusion

It is now feasible to calculate decomposition and stabilization yields, and isomerization fluxes in external activation systems with multiple isomerizations of any complexity with any reasonable energy transfer model. The scheme presented here can be used in obtaining isomerization and decomposition energy parameters and in testing models for activated complexes in systems where otherwise such analysis would be very difficult or approximate.[3] Microscopic rate constants are calculated from the activated complex models and the energy parameters using RRKM theory;[6] the assignment statements obtained as described above are used to obtain steady-state populations needed for the calculation of decomposition or stabilization yield ratios, which aré compared with experimental values. The Fortran programs used are available from the authors.[12]

Appendix. Program for Obtaining Assignment Statements

The main features of the computer program producing assignment statements for use in obtaining steady-state populations is given below. Correct Fortran syntax is sacrificed in places to improve clarity. The following symbols are used, and are assumed to be appropriately defined before the subroutine given below is entered: N = number of isomers; I, J, K index isomers; $R(I)$ = name of isomer I (*i.e.*, location $R(I)$ contains characters giving isomer name); $F(I)$ = name of input flux if external activation input into isomer I (If no such input, $F(I)$ must contain blank characters); $L(I,I)$ = symbol corresponding to isomer I, but not the same as $R(I)$; $L(I,J)$ = rate constant name for isomerization of isomer J to I (If no such isomerization, $L(I,J)$ should be blank). A statement such as WRITE $R(I),' = ', L(I,I)$, etc. refers to writing the characters in $R(I)$, the character "=", etc. On the other hand, the statement WRITE ..., J, ... says to write the integer which is the current value of J. The program follows.

```
SUBROUTINE EXAMPLE (R,F,F,L)
IMPLICIT INTEGER*4 (A-Z)
DIMENSION R(N),F(N),L(N,N)
DATA BLANK/'    '/
LOGICAL SUM
C
      DO 10 K=1,N-1
      WRITE L(K,K),'=1.0/',L(K,K)
      DO 11 I=K+1,N
      DO 12 J=K+1,N
      IF ((L(I,K).EQ.BLANK).OR.(L(K,J).EQ.BLANK)) GO TO 12
      IF (I.NE.J) GO TO 121
C I=J
      WRITE L(I,I),'=',L(I,I),'-',L(I,K),'*',L(K,K),'*',
     X L(K,I)
      GO TO 12
C I≠J
 121 IF(L(I,J).NE.BLANK) WRITE 'X',I,J,'=',L(I,J),'+',L(I,K),
     '*',L(K,K),'*'.L(K,J)

      IF(L(I,J).EQ.BLANK) WRITE 'X',I,J,'=',L(I,K),'*',L(K,K),
     '*',L(K,J)
      L(I,J) = 'X',I,J
C I.E., IF I=2,J=3 THEN SET L(2,3) = 'X23'
 12   CONTINUE
 11   CONTINUE
 10   CONTINUE
      WRITE L(N,N),'=1.0/',L(N,N)
C
      DO 20 K=1,N
      IF (F(K).EQ.BLANK) GO TO 20
      WRITE R(K),'=',I(K,K),'*',F(K)
      F(K)=R(K)
      IF (K.EQ.N) GO TO 20
      DO 21 I=K+1,N
      IF (L(I,K).EQ.BLANK) GO TO 21
      IF (F(I).EQ.BLANK) GO TO 201
      WRITE R(I),'=',F(I),'+',L(I,K),'*',R(K)
      F(I)=R(I)
      GO TO 21
 201  WRITE R(I),'=',L(I,K),'*',R(K)
      F(I)=R(I)
 21   CONTINUE
 20   CONTINUE
C
      DO 30 K=N-1,1,-1
      SUM=.FALSE.
      DO 31 I=K+1,N
      IF ((L(K,I).EQ.BLANK).OR.(F(I).EQ.BLANK)) GO TO 31
      IF (SUM) GO TO 311
      SUM=.TRUE.
      WRITE 'X =',L(K,I),'*',R(I)
      GO TO 31
 311  WRITE 'X = X +',L(K,I),'*',R(I)
 31   CONTINUE
      IF (SUM.AND.(F(K).NE.BLANK)) WRITE R(K),'=',R(K),'+',
     X L(K,K),'* X'
      IF (SUM.AND.(F(K).EQ.BLANK)) WRITE R(K),'=',L(K,K),
     X '* X'
 30   CONTINUE
C NOW ALL ASSIGNMENT STATEMENTS HAVE BEEN WRITTEN
      RETURN
      END
```

References and Notes

(1) Taken in part from the doctoral thesis of W. P. L. Carter, University of Iowa, 1973.

(2) J. W. Simmons and B. S. Rabinovitch, *J. Phys. Chem.*, **68**, 1322 (1964); E. Jakubowski, H. S. Sandhu, and O. P. Strausz, *J. Amer. Chem. Soc.*, **93**, 2610 (1971).

(3) W. P. L. Carter and D. C. Tardy, *J. Phys. Chem.*, submitted for publication.

(4) K. W. Watkins and L. A. O'Deen, *J. Phys. Chem.*, **75**, 2265 (1971); **76**, 1089 (1972).

(5) C. W. Larson, P. T. Chua, and B. S. Rabinovitch, *J. Phys. Chem.*, **76**, 2507 (1972).

(6) R. A. Marcus and O. K. Rice, *J. Phys. Colloid. Chem.*, **55**, 894 (1951); R. A. Marcus, *J. Chem. Phys.*, **20**, 359 (1952); See also P. J. Robinson and K. A. Holbrook, "Unimolecular Reactions," Wiley-Interscience, London, 1972, for discussion and review of RRKM theory.

(7) D. C. Tardy and B. S. Rabinovitch, *J. Chem. Phys.*, **45**, 3720 (1966).

(8) J. D. Rynbrandt and B. S. Rabinovitch, *J. Phys. Chem.*, **74**, 1679 (1970).

(9) D. C. Tardy and B. S. Rabinovitch, *J. Chem. Phys.*, **48**, 5194 (1968); D. W. Setser and E. E. Siefert, *ibid.*, **57**, 3616 (1972).

(10) B. S. Rabinovitch and R. W. Diesen, *J. Chem. Phys.*, **30**, 735 (1959); R. E. Harrington, B. S. Rabinovitch, and R. W. Diesen, *ibid.*, **32**, 1245 (1960).

(11) R. A. Frazer, W. J. Duncan, and A. R. Collar, "Elementary Matrices," Cambridge University Press, New York, N. Y., 1950, p 112.

(12) W. P. L. Carter, Ph.D. Thesis, University of Iowa, Iowa City, Iowa, 1973.

Dual Photon Effects in Nitrogen Dioxide Photolysis

D. Hakala, P. Harteck,* and R. R. Reeves

Rensselaer Polytechnic Institute, Department of Chemistry, Troy, New York 12181 (Received December 7, 1973)

The photolysis of NO_2 has been studied using the pulsed ruby laser. As reported earlier the NO and O_2 is formed where the energy of the photons of wavelength 6943 Å corresponds to 41.2 kcal, while the dissociation energy of NO_2 (to NO + O atom) corresponds to 71.8 kcal. The process required the assumption of energy pooling of some type and the consecutive absorption of two photons was postulated. The production of oxygen by NO_2 photolysis was anticipated to be dependent on the square of the intensity of the laser pulse. Results reported here confirm this relationship over a range of intensity from 2×10^{18} to 6×10^{18} photons per pulse. Fluorescence around 4000 Å is observed which is of short duration with intensity and lifetime dependent on pressure. At constant pressure the intensity of fluorescence is also approximately dependent on the square of the intensity of the laser pulse. The fraction of fluorescence emission is estimated to be less than 10^{-11} of the laser pulse intensity.

Introduction

A previous study done in this laboratory demonstrated two-photon consecutive absorption as being the most probable mechanism for the photodissociation of NO_2 using a pulsed ruby laser at 6943 Å.[1] Additional data reported here confirmed this and also examined associated phenomenon, that of multiphoton induced fluorescence.

The dissociation of NO_2 by ON-O bond cleavage requires 3.14 eV, while the laser energy corresponds to 1.785 eV.[2] The pooling of the energy of two photons would give more than enough energy to dissociate the NO_2 into NO + O.

Several mechanisms including one, simultaneous absorption of two photons; two, reaction of two singly excited NO_2; three, reaction of a singly excited NO_2 with a ground state NO_2; and four, consecutive absorption of two photons were examined. All but the last, the consecutive absorption of two photons (mechanism four), were eliminated since for mechanism one, there would have been too low a yield of O_2 to otherwise account for the observed product; for two, an (NO_2) pressure squared dependence would have been expected whereas a first-order dependence on (NO_2) was observed at lower pressures and the yield of O_2 would have been lower than that observed; and for three, although energetically possible this third mechanism has never been observed as would be expected in other normal photolysis experiments of NO_2 with wavelength above the dissociation limit.

In earlier experiments direct evidence that the reaction was second order with respect to laser intensity had not been observed. This evidence along with the observation of a fluorescence in the blue region of the spectrum was found and is reported below.

Experimental Section

The same Korad K-1 laser system was used as before except that the cryptocyanine dye passive Q switch had been replaced by an electronic Q switch providing much greater reproducibility and nearly eliminating all problems with multiple pulsing. Energy of the laser output was found to be 2.28 J (or 8×10^{18} photons/pulse) with a half width duration of 10 nsec.

Laser intensity was varied by firing the laser through optically flat Pyrex plates held at set angles in slotted aluminum channeling mounted on an optical rail. This apparatus was calibrated using a Spectra-Physics continuous mode He–Ne laser, monitoring the transmitted intensity with a filtered RCA 1P21 photomultiplier.

The O_2 formed was analyzed using a CEC 21-130 mass spectrometer. The sample was flowed through a U-tube at liquid nitrogen temperature before entering the mass spectrometer. All the NO_2 was frozen out on the walls, and the O_2 and Ar were measured without interference at m/e 32 from the $^{14}N^{18}O^+$ peak which ordinarily would make impossible measurement of small amounts of O_2 in NO_2. Back reaction of O_2 with either NO or solid N_2O_3 was estimated to be negligible under the conditions used in the time period from start of photolysis to end of analysis (20 min). The fluorescent emission was observed using an RCA 8575 photomultiplier, following the decay on a Tektronix 7904 oscilloscope and photographing the trace with the C51 camera unit. The fluorescence unit was of conventional arrangement with the important exception of the roles of the primary and secondary filters being reversed. Therefore the exciting light beam passed through a cutoff filter with wavelengths above the cutoff wavelengths being transmitted and the fluorescent light was passed through a filter combination with a window of 3700-4400 Å, wavelength much smaller than the exciting beam. The filters used for excitation were two Corning CS2-64; for emission they were two Corning CS4-72, a Corning CS5-57, and a Kodak Wratten 38A.

Gases were handled as mentioned previously, and the equilibrium constants of Harris and Churney were used for correcting the pressure of NO_2 for the NO_2–N_2O_4 equilibrium.[3] The gas mixture was $^2/_3(NO_2 + N_2O_4)$ and $^1/_3$ Ar.

Results

The results were obtained using two methods of analysis. The O_2 produced by NO_2 photolysis was analyzed using the mass spectrometer. By varying the laser intensity we measured O_2 produced as a function of laser intensity, I_l. A log–log plot (Figure 1) of O_2 vs. I_l gives a
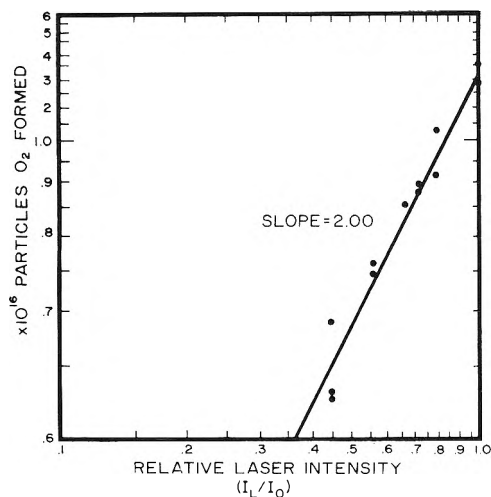
Figure 1.

Figure 2.

straight line with a least-squares slope of 2.00 (σ = ±0.053).[4] This was done at a constant total pressure of 23.2 Torr, corresponding to (NO_2) = 14 Torr.

A weak emission of light in the range of 3700–4440 Å from the flask irradiated with the laser light was observed and the integrated fluorescent intensity, I_F, measured by photographing the oscilloscope display. The log–log plot (Figure 2) of I_F vs. I_L gave a straight line of least-squares slope 2.45 (σ = ±0.063). The total pressure used for these measurements was 65.1 Torr, corresponding to (NO_2) = 32 Torr. The higher pressure was used to obtain sufficient intensities to perform the log–log plot, since the efficiency of fluorescence was very low. At this point it can be noted that the scatter in the data is within the estimated limits of instrumental and experimental error; it is fairly difficult to perform these measurements with greater accuracy. This emission was observed through filters in a wavelength band of 3700–4400 Å.

A plot of I_F vs. (NO_2) was also done (Figure 3) and shows that an intensity maximum is reached around (NO_2) = 40 Torr. The observed lifetimes varied from 40 to 140 nsec over the pressure range studied, with lifetime inversely proportional to pressure.

Discussion

The results of the laser experiments determining oxygen produced at various intensities of the laser were given in the log–log plot (Figure 1). The slope of the least-squares line through these points was 2.0, or the oxygen produced was proportional to the square of the intensity of the laser pulse. That we get an experimental value of 2.0 for O_2 production confirms the previous indication of two-photon consecutive absorption taking place, the mechanism being given by

$$NO_2 + h\nu_L \xrightarrow{\gamma_1} NO_2*$$

$$NO_2* + h\nu_L \xrightarrow{\gamma_2} (NO_2**) \longrightarrow NO + O$$

$$NO_2* + M \xrightarrow{\lambda} NO_2 + M$$
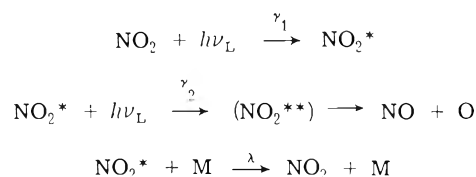
Here M can be any quenching species and λ is the pseudo-first-order quenching constant where $\lambda = k_q(M)$ and (M) is assumed to be constant.[1] This is rapidly followed by

Figure 3.

$$NO_2 + O \longrightarrow NO + O_2$$
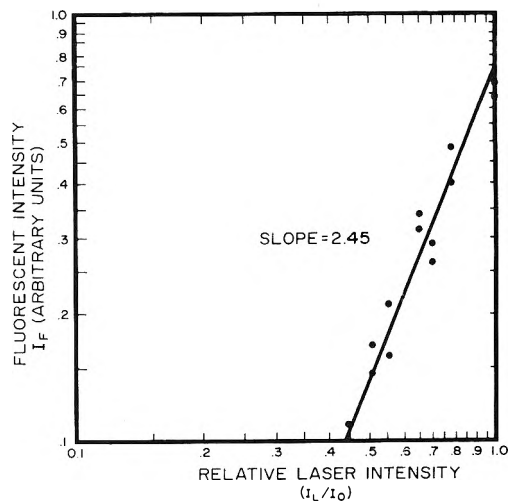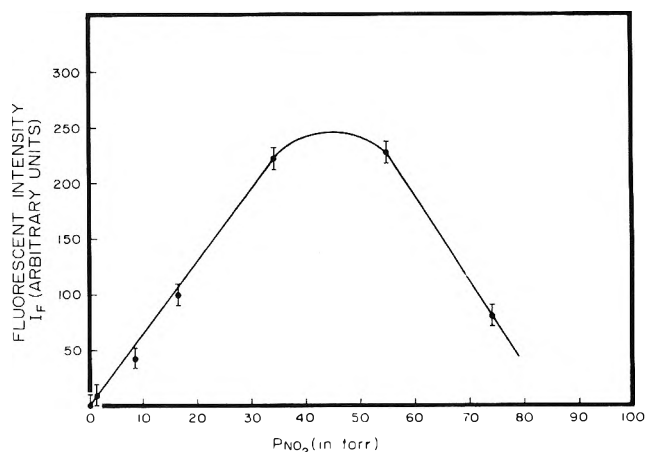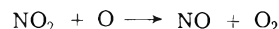
The short-lived intermediate NO_2** will be quenched very little at the pressures of interest, however, quenching of the NO_2* during the 10^{-8} sec pulse duration must be considered for an accurate appraisal of the situation. An equation describing the amount of O_2 produced has been previously developed using the three rate equations for the mechanism above.

$$+ d(NO_2*)/dt = \gamma_1(NO_2)$$

$$+ d(O_2)/dt = \gamma_2(NO_2)$$

$$- d(NO_2*)/dt = [\gamma_2 + \lambda](NO_2*)$$

and assuming that (NO_2) is essentially constant in time (which it is under the experimental conditions used, less than 1% of the NO_2 being excited).

$$(O_2) = \frac{\gamma_1\gamma_2(NO_2)I}{(\gamma_2 + \lambda_1 + \lambda_2 + \ldots)} \times \left[1 + \frac{e^{-(\gamma_2+\lambda_1+\lambda_2+\cdots)T} - 1}{(\gamma_2 + \lambda_1 + \lambda_2 + \ldots)T}\right]$$

Letting quenching of NO_2* equal to zero gives the relation

$$(O_2) = \gamma_1(NO_2)T\left[1 + \frac{e^{-\gamma_2 T} - 1}{\gamma_2 T}\right]$$

Using a power series expansion for e^{-x} and keeping the first three terms gives the simplified equation for the low-pressure limit description of O$_2$ formation

$$(O_2) = \gamma_1 \gamma_2 (NO_2) T^2 / 2$$

where $\gamma_1 = I_L \alpha_1$, $\alpha_1 \simeq 0.15$ cm^{-1} atm^{-1};[5] $\gamma_2 = I_L \alpha_2$, $\alpha_2 \simeq 3.5$ cm^{-1} atm^{-1};[1] T = time of laser pulse = 10^{-8} sec; (NO$_2$) = pressure of NO$_2$. This predicts an I_L dependence on O$_2$ production as was found.

One possible phenomena was that of the energy of two photons "pooling" in some manner that would allow emission of radiation with wavelengths smaller than that of the laser to be observed. A very weak emission was observed and demonstrated a two-photon dependence as indicated by the log-log plot of I_F vs. I_L.[6]

The quantum efficiency, ϕ_f, was estimated for the process

$$NO_2^{**} \longrightarrow NO_2 + h\nu_F$$
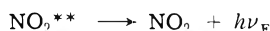
where $\nu_F > \nu_L$, ν_F = frequency of fluorescent light, ν_L = frequency of laser light, and the quantum efficiency is defined as

$$\phi_F = \frac{\text{no. of } h\nu_F \text{ observed}}{\text{no. of possible } NO_2^{**} \text{ formed}}$$

The number of NO$_2$** formed is estimated from the relation describing oxygen formation, assuming that every NO$_2$** dissociates and one O$_2$ is formed. The number of photons is estimated by integrating the signal with respect to time to get the total signal in coulombs, then dividing this by the gain of the photomultiplier tube, the quantum efficiency of the tube in that wavelength region, and the transmittance of the filter combination and finally by multiplying by 1.602×10^{19} (the number of electrons/coulomb) and by $\sim 3 \times 10^3$ which is the estimated geometric factor assuming inverse square dimunition of the light intensity and assuming no effective diffusion of fluorescing species from the beam path. This leads to a value of $\phi_f \sim 6 \times 10^{-9}$ or less than 10^{-11} of the laser pulse is converted to fluorescent light.

The collision-free radiative lifetime of NO$_2$* below its dissociation limit is about 5×10^{-6} sec.[7,8] Since an NO$_2$** above its dissociation limit, probably in the $^2B_2$ upper electronic state, will live for a lifetime of approximately 2×10^{-13} sec,[9,10] one might expect a quantum efficiency for fluorescence on the order of $(2 \times 10^{-13}/5 \times 10^{-6} \sim 4 \times 10^{-8})$. The estimated experimental quantum efficiency is therefore in the neighborhood of one-tenth of that predicted. Characteristic of this emission would be its very short lifetime since no NO$_2$** will last longer than the time of a few vibrations. The experimentally determined relatively long lifetimes of 4×10^{-8} to 1.4×10^{-7} sec indicate that the NO$_2$** is quenched prior to emission or that NO$_2$* is vibrationally quenched before absorbing the second photon. These lifetimes are compatible with the collision-limited lifetimes calculated using the known quenching constants of Myers, Silver, and Kaufman.[11] Using values from the literature for the vibrational energy of NO$_2$* one sees that some combination of three-four vibrational quanta must be lost to yield an NO$_2$* that will have the radiative lifetime observed.[7,8] This fact coupled with the knowledge that an NO$_2$* during the 10^{-8} sec laser pulse will undergo $\sim 5 \times 10^4$ times as many collisions as an NO$_2$** during its 2×10^{-13} sec lifetime leads one to conclude that the mechanism for the dual-

photon-induced fluorescence in the spectral region observed must be

$$NO_2 + h\nu_L \longrightarrow NO_2^*$$
$$NO_2^* + M \longrightarrow NO_2' + M$$
$$NO_2' + h\nu_L \longrightarrow NO_2''$$
$$NO_2'' \longrightarrow NO_2 + h\nu_F$$
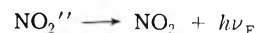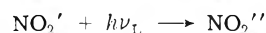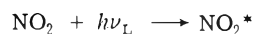
with $\nu_D > \nu_F > \nu_L$ and where NO$_2$' is somewhat vibrationally deactivated, but still in the $^2B_1$ electronically excited state, and ν_D is the frequency of light necessary to dissociate NO$_2$. That the fluorescence process reached its peak at a much higher pressure than the O$_2$ formation is indicative of the role quenching has in enhancing this phenomena.

The marked decrease in I_F with increasing pressure after reaching its maximum value may be attributed to the increasing concentration of N$_2$O$_4$ present at higher pressures. The N$_2$O$_4$ apparently has a very high efficiency for quenching the $^2B_1$ state to the ground level. Also, N$_2$O$_4$ may have an added effect in this scheme since the reaction

$$NO_2^{**} + N_2O_4 \longrightarrow NO_2' + 2NO_2$$

may yield an electronically excited NO$_2$ lower in energy by at least the strength of the O$_2$N–NO$_2$ bond (about 13.0 kcal/mol).[12] This brings the excitation energy below the dissociation limit with one collision and may be one reason that the two-photon process peaks at a higher pressure than O$_2$ production.

No short-lived fluorescence was observed, as might have been expected from NO$_2$* with excitation energy greater than the dissociation. This is not to imply that this and other photon effects were not occurring, but simply were not detectable using our present experimental apparatus. Nevertheless, this technique, for example, did allow the observation of a rare photochemical phenomena without a great deal of interference from the laser beam since the observations were performed at wavelengths both far from the laser line and of much greater energy than the laser line.

In summary we can write a general mechanism for processes induced by the laser photolysis of NO$_2$ as follows

$$NO_2 + h\nu_1 \longrightarrow NO_2^*$$

$$NO_2^* + \begin{cases} M \longrightarrow NO_2 + M \\ M \longrightarrow NO_2' + M \\ h\nu_2 \longrightarrow NO_2^{**} \end{cases}$$

$$NO_2^{**} \begin{cases} \longrightarrow NO(^2\Pi) + O(^3P) \\ + M \longrightarrow NO_2'' + M \end{cases}$$

$$O + NO_2 \longrightarrow NO + O_2$$
$$NO_2' + h\nu_2 \longrightarrow NO_2''$$
$$NO_2'' \longrightarrow NO_2 + h\nu_F$$
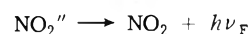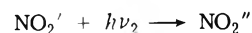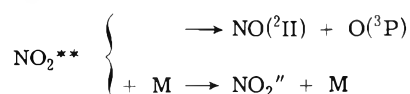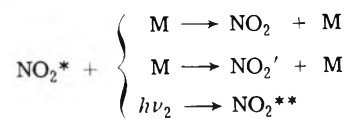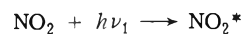
where NO$_2$*, NO$_2$', and NO$_2$'' are all $^2B_1$ excited states but differ in vibrational energy, and NO$_2$** is in the $^2B_2$ state. For reactions where competition can take place the relative rates are determined by laser intensity and pressure. Under our conditions about 20% of the NO$_2$* react to form O$_2$.

Further work on the spectral distribution of this fluorescence and the effects of quenching (for example, Kr $vs.$ CO_2 and particularly that of N_2O_4) on enhancing one pathway over the other is underway.

References and Notes

(1) J. Gerstmayr, P. Harteck, and R. Reeves, *J. Phys. Chem.*, **76**, 474 (1972).
(2) G. Herzberg, "Electronic Spectra of Polyatomic Molecules," Van Nostrand, Princeton, N. J., 1966, p 602.
(3) L. Harris and D. Churney, *J. Chem. Phys.*, **47**, 1703 (1967).
(4) σ = one standard deviation.
(5) J. K. Dixon, *J. Chem. Phys.*, **8**, 157 (1940).
(6) The least-squares slope was 2.45 but some systematic error may account for its being larger than 2.00. It is certainly not less than 2.00. No explanation for a real value of 2.45 is being put forth at this time only for that of 2.00.
(7) L. Keyser, S. Levine, and F. Kaufman, *J. Chem. Phys.*, **54**, 355 (1971).
(8) S. Schwartz and H. Johnston, *J. Chem. Phys.*, **51**, 1286 (1969).
(9) H. Gaedtke, H. Hippler, and J. Troe, *Chem. Phys. Lett.*, **16**, 177 (1972).
(10) G. Busch and K. Wilson, *J. Chem. Phys.*, **56**, 3638 (1972).
(11) G. H. Myers, D. M. Silver, and F. Kaufman, *J. Chem. Phys.*, **44**, 718 (1966).
(12) J. Kerr, *Ann. Rep. Chem. Soc. A*, **64**, 73 (1967).

Cross Disproportionation of Alkyl Radicals

Richard D. Kelley and Ralph Klein*

Surface Chemistry Section, National Bureau of Standards, Washington, D. C. 20234   (Received April 4, 1974)

The cross disproportionation of several alkyl radicals has been measured using a novel technique that eliminates most of the uncertainties characterizing previous gas-phase results. The radicals are prepared in the condensed phase at 90 K by the H atom addition to a mixture of two olefins. The concentrations are adjusted so that one of the two radicals produced is in great excess. The other radical, then, is involved only in cross and not in autodisproportionation. From the results of a number of measurements, it is shown that alkyl radical disproportionation is governed almost completely by steric factors whereby the hydrogen acceptor–donor characteristics of each radical of the cross-disproportionating pair are independent of the counter radical. The cross disproportionation of an alkyl radical containing a double bond shows that the double bond has an orienting effect on the approach to and reaction with a second radical.

Alkyl radicals are intermediates in many reactions such as alkane pyrolysis, hydrogen atom addition to olefins, and photolysis and pyrolysis of appropriate carbonyls. The elementary reaction steps in the reaction of two alkyl radicals are combination and disproportionation. As an illustration, the reactions between the two radicals, *tert*-butyl and *sec*-butyl are

$$CH_3-\overset{\displaystyle |}{\underset{\displaystyle CH_2}{C}}-CH_3 \ + \ CH_3-CH_2-\overset{\displaystyle \cdot}{C}H-CH_3 \longrightarrow$$

$$CH_3-\overset{\displaystyle CH_3}{\underset{\displaystyle CH_3}{C}}-\overset{}{C}H-CH_2-CH_3 \qquad (A)$$

$$CH_2{=}\overset{\displaystyle |}{\underset{\displaystyle CH_3}{C}}-CH_3 \ + \ CH_3-CH_2-CH_2-CH_3 \qquad (B)$$

$$CH_3\overset{\displaystyle |}{\underset{\displaystyle CH_3}{C}}H-CH_3 \ + \ CH_3-CH_2-CH{=}CH_2 \qquad (C)$$

$$CH_3\overset{\displaystyle |}{\underset{\displaystyle CH_3}{C}}H-CH_3 \ + \ CH_3-CH{=}CH-CH_3$$
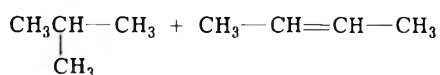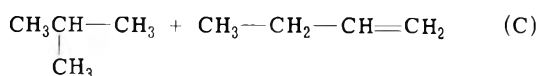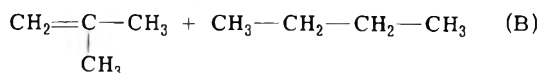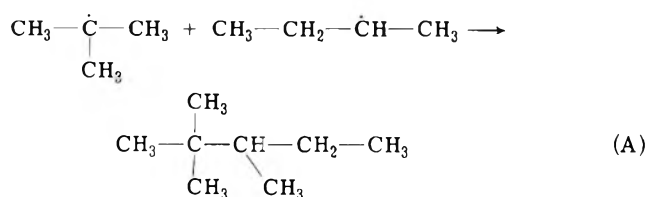
The combination reaction is given by A. In the disproportionation reaction B, the *tert*-butyl acts as hydrogen donor, and the 2-butyl radical as acceptor. There are nine "available" and equivalent primary hydrogens in the *tert*-butyl radical, all leading to isobutylene. The donor radical in C is 2-butyl. The transfer of a primary hydrogen leads to 1-butene and that of either of the two secondary hydrogens gives 2-butene. The hydrogen transfer is accompanied by olefinic bond formation. Only hydrogens on the carbon adjacent to the carbon with the unpaired electron are transferable.

The disproportionation–combination ratios for a number of straight as well as branched chain alkyl radical pairs have been measured and reviewed.[1] It has been suggested that the k_d/k_c ratio is strongly related to the number of transferable hydrogens. Kraus and Calvert,[2] in observations on butyl radicals (t-C_4H_9, i-C_4H_9, and s-C_4H_9), reported an excellent correlation for various butyl radicals on this basis if it is assumed that the specific rates for combination are equal for all radical pairs. Bradley, in his discussion of the mechanism of disproportionation in alkyl radical reactions stated that "the disproportionation rate constant must be referred to the number of 'available' hydrogen atoms."[3] We shall refer to this as the "available hydrogen hypothesis" for disproportionation. It has been

shown that the available hydrogen hypothesis is, in fact, not very satisfactory. There is, however, a paucity of accurate data on alkyl radical interactions.

Georgakakos, Rabinovitch, and Larson[4] have investigated two larger, branched radicals, 4,4-dimethyl-2-pentyl and 2,4-dimethyl-2-pentyl in their reactions with several smaller radicals. Terry and Futrell,[5] as well as Falconer and Sunder,[6] have extended some of these data on the small radical disproportionation–combination reactions.

To provide additional and more precise information, we have investigated the interaction of a number of alkyl radical pairs in condensed olefin films at cryogenic temperatures. A convenient route to alkyl radical preparation for this purpose is by way of addition of atomic hydrogen to an olefin. Atomic hydrogen may be prepared by thermal dissociation on a tungsten filament. The elementary reaction step of addition of a hydrogen atom to an olefin is characterized by a low activation energy [about 4800 J/mol (1200 cal/mol) for propylene]. For condensed olefins, the reaction between H and the olefin gives the alkyl radical unaccompanied by "cracking" reactions. We have previously developed a model for the reaction of atomic hydrogen, produced in the gas phase, with condensed olefins at low temperatures.[7] Reaction occurs within a few molecular layers of the surface to produce alkyl radicals. The secondary processes observed are alkyl radical–alkyl radical and hydrogen atom–alkyl radical disproportionation and combination reactions. The former predominate in matrices where diffusion is rapid, while the latter are the major secondary reactions when high viscosity matrices are employed.[7] The two sets of disproportionation–combination reactions can be independently observed by adjusting the viscosity of the matrix. Both the sec-butyl, sec-butyl and the H atom, sec-butyl disproportionation–combination reactions were previously observed in this way.[8] In the work reported here, the matrix is chosen such that diffusion is not rate controlling and that hydrogen atom–alkyl radical reactions are negligible.

The disproportionation reactions for sec-butyl radicals are
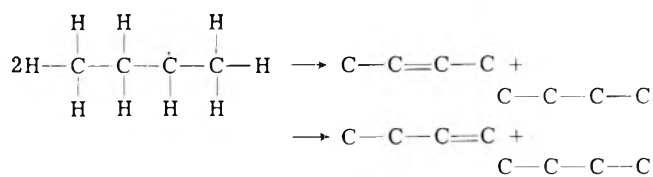
The products are 1-butene, cis-2-butene, trans-2-butene, and butane. The ratio of trans to cis-2-butene observed at 90 K is 40, approximately the equilibrium value.[8] For the higher homologs, the trans/cis ratio is somewhat less, about 30 for 2-pentene or 2-hexene, for example. Through the use of the pure cis form of the preparative olefin, the reaction products are distinguishable. In contrast, if 1-butene were used as the source of the sec-butyl radical, it is evident that the analysis of reaction products of the radical disproportionation would be uncertain because of the loss of information due to the identity of one of the products, 1-butene, with the 1-butene used as the sec-butyl source. A powerful tool for investigating reactions of alkyl radicals which can be prepared from olefins by H atom addition at low temperatures is thus available.

The radical–radical reactions reported here are those in the condensed phase at low temperatures. Comparison of these results with those of the gas phase is considered

valid. Effects due to the hydrocarbon matrix appear to be negligible.

We have applied a novel technique, which includes the use of cis-2-butene at low temperatures, to examine several cross disproportionation reactions. The number of available hydrogens has been varied from 3 through 8 by the use of the appropriate alkyl radical. A detailed description of the rationale of the procedure is appropriate. Represent two olefins by A and B, the radicals by AH and BH, alkanes by AH_2 and BH_2, and product olefins by A' and B', where A' and B' may include several species. Suppose that AH has l available hydrogens and BH has m. The exposure of a mixture of A and B to H atoms then gives the following reactions

$$A + H \longrightarrow AH \tag{1}$$

$$B + H \longrightarrow BH \tag{2}$$

$$AH + AH \longrightarrow A' + AH_2 \tag{3}$$

$$BH + BH \longrightarrow B' + BH_2 \tag{4}$$

$$AH + BH \longrightarrow A' + BH_2 \tag{5}$$

$$AH + BH \longrightarrow B' + AH_2 \tag{6}$$

in addition to the three possible combinations. The available hydrogen hypothesis would require that $k_6/k_5 = m/l$. From the above, $[d(B')/dt]/[d(BH_2)/dt] = [k_4(BH)^2 + k_6(AH)(BH)]/[k_4(BH)^2 + k_5(AH)(BH)]$.

If $(BH) \ll (AH)$, then the expression reduces to $(B')/(BH_2) = k_6/k_5$. The inequality $(BH) \ll (AH)$ can readily be attained by adjusting the initial olefin mixture, A and B, so that $k_1(A)(H) \gg k_2(B)(H)$. The utility of cis-2-butene as the B in the above scheme is apparent. In reaction 6, for example, the product B' is a mixture of 1-butene and trans-2-butene with only negligible cis-2-butene. Thus, the product analysis is virtually unambiguous and the ratio k_6/k_5 is measured by (1-butene + trans-2-butene)/n-butane. Experimentally, a mixture of cis-2-butene with a considerable excess of a second olefin is condensed as a film with propane as a diluent. The measurement of the products A', AH_2, B', and BH_2 formed in the disproportionation reactions provides an approximate measure of the relative radical (AH and BH) concentrations and serves as the experimental basis for establishing the condition, $(BH) \ll (AH)$ where in the given instance (BH) is 2-butyl. The absence of 3,4-dimethylhexane, formed in the combination reaction, is a further indication that this condition has been met and that reaction 4 can be neglected. Hence, the only significant reactions involving 2-butyl radicals are those of cross disproportionation and combination.

In order to assess the cross disproportionation of two alkyl radicals with the technique described, one radical must be present in large excess. The 2-butyl radical concentration was less than 5% of that of the total alkyl radicals in all cases. The reaction scheme as given is now particularized for cis-2-butene and the 2-butyl radical. AH will be retained to designate the probed radical.

$$A + H \longrightarrow AH \tag{7}$$

$$AH + AH \longrightarrow A' + AH_2 \tag{9}$$

$$AH + C\text{---}C\text{---}\dot{C}\text{---}C \longrightarrow AH_2 + C\text{---}C\text{=}C\text{---}C \quad (11)$$

$$AH_2 + C\text{---}C\text{---}C\text{=}C \quad (12)$$

$$AH_2 + C\text{---}C\text{=}C\text{---}C \quad (\text{trace})$$
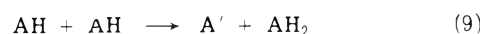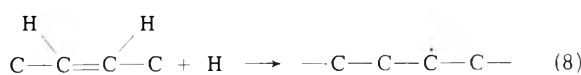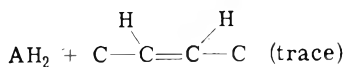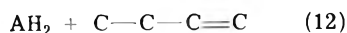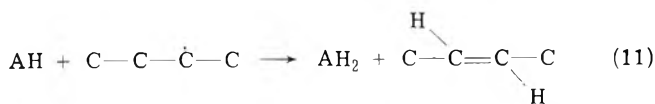
The ratio $(CC\text{=}CC + CCC\text{=}C)/C_4H_{10}$ is a measure of k_6/k_5, the acceptor–donor propensity of the radical AH with respect to 2-butyl.

The ratio of product butenes to butane changes with the extent of reaction because some of the product butenes react. Further, the establishment of the ratio of primary hydrogen to secondary hydrogen abstraction from the butyl radical is measured by the ratio of 1-butene to trans-2-butene. Product reaction would lead to incorrect results if 1-butene and trans-2-butene differed in reaction rates. In fact, they do differ. Therefore, all data are derived from extrapolation to zero conversion.

That extrapolation to zero conversion is required is shown by a consideration of the reaction system. The simple assumption is made that the system may be considered equivalent to a stirred reactor. The system is taken to be cis-2-butene diluted with an inert diluent such as propane. cis-2-Butene will be denoted by A, trans-2-butene by B, 1-butene by C, and n-butane by F. The radical formed by H atom addition to these butenes, 2-butyl, is designated by R. Reactions of R are

$$R + R \xrightarrow{k_{11}} B + F$$

$$R + R \xrightarrow{k_{12}} C + F$$

$$d(A)/dt = -k_A(A) \quad (13)$$
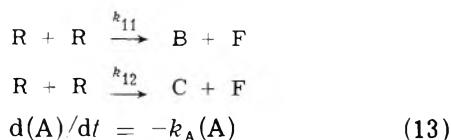
$$d(B)/dt = -k_B(B) + k_{11}(R)^2 \quad (14)$$

$$d(C)/dt = -k_C(C) + k_{12}(R)^2 \quad (15)$$

$$d(R)/dt = -2(k_{11} + k_{12})(R)^2 + k_A(A) + k_B(B) + k_C(C) \quad (16)$$

$$d(F)/dt = (k_{11} + k_{12})(R)^2 \quad (17)$$

It is noted that k_A, k_B, and k_C include an H atom concentration at the surface and a factor equal to the reciprocal of the film thickness. A steady-state approximation is represented by $d(R)/dt = 0$. Further, very little error is made by neglecting $k_B(B)$ and $k_C(C)$ in (16). This leads to

$$(R)^2 = \frac{k_A(A)}{2(k_{11} + k_{12})} \quad (18)$$

$$\frac{d(B)}{dt} = -k_B(B) + \frac{k_A k_{11}(A)}{2(k_{11} + k_{12})} \quad (19)$$

$$\frac{d(C)}{dt} = -k_C(C) + \frac{k_A k_{12}(A)}{2(k_{11} + k_{12})} \quad (20)$$

$$d(F)/dt = k_A(A)/2 \quad (21)$$

The ratios of interest are B/C and (B + C)/F. Equations 13, 19, 20, and 21 give

$$\frac{B}{C} = \frac{k_{11}}{k_{12}} \frac{k_C - k_A}{k_B - k_A} \frac{e^{-k_A t} - e^{-k_B t}}{e^{-k_A t} - e^{-k_C t}} \quad (22)$$

$$\frac{B + C}{F} = \left[\frac{k_{11}}{k_B - k_A} (e^{-k_A t} - e^{-k_B t}) + \frac{k_{12}}{k_C - k_A} (e^{-k_A t} - e^{-k_C t}) \right] / (k_{11} + k_{12}) e^{-k_A t} \quad (23)$$

With regard to rates of hydrogen atom addition, it has been found that at 90 K the rate of addition to cis-2-butene is equal to that of trans-2-butene, but these rates are lower by a factor of 10 compared to 1-butene. Hence, $k_A = k_B < k_C$. Equations 22 and 23 become

$$\frac{B}{C} = \frac{k_{11}}{k_{12}} \frac{(k_C - k_A)t}{1 - e^{(k_A - k_C)t}} \quad (24)$$

$$\frac{B + C}{F} = \frac{k_A k_{11}}{k_{11} + k_{12}} \frac{t}{e^{k_A t} - 1} + \frac{k_A k_{12}}{(k_{11} + k_{12})(k_C - k_A)} \left(1 - e^{(k_A - k_C)t}\right) \quad (25)$$

It is evident that extrapolation to zero conversion (zero time) leads to $B/C = k_{11}/k_{12}$ and $(B + C)/F = 1$. The stirred reactor is a limiting case. In actual systems, diffusion effects are operative. For low conversions, the product ratio is essentially unperturbed by diffusion considerations. It is to be noted in this regard that if the rate of production of the probe radical (2-butyl in most cases discussed) is slow, concentration gradients will tend to be small and $\partial[(B + C)/F]/\partial(\text{conversion})$ will be either zero or very small. On the other hand, fast production leads to larger values of concentration gradients and the derivative with respect to conversion will not show a zero value. In the latter case, extrapolation to zero conversion is easily made.

We note that care must be used in the choice of A to ensure the predominance of one radical species AH. Unless the olefin is symmetrical, comparable quantities of two radical species can be produced in the H atom addition reaction. Therefore, A must be either a symmetrical olefin, or one in which the addition of an H atom is known to produce predominantly one radical species. A number of results in which appropriate olefins have been utilized will be described.

Experimental Methods and Results

Research grade olefins were used throughout. Where necessary, gas chromatographic purification was employed. The cis-2-butene used contained no detectable isomeric impurities after purification. The experimental techniques used in this study have been described in detail elsewhere.[8] Briefly, hydrogen atoms produced on a hot filament (1400 K) interact with a condensed phase of an appropriate olefin in an inert diluent at 90 K. Typically, a 5% olefin in propane mixture was used. Following the reaction, the entire mixture, approximately 0.5×10^{-3} mol, was analyzed. The procedure consisted of preliminary separation into various fractions using gas chromatography with a 6 m, 0.63 cm o.d., squalane (20% by weight on Chromosorb P) column at 298 K. Analysis of the individual fractions, in particular the four carbon fraction, was accomplished with a 15 m, 0.63 cm o.d., 3,3'-oxydipropionitrile (20% by weight on Chromosorb P) column at 298 K. These procedures were tested with standardized mixtures and found to be suitable for accurate quantitative analysis.

The autodisproportionation reaction of 2-butyl is of in-
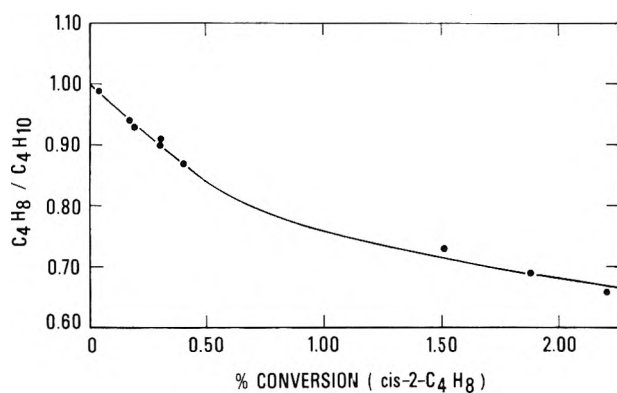
Figure 1. Autodisproportionation of 2-butyl radicals at 90 K. Extrapolation of the product ratio, C_4H_8/C_4H_{10}, to zero conversion.

Figure 2. Cross disproportionation of 2-pentyl with 2-butyl radicals at 90 K. Extrapolation of the product ratio, C_4H_8/C_4H_{10}, to zero conversion.

TABLE I: Product Yields[a] from the Autodisproportionation of 2-Butyl Radicals at 90 K

% conversion (cis-2-C_4H_8)	n-C_4H_{10}	1-C_4H_8	t-2-C_4H_8	C_4H_8/C_4H_{10}	1-C_4H_8/t-2-C_4H_8
2.2	1556	612	408	0.66	1.50
1.7	778	418	219	0.82	1.91
1.4	1157	643	353	0.86	1.82
0.40	166	93	51	0.87	1.82
0.30	202	123	62	0.91	1.98
0.30	269	163	80	0.90	2.03
0.18	74	45	24	0.93	1.88
0.17	107	65	35	0.94	1.87
0.02	46	29	16	0.99	1.80
Extrapolated value				0.99	1.9 ± 0.1

[a] Units 10^{-9} mol.

Figure 3. Cross disproportionation of 3-ethyl-2-methyl-3-pentyl with 2-butyl radicals at 90 K. Extrapolation of the product ratio, C_4H_8/C_4H_{10}, to zero conversion.

terest, and can be easily resolved if *cis*-2-butene is the olefin reactant. If AH in (11) is taken as 2-butyl, then (11) and (12) become

$$2(C-\overset{\cdot}{C}-C-C) \longrightarrow C-C-C-C + \overset{H}{\underset{C}{>}}C=C\overset{C}{\underset{H}{<}}$$

(26)

$$\longrightarrow C-C-C-C + C-C-C=C$$

The ratio of products with respect to conversion of the reactant is given in Table I and plotted in Figure 1. The ratio butenes/butane approaches 1 at low conversion as required by the stoichiometry. The departure from 1 at higher conversions is an indication of H atom reaction with product olefins. Further, the ratio of 1-butene to *trans*-2-butene decreases with increasing conversion since 1-butene is more reactive to H atoms at 90 K than *trans*-2-butene. Previous determinations of the 1-butene/*trans*-2-butene ratio indicated an approximate value of 1.5.[2,4] The present results give 1.9 ± 0.1, Table I. The hypothesis that the removal of H from the primary and secondary position occurs in a strictly statistical manner requires modification.

The results for the cross disproportionation of a number of radicals with 2-butyl are given in Table II. The olefin serving as the source of the indicated radical by H atom addition is shown in the column labeled source. The butenes/butane column is the experimental value found in the cross disproportionation reaction of the radical with 2-butyl. AHH is simply the ratio of the number of avail-

Figure 4. Cross disproportionation of 3-ethyl-3-pentyl with 2-butyl. Extrapolation of the product ratio, C_4H_8/C_4H_{10}, to zero conversion.

able hydrogens from 2-butyl with the number of available hydrogens from the radical under consideration. The extrapolation technique for determining the correct ratio of H donor products to H acceptor products in a cross disproportionation is shown in Figure 2 for 2-pentyl, in Figure 3 for 3-ethyl-2-methyl-3-pentyl, and in Figure 4 for 3-ethyl-3-pentyl.

The autodisproportionation of 4-penten-2-yl at 90 K gives relative product yields as shown in Table III. The ratio $1,4$-$C_5H_8/1,3$-C_5H_8 is 3.8. A statistical hydrogen transfer would give 1.5. The autodisproportionation of 3-

TABLE II: Cross-Disproportionation Rate Ratios for Some Alkyl Radicals with 2-Butyl Radicals at 90 K

Entry	Radical	Source	Available hydrogens	(C_4H_8/C_4H_{10}) AHH	Measured	$(1\text{-}C_4H_8/t\text{-}2\text{-}C_4H_8)$
1	CCĊC	cis CC=CC				1.9 ± 0.1
2	C. CCCC C	C CCC=C C	3	1.67	1.14	2.0 ± 0.1
3	C. CCCC	C CCC=C	4	1.20	0.80	1.9 ± 0.1
4	CCĊCC	CCCC=C	5	1.00	1.00	2.0 ± 0.1
5	C . CCCCC	C CCCC=C	5	1.00	0.75	1.9 ± 0.1
6	C CC CCCCC	C CC CCC=CC	5	1.00	0.69	1.9 ± 0.2
7	C=CĊCC	C=CCC=C	5	1.00	0.73	1.9 ± 0.1
8	CCCĊCC	CCCCC=C	5	1.00	0.99	2.0 ± 0.1
9	C=CCĊCC	C=CCCC=C	5	1.00	0.79	2.0 ± 0.1
10	CĊC	CC=C	6	0.833	1.20	1.7 ± 0.2
11	C C CCCCC	C C CCC=CC	6	0.833	0.70	2.0 ± 0.1
12	CC CCCCC	CC CCC=CC C CC CCC=C	6	0.833	0.59	2.0 ± 0.1
13	C CCCCC	CCC=C C C	7	0.714	0.61	2.1 ± 0.1
14	CC CCCC	C C CC=CC	7	0.714	0.61	1.9 ± 0.1
15	C CCCC	C CC=CC	8	0.625	0.62	2.1 ± 0.1

TABLE III: Product Distribution in the Autodisproportionation of 4-Penten-2-yl Radicals at 90 K

Product	Relative concn[a]
1-C_5H_{10}	4.97
trans-1,3-C_5H_8	1.00
cis-1,3-C_5H_8	0.043
1,4-C_5H_8[b]	3.93

[a] At zero conversion. [b] Product 1,4-C_5H_8 is determined from the stoichiometric relation [1-C_5H_{10}] = [1.3-C_5H_8] + [1,4-C_5H_8].

TABLE IV: Product Distribution from the Autodisproportionation of 3-Methyl-3-Pentyl Radical at 90 K

Product	Relative concn
3-Methylpentane	2.8
3-Methyl-2-pentene[a]	1.0
2-Ethyl-1-butene[b]	1.8

[a] Cis and trans forms. [b] Calculated from the stoichiometric relation (3-methylpentane) = (3-methyl-2-pentene) + (2-ethyl-1-butene).

methyl-3-pentyl radicals results in product yields shown in Table IV. The ratio 2-ethyl-1-butene/3-methyl-2-pentene is 1.8 and the statistical (available hydrogen) value would be 0.75.

Disproportionation–combination ratios in the system 2-methyl-2-butyl with 2-butyl at 90 K can be determined from the results of the analysis of reaction products as shown in Table V.

Finally, 2,3-dimethyl-3-pentyl radical can be prepared

by the H atom addition to 3,4-dimethyl-2-pentene or alternatively to 2-ethyl-3-methyl-1-butene. Results obtained, insofar as product distribution in the cross disproportionation with 2 butyl, were identical. The autodisproportionation of the C_7H_{15} radical is particularly interesting since this radical has primary, secondary, and tertiary hydrogens available for transfer. The results are shown in Table VI for two temperatures, 90 and 143 K, and for the two radical sources. Statistical transfer of available hydrogens would give the ratio for 2-ethyl-3-methyl-1-bu-

TABLE V: Product Distribution from the Disproportionation–Combination Reactions of 2-Methyl-2-butyl and 2-Butyl Radicals at 90 K

Product	Relative concn
2-Methylbutane	4493.0
3,3,4,4-Tetramethylhexane	2.87
1-Butene	8.80
trans-2-Butene	4.24
n-Butane	21.77
3,3,4-Trimethylhexane	1.00
3,4-Dimethylhexane	<0.01

Disproportionation–combination ratios	k_{disp}/k_{comb}
2-Methyl-2-butyl + 2-methyl-2-butyl	1566
2-Methyl-2-butyl + 2-butyl	35
2-Butyl + 2-butyl	11[a]

[a] Reference 8.

TABLE VI: Product Distribution from the Autodisproportionation of 2,3-Dimethyl-3-pentyl at 90 and 143 K[a]

Temp, K	2-Ethyl-3-methyl-1-butene[b]	*t*-3,4-Dimethyl-2-pentene[b]	2,3-Dimethyl-2-pentene[b]
90	3.00	(1.84)	0.20
90	(3.00)	1.88	0.18
143	3.00	(1.93)	0.20

[a] Product olefins are shown in the columns. Where the preparative olefin is the same as the product olefin, the product olefin is shown in parentheses and has been calculated on the basis of the stoichiometric relation [product alkane] = [product olefin]. [b] Relative yield.

tene:3,4-dimethyl-2-pentene:2,3-dimethyl-2-pentene = 3:2:1. The ratio found is 3.0:1.9:0.2.

Discussion

The mechanism of alkyl radical reactions, particularly those of disproportionation and combination, has elicited much interest because of the fact that the disproportionation occurs at rates that are similar and, in the case of branched radicals, even considerably greater than that of combination. It had been previously proposed that radical combination exhibited no activation energy. However, it has been shown that the disproportionation reaction has a lower activation energy than that of combination.[7,9] It must be emphasized, nevertheless, that the activation energy differences are in the range 800–2000 J/mol (200–500 cal/mol). We examine here disproportionation and particularly cross disproportionation. A general discussion of the mechanism of disproportionation in terms of the four center and the head-to-tail complexes has been given by Benson.[10] The four center hypothesis is not considered to be a reasonable alternative. The low activation energy of the disproportionation does imply that it is a concerted type of process, the exchange of hydrogen occurring simultaneously with the formation of the olefinic bond.

It is the purpose of this section to examine alkyl radical cross disproportionation reactions to gain some insight into their mechanisms. The number of available hydrogens will serve as a reference for comparison of a number of disproportionation reactions. The deviation from the available hydrogen hypothesis will be useful in assessing the characteristics of the radical species with which these deviations can be correlated.

The ratio of 1-butene to *trans*-2-butene is 1.9 in the 2-butyl with 2-butyl disproportionation. This would be 1.5

TABLE VII: Product Distribution from the Autodisproportionation of 5-Hexen-2-yl at 90 K

Product	Relative concn
1-Hexene	4.18
trans-1,4-Hexadiene	1.00
cis-1,4-Hexadiene	0.046
1,5-Hexadiene[a]	3.13

[a] Product 1,5-hexadiene is determined from the stoichiometric relation $1\text{-}C_6H_{12} = 1,4\text{-}C_6H_{10} + 1,5\text{-}C_6H_{10}$.

TABLE VIII: Temperature Effect on Cross-Disproportionation Rates of 4-Methyl-2-pentyl (AH) with 2,3-Dimethyl-3-pentyl (BH) Radicals (Eq 5 and 6)

Temp, K	BH_2 (2,3-Di-methyl-pentane)	B′ (2-Ethyl-3-methyl-1-butene)[a]	B′ (2,3-Di-methyl-2-pentene)[a]	B′ (3,4-Di-methyl-2-pentene)[a]	k_6/k_5
90	1.28	1.00	0.071	0.588	1.29
143	1.27	1.00	0.066	0.588	1.30

[a] Relative concentration at zero conversion.

on the available hydrogen hypothesis, three primary and two secondary hydrogens being available. Reference to models suggests that steric effects could be significant in accounting for the difference. Thus, in the 2-butyl radical, the solid angle swept out by that methyl group not adjacent to the "free electron" carbon in its rotation about the $-C(H)-C(H_2)-$ axis is about a factor of 9 larger with respect to the carbon with abstractable secondary hydrogens than with respect to the carbon with the abstractable primary hydrogens. No doubt the efficiencies of the primary hydrogens and secondary hydrogens as donors depend on the configuration of the acceptor radical. We suggest, however, that the geometry of the donor radical determines the relative efficiency of the donor effect of the primary and secondary hydrogens. Thus, Table II shows the ratio of 1-butene to 2-butene to be 1.9, approximately independent of the other radical in the disproportionation reaction.

The autodisproportionation of 2,3-dimethyl-3-pentyl radicals affords a comparison of primary, secondary, and tertiary hydrogen transfer. Three possible olefins are formed, 2-ethyl-3-methyl-1-butene, 3,4-dimethyl-2-pentene, and 2,3-dimethyl-2-pentene. They are uniquely associated with the transfer of primary, secondary, or tertiary hydrogen, respectively. On the available hydrogen hypothesis, they should be in the ratio of 3.0:2.0:1.0 but, in fact, are found to be 3.0:1.9:0.2. The primary to secondary transfer ratio from the point of view of available hydrogens is 1.5, the same as for the 2-butyl radical. The ratio found is 1.6, somewhat lower than the 1.9 value for 2-butyl. The larger size and complexity of the 2,3-dimethyl-3-pentyl compared to the 2-butyl radical introduces steric effects blocking the approach of the reacting radical to both the primary and secondary hydrogens. This can be seen from models. The steric effect is especially large with tertiary hydrogens. The available number ratio of primary to tertiary hydrogens for the 2,3-dimethyl-3-pentyl radical is 3, but the ratio of the two types of hydrogens transferred in the autodisproportionation is 15.

The experimental results are explicable for the most part as steric effects. There remain, however, some exceptions. The 2-pentyl radical, with five abstractable hydrogens, shows a k_6/k_5 ratio, referenced to 2-butyl, of 1.0,

TABLE IX: Acceptor Donor Ratios for Some Alkyl Radical Pairs

Radical designation			$[(AH)_a/(AH)_d \rightarrow BH]^a$	$[(CH)_a/(CH)_d \rightarrow BH]^a$	$[(AH)_a/(AH)_d \rightarrow CH]^a$	
(AH)	(BH)	(CH)			Measured	Calculated[b]
C=CCCCC	CCCC	C CCCC	0.79	0.62	1.21	1.27
CCC	CCCC	C CCCC	1.20	0.62	1.88	1.93
C CCCC	CCCC	CC CCCC	0.75	0.59	1.33	1.27

[a] $[(AH)_a/(AH)_d \rightarrow BH]$ is the ratio k_a/k_d for the cross disproportionation of the radicals AH and BH, where $(AH)_a$ represents the radical AH acting as the hydrogen acceptor and $(AH)_d$ as the hydrogen donor, etc. [b] From the relation $[(AH)_a/(AH)_d \rightarrow BH]/[(CH)_a/(CH)_d \rightarrow BH] = [(AH)_a/(AH)_d \rightarrow CH]$.

precisely that expected on the available hydrogen basis. The similarity of the two radicals would dictate these results. The radical 3,3-dimethyl-2-butyl with three abstractable hydrogens, all of which are primary, shows a large disparity from the statistical value (1.14 as compared to 1.67 for k_6/k_5). It might be suggested that in this case the *tert*-butyl group exerts a steric effect in shielding the free electron carbon from reacting effectively as an acceptor. This is seen also with the 3-methyl-2-butyl radical (0.8 as compared to 1.2 for k_6/k_5).

Four different radicals, each with five available hydrogens, have been examined in cross disproportionation with 2-butyl. 2-Pentyl, as noted, is equivalent to the 2-butyl radical. 4-Penten-2-yl is a comparatively poorer hydrogen acceptor (equivalently, a better hydrogen donor). Here the explanation invoked must be other than steric. The effect of the olefinic bond must be either to make the free electron carbon a poorer hydrogen acceptor or to enhance the reactivity of the available hydrogen of that radical in the disproportionation. One possibility for the latter case might be a hyperconjugation effect involving the secondary hydrogens. The resonance stability of a conjugated system formed when a secondary hydrogen is donated may be presumed to enhance the secondary hydrogen lability. However, the data show, Table III, that in the autodisproportionation of 4-penten-2-yl, the ratio of 1,4-pentadiene to 1,3-pentadiene is about 3.8. The available hydrogen hypothesis, if operative, would give 1.5. It is the primary hydrogens in the 4-penten-2-yl radical that are donor enhanced. As noted, this is all the more surprising from the point of view that the formation of the conjugated diene would be expected to be favored energetically.

A further informative comparison is that between the pair 2-hexyl (CCCCCC) and 5-hexen-2-yl (C=CCCCC) in their disproportionation with 2-butyl. For 2-hexyl, the C_4H_8/C_4H_{10} ratio is 0.99 while for 5-hexen-2-yl it is 0.79 (Table II). Again, the contrast between 2-hexyl and 5-hexen-2-yl is also striking and similar to that between 2-pentyl and 4-penten-2-yl. The products of the autodisproportionation of 5-hexen-2-yl radicals is given in Table VII. The product ratio, 1,5-hexadiene/1,4-hexadiene, is seen to be 3.0 (the available hydrogen hypothesis would give 1.5).

The radicals 4-methyl-2-pentyl and 3-ethyl-2-methyl-3-pentyl are also in the five available hydrogens category; the former has three primary and two secondary hydrogens, the latter four secondary and one tertiary. Both give the same butenes/butane ratio in cross disproportionation with 2-butyl. Insofar as donor effectiveness is concerned, primary is greater than secondary which, in turn, is greater than tertiary hydrogen. On the basis of donor effectiveness, it would be expected that 4-methyl-2-pentyl should

show a smaller butenes/butane ratio than that of 3-ethyl-2-methyl-3-pentyl. The equivalence of these two radicals shows clearly that steric effects involving both radicals of the disproportionating pair determine the course of the reaction.

The series of radicals observed with six available hydrogens is quite interesting. The propyl radical, the first of these, is conspicuous because of all the radicals studied, it is the only one showing a positive deviation from the available hydrogen ratio as measured with 2-butyl. The propyl radical is reacting as a better hydrogen acceptor, poorer hydrogen donor, than all others. Minimal steric effects with respect to the approach of the counter radical, *i.e.*, 2-butyl, to the available hydrogens is postulated as the basis of a reasonable explanation. The other six available hydrogen radicals are 3-ethyl-3-pentyl with six secondary hydrogens, and 2,3-dimethyl-3-pentyl with three primary, two secondary, and one tertiary hydrogen. The deviation of the acceptor/donor ratio from the available hydrogen factor of 5/6 shows values of +0.4, −0.1, and −0.3, for propyl, 3-ethyl-3-pentyl, and 2,3-dimethyl-3-pentyl, respectively.

Two radicals, 3-methyl-3-pentyl and 2,3-dimethyl-2-butyl, with seven available hydrogens have three primary and four secondary hydrogens, and six primary and one tertiary hydrogens, respectively. Both showed the same deviation, 14%, from the available hydrogen ratio of 5/7. The radical 2-methyl-2-butyl, with eight available hydrogens, shows no deviation from the available hydrogen ratio.

The temperature effect on the distribution of products in the cross disproportionation reaction was evaluated by comparing the results at 90 and 143 K for a pair of radicals, 2,3-dimethyl-3-pentyl and 4-methyl-2-pentyl. The results are shown in Table VIII. It is evident that, at least over the range 90–143 K, temperature effects on the reaction are either absent or so small as to be negligible. An activation energy as small as 400 J/mol (100 cal/mol) would have been detected. The absence of a temperature effect for the disproportionation reactions, whether the donor–acceptor aspect or the relative donor effect of primary, secondary, or tertiary hydrogens are considered, Tables VIII and VI, demonstrates that the reactions are of the steric type. This conclusion is supported further by the finding that the order of increasing donor effect is tertiary, secondary, primary hydrogen, opposite to the effect expected on the basis of bond strengths.

If cross disproportionation reactions are controlled by steric effects, and this is the interpretation required by the data, the structure of both radicals must be assessed in the reaction. However, an important conclusion is

drawn from the data of Table II. Regardless of the configuration of the second radical, the ratio of the donor effect for the different hydrogen species of the first radical is invariant. It is seen that the ratio of 1-butene to 2-butene, a measure of the donor effect of primary to secondary hydrogens in the 2-butyl radical, is 1.9 ± 0.1. The radicals of Table II represent a wide variation in structure. The butenes/butane ratio spans the range 0.59-1.2. Nevertheless, the trans-2-butene/1-butene ratio remains constant. In the steric interaction of the hydrogen acceptor and hydrogen donor radicals, the donor rates of the primary and secondary hydrogens are affected proportionately by substitution of an acceptor radical with a different acceptor characteristic. We generalize this to include tertiary hydrogens as well.

A most interesting finding is that if the acceptor-donor ratio for radical AH with respect to radical BH is obtained and if the acceptor-donor ratio for radical CH is obtained with respect to radical BH, the acceptor-donor ratio for radical AH with respect to radical CH is found to be given by dividing the first by the second ratio. If the acceptor-donor ratio for radical AH with respect to radical BH is designated as $AH_a/AH_d \rightarrow BH$, then the above theorem is

$$\left[\frac{AH_a}{AH_d} \rightarrow BH\right] \bigg/ \left[\frac{CH_a}{CH_d} \rightarrow BH\right] = \left[\frac{AH_a}{AH_d} \rightarrow CH\right] \quad (27)$$

That this relationship holds is shown in Table IX for three radical pairs spanning the extremes of the acceptor-donor ratios measured. The strong inference is that the relationship is general for alkyl radical disproportionation.

The implication of this relationship is that the specific rate constant of a cross disproportionation reaction is decomposable into two factors characteristic of each of the two radical reactants. Equations 5 and 6 are rewritten, and included herewith will be equations involving the radical CH.

$$AH + BH \xrightarrow{k_e} A + BH_2$$
$$\xrightarrow{k_f} AH_2 + B \quad (28)$$

$$CH + BH \xrightarrow{k_g} C + BH_2$$
$$\xrightarrow{k_h} CH_2 + B \quad (29)$$

$$AH + CH \xrightarrow{k_i} A + CH_2$$
$$\xrightarrow{k_j} AH_2 + C \quad (30)$$
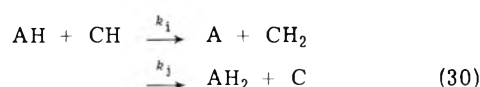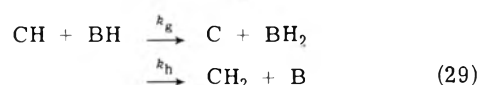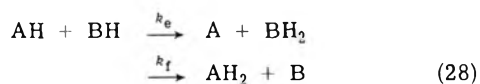
$(AH_2)/(A)$ is the acceptor-donor ratio for AH and, when measured against BH as the probe radical, is determined from a measurement of the ratio B/BH_2. When more than one species of B is produced (as in the case of the 2-butyl radical, where trans-2-butene and 1-butene are the B's), B represents the total product olefins from BH. From eq 28 $AH_2/A = k_f/k_e$. It is hypothesized that $k_f = k_a{}^{AH} k_d{}^{BH}$ where $k_a{}^{AH}$ refers to the radical AH as a hydrogen acceptor and $k_d{}^{BH}$ to BH as a hydrogen donor. Similarly, $k_e = k_d{}^{AH}k_a{}^{BH}$. Thus, we have

$$\left[\frac{AH_a}{AH_d} \rightarrow BH\right] = \frac{k_f}{k_e} = \frac{k_a{}^{AH}k_d{}^{BH}}{k_d{}^{AH}k_a{}^{BH}} \quad (31)$$

$$\left[\frac{CH_a}{CH_d} \rightarrow BH\right] = \frac{k_j}{k_g} = \frac{k_a{}^{CH}k_d{}^{BH}}{k_d{}^{CH}k_a{}^{BH}} \quad (32)$$

TABLE X: Product Distribution from the Autodisproportionation of 2-Methyl-2-butyl Radicals at 90 K

% conversion	2-Methylbutane/ 2-methyl-1-butene	2-Methyl-1-butene/ 2-methyl-2-butene[a]
0.50	1.238	4.16
0.20	1.245	4.07
0.17	1.252	3.96
0.15	1.247	4.04
Mean values	1.245	4.08

[a] The 2-methyl-2-butene formed in the disproportionation reaction is calculated from the stoichiometric relation (at zero conversion) [2-methylbutane] = [2-methyl-1-butene] + [2-methyl-2-butene].

$$\left[\frac{AH_a}{AH_d} \rightarrow CH\right] = \frac{k_j}{k_i} = \frac{k_a{}^{AH}k_d{}^{CH}}{k_d{}^{AH}k_a{}^{CH}} \quad (33)$$

from which eq 27 follows. The cross disproportionation reaction is essentially determined by steric effects. The probability of reaction is related to the achievement of a favorable configuration of the reacting pair, and is expressible as a product of probabilities for each of the reactants.

Some radicals, the simplest being 2,3-dimethyl-3-pentyl, have three types of C-H bonds, primary, secondary, and tertiary, which can donate hydrogen in a disproportionation reaction. The donor effectiveness, based on primary H as 1, is secondary 0.9 and tertiary 0.2, for 2,3-dimethyl-3-pentyl. As in the case of 2-butyl discussed previously, these values are a reflection of steric effects, and it is to be expected that the order of donor effectiveness should be primary > secondary > tertiary. It is further noted that these ratios are independent of the acceptor radical. It has been shown that the ratio of 1-butene to trans-2-butene is 1.9. The donor effectiveness of the primary to the secondary H is as 1 to 0.8. The greater complexity of 2,3-dimethyl-3-pentyl compared to 2-butyl with increased inaccessibility of the primary hydrogens in the former radical explains the difference in the primary-secondary effectiveness ratios for the two radicals. The 2-methyl-2-butyl radical has six primary and two secondary hydrogens that can participate in a disproportionation reaction. Although only the transfer of a secondary hydrogen gives an olefin distinct from the initial olefin from which the radical is derived by H atom addition, nevertheless reliable results may be derived from the stoichiometry of the disproportionation reaction since the sum of the product olefins must equal the sum of the product alkanes. Table X shows the product distribution at essentially zero conversion. On a per atom basis, the donor effectiveness of primary to secondary hydrogen is 1 to 0.8, the same as for 2-butyl. The acceptor-donor ratio of 2-methyl-2-butyl with respect to 2-butyl shows an apparent equivalency between the two radicals for hydrogen transfer. That is, the k_6/k_5 ratio (Table II) is equal to 0.62 as would be expected on the simple available hydrogen hypothesis. The 2-methyl-2-butyl radical has six primary and two secondary hydrogens while 2-butyl has three primary and two secondary hydrogens. It has been shown that for donor effectiveness, primary > secondary. Therefore, an average donor effectiveness per transferrable H atom in the 2-methyl-2-butyl radical should exceed that of 2-butyl. As noted, however, this is not the case. Either the acceptor effectiveness of the 2-methyl-2-butyl radical is greater than the 2-butyl, or the donor effectiveness of both types of hydrogen in the 2-methyl-2-butyl radical is diminished compared with the hydrogens of the 2-butyl. The

TABLE XI: Cross-Disproportionation Rate Ratios for Some Alkyl Radicals (AH) with 2-Methyl-2-butyl Radicals (BH) at 90 K (Eq 5 and 6)

AH	k_6/k_5	AH	k_6/k_5
CĊCC	1.62	C=CCCĊC	1.21
CĊC	1.88	CĊC C	0.88

second alternative is favored from structural considerations. Only about a 10% reduction in donor effectiveness, compared to 2-butyl, is required.

We consider now the *tert*-butyl radical, as probed with the 2-methyl-2-butyl radical, Table XI. It is found that $[(tert\text{-butyl}_a/tert\text{-butyl}_d) \rightarrow 2\text{-methyl-2-butyl}] = 0.88$ compared to 8/9 or 0.89 on the available hydrogen hypothesis. Again, since there are nine primary donatable hydrogens in *tert*-butyl and six primary and two secondary hydrogens in 2-methyl-2-butyl, a compensation effect related to steric properties must occur. Assigning the value 1 to the donor effectiveness of primary H in 2-methyl-2-butyl, the secondary H is found to have a value of 0.8 per atom. Therefore, $[6(1) + 2(0.8)]/9X = 0.88$ where X is the compensation factor, and is 0.95. That is to say that on a relative basis the donor effectiveness of the primary H in the *tert*-butyl would have to be 0.95 compared to 1 for the primary H's of 2-methyl-2-butyl. This assumes, of course, that the acceptor factor for *tert*-butyl is equal to that of 2-methyl-2-butyl. If the assumption is made that the H donor property of the primary H's of the two radicals are equal, then the acceptor factor for *tert*-butyl would be 5% higher than that of 2-methyl-2-butyl.

Gibian and Corley[1] in a review article on disproportionation–combination of reactions of free radicals point out that "The cross disproportionation between two secondary radicals, isopropyl and 3,4-dimethyl-2-pentyl, shows a twofold preference for abstraction by isopropyl rather than from it." It is also noted that the effect is more likely to be steric than energetic.

We find the 2-propyl radical to be anomolous in that of all the radicals studied, this was the only one showing a positive deviation of the acceptor/donor ratio, with respect to 2-butyl, from the available hydrogen hypothesis. The ratio was found to be 1.2 compared to 0.83 on the AHH. As has been repeatedly noted, the available hydrogen hypothesis neglects steric effects, including both donor and acceptor factors. If account is taken of these effects, the acceptor factor of 2-propyl must be 57% greater than that of 2-butyl to give the experimental value. It is not reasonable to postulate that the donor effectiveness of the primary hydrogens of the 2-propyl radical is 64% of that of the primary hydrogen of 2-butyl.

Aliphatic radicals containing one olefinic bond are of especial interest. The 2-pentyl radical, with an acceptor–donor ratio of 1.0 in disproportionation with 2-butyl, contrasts with 4-penten-2-yl in which the ratio is 0.73. The better donor, poorer acceptor characteristic of the 4-penten-2-yl with respect to 2-pentyl cannot be explained on a steric basis. Indeed, it would appear that the rigidity of the olefinic bond, together with two less hydrogens of 4-penten-2-yl compared to 2-pentyl, should show less steric hindrance for the 4-penten-2-yl compared with the 2-pentyl radical, and hence result in better acceptor characteristics of the 4-penten-2-yl radical. This, of course, is contrary to observation. The double bond does not interact

with the unpaired spin in an allylic manner, as would be the case for 3-penten-2-yl. The high electron density associated with the olefinic bond of the 4-penten-2-yl would show a repulsive interaction with the free electron of the interacting partner, 2-butyl, to give a bias in favor of the opposite end of the molecule, *viz.*

$$C=C-C-\overset{\cdot}{C}-C \longrightarrow \cdot \overset{\overset{\displaystyle C}{\overset{|}{C}}}{\underset{\underset{\displaystyle C}{|}}{C}}$$
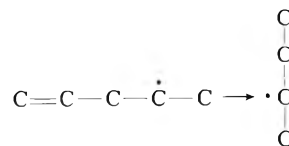
This concept is further supported by the fact that the ratio of product 1,4-C_5H_8 to 1,3-C_5H_8 is 3.8. On a per atom basis, normalizing the primary H to 1, the ratio of primary to secondary donor effectiveness is 1 to 0.39. For secondary hydrogen, this is considerably lower than any other case examined. Also, it must be noted, that donation of the secondary hydrogen results in the more stable conjugated diene. Nevertheless, transfer of primary hydrogen is highly favored.

The effect of the position of the double bond in relationship to the unpaired electron was determined through the use of the 5-hexen-2-yl radical. Here there are two carbons intervening between the double bonded carbon and the unpaired spin, compared to one in the 4-penten-2-yl radical. The 2-hexyl radical cross disproportionating with 2-butyl reacts almost identically with the 2-pentyl radical in its acceptor–donor ratio of 1, Table II. The experimental value for the acceptor–donor ratio of 5-hexen-2-yl is 0.79 (Table II), somewhat higher than the 0.73 ratio found for 4-penten-2-yl. The reduced influence of the double bond is also evidenced by the fact that the product ratio 1,5-C_6H_{10} to 1,4-C_6H_{10} is 3.0 (Table VII) in the autodisproportionation of 5-hexen-2-yl radicals. The ratio of primary to secondary donor effectiveness (with the primary H normalized to 1) is 1 to 0.50, considerably higher than that of 4-penten-2-yl. It is concluded that the effect of the double bond is not of a short range character and could be consistent with the long range electrical forces postulated for the required orientation effects.

Summary

A new technique for determining cross radical disproportionation at low temperatures in the condensed phase has been developed. It is capable of increased accuracy over similar determinations in the gas phase. Many subtle characteristics, unavailable to the usual gas-phase work, can be determined. Advantage is taken of the facts that (1) radicals can be prepared easily and cleanly by H atom addition to appropriate olefins; (2) in a system with two alkyl radical species present, one of which is in large excess, the cross disproportionation reaction can be studied. The 2-butyl is the "low concentration" radical most useful as a probe; (3) *cis*-2-butene is an excellent source of 2-butyl radicals at low temperatures. Other radicals can be used as probes provided their disproportionation products can be determined unambiguously.

The data obtained are consistent with much of the relevant gas-phase work. Over a limited range of temperature, 90–143 K, no temperature effect has been found.

The conclusion that the alkyl radical–radical disproportionation reactions are almost completely a manifestation of steric effects is rather firmly based.

Disproportionation reactions are characterized by rate constants that are products of the hydrogen transfer effec-

tiveness of one radical with the hydrogen acceptor effectiveness of the other. Where hydrogen transfer effectiveness of two or more hydrogen types within a given radical can be compared, the ratios are found to be invariant with respect to the identity of the second radical. Both hydrogen transfer and hydrogen acceptor characteristics are steric in origin.

Finally, the presence of a double bond in an alkyl radical is not negligible in its effect on disproportionation reactions. A tentative explanation of a bias in the orientation of approach due to electrical forces has been advanced.

References and Notes

(1) M. J. Gibian and R. C. Corley, *Chem. Rev.*, 73, 441 (1973).
(2) J. W. Kraus and J. C. Calvert, *J. Amer. Chem. Soc.*, 79, 5921 (1957).
(3) J. V. Bradley, *J. Chem. Phys.*, 35, 748 (1961).
(4) H. H. Georgakakos, B. S. Rabinovitch, and C. W. Larson, *Int. J. Chem. Kinet.*, 3, 535 (1971).
(5) J. O. Terry and J. H. Futrell, *Can. J. Chem.*, 45, 2327 (1967).
(6) W. E. Falconer and W. A. Sunder, *Int. J. Chem. Kinet.*, 3, 523 (1971).
(7) R. Klein and M. D. Scheer, *J. Phys. Chem.*, 66, 2677 (1962).
(8) R. Klein, M. D. Scheer, and R. Kelley, *J. Phys. Chem.*, 68, 598 (1964).
(9) P. S. Dixon, A. P. Stefani, and M. Szwarc, *J. Amer. Chem. Soc.*, 85, 2551 (1963).
(10) S. W. Benson, *Advan. Photochem.*, 2, 1 (1964).

Intermolecular Potentials from Crystal Data. III. Determination of Empirical Potentials and Application to the Packing Configurations and Lattice Energies in Crystals of Hydrocarbons, Carboxylic Acids, Amines, and Amides[1]

F. A. Momany,[2a] L. M. Carruthers, R. F. McGuire,[2b] and H. A. Scheraga*[2c]

Department of Chemistry, Cornell University, Ithaca, New York 14850, and Department of Biophysics, Weizmann Institute, Rehovoth, Israel

(Received December 11, 1973)

Crystals of hydrocarbons, carboxylic acids, amines, and amides are used to obtain a self-consistent set of empirical interatomic potentials for the atoms of which polypeptides and proteins are constituted. Simple mathematical forms are adopted for the empirical potential energy functions, and their parameters are determined by a combination of *a priori* calculations and minimization of the potential energies of the crystal lattices. The partial charges on all atoms are computed by the CNDO/2 (ON) procedure. The coefficients of the attractive $(1/r^6)$ term of the Lennard-Jones 6-12 potential are computed by the Slater-Kirkwood method, and the coefficients of the attractive $(1/r^{10})$ term of an empirical general hydrogen bond potential were derived from previous CNDO/2 calculations of hydrogen bond strengths. The coefficients of the repulsive $(1/r^{12})$ terms of both the Lennard-Jones potential and of the general hydrogen bond potential were obtained by varying these coefficients until the energy-minimized lattice constants agreed as closely as possible with the observed ones. The heavy atoms of the individual molecules in the unit cell were treated as rigid bodies, with no internal degrees of freedom. Their movement in the potential energy minimization procedure was governed by the crystal symmetry operators. The coordinates of the heavy atoms of the molecules were taken directly from the X-ray data, and a procedure was adopted to obtain the coordinates of the hydrogen atoms. The total potential energy function was then used to compute the binding energy of the lattice; in a few cases, some interatomic force constants were computed for interactions between specific pairs of atoms. The computed lattice constants, binding energies, and interatomic force constants are in good agreement with experimental values. Some discussion of the factors governing the determination and the resulting precision of the parameters of the computed potential function is presented.

I. Introduction

In order to calculate conformational energies of macromolecules, it is necessary to have accurate potential energy functions and parameters.[3-6] In recent years, considerable effort[7-13] has been devoted to the calculation of the intermolecular potential energy between molecules in crystals in order to obtain suitable interatomic potential functions. Thus far, more attention has been paid to the packing of crystals of nonpolar molecules, using empirical interatomic potentials to approximate molecular interactions.[7,8,10,12] However, in order to study polypeptide or protein confor-

mations, heteroatomic interactions (including electrostatic and hydrogen-bonding contributions)[9,14,15] must be included in the total intermolecular potential.

In this paper, we present a method for determining the parameters of empirical potential energy functions for interatomic interactions between atoms of molecules in crystals. X-Ray diffraction data on crystals of hydrocarbons, carboxylic acids, amines, and amides are used, and the precision of the derived potential energy parameters is assessed by comparing calculated and experimental values of lattice constants, lattice binding energies, and (in some cases) interatomic force constants. Several reviews of inter-
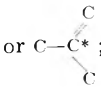
and intramolecular forces[16-21] should be consulted for general background and for a discussion of earlier work in this field.

II. Theory

A. General. In the first paper of this series,[11a] we presented a method for obtaining parameters of empirical potential functions for pairwise-additive interatomic interactions. The equations of static equilibrium (used together with the heat of sublimation) were applied to the single-crystal coordinates and cell constants of benzene found from high-resolution X-ray diffraction data, and the parameters of the Lennard-Jones 6-12 potential were obtained. Further studies with this method (unpublished) indicated that the equations of static equilibrium would be exceedingly difficult to adapt to heteroatomic molecules[22] where there are usually more unknown potential energy parameters in these equations than available independent experimental data, and thus we have approached the problem in an alternative manner. The procedure used here, and discussed briefly elsewhere,[4] is similar in some respects to that used by Williams[8c,d] for hydrocarbons and Ferro and Hermans[9] for heteroatomic molecules. However, there are several major differences from the approaches of Williams and Ferro and Hermans which will be considered in the Discussion section of this paper.

In the procedure used here, the partial charges on each atom are computed by the molecular orbital CNDO/2 (ON) method,[14] the London-van der Waals attractive term is obtained by the Slater-Kirkwood method, and the repulsive term of the Lennard-Jones 6-12 nonbonded energy is computed by minimizing the lattice binding energy with respect to the lattice constants of a number of crystals (adjusting the repulsive terms until the energy-minimized lattice constants best fit the experimentally observed lattice constants). In crystals containing hydrogen bonds, the attractive term of a "general hydrogen bond" (GHB) potential[14c] was taken from previous CNDO/2 computations[14c] of hydrogen bond strengths, and the repulsive term was obtained by the same energy minimization procedure used to compute the repulsive term of the 6-12 nonbonded energy. The total intermolecular potential obtained in this way combines theoretically determined quantities with experimentally adjusted quantities, and is self-consistent with respect to all contributions to the total potential energy. The coordinates of the heavy atoms (i.e., C, O, N, and S) are taken directly from the X-ray data for the crystal structures treated here, and the positions of the hydrogens are generated as described in section IID. No intramolecular interactions are calculated, and no torsional potentials are included. A small set of crystals (pentane, benzene, anthracene, pyrazine, bipyridine, thianthrene, acetic acid, succinic acid, adipamide, oxamide, and methylamine) was first used to obtain a preliminary set of parameters; then the set was expanded to include these crystals as well as the following additional ones to obtain the final refined set of parameters: hexane, formic acid, oxalic acid, suberic acid, formamide, and N-methylacetamide. Finally, the final set of parameters was tested in the treatment of the crystals: octane, sebacic acid, butyric acid, α-phenazine, suberamide, and succinamide. The structures of all of the molecules (except sebacic acid, adipamide, and suberamide), together with their partial charges, are shown[23] in Figures 1-3. The application of the parameters determined here to crystals of amino acids appears in the next paper of this series.[24]

TABLE I: Designation of Atom Types

Atom type	Description
H₁	Aliphatic hydrogen
H₂	Primary and secondary amine or amide hydrogen
H₃	Aromatic hydrogen
H₄	Hydroxyl or carboxylic acid hydrogen
H₅[a]	Sulfhydryl hydrogen; taken as H₃[b]
C₆	Aliphatic carbon
C₇	Carbonyl, carboxylic acid, or peptide bond carbon
C₈	Aromatic carbon
C₉[a]	Aliphatic carbon (but with three heavy atoms attached, e.g., as Cα of amino acid); taken as C₆[b]
C₁₀	Carbon (with asterisk) in $C-C^*$ or $C-C^*$; taken as C₈
C₁₁[a]	Carboxylate ion carbon; taken as C₇[b]
C₁₂	Not used
N₁₃	Primary or secondary amide nitrogen
N₁₄	Uncharged primary or secondary amine nitrogen, or (only in the GHB term) primary or secondary amide nitrogen (N₁₃) as hydrogen (H₂) acceptor in a hydrogen bond
N₁₅[a]	Nitrogen of charged NH₃⁺ group; taken as N₁₃[b]
N₁₆	Not used
O₁₇	Carbonyl or carboxylic acid (C=O) oxygen
O₁₈	Hydroxyl or carboxylic acid (C-O-H) oxygen
O₁₉[a]	$-C-O^*-C$ ester oxygen (with asterisk); taken as O₁₈[b]
S₂₀	Sulfur, as found in sulfur-containing heterocyclic ring systems, sulfhydryl groups, and thio ethers
S₂₁[a]	Disulfide sulfur; taken as S₂₀[b]

[a] This atom type appears in the next paper[24] of this series. [b] This assignment will be used in ref 24.

The initial nonbonded repulsion parameters (including those for hydrogen bonds where applicable) were obtained as follows: aliphatic C₆ and H₁ from n-pentane and refined further using hexane and other molecules containing C₆ and H₁ type atoms, aromatic C₈ and H₃ from benzene and anthracene, ring N₁₄ from pyrazine and bipyridine, ring S₂₀ from thianthrene, each of the parameters for the H₄, C₇, O₁₇, and O₁₈ atoms (as well as the repulsive term of the hydrogen bond function) of the COOH group from acetic and succinic acids, amide N₁₃ and H₂ from adipamide and oxamide, and the H₂···N₁₄ hydrogen bond term from methylamine. Refinement of this initial set (in particular the C₆, C₇, and O₁₈ parameters) was obtained by including a second set of molecules as described above. The remaining parts of the total potential energy function were obtained by a priori considerations, as will be outlined in section IIB. All of the resulting parameters were then used to compute (energy-minimized) lattice constants, binding energies, and some interatomic force constants, which were then compared with experimental values.[25] It must be emphasized that the experimental sublimation energies and force constants are not used in determining the parameters of the potential function, but are used only as a check on the interatomic potentials derived here.

Before outlining the details of the method used to obtain the repulsive parameters of the potential function, it is necessary to discuss six basic assumptions which are adopted in this work as well as in the work of others.[7-9,12,13]

(1) The assumption of pairwise interatomic interactions is used throughout this work. Kitaigorodskii[7a] has argued effectively that the binding energy of the lattice of a molecular crystal (almost exclusively hydrocarbons, in the cases studied by Kitaigorodskii) may be calculated as the sum of the pairwise interactions between the atoms of one molecule and the atoms of all surrounding molecules.

(2) We use the method of "electrons on atoms" to obtain the partial charges positioned at the atomic positions of a molecule, and take these charges [computed by the CNDO/2 procedure] as those of the isolated molecule. Since it is impossible at present to use molecular orbital methods to compute the charges for molecular systems as large as a microcrystal (i.e., the group of molecules included in the generated crystal used here), we argue here that, to a first approximation, the partial charges on the atoms of a molecule in a crystal (in which no hydrogen bonds are involved) can be taken as those of the isolated molecule, i.e., with no perturbations from neighboring molecules. This procedure is equivalent to a quantum mechanical perturbation treatment without exchange.[26] When no exchange is present, the interaction energy between molecules can be considered to be made up of two major, and one minor component: The major components are the point charge or monopole electrostatic (i.e., 1/r) contributions and the dispersion energy (i.e., $1/r^6$) term; the minor component arises from the polarization of one molecule by another (i.e., $1/r^4$ term). The monopole approximation is used because the calculation of the electrostatic energy as a dipole-dipole interaction is not correct for molecules whose dimensions approach the distance between them, and we must therefore use a method that is valid over all interatomic distances found in crystals. We argue below that, in first order, the minor component can be neglected, when no hydrogen bonding is present.

It was found in our earlier work[11] that, when two polar molecules interact in a stacked or plane-to-plane orientation (as in the case of the parallel dimer of the formamide molecule which is not in a hydrogen-bonded configuration), the electron orbital overlap is important and may cause considerable changes in the atomic charges. However, because the reference molecule is always surrounded by symmetry-related molecules in the crystalline state, it seems likely that any large contributions from directional polarization (like those found in the theoretical study of the amide dimers[11]) will be balanced out by the symmetry-related near-neighbor molecules. Further evidence that supports the view, that changes in charge of atoms in a crystal are essentially negligible, comes from the spectral properties of molecular crystals; i.e., the intramolecular infrared and Raman

vibrational transitions show very small spectral shifts, and only modest intensity changes from the electronic redistribution[27] when examined in the gas phase compared to the liquid or solid phase (when no hydrogen-bonding is present). It appears then that induced polarization in a molecule will not be serious in the molecular crystals studied here, and we will use partial charges [i.e., CNDO/2 (ON)] obtained for the isolated molecule[14] in computations of crystal energy. It should be pointed out that the CNDO/2 (ON) charges reproduce only about 65% of the magnitude, while giving good agreement with experiment for the direction of dipole moments in a series of model amides.[14] The relationship of these partial charges to the total intermolecular energy will be discussed in section B1.

(3) Separate considerations apply when hydrogen bonding is present. In a previous paper,[14c] we showed that the energy contributions to hydrogen bonding arising from induced polarization, as well as any exchange energy, could be treated by a special (general hydrogen bond) potential, the GHB potential, between the donor hydrogen atom and some acceptor atom X, plus the total "empirical" potential between all the other atoms of the molecules forming the hydrogen bond. The total "empirical" potential derived previously for dimeric molecular systems reproduced very well some calculated structural and thermodynamic data for the dimers considered, and these hydrogen-bond parameters (as well as the new nonbonded parameters obtained in this paper) will be applied and refined in the crystal calculations presented here. In addition, we showed previously[14b] that the central molecule in a linear hydrogen-bonded trimer also exhibits no significant change in charge distribution.

(4) Because of the large amount of computer time required, it is not feasible to consider all possible packing patterns in cells of different dimensions and different symmetry for a given molecule, nor is it possible to treat all possible conformations of the given molecule in the particular crystal. Therefore, several computationally-advantageous simplifications are made. The first simplification arises from the fact that the observed structure (which may even be a metastable one) is the one of lowest free energy in a given (local) potential energy well; we assume that this structure is attainable by minimization of the potential energy of the lattice.[28] Further, since we want to obtain potential functions which reproduce observed structures, we make the assumption that the heavy atom coordinates in the crystal are fixed relative to each other within a given molecule, i.e., that the molecules may be treated as rigid bodies with no internal degrees of freedom for the heavy atoms. Strictly speaking, the total intra-

inter-molecular potential energy should be minimized. However, the intramolecular energy is omitted because (a) the amount of required computer time would become excessive if the internal degrees of freedom were included, (b) additional considerations, to be discussed in a subsequent paper,[29] must be taken into account to compute the intramolecular potential energy, i.e., interactions between atoms separated by three single bonds about which rotation can take place require intramolecular potential functions[29] which differ from the intermolecular functions considered here (and inclusion of such internal degrees of freedom would, in most cases, make the number of parameters to be determined exceed the number of available data), and (c) we do not believe that the intramolecular energy contributes much to the observed molecular packing of the crystals (although it certainly determines the internal molecular conformation) since a consistent set of potential parameters is obtained for many crystals (even though the intramolecular energy would be expected to vary from one crystal to another); to the extent that the intramolecular energy does contribute to the observed molecular packing, this would reflect itself in errors in the parameters of the potential function.

While the coordinates of the heavy atoms are fixed within a given molecule, we do allow rotations about bonds (which involve the movement of only hydrogen atoms) to take place, and these rotations will be discussed individually as they occur. The reason for this is the lack of precise experimental crystal data positioning the hydrogens (i.e., the hydrogens are not readily detected by x-ray diffraction).

A further simplification is made by choosing a subset of the total number of variables that may be used to describe the energy of the crystal. The lattice energy (excluding the intramolecular energy) is a function of the following variables:

(a) lattice constants, $\underline{a}$, $\underline{b}$, and $\underline{c}$.

(b) unit cell angles, α, β, and γ.

(c) Eulerian angles θ, φ, and ψ which describe the rotational position of the reference molecule relative to the crystal axes.

(d) coordinates of the center of mass X, Y, and Z of the reference molecule.

By taking the observed internal molecular coordinates as fixed, and by demanding that the crystal symmetry be preserved, (c) and (d) above are no longer variables, and only the quantities (a) and (b) remain to be varied. By considering only quantities (a) and (b) as variables, these are determined by the condition that the first derivative of the potential energy vanishes at equilibrium, thereby

yielding the parameters of the potential function; those properties (e.g., spectra) which depend on the second derivative will not be used to obtain these parameters. The reason for this approach is (a) the lack of good spectral data on crystals of many of the molecules studied here, and (b) the considerably more expensive calculations necessary for this added refinement. However, some interatomic force constants, which are directly related to the spectra, will be computed, after the potential function is determined, and compared with experimental values. It is clear that any errors arising from fixing (c) and (d) will appear as errors in (a) and (b).

(5) We adopt a principle of transferability, i.e., we assume that potentials determined from one set of crystals are applicable to crystals of other molecules containing similar types of atoms. Kitaigorodskii[7] has observed that experimental distances between pairs of atoms in contact vary within rather narrow limits (viz., ~ 0.5 Å) from one molecular crystal to another. For example, the H···H contact distances are nearly the same in pentane, adipamide, and succinic acid, even though these molecules pack quite differently in their respective crystals. This is the primary reason for the probable validity of the above assumption.

Large variations in contact distances, which would vitiate the principle of transferability, might conceivably arise primarily from two sources: (a) different roles of molecular vibrations in different crystals, and (b) different temperatures at which the structural data are obtained. We have tried to minimize large variations in contact distances by selecting data in which these effects are small, e.g., by selecting low-temperature data where these are available. Since the closest contact distances for specific pairs of atoms do not vary much between the crystals selected here, we expect the principle of transferability to be valid.

(6) The thermodynamics of the molecular binding energy in crystals, and the effect of the various energy terms and their derivatives on the determination of

the coefficients of the potential, is complicated. In the simplest case (viz., at 0°K) the intermolecular energy can be thought of as being made up of a potential energy plus an intermolecular zero point contribution.[30] The intramolecular energy also contains a zero point contribution; however, as pointed out in paragraph 4, we are neglecting the intramolecular energy. For the molecules of interest here, the role of the several heavy atoms per molecule is to make the potential energy essentially classical (i.e., the intermolecular zero point energy is small compared to the binding energy[7]), and we will not consider the quantum mechanical intermolecular zero point energies further.[31,32]

Even when this approximation is made, an additional problem arises from the fact that the x-ray crystal data used here were not obtained at 0°K, and the thermal contributions to the lattice constants may cause considerable difficulty in the interpretation of the energy parameters derived here. The dependence of the molecular vibrations within a crystal on temperature is not well understood, and cannot be predicted or explained theoretically in sufficient quantitative detail for molecules of the type studied here. The problems that thermal effects introduce in this study can be stated as follows: As the temperature of a crystal rises from 0°K to room temperature, molecules can be assumed to remain largely in their electronic ground state. However, the higher-energy levels for the low-frequency molecular rotational and weak bending modes of the molecule will become excited. Further, the population of upper crystal lattice vibrational energy states will increase (which is observed experimentally as small increases in line width and in the intensities of combination lines in the far infrared spectra of crystals).[27] These effects are anharmonic in nature, and usually manifest themselves in an expansion of the lattice and in an increase in the distances between nonbonded atoms of different molecules. Since the experimental x-ray data pertain to the thermally-expanded cell, we must expect that the parameters ob-

tained here (essentially the repulsive terms[33]) will include the average thermal (i.e., kinetic energy) contributions of many different molecules. The complexity of the effect of thermal vibrations can be seen in the case where large vibrational amplitudes occur between layers or planes (i.e., in the directions of weak van der Waals forces), and cause a contraction (i.e., a smaller change of distance than expected from an isotropic thermal expansion) within the plane. An example of this, among the crystals considered here, may be the long-chain carboxylic acids, where there are small vibrational amplitudes within the planes because of large (hydrogen-bonding) forces and large vibrational amplitudes between the weakly-bonded planes. For these reasons, we cannot hope to obtain perfect fits to the lattice of any one molecular crystal, but rather an average best fit for many crystals with similar thermal properties. By selecting the crystals for study here properly,[33] we hope we have minimized the effects of varying temperature for different structures.

Williams[8d] has considered the thermal corrections to empirical parameters for the noble gases and anthracene crystal structures at different temperatures. By making the requisite coefficient a function of temperature, he was able to predict the observed thermal expansion of some crystals. Unfortunately, the lattice constants are not available at various temperatures for low-temperature structures of many polar molecules, and this lack of data makes it difficult to apply Williams' procedure in this study. Other attempts to solve this problem were made by Lifson and Warshel[12] and Kitaigorodskii,[7] who extrapolated the experimental hydrocarbon crystal lattice constants to approximate those at 0°K, before carrying out the computations on the crystals.

With the above approximations in mind, it must be recognized that any success that results from the application of these empirical potentials must be due to compensations, within the empirically-determined coefficients, for their many theoretical shortcomings.[34]

B. Intermolecular Potential Energy.

The intermolecular potential energy (i.e., lattice binding energy)[35,36] is taken to be the sum of all *pairwise* interatomic interactions (with three-body and higher interactions being neglected) between the atoms of a central (i.e., 0th) molecule and the atoms of all the symmetry related molecules, generated by the crystal symmetry operators, which surround it; the surroundings include a three-dimensional array of several unit cells along each crystal axis, the number being determined by the unit cell length along each axis in the positive and negative directions, and we require that all molecules within 10 Å of the 0th one (and some others beyond)[37] be included.

The total pairwise interatomic interaction energy is constructed from the following terms: (1) the monopole coulombic (electrostatic) interaction, (2) the London–van der Waals attraction, (3) the repulsive nonbonded term, and (4) the hydrogen-bond contribution.

1. Electrostatic. The pairwise electrostatic contribution is obtained from the interaction between atom i of molecule 0 and atom j of all other molecules in the crystal surroundings. Coulomb's law is used to calculate the monopole interactions as

$$U_{el}(r_{ij}) = \sum_{i=1}^{n} \sum_{j=1}^{M} 332.0 q_i q_j / D r_{ij} \qquad (1)$$

where n is the number of atoms in molecule 0, and M is n times the number of molecules surrounding molecule 0 and depends on the number of molecules per unit cell and on the number of unit cells used in the calculation. The number 332.0 is a conversion factor to give U_{el} in kcal/mole when r_{ij} (the distance between atom i and atom j) is in ångström units, and the q's are in electronic charge units. In applying the crystal symmetry conditions, edge and surface effects must be taken into account because of the slow fall-off of the electrostatic energy. This effect will be discussed later in section IIIA.

The partial electronic charges, q_i, are centered on each atom, and are determined by the molecular orbital CNDO/2 (ON) method[14] for the geometry and conformation of the molecule of interest. The charges on the atoms[23] of the various molecules are shown in Figures 1–3, the net charge on each molecule being zero. The "*effective* dielectric constant," D, is taken to be equal to 2 in all cases. This value matched the CNDO/2 interaction energy at large separation distances of dimers obtained in our earlier study of the hydrogen bonding of dimers,[14b,c] and probably does not correctly reflect the bulk dielectric properties of all of the molecules studied here (i.e., the pertinent experimental dielectric constants lie in the range of 2–7). However, because of the low value of the dipole moments, obtained with these charges, coupled with the "effective" dielectric constant of
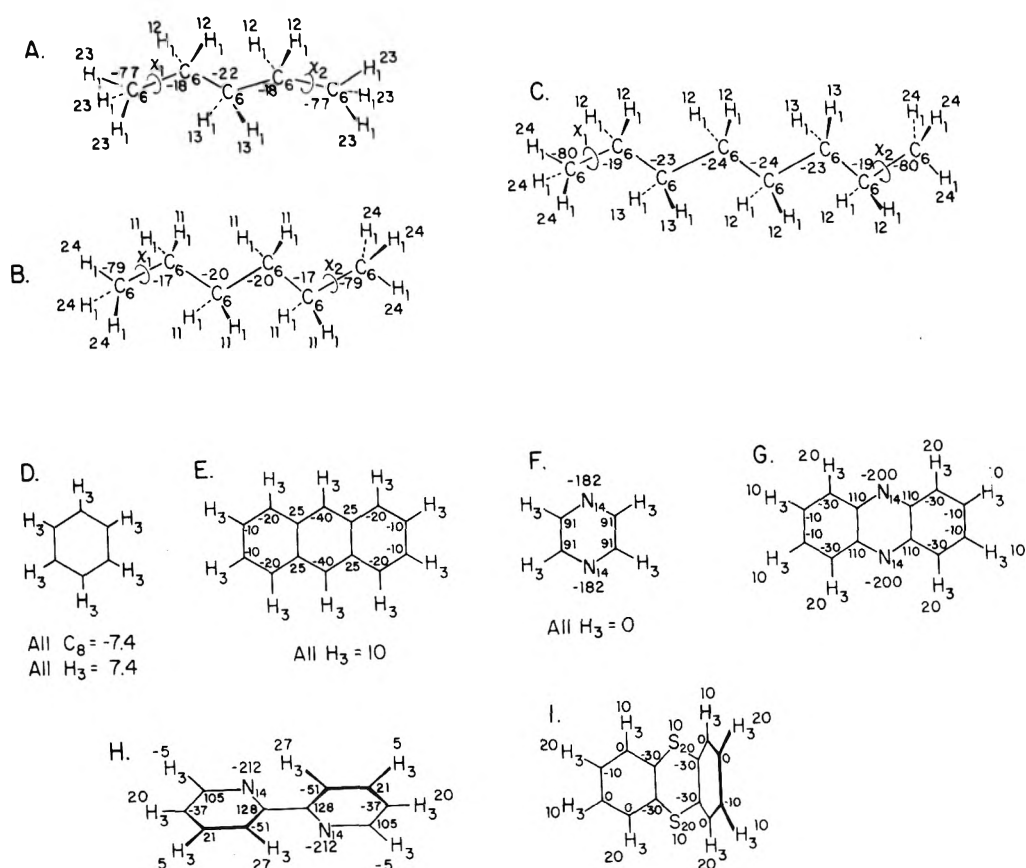
Figure 1. The structures and CNDO/2 (ON) partial atomic charges (in electronic units ×1000) for the molecules:[23] (A) pentane, (B) hexane, (C) octane, (D) benzene, (E) anthracene, (F) pyrazine, (G) α-phenazine, (H) 2,2′-bipyridine, (I) thianthrene. The asymmetry in the charges of thianthrene arises from a slight deviation of the heavy-atom geometry from symmetry, in the crystal.
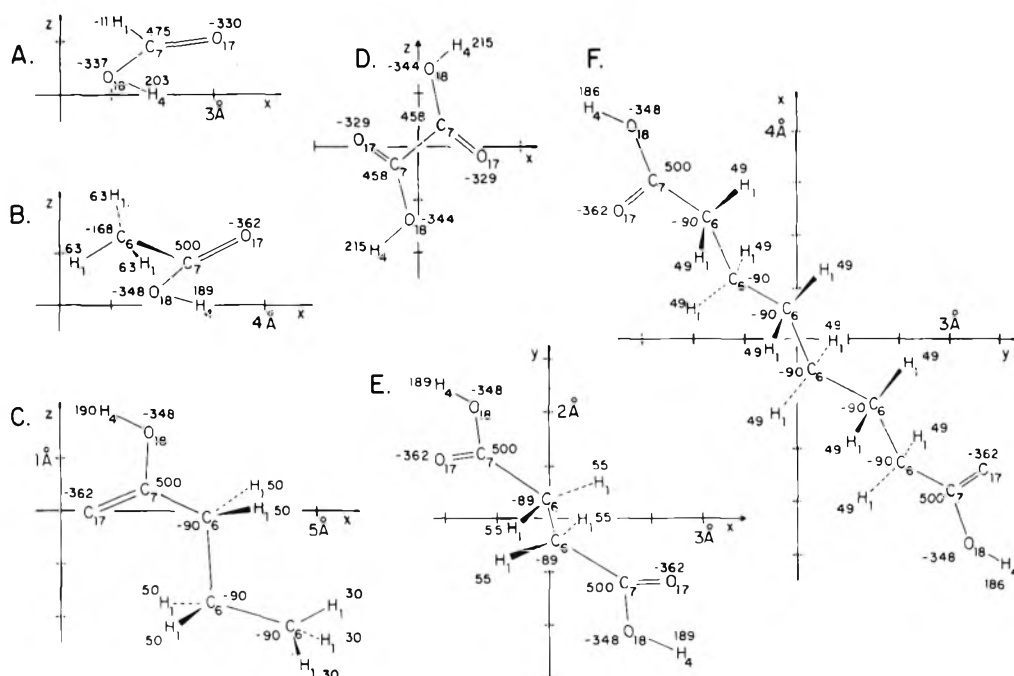
Figure 2. The structures and CNDO/2 (ON) partial atomic charges (in electronic units ×1000) for carboxylic acid molecules:[23] (A) formic, (B) acetic, (C) butyric, (D) oxalic, (E) succinic, (F) suberic.
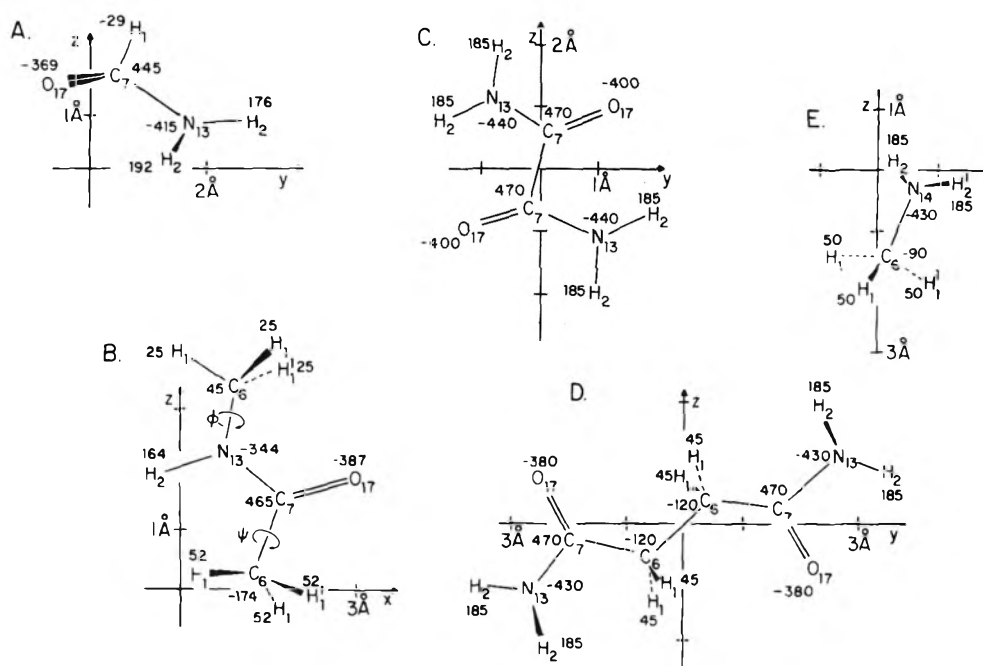
Figure 3. The structures and CNDO/2 (ON) partial atomic charges (in electronic units ×1000) for various amine and amide molecules:[23] (A) formamide, (B) N-methylacetamide, (C) oxamide, (D) succinamide, (E) methylamine.

2 used here, the net calculated long-range electrostatic interactions are equivalent to those with a dielectric constant of ~4. On a microscopic scale, the true dielectric constant varies with distance in a complex manner. Since we are seeking a universal and self-consistent set of interatomic potentials, we ignore the variation of the dielectric constant from crystal to crystal, which would only complicate the computations, and also would require a drastic change in the hydrogen-bond potential.[14c]

In the data in the tables reported here, a number of unit cells (specified in the tables) was taken so that, in general, the longest interaction distance was greater than 10 Å.[37]

2. London–van der Waals Attraction. Since there is insufficient information in the crystal data to determine all the energy parameters uniquely, we have computed the C^{kl} coefficients from the London (or Slater–Kirkwood) formulation,[38] where the nonbonded interaction is given by the Lennard-Jones 6–12 expression

$$U_{NB}(r_{ij}) = \sum_{i=1}^{n}{}' \sum_{j=1}^{M}{}' (A^{kl}/r_{ij}^{12} - C^{kl}/r_{ij}^{6}) \quad (2)$$

where k and l refer to particular atom types. The prime signifies that H⋯X interactions, where H and X are hydrogen-bonding types of atoms and are treated in section IIB4 on hydrogen bonding, are excluded from the summations. The coefficient, C^{kl}, of the attractive term is obtained from[38]

$$C^{kl} = \frac{3}{2}\left[\frac{e\hbar}{m_e^{1/2}}\right] \frac{\alpha_k \alpha_l}{(\alpha_k/N_k)^{1/2} + (\alpha_l/N_l)^{1/2}} \quad (3)$$

where α_k and α_l are the experimentally determined polarizabilities,[39] and N_k and N_l are the effective number of electrons for atom types k and l, respectively, and are taken from Scott and Scheraga.[38] The values of α_k and N_k used are given in Table II. The fundamental constants, $e, \hbar$, and m_e have their usual meanings. Having fixed the C^{kl} coefficients, this leaves only the repulsive coefficient to be varied; this is discussed in paragraph 3 of this section.

3. Repulsive Nonbonded Interaction. Different types of atoms (*e.g.*, hydrogen, oxygen, nitrogen, etc.) are in contact

TABLE II: Polarizabilities and N_k of Various Atoms[a]

Atom	$\alpha \times 10^{24}$, cm^3	N_k
H$_{all\ types}$	0.42	0.85
C$_6$ and C$_8$	0.93	5.20
C$_7$	1.51	5.20
C$_{unsaturated}$[b]	1.65	5.20
N$_{13}$	0.87	6.10
N$_{14}$	0.93	6.10
O$_{17}$	0.84	7.00
O$_{18}$	0.59	7.00
S$_{20}$	0.34	14.8

[a] References 38 and 39. [b] These values of α and N_k were used initially for the aromatic hydrocarbons. All attempts to find reasonable fits to lattice constants, with resulting binding energies in agreement with available sublimation data, failed; hence, the values for C$_6$, which gave better agreement with experimental values, were subsequently used.

with one another in the various crystals studied.[33] These closest contacts between atoms in a crystal are generally repulsive interactions,[33] since the whole crystal must be in a state of equilibrium between short-range repulsive forces and attractive forces, and both forces must be in balance for the potential energy to be a minimum. By considering those interatomic interactions which exhibit the largest repulsive effect in a particular crystal, we can select particular pairs of atoms which are in close contact and use them to determine the A^{kl} coefficients of eq 2. We do not mean that only a few repulsive coefficients are used for any one crystal; indeed, all interactions are included for every crystal. Rather, we can use a knowledge of the types of atom which are in nearest-neighbor contact to select crystals whose energies will be most sensitive to these different repulsive terms. The repulsive coefficients A^{kk} (where the superscript kk indicates that both atoms k and l are of the same type) of eq 2 are then determined by obtaining a best fit to the lattice constants of the crystals of *many* molecules, by energy minimization, as described in section IIIB. From the definition of the depth of the potential well, ϵ^{kk} at the minimum position,[11a] $\langle r_g^{kk}\rangle$, the parameter A^{kk} can be written as

$$A^{kk} = -\epsilon^{kk}\langle r_g{}^{kk}\rangle^{12} \qquad (4)$$

The fences around the $r_g{}^{kk}$ parameter are used only to imply that this is an average value derived from many different crystals whose structures were determined at different *temperatures*. The *mean-value law* is then used to find the position of the minimum for the cross terms, *i.e.*

$$\langle r_g{}^{kl}\rangle = (\langle r_g{}^{kk}\rangle + \langle r_g{}^{ll}\rangle)/2 \qquad (5)$$

However, the energy, ϵ^{kl}, is calculated from the values of C^{kl}, obtained from eq 3, for each atom–atom type interaction, using the expression

$$-\epsilon^{kl} = C^{kl}/2\langle r_g{}^{kl}\rangle^6 \qquad (6)$$

Thus, for each A^{kk}, all cross terms (*i.e.*, A^{kl}) may be found easily from

$$A^{kl} = -\epsilon^{kl}\langle r_g{}^{kl}\rangle^{12} \qquad (7)$$

and eq 5 and 6.

4. Hydrogen-Bond Interactions. In a previous paper,[14c] we found that the properties of hydrogen-bonded dimers could be well represented by a general hydrogen bond (10–12) potential (GHB) of the following form

$$U_{GHB}(r_{H\cdots X}) =$$
$$\sum_{i=1}^{n}\sum_{j=1}^{M}(A'_{H\cdots X}/r_{H\cdots X}{}^{12} - B_{H\cdots X}/r_{H\cdots X}{}^{10}) \qquad (8)$$

where the sum over i is taken only over the hydrogen-bonding atoms [*i.e.*, H(N), H(O), O or, in some cases, N] among the n atoms in the 0th molecule, and the sum over j is taken only over the donor (H) or acceptor (X) atoms among the M atoms of other molecules [H(N) or H(O) atoms always interact with O or N atoms for hydrogen bonding; in the case where H(N) interacts with H(O), for example, a normal nonbonded parameter would be used]. Thus, while the interacting H and X atoms (treated by eq 8) are excluded from the summations in eq 2, they *are* included in the summations of eq 1. The H's considered here are those in amide, amine, acid, or alcohol groups, the X's are acid, alcohol, carbonyl, or amine oxygen, or nitrogen, acceptor atoms, and $A'_{H\cdots X}$ and $B_{H\cdots X}$ depend on the type of hydrogen bond formed.[14c] When used with all the other interatomic interactions in the molecules forming the hydrogen bond (which was simply a dimer in the previous study[14c]), this potential was shown to give a good fit to both quantum mechanical (CNDO/2) results, and experimental dimerization energy and dimer structure.[14c] The fit was achieved[14c] by making the A' and B coefficients consistent with gas-phase electron diffraction data on the acetic acid dimer, and with thermodynamic data for the stability of the dimer, as well as with the attractive part of the CNDO/2 curves. We will retain the earlier values[14c] of $B_{H\cdots X}$ for the different types of hydrogen bond, and (by minimizing the binding energy of the crystal) will adjust the $A'_{H\cdots X}$ values.

In the earlier paper,[14c] we compared the total empirical *energy of a dimer* with the CNDO/2 energy. Since the $1/r^6$ term (of eq 2) arises from quantum mechanical theory (*i.e.*, with the molecules sufficiently far apart so that the electronic clouds of the atoms are not in contact), and since this term is not included in the CNDO/2 calculations, it was not rigorously correct to use[14c] eq 2 when comparing the empirical and CNDO/2 energies. Since the N and O atoms in, *e.g.*, an N–H$\cdots$O hydrogen bond are within 3–4 Å of each other, the use of a 6–12 potential for the N$\cdots$O in-

teraction (in the evaluation of the GHB potential for the H$\cdots$O interaction) was probably incorrect, *i.e.*, the molecular orbital interactions in the range of distances found for closest approach of the heavy atoms in the hydrogen bond may not follow the $1/r^6$ attraction, nor do the very close repulsive interactions follow the $1/r^{12}$ repulsion. Apparently, the GHB term helps correct for these inconsistencies in the fit to the CNDO/2 energies and also for the discrepancies reported[14c] for the close-contact repulsions determined by the CNDO/2 method (*i.e.*, atoms were found to approach one another too closely, when compared to experimental contact distances).

It should be noted that we have not included in our empirical potential a contribution from the energy of interaction between the dipole induced in an atom by nearby charges with those charges. Nor have we allowed the partial atomic charges to vary[14c] as a function of the H$\cdots$X distance as a hydrogen bond is formed in the crystal. Probably, some contribution to the energy from these terms is absorbed into the GHB function, although it is difficult to make a quantitative estimate of these effects at this time. It is also clear that no cooperativity (whereby the formation of one hydrogen bond enhances the subsequent formation of a second hydrogen bond in some cooperative manner) is explicitly included in our potential functions.

5. Total Intermolecular Potential. The total intermolecular potential, U_{Tot}, is taken as the sum of all the interatomic interactions just described, and it is this sum that is minimized in the energy minimization part of the fitting procedure described in section IIIB.

During the energy minimization (in which the lattice constants are varied, which implies that the r_{ij}'s are varied), the different components of the total intermolecular potential energy will contribute to different extents. Thus, it is necessary to consider the relative contributions of each component, for a given set of coefficients of the potential function. If we use the interatomic force F (*i.e.*, the negative of the first derivative of U_{Tot} with respect to r_{ij}) as an indication of the relative contributions of the various components of the potential, then

$$F = -\frac{\partial U_{Tot}}{\partial r_{ij}} = \frac{332.0q_i q_j}{Dr_{ij}{}^2} + \frac{12A^{kl}}{r_{ij}{}^{13}} - \frac{6C^{kl}}{r_{ij}{}^7} + \frac{12A'_{H\cdots X}}{r_{H\cdots X}{}^{13}} - \frac{10B_{H\cdots X}}{r_{H\cdots X}{}^{11}} \qquad (9)$$

where the summation symbols have been omitted for convenience. From eq 9, we see that, for hydrocarbons (where the hydrogen-bond coefficients are zero, and the partial atomic charges are insignificantly small), the repulsive forces are very sensitive to changes in r_{ij} (varying as $1/r_{ij}{}^{13}$). However, for crystals for which a hydrogen-bond term must be included, the term $12A'_{H\cdots X}/r_{H\cdots X}{}^{13}$ dominates over the term $12A^{kl}/r_{ij}{}^{13}$ because the H$\cdots$X distance in a hydrogen bond ($\sim$1.6–2.0 Å) is smaller than the usual van der Waals contact distances ($\sim$3.5 Å or greater) for most heavy atoms. In some crystals containing hydrogen bonds (*e.g.*, succinic acid), this bond is the dominant contribution to the force along only one crystal lattice axis. Thus, A^{kl} can be determined for such crystals by examining the effect of variation in A^{kl} on the force along axes perpendicular, or nearly so, to the direction of the hydrogen bond. Finally, the contribution of the GHB potential to the force will be greater for the carboxylic acids (*i.e.*, the H$_4\cdots$O$_{17}$ interac-

tion) than for amides (*i.e.*, the $H_2\cdots O_{17}$ interaction) because the former is a stronger hydrogen bond (see Table V).

We have not found it necessary to introduce spurious or "dummy" atoms to take lone-pair electrostatic contributions into account.[9] In all cases, the interatomic interactions are taken between the coordinates of the atoms involved in the interaction, *i.e.*, the positions of both the attractive and repulsive interactions were placed directly on the atom and not moved into the bond.[8a]

C. Intramolecular Energy. The intramolecular energy, which is the contribution from the internal energy of each individual molecule to the total energy of the crystal and is a function of the dihedral angles of the molecule,[40] is not included in the energy which is minimized, as already discussed in section IIA4. Hence, the heavy atoms (*i.e.*, all atoms except some hydrogens) were held fixed at the positions given by the X-ray data, and no internal rotations involving movement of heavy atoms were allowed. However, in the case of molecules which have methyl ($-CH_3$) or hydroxyl ($-OH$) groups, the positions of the hydrogens are usually not well determined by X-ray studies, and rotation about the bond which varies the positions of the hydrogens is therefore carried out to find the hydrogen conformation of lowest intermolecular energy. Each case in which the hydrogens are rotated is discussed separately as it arises in the analysis of the molecules studied here.

The use of the intermolecular potentials obtained in this study to calculate intramolecular interactions in amino acids and polypeptides is presented elsewhere.[29,41-43]

D. Geometry. The geometry for each molecule is taken from the X-ray diffraction coordinates for the heavy atoms (*i.e.*, carbon, oxygen, nitrogen, and sulfur). The hydrogen atom positions are deduced from structures of similar molecules, determined by electron[4c,45] and neutron diffraction.[46-50] Data for placing hydrogens are available for all of the molecular groups studied here. The bond lengths and bond angles for the different types of hydrogens used here are given in Table III. Aside from the rotation of $-CH_3$ and $-OH$ groups (mentioned in section IIC), we have not found it necessary to move the hydrogens (*i.e.*, change the bond lengths or bond angles from those given in Table III) to obtain good fits to the crystals studied here, even though alternative positions of the hydrogens were examined in some cases.

E. X-Ray Data. The molecular crystals chosen for study were picked from hundreds of known X-ray and neutron diffraction structures. As far as possible, the criteria used for choosing the crystals studied here were the following. (a) There should be no water of hydration or miscellaneous anions or cations (such as Cl^-, Br^-, Na^+, etc.) in the crystal. (b) The bond lengths and bond angles must be in reasonable agreement with similar data from other crystals; the diffraction pattern must yield a sufficiently large ratio of data to parameters (*i.e.*, a ratio of five or six to one), and the resulting R factor must be relatively low (*e.g.*, 20% would be a marginal structure). (c) The crystal must have only one crystallographic asymmetric molecule per unit cell, so that all other molecules in the unit cell can be generated by crystal symmetry operators (rotations and translations) acting on the first molecule. For hydrogen-bonded systems, the asymmetric molecule is a monomer, except when an inversion center lies between the two monomers in the hydrogen bonded dimer; in the latter case, the asymmetric molecule is a dimer. (d) The crystal must have some relevance to protein structure or be a model for the various

TABLE III: Bond Lengths and Bond Angles Involving Hydrogen Atoms

Bond	Type	Length, Å
C–H	$\diagdown$CH$_2$ (aliphatic)	1.09[a]
	$\diagdown$CH$_2$ (glycine)	1.00[b,c]
	–CH$_3$	1.09[a]
	$\diagdown$C–H (aromatic)	1.09[a]
	–$\diagdown$C–H	1.00[b]
N–H	–NH$_2$	1.00[d]
	$\diagdown$N–H	1.00[d]
	–NH$_3^+$	1.00[c,d]
O–H	–O–H	1.00[e]

Bond angles	Type	Angle, deg
H–C–H	$\diagdown$CH$_2$ (aliphatic)[f]	107.0
	$\diagdown$CH$_2$ (glycine)[c,f]	107.0
	–CH$_3$ (tetrahedral)	109.5
	$\diagdown$C–H (aromatic)	*g*
X–C–H	X$\diagdown$Y–C–H$\diagup$Z	*h*
H–N–H	–NH$_2$	120.0[i]
X–N–H	X–NH$_2$ (X $\neq$ H)	120.0[i]
	X–NH$_3^+$ (tetrahedral)	109.5[c]
	X$\diagdown$N–H (Y $\neq$ H, Y$\diagup$ X = C')	124.0[i,k]
X–O–H	X–O–H	110.0

[a] Electron[44,45] and neutron[46-50] diffraction data give values for C–H bond lengths in methyl and methylene groups of around 1.09 ± 0.03 Å. While most X-ray results are shorter (see original papers on the molecules studied here), we have chosen 1.09 Å as a best value for these groups as well as for C–H bond lengths in aromatic rings. [b] The position of this hydrogen is not well defined in the literature, and the bond length has been chosen to be somewhat short in order to avoid complications in the intermolecular energy which may arise from the uncertainty about its position. [c] Found in amino acids studied in the accompanying paper.[24] [d] Neutron diffraction results give N–H distances around 1.0 ± 0.05 Å.[46-50] [e] Neutron diffraction results give O–H values near 1.0 ± 0.02 Å.[47,48] [f] The plane defined by the atoms H–C*–H bisects the C–C*–C angle, and is perpendicular to the C–C*–C plane. [g] The hydrogens on aromatic rings are positioned on the vector bisecting the angle between the heavy atoms. [h] The hydrogen is positioned on the vector which runs through the central carbon atom to the midpoint of the triangle defined by the heavy atoms (X, Y, and Z). [i] Hydrogens on amide nitrogens were chosen to lie in the plane defined by the $-C(=O)N$ atoms, in agreement with the neutron diffraction results for similar molecules.[46] This result has been confirmed in more recent[18,49] neutron diffraction studies. [j] In section IVF6, it was found necessary to investigate nonplanar $-NH_2$ configurations. In that case, the two hydrogens were placed tetrahedrally (*i.e.*, at 109.5°) with respect to the X–N bond. In all other amides, the value 120.0° was used. [k] Y–N–H bond angle is 115° if Y = C^α and X = C'.

functional groups found in proteins (such as amides, carboxylic acids, etc.). (e) The crystal must contain close contacts between atoms whose A^{kl} coefficients are to be determined.[33]

It should be noted here that, although very precise lattice constants are obtainable experimentally, the determination of atomic positions within the unit cell are generally much more difficult to obtain with good precision (*i.e.*, there is only modest precision in bond lengths and bond

TABLE IV: Parameters of the 6–12 Nonbonded Potential

Atom pair[a]	$C^{kk,b}$ kcal Å^6/mol	$A^{kk,c}$ × 10^{-4} kcal Å^{12}/mol,	$-\epsilon^{kk,d}$ kcal/mol	$\langle r_0^{kk}\rangle$,[e] Å	$-\epsilon^{kk,d,f}$ kcal/mol	$\langle r_0^{kk}\rangle$,[d,e,f] Å
H$_1$···H$_1$	45.5	1.410	0.037	2.92	0.123	2.40
H$_2$···H$_2$	45.5	0.843	0.062	2.68		2.40
H$_3$···H$_3$	45.5	1.439	0.036	2.93		2.40
H$_4$···H$_4$	45.5	1.169	0.044	2.83		2.40
C$_6$···C$_6$	370.5	90.603	0.038	4.12	0.120	3.40
C$_7$···C$_7$	766.6	104.898	0.141	3.74		3.40
C$_8$···C$_8$	370.5	47.530	0.073	3.70		3.40
N$_{13}$···N$_{13}$	363.1	73.254	0.045	3.99	0.204	3.10
N$_{14}$···N$_{14}$	401.0	37.494	0.107	3.51		3.10
O$_{17}$···O$_{17}$	369.0	17.019	0.200	3.12	0.233	3.04
O$_{18}$···O$_{18}$	217.2	12.563	0.094	3.24		3.04
S$_{20}$···S$_{20}$	249.0	36.318	0.043	3.78		

[a] The subscripts are described in Table I. [b] The C^{kl} coefficients of all cross terms are calculated from eq 3. [c] The A^{kl} coefficients of all cross terms are calculated from eq 5–7. [d] ϵ^{kk} is the energy at the minimum of the potential, i.e., at $\langle r_g^{kk}\rangle$ (or r^{kk} of ref 59). [e] $\langle r_g^{kk}\rangle$ is the position of the minimum of the potential for the parameters derived in this work; r^{kk} is the position of the minimum of ref 59. [f] From ref 59.

TABLE V: Parameters for General Hydrogen Bond Potential[a,f]

Donor and acceptor atoms	$A'_{\text{H}\cdots\text{X}}$, kcal Å^{12}/mol	$B_{\text{H}\cdots\text{X}}$, kcal Å^{10}/mol	$r_{\min}$,[b] Å	$U_{\min}$,[c] kcal/mol
H$_2$···O$_{17}$	12,040	4014	1.90	−1.11
H$_4$···O$_{17}$	13,344[d]	5783[d]	1.66	−5.92
H$_4$···O$_{18}$	13,033	4610	1.84	−1.71
H$_2$···N$_{14}$	32,897[e]	8244[e]	2.19	−0.55

[a] The crystals used to obtain these parameters were (H$_2$···O$_{17}$) formamide, oxamide, and adipamide; (H$_4$···O$_{17}$ and H$_4$···O$_{18}$) acetic acid and succinic acid; (H$_2$···N$_{14}$) methylamine. [b] $r_{\min}$ = $[1.2A'/B]^{1/2}$, and is the value of $r_{\text{H}\cdots\text{X}}$ at which $U_{\min}$ occurs. This is *not* the hydrogen-bond distance found for any energy-minimized crystal; rather, all interactions must be included to obtain the observed distances. [c] $U_{\min}$ = $-0.067B^6/A'^5$; it is the lowest value of the potential energy, and occurs at $r_{\min}$. [d] These values are in very close agreement with those found previously for formic acid dimers.[14c] All GHB parameters (including this one) have been refined in the present paper. [e] These values are also used for the H$_2$···N$_{13}$ type of hydrogen-bond interaction. [f] Reference 14c.

angles compared to the precision of the lattice constants). Since we use the reported atomic coordinates for the heavy atoms, the errors inherent in these coordinates will reflect themselves, along with other errors, in our minimum-energy variables (i.e., the lattice constants, a, b, c, α, β, γ). Further, since each crystal may have been studied under different physical conditions (e.g., temperature), different methods of collecting and analyzing the data, and to different degrees of reliability (i.e., R index), it is clear that all the data used here are not of comparable quality. By using a considerable number of crystals, it is hoped that any abnormal structural deviations, that a particular (possibly poorly) refined crystal structure might contribute to the determination of our potential energy coefficients, are minimized. The discrepancy indices R, reported for each crystal, are given in Tables VI–VIII.

F. Force Constants. The second derivative of the total empirical potential energy function with respect to a particular interatomic distance gives the force constant for that interaction at any given distance between the atoms of interest. The force constants obtained from these potentials will be compared to similar constants obtained from spectral data and to force constants for pairs of *isolated* atoms obtained from Hartree–Fock and Thomas–Fermi–Dirac repulsive potentials fitted with analytical functions.[51,52] It will be shown that, in the range of contact distances observed in molecular crystals, the agreement between our empirical force constants and those obtained from the more rigorous atomic theory[51,52] and from the

limited experimental data on benzene[53] and naphthalene[54] is very good. Reliable force constant data are not available for other interatomic interactions in the crystals studied here.

In order to understand the origin of the forces involved in hydrogen-bonding interactions, it would be necessary to make an assumption as to which atoms must be included in the reduced mass (i.e., whether the reduced mass is that of the three or four atoms involved in the hydrogen bond or that of the two complete molecules involved in the hydrogen bond); this assumption is also required in order to obtain the force constant. Most likely the masses of the whole molecules will determine the frequency (i.e., force constant) to some extent when the molecules have compact molecular frames or are rigid (such as aromatic molecules and H$_2$O). On the other hand, as the number of bonds about which relatively unhindered rotation can take place increases, the vibration of interest may tend to become a localized one, and its force constant would become more difficult to interpret or calculate. No attempt will be made in this paper to correlate the derived potentials with the force constants for hydrogen bonds; however, unpublished results of work carried out in this laboratory indicate that our interaction potential for hydrogen bonds may be somewhat stiff, resulting in a force constant at equilibrium which is too high.

III. Procedure

A. Generation of Crystal. The basic principles and equations for generating the positions of the molecules in a unit cell and, from this, constructing a microcrystal from repeating unit cells may be found elsewhere.[8,11a] First, the cell coordinates of the heavy atoms of the 0th molecule are converted to cartesian coordinates[8] by multiplying by a transformation matrix,[8] made up of the experimental unit cell lattice constants a, b, c, α, β, and γ. Hydrogen atoms are then generated onto the 0th molecule as described in section IID. In order to generate the other molecules from the 0th molecule, all molecules are treated as rigid bodies (with three rotational and three translational degrees of freedom). Three translational degrees of freedom are used to position the center of mass of the other molecules in the unit cell (i.e., the translational operators are taken as fractions of the unit cell axis), and the three rotational degrees of freedom are used to orient each molecule relative to the 0th with a rotational matrix operator (with diagonal terms ±1 and off-diagonal terms 0 for *these* crystals). The trans-

TABLE VI: Results for Aliphatic and Aromatic Hydrocarbons and for Heterocyclic Compounds

Molecule[a]	Author	Space group	No. of molecules per unit cell	Discrepancy index R,[b] %	Cell[c] index	a, Å / Δa,[d] Å	b, Å / Δb,[d] Å	c, Å / Δc,[d] Å	α, deg / $\Delta\alpha$,[d] deg	β, deg / $\Delta\beta$,[d] deg	γ, deg / $\Delta\gamma$,[d] deg	V, Å³ / ΔV,[d] Å³	σ,[e] Å	Binding energy U_{exptl} or calcd, kcal/mol
Pentane[f] $T = -150°$	Exptl	P_{bcn}	4	5.6	321	4.10	9.04	14.70	90.0	90.0	90.0	545		-10.0[p]
	This work					0.16	-0.14	0.13				9	0.16	-9.9
	Ref 8a					0.03	-0.13	0.08				4	0.13	-8.0
	Ref 9					0.03	-0.44	0.14				-16	0.23	-9.3
Hexane[h] $T = -115°$	Exptl	$P\bar{1}$	4	6.4	232	8.34	4.70	8.57	96.6	87.2	105.0	322		-12.2[g]
	This work					0.27	-0.14	0.05	0.2	0.4	-1.4	4	0.09	-12.0
	Ref 8a					0.04	-0.13	0.04	NR[j]	NR	NR		0.06	-9.7
	Ref 12					0.15	-0.12	-0.07	-0.5	0.8	-1.9	2	0.07	-12.2
Octane[i] $T = -70°$	Exptl	$P\bar{1}$	4	7.0	231	8.32	4.75	11.00	94.8	84.5	105.1	416		-16.3[g]
	This work					0.19	-0.16	0.03	0.4	0.1	-1.7	1	0.09	-15.7
	Ref 8					NR	NR	NR	NR	NR	NR			-12.5
	Ref 9					0.00	-0.31	0.01	-0.3	0.1	-1.6	-24	0.09	-14.4
	Ref 12					0.34	-0.12	0.08	-0.7	0.4	-1.7	-12	0.10	-16.2
Benzene[k] $T = -135°$	Exptl	$P_{2_12_12_1}$	4	7.6	222	7.39	9.42	6.81	90.0	90.0	90.0	475		-11.3[l] (-9.7 to -11.7)[m,n,o]
	This work					-0.11	0.01	-0.05				-4	0.11	-9.5
	Ref 8					0.05	-0.06	-0.04				-3	0.10	NR
	Ref 9					-0.23	0.15	-0.04				-21	0.17	-11.4
	Ref 71					0.08[p]	-0.10[p]	-0.01[p]				-1	0.12	-11.7
Anthracene[q] $T = -178°$	Exptl	$P_{2_1/a}$	2	4.4	221	8.44	6.00	11.12	90.0	125.6	90.0	458		-22.6[m] (-24.5[n])
	This work					0.18	-0.11	0.10		0.0		4	0.12	-19.4
	Ref 8a					0.10	-0.10	0.05		NR			0.10	-23.0
	Ref 9					-0.11	0.07	-0.40		-1.2		-11	0.16	-24.0
	Ref 72					-0.05[p]	-0.04[p]	-0.08[p]		-0.1[p]		-8	0.08	-23.0
Pyrazine[r]	Exptl	P_{mnn}	2	8.3	232	9.32	3.82	5.91	90.0	90.0	90.0	210		NR
	This work					0.62	-0.35	-0.14				-12	0.28	-9.9
	Ref 9 (set I)[s]					-0.70	-0.19	0.57				-8	0.32	-13.6
	Ref 9 (set II)[s]					0.34	0.22	-0.60				-3	0.28	-11.8
2,2'-Bipyridine[t]	Exptl	$P_{2_1/c}$	2	23.0	221	5.66	6.24	13.46	90.0	118.0	90.0	420		NR
	This work					-0.36	0.17	-0.04		-1.2		-13	0.16	-16.5
α-Phenazine[u] $T = -190°$	Exptl	P_{2_1a}	2	11.4	132	12.97	4.98	7.06	90.0	109.0	90.0	432		NR
	This work					0.47	-0.22	0.14		0.5		-2	0.16	-20.1
Thianthrene[v]	Exptl	$P_{2_1/a}$	4	12.0	121	14.48	6.15	11.93	90.0	109.0	90.0	1000		-13.7
	This work					-0.37	-0.20	-0.05		0.0		-63	0.16	

TABLE VII: Results for Carboxylic Acids

Acid[a]	Author	Space group	Discrepancy index R, %	No. of molecules per unit cell	Cell index	a, Å; Δa, Å	b, Å; Δb, Å	c, Å; Δc, Å	α, deg; Δα, deg	β, deg; Δβ, deg	γ, deg; Δγ, deg	V, Å³; ΔV, Å³	σ[b], Å	Binding energy U exptl or calcd, kcal/mol	r(H...O17) exptl[c], Å; Δr(H...O17) calcd, Å
Formic[d] T = −50°	Exptl	P_{na}	9.0	4	132	10.23	3.64	5.34	90.0	90.0	90.0	199		−14.4[e]	1.59
	This work					0.63	−0.17	−0.20				−5	0.25	−13.4	0.08
Acetic[f] T = −190°	Exptl	P_{n4_21}	5.3	4	132	13.21	3.92	5.77	90.0	90.0	90.0	299		−9.96[g]	1.66
	This work					0.18	0.01	−0.07				1	0.18	−14.3	0.02
Butyric[h] T = −43°	Exptl	$C_{2/m}$	15.9	4	221	8.01	6.82	10.14	90.0	111.4	90.0	516		NR	1.62
	This work					−0.03	0.08	−0.12		0.0		3	0.07	−15.4	0.00
Oxalic[i]	Exptl	P_{cab}	14.5	4	222	6.55	7.85	6.09	90.0	90.0	90.0	312		−23.5[j]	1.80
	This work					−0.24	−0.79	0.82				−4	0.67	−25.9	−0.12
Succinic[k]	Exptl	$P_{2_1/a}$	12.4	2	222	5.13	8.88	7.62	90.0	133.6	90.0	251		−28.1[l]	1.66
	This work					−0.18	−0.16	0.0		1.1		−17	0.12	−28.9	0.02
Suberic[m]	Exptl	$P_{2_1/c}$	10.0	2	221	8.98	5.06	10.12	90.0	97.8	90.0	456		−34.2[l]	1.67
	This work					−0.04	0.07	0.23		1.5		12	0.12	−32.2	0.05
Sebacic[n]	Exptl	$P_{2_1/c}$	15.0	2	121	15.04	5.00	10.07	90.0	133.2	90.0	551		−38.4[l]	1.65
	This work					0.05	−0.01	0.24		1.8		−11	0.13	−33.7	0.04

[a] The structures reported were determined at or near room temperature, except for those where a temperature is given. [b] σ is defined in eq 10; the Δ's are defined in footnote d of Table VI. [c] The values of $r_{H...O17}^{exptl}$ are those obtained with the geometry for the hydrogens used here, when the experimental values for the heavy-atom geometry and the experimental lattice constants are used. $\Delta r_{H...O17}^{calcd}$ is the difference $r_{H...O17}^{exptl} - r_{H...O17}^{calcd}$, with the calculated value being obtained after energy minimization. [d] Reference 83. [e] Reference 84. [f] Reference 79. [g] Reference 80. [h] Reference 86. [i] Reference 87. [j] Reference 89. [k] Reference 90. [l] Reference 93. [m] Reference 96. [n] Reference 97.

TABLE VIII: Results for Amides and Amine

Molecule[a]	Author	Space group	Discrepancy index R, %	No. of molecules per unit cell	Cell index	a, Å; Δa, Å	b, Å; Δb, Å	c, Å; Δc, Å	α, deg; Δα, deg	β, deg; Δβ, deg	γ, deg; Δγ, deg	V, Å³; ΔV, Å³	σ[b], Å	Binding energy U exptl or calcd, kcal/mol	r(H...O17) exptl[c], Å; Δr(H...O17) calcd, Å
Formamide[d] T = −50°	Exptl	$P_{2_1/n}$	19.0	4	322	3.69	9.18	6.87	90.0	98.0	90.0	231		−17.0[e]	1.90; 1.95
	This work					−0.10	0.16	−0.18		−2.3		−8	0.13	−11.3	0.02; −0.03
N-methyl-acetamide[f] T = −35°	Exptl	P_{nma}	13.4	4	222	9.61	6.52	7.24	90.0	90.0	90.0	454		−11.2[g]	1.83
	This work					0.24	−0.11	−0.01				2	0.15	−11.3	0.09
Oxamide[h]	Exptl	$P\bar{1}$	18.0	2	222	7.25	5.19	5.66	83.7	114.1	115.1	175		−27.1[i]	2.04; 1.95
	This work					0.20	−0.08	−0.01	−1.4	−0.2	6.0	−8	0.09	−19.5	−0.07; 0.00
Succinamide[j]	Exptl	$C_{2/c}$	8.9	4	222	6.93	7.99	9.88	90.0	102.5	90.0	534		NR	1.94
	This work					−0.15	0.05	0.06		0.3		−14	0.09	−23.1	0.00
Adipamide[k]	Exptl	$P_{2_1/c}$	15.0	2	221	6.89	5.15	10.67	90.0	111.0	90.0	353		−27.0	1.96; 2.07
	This work					−0.03	−0.07	0.09		−0.3		−3	0.05	NR	−0.01; −0.07
Suberamide[l]	Exptl	$C_{2/c}$	12.0	4	121	14.44	5.13	14.17	90.0	117.5	90.0	932		NR	1.98; 2.02
	This work					−0.06	−0.06	−0.07		−0.2		−17	0.05	−29.4	−0.03; −0.06
Methylamine[m] T = −150°	Exptl	P_{cab}	13.1	8	221	5.75	6.18	13.61	90.0	90.0	90.0	484		NR	2.19
	This work					0.09	−0.13	0.04				−2	0.09	−6.3	0.05

[a] The structures reported were determined at or near room temperature, except for those where a temperature is given. [b] σ is defined in eq 10; the Δ's are defined in footnote d of Table VI. [c] The values of $r_{H...O17}^{exptl}$ are those obtained with the geometry for the hydrogens used here, when the experimental values for the heavy-atom geometry and the experimental lattice constants are used. Only two representative values are listed for this distance even though the molecule may have up to six hydrogen bonds. $\Delta r_{H...O17}^{calcd}$ is defined as in footnote c of Table VII. [d] Reference 104. [e] Calculated here from data of ref 105. [f] Reference 106. [g] Reference 107. [h] Reference 102. [i] Reference 103. [j] Reference 101. [k] Reference 100. [l] Reference 99. [m] Reference 98.
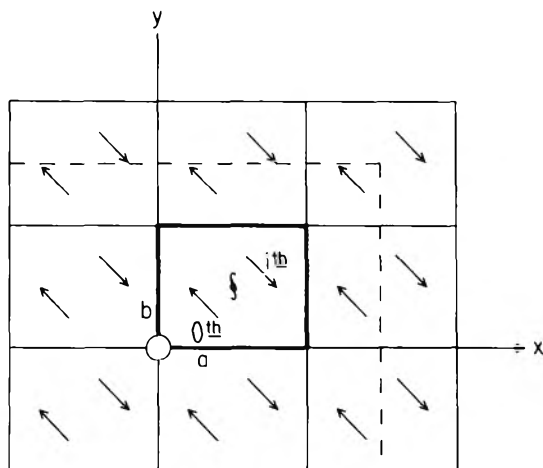
Figure 4. A two-dimensional schematic representation of the unit cell (containing the 0th molecule) with one additional unit cell generated in each direction. The symmetrically balanced interactions are illustrated; *i.e.*, the molecules outside of the dashed lines are *not* included in the calculations of the interactions with the 0th molecule.

lational and rotational operators are defined uniquely by the crystal symmetry, and are not allowed to change as the lattice constants are varied during energy minimization. Only those lattice constants which are themselves independent[55] are taken as the independent variables which are altered during energy minimization. For each change in the independent variables during energy minimization, the geometry and conformation of the molecules and the *relative* positions of the molecules in the (altered) unit cell (*i.e.*, the translational and rotational operators) are kept constant, but the actual distances between their centers of mass vary.

The crystal (*i.e.*, binding) energy is calculated as indicated at the beginning of section IIB. During the minimization of this crystal energy, the space group remains invariant while the size and shape of the unit cell are changed to obtain a minimum in the crystal lattice energy. The number of unit cells taken along any axis was such that the distance from the 0th molecule to the edge of the microcrystal was generally greater than 10 Å in both directions[37] *along each axis.* This size microcrystal is large enough to incorporate the compressive effect of the crystal[33] and also to yield ~90% or greater of the lattice binding energy.[56] Since the 0th molecule is generally not found crystallographically to be at the center of the unit cell (see Figure 4), it is not surrounded by symmetrically arranged molecules in the microcrystal when an integral number of unit cells is generated. Such asymmetry (*i.e.*, edge effects) will lead to errors in the lattice binding energy because of unbalanced interactions. Thus, some of the molecules in the generated cells are eliminated by symmetry conditions in the computation of the energy. As illustrated in the two-dimensional schematic representation of Figure 4, those molecules outside of the dashed line (in practice this is carried out in three dimensions, using the translational operators) must be eliminated in order to obtain an arrangement of molecules around the 0th molecule, which is symmetric in the translational operators. Hence, in all the crystals considered here, the 0th molecule was always surrounded by an arrangement of other molecules such that the forces operating on the 0th molecule are balanced in all directions in the crystal.

B. Computation of Repulsive Parameters. The crystal energy was minimized with respect to a, b, c, α, β, and γ for

various values of A^{kl} of eq 2 and $A'_{H\cdots X}$ of eq 8, with all other parameters of the potential function computed first, as described in section IIB. The optimal set of values of A^{kl} and $A'_{H\cdots X}$ was then obtained as the one which gave the minimum value of the root-mean-square deviation σ, defined as

$$\sigma = \left[(1/N) \sum_{i=1}^{N} (l_i^{\text{calcd}} - l_i^{\text{obsd}})^2 \right]^{1/2} \quad (10)$$

where $l = a, b, c, \alpha, \beta, \gamma$, or any subset of these being varied, and N is the total number of such quantities for a given crystal. The deviations of the lattice axes are in ångström units, while those of the angles are in radians. Thus, two separate, but nested, minimizations were carried out: (a) for each set of energy coefficients, the crystal lattice energy was minimized (through at least one cycle of the minimizer) with respect to the lattice constants (only those that are independent were varied), *viz.*

$$\frac{\partial U_{\text{Tot}}}{\partial a} = \frac{\partial U_{\text{Tot}}}{\partial b} = \ldots \frac{\partial U_{\text{Tot}}}{\partial \gamma} = 0 \quad (11)$$

A root-mean-square deviation, σ, was then calculated for the cell lattice of minimum energy. (b) The deviation, σ, was then minimized with respect to the repulsive coefficients,[57] A^{kk} or $A'_{H\cdots X}$, *viz.*

$$\frac{\partial}{\partial A^{kk}} \{[a^{\text{obsd}} - a^{\text{calcd}}]^2 + \ldots + [\gamma^{\text{obsd}} - \gamma^{\text{calcd}}]^2\} = 0 \quad (12)$$

This procedure was carried out for each separate crystal for the particular set of A^{kk}'s being determined from that crystal, and the final set of coefficients represents an average over a selected set of crystals,[25] and tested on other crystals (see section IIA).

The minimization procedure was the same as that used previously.[11b,58] The number of independent variables (lattice constants) in the energy minimization cycle depends on the symmetry of the particular crystal, which is always maintained (as described in section IIIA). Further, care was taken to assure that the number of different A^{kk} (and $A'_{H\cdots X}$) coefficients to be varied in the σ minimization cycle did not exceed the number of independent data (lattice constants).

As a check on the minimization procedure, we have examined the variation of the crystal lattice energy with lattice constants (for the optimized set of repulsive parameters) around the position of the computed energy minimum. In every case examined in detail (*viz.*, hexane, benzene, anthracene, and adipamide), the attainment of the minimum was verified by the fact that the magnitude of the first derivative of the energy with respect to each variable was nearly zero (*i.e.*, ~0.001 kcal/Å).

After the optimum repulsive parameters were determined from the selected set of crystals and tested by energy minimization on the second group of crystals, the values of σ were within the experimental errors in the data and procedure associated with each crystal. The final sets of nonbonded and hydrogen-bond parameters are given in Tables IV and V, respectively. The nonbonded parameters are compared with earlier ones[59] in the Table IV. It must be emphasized that the parameters in Tables IV and V have no meaning by themselves; they must be combined with the electrostatic potentials used here, to give the *total* empirical potential.

It should be pointed out here that the crystal binding energy is not an input parameter in this method, but rather is a computed result of the energy minimization. Thus, one test of the success of this approach is to compare the agreement between the calculated binding energies and observed values of the sublimation energy. Similarly, comparison of interatomic force constants computed from our total potential function with those computed from spectra provides an additional test of the validity of the potential energy functions and coefficients. In the procedure adopted here, all types of hydrogens have the same C^{kk} coefficient, while the A^{kk} coefficients are allowed to vary for different types of hydrogen atoms. The implication of this is that the polarizability of all types of hydrogen atoms is the same, and that no change in polarizability occurs when the hydrogen is attached to polar or nonpolar heavy atoms. Although it is realized that this approximation is not rigorously valid, the polarizability data for all these types of atoms are not available. Therefore, we have had to resort to variations in partial charge and in repulsive coefficients to represent the different types of atoms. In future work, it may become possible to distinguish among the C^{kk}'s for different types of hydrogen atoms.

The separation of the heavy atoms (C, O, N, and S) into different types is consistent with the differences in their polarizabilities (e.g., the polarizabilities of carbonyl and hydroxyl oxygens differ).

The number of unit cells used in the *initial* computations to obtain the optimum set of repulsive parameters was smaller (i.e., such that the distances from the 0th molecule were at least ~ 7 Å or greater) than that used in the *final* computations of lattice constants, binding energies, and force constants for *all* of the crystals (cutoff distance > 10 Å).[37,56] Thus, the possibility exists that some of the compressive effect might be absent from the computed repulsive parameters, and manifest itself as a smaller volume per unit cell than that observed in each individual crystal. However, no trends toward negative errors in the computed volumes are detected (see section IV); therefore, the *initial* use of a limited crystal size (to conserve computer time) does not appear to have introduced any detectable errors in the computed repulsive parameters.

As a check on the sensitivity of the A^{kk} coefficients to variation in the lattice constants, we have examined the range over which the individual coefficients could be altered without producing a value of σ for the energy-minimized cell of more than $\sim 20\%$ (i.e., with no value of Δa, Δb, etc., greater than $\sim 10\%$). The results of this test will be presented in section IVC (Figure 6) for pyrazine. However, it must be realized that, even though a specific A^{kk} may be insensitive to changes in the lattice constant of a particular crystal, it may be very sensitive to such changes in another crystal. For example, for formamide, no significant change is detected in the lattice constants of the energy-minimized cell for a variation of $\langle r_g^{N13\cdots N13} \rangle$ over a range of about 3.9–4.3 Å but, for oxamide, this range is reduced to 3.98–4.02 Å (with all other parameters of the potential function held constant). Obviously, those crystals in which a given contact distance is very short will have the most influence on the repulsive coefficient for that particular pairwise interaction (see point e in section IIE). While some crystals are more important than others in their influence on a particular repulsive coefficient, the final values of all the A^{kk} coefficients are determined by *all* of the crystals used to obtain these coefficients.

IV. Results

A. Aliphatic Hydrocarbons. The CNDO/2 (ON)[14] partial charges of the atoms of the molecules pentane,[60] hexane,[61] and octane[62] are shown in Figure 1. The crystal structure of pentane[60] was used to obtain *initial* repulsive coefficients for the $C_6\cdots C_6$ and $H_1\cdots H_1$ nonbonded interactions, even though it is recognized that these experimental data (available at only one temperature) are not of highest precision. The cross terms (here, $C_6\cdots H_1$) are computed by the procedure described in section IIB3. Starting from the A^{kk} coefficients of Ooi, *et al.*,[59] and the C^{kk} coefficients given in Table IV, the A^{kk} coefficients were varied until a best fit (i.e., lowest value of σ) of the experimental lattice constants (i.e., a, b, and c) of pentane was obtained. [It should be noted that the parameters of Ooi, *et al.*,[59] result in an energy-minimized cell (citing data not reported here) whose cell dimensions are $\sim 20\%$ smaller than the observed ones]. Since the crystal lattice requires three variables for its description (viz., $a \neq b \neq c$, with $\alpha = \beta = \gamma = 90°$), the two unknowns $A^{C_6\cdots C_6}$ and $A^{H_1\cdots H_1}$ were computed. A slight refinement in the A^{kk} coefficients was made by using hexane[61] and then recycling through pentane again to get a best fit of both crystals. Two different sets of $A^{C_6\cdots C_6}$ and $A^{H_1\cdots H_1}$ coefficients were found which fit the lattice constants of pentane and hexane equally well. However, when other crystals (viz., acetic acid, N-methylacetamide, and adipamide) were examined, one of these sets of $A^{C_6\cdots C_6}$ and $A^{H_1\cdots H_1}$ coefficients gave considerably better fits (when used in combination with the coefficients for other types of atoms) than the other, thereby enabling a unique choice to be made; it is this set which is given in Table IV.

The methyl end groups of pentane and hexane were initially positioned so that the dihedral angles $\chi_1 = \chi_2 = 60°$ (i.e., the staggered conformation; see Figure 1A and 1B for definitions of χ_1 and χ_2). In order to test whether these are the optimum positions for the methyl hydrogens, the two methyl end groups were rotated about their respective C–C bonds. The lattice parameters and heavy-atom coordinates were fixed at the experimentally observed values, and the crystal energy was calculated at 30° intervals in χ_1 and χ_2 (using the optimized parameters given in Table IV). It was found that the conformation of pentane which yielded the lowest crystal energy was indeed that with staggered methyl groups (i.e., with $\chi_1 = \chi_2 = 60°$), as shown in the χ_1–χ_2 energy contour diagram of Figure 5. These methyl groups appear to be sufficiently tightly packed in the crystal so that rotation would require a cooperative motion of methyl groups on different molecules. Because of *intermolecular* interactions (i.e., even without including an intrinsic torsional contribution for the –CH_2–CH_3 rotation), the barrier to rotation of the methyl groups is seen in Figure 5 to be slightly greater than 2.0 kcal/mol. This result is in agreement with general trends which indicate that the barrier to rotation in the solid phase is generally nearly twice that found in the gas phase[63] (since the generally accepted torsional barrier for a methyl group in the gas phase is ~ 3.0 kcal/mol,[64] that in the solid phase would be expected to be 3.0 + 2.0 or 5.0 kcal/mol). The oscillatory motions of the methyl groups are coupled with one another, as can be seen by the asymmetry of the elongated loop in the central low-energy region in Figure 5; however, the coupling of the motions is not strong and may be overcome by thermal vibrations at room temperature.

The parameters determined from pentane and hexane (and subsequently refined further using other molecules as
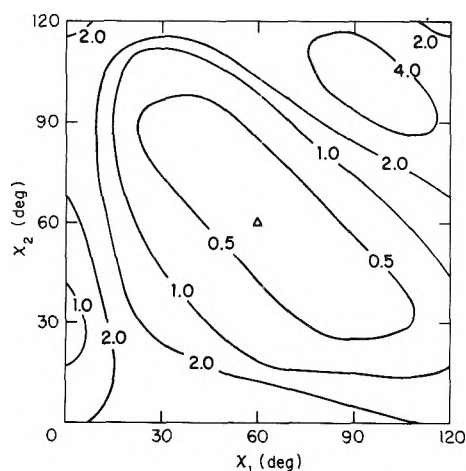
Figure 5. Energy contour diagram for the molecule pentane, in the crystal. The binding energy was computed as a function of χ_1 and χ_2, using the experimental heavy-atom X-ray structure and lattice parameters. The energy (expressed in kcal/mol) was normalized to zero at the minimum (i.e., $\chi_1 = \chi_2 = 60°$), indicated by the open triangle.

Figure 6. Dependence of lattice deviation on $\langle r_g^{N_{14}\cdots N_{14}} \rangle$ in the crystal of pyrazine. Δa, Δb, and Δc are the deviations of the lattice parameters of the energy-minimized cell from the experimental lattice parameters. U_{Tot} is the minimized crystal lattice energy for the potentials of Table IV, except $A^{N_{14}\cdots N_{14}}$ which changes for each value of $\langle r_g^{N_{14}\cdots N_{14}} \rangle$.
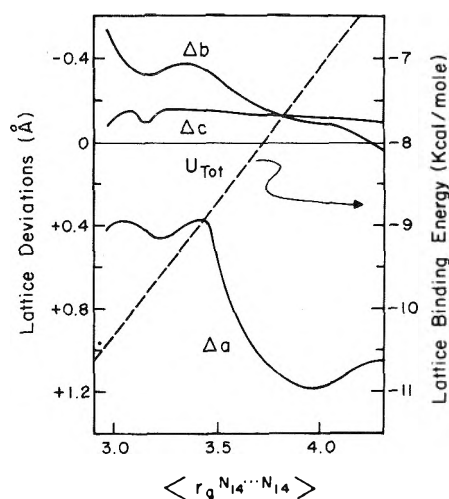
indicated above), and recorded in Table IV, were then applied to octane.[62] Before minimizing the energy of the octane crystal, the rotational minima of the methyl groups were found, as described above for pentane. The intermolecular barriers to rotation of the methyl groups in both hexane and octane were only slightly less (viz., ~1.5 kcal/mol) than that found for pentane, and the minima were again found to be at $\chi_1 = \chi_2 = 60°$ in both molecules.

The results of these computations, and a comparison of our lattice fits with those of other authors are shown in Table VI. It would appear that the potentials used by other authors, which have a larger number of adjustable parameters (i.e., most other workers used a two-parameter repulsive potential of an exponential form for each pairwise interaction, compared to the single coefficient of the $1/r_{ij}^{12}$ term used here), yield fits to the lattice parameters of the normal hydrocarbon crystals which are equivalent to those obtained here. Our lattice binding energies for hydrocarbons agree to within ~10% of the experimental sublimation energies [without correction for temperature (i.e., heat capacity), nor rotational isomerization].

Another way to compare the computed and experimental lattice parameters is in terms of the volume of the unit cell. From Table VI, it can be seen that the volumes have an error of 1–4%, which is about the magnitude of the error in the crystallographic parameters (i.e. the atomic coordinates are much less precise than the lattice constants).

B. Aromatic Hydrocarbons. The molecules benzene[65–69] and anthracene[70] were used to obtain parameters for aromatic $C_8\cdots C_8$ and $H_3\cdots H_3$ interactions. The low-temperature structures (viz., those at −135° for benzene[65] and at −178° for anthracene[70]) were selected for this purpose in order to minimize the effects of thermal motions. There are no bonds about which rotation takes place in these molecules. The CNDO/2 (ON) partial charges are given in Figure 1D and 1E, and the repulsive coefficients (obtained by minimizing the deviations between the computed and experimental lattice parameters, as described previously) are given in Table IV.

The results of the energy minimization are shown in Table VI together with the results of other workers. As was found for the aliphatic hydrocarbons, the fits to the lattice parameters are very good, having deviations of ~2% of the

lattice constant. The binding energies are slightly smaller than the experimental sublimation energies for the crystal temperatures used, and this may be a result of using aliphatic polarizabilities to calculate the C^{kk} coefficients. We have investigated the use of aromatic carbon atom polarizabilities, and (upon minimization) found much larger binding energies (viz., approximately twice the value reported here) and considerably poorer fits to the lattice constants (viz., ~10% in σ). The aliphatic C^{kk} coefficients, used here for aromatic carbon and hydrogen (370.5 and 45.5, respectively), may be compared to those obtained by Williams[8] (437 to 602, and 36 to 71), Kitajgorodskij[7] (358 and 57), Mason[20] (522 and 68), and Ferro and Hermans[9] (600 and 23). Williams[8] shifted the center of repulsion and attraction for a bonded hydrogen atom (in aromatic hydrocarbons) 0.07 Å into the C–H bond (by taking a C–H bond length of 1.097 − 0.07 = 1.027 Å) in order to obtain a good fit to the lattice parameters. Similarly, Mason[20] introduced a shift of 0.3 Å into the C–H bond. We have not adopted this procedure since we wish to obtain atom-centered potentials. Other theoretical results for benzene[71] and anthracene[72] are also compared in Table VI.

C. Heterocyclic Compounds. The molecules pyrazine,[73] bipyridine,[74] and thianthrene[75] were used to obtain parameters for ring nitrogens and ring sulfur atoms. These parameters were then tested on α-phenazine.[76]

The molecule pyrazine [see Figure 1F for structure and CNDO/2 (ON) partial charges] has two ring nitrogen atoms. The parameters for carbon and hydrogen were fixed at the values found for benzene and anthracene (see Table IV), and the repulsive coefficient of only the nitrogens (i.e., $A^{N_{14}\cdots N_{14}}$) was allowed to vary to obtain the best fit of the lattice. The fit to the lattice constants (shown in Table VI, using parameters of Table IV) is not very satisfactory.

In order to see why a better fit is not obtained, we investigated the dependence of the deviations in the lattice constants on the parameter $\langle r_g^{N_{14}\cdots N_{14}} \rangle$, which is directly related to the coefficient $A^{N_{14}\cdots N_{14}}$. For each value of $\langle r_g^{N_{14}\cdots N_{14}} \rangle$ (and the corresponding cross terms), the binding energy was minimized with respect to the lattice constants (without, of course, carrying out the second minimization of eq 12). The results are shown in Figure 6 (the value of

$\langle r_g^{N_{14}\cdots N_{14}}\rangle$ which minimizes σ being ~3.45 Å). It is immediately apparent that the lattice constant a is most sensitive to the value of $\langle r_g^{N_{14}\cdots N_{14}}\rangle$. At values of $\langle r_g^{N_{14}\cdots N_{14}}\rangle$ greater than ~3.45 Å, the value of a deviates much faster than does that of b, whereas c is relatively insensitive to the $N_{14}\cdots N_{14}$ repulsive coefficient. The shortest contact distances in this crystal are $N_{14}\cdots H_3$ (2.60 Å) and $H_3\cdots H_3$ (also 2.60 Å), whereas the shortest $N_{14}\cdots N_{14}$ distance is much larger (3.80 Å). In fact, the $N_{14}\cdots H_3$ distance is considerably less than the sum of the van der Waals radii (2.75 Å) for these atoms, as calculated with parameters of Bondi,[77] and it is this short $N_{14}\cdots H_3$ contact distance which strongly influences the $N_{14}\cdots N_{14}$ repulsive coefficient at values of $\langle r_g^{N_{14}\cdots N_{14}}\rangle$ larger than 3.5 Å. Conceivably, this short $N_{14}\cdots H_3$ contact distance may result from a possible C–H···N hydrogen bond. The poor fit to the lattice constants, at values of $\langle r_g^{N_{14}\cdots N_{14}}\rangle$ less than 3.5 Å, is apparently due to the shrinkage in the interplanar distance along the b axis, and arises from the use of $C_8\cdots C_8$ and $H_3\cdots H_3$ repulsive coefficients which were determined from low-temperature X-ray data for benzene and anthracene. The interplanar stacking distance in these latter crystals was ~3.6 Å which is considerably smaller than the interplanar distance of ~3.8 Å found in pyrazine. Thus, when the b axis of pyrazine contracts, the a axis is forced to expand (because the attractive forces are weaker along the a axis then along the b axis). At larger values of $\langle r_g^{N_{14}\cdots N_{14}}\rangle$, the deviation in b from the observed experimental value approaches zero, but, since only the value of $\langle r_g^{N_{14}\cdots N_{14}}\rangle$ is allowed to increase, the packing arrangement is not correctly reproduced, and the result is that shown in Figure 6.

The $A^{N_{14}\cdots N_{14}}$ coefficient, reported in Table IV, was obtained by further refinement using bipyridine, and finally tested on α-phenazine. It is interesting that the cell volumes of pyrazine, bipyridine, and α-phenazine are not seriously in error, even though the individual lattice constants show somewhat large deviations from the experimental values. This must indicate that the relative effective volumes of the potentials (the effective volume that an atom sweeps out being directly related to the repulsive parameters) are reasonable. Our results on pyrazine (in which no effect of the lone-pair electrons was included) are as good as those of Ferro and Hermans[9] (see Table VI) who positioned their potentials so that they included the effect of the lone-pair electrons (parameter set II of ref 9); thus we do not feel that this modification is necessary.

Thianthrene has sulfur atoms in a condensed ring system and, similarly to pyrazine, the repulsive coefficient of only $S_{20}\cdots S_{20}$ and the related cross terms were allowed to vary to achieve a best fit of the lattice constants. The carbon and hydrogen parameters were those determined earlier for benzene and anthracene. The lattice fit is reasonable (i.e., ~3% in lattice deviations), although the higher temperature (25°) at which the thianthrene data were taken, compared to the low-temperature data of benzene and anthracene, manifests itself as a 6% shrinkage in the lattice volume of the energy-minimized crystal. Again, no attempt was made to account for lone-pair effects.

In general, the results for the aliphatic and aromatic hydrocarbons, and for the heterocyclic compounds, are satisfactory. In most cases, the lattice constants which were varied were sensitive to the variation in the parameters of the potential function, and the fits to the lattice constants, which reflect this sensitivity, were as good as those obtained by other authors (see Table VI).
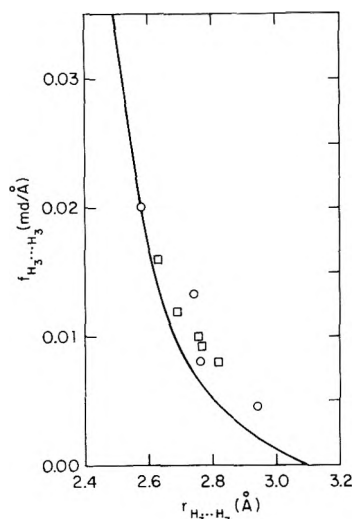
Figure 7. Dependence of force constant, $f_{H_3\cdots H_3}$, on distance, $r_{H_3\cdots H_3}$. The solid line was obtained from the second derivative of the Lennard-Jones 6–12 $H_3\cdots H_3$ potential with respect to $r_{H_3\cdots H_3}$. The squares were obtained from experimental data[53,54] on benzene and naphthalene, and the circles from experimental data on polyethylene.[78]
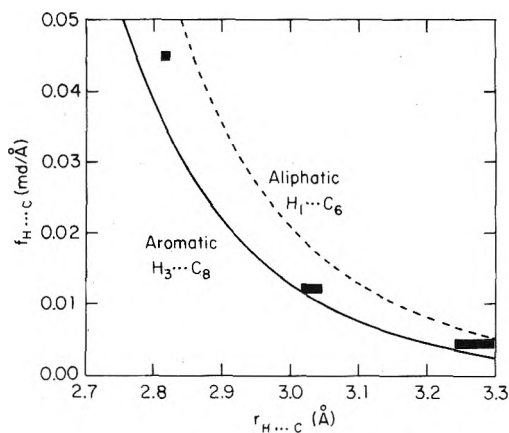
Figure 8. Dependence of force constant, $f_{H\cdots C}$, on distance, $r_{H\cdots C}$. The solid and dashed lines were obtained from the Lennard-Jones 6–12 potentials for aromatic $H_3\cdots C_8$ and aliphatic $H_1\cdots C_6$ interactions, respectively. The solid rectangles are experimental data[53,54] for benzene and naphthalene, and should be comparable to our data for $H_3\cdots C_8$ interactions.

D. Force Constants for Carbon and Hydrogen Interactions. A further check of the potentials obtained above may be made by examining the corresponding force constants for the interaction of each pair of atoms at the intermolecular contact distances observed in the crystal, and comparing these to results found by fitting spectral frequencies of crystal vibrations. Harada and Shimanouchi[53,54] studied the far-infrared spectra of benzene and naphthalene crystals. The important intermolecular interactions were considered to be those between hydrogen atoms of different molecules, as well as carbon–hydrogen interactions of different molecules. They assumed an exponential form for the repulsive interaction potentials (with no attractive terms), and varied the coefficients of the repulsive term to obtain values of the nonbonded force constants, which best reproduced their experimental intermolecular lattice frequencies. Some representative values of their force constants, as well as those found for polyethylene,[78] obtained using a similar technique, are shown in Figures 7 and 8 for
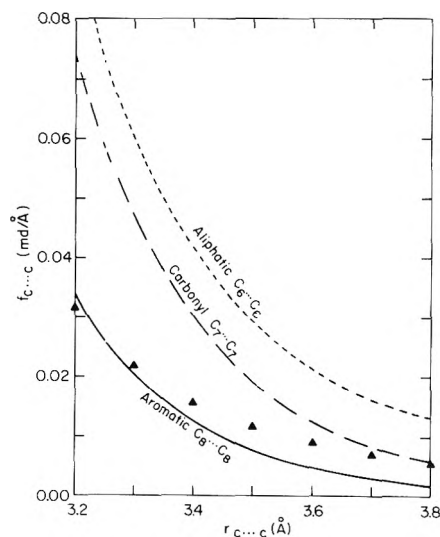
Figure 9. Dependence of force constant $f_{C\cdots C}$ on distance, $r_{C\cdots C}$. The curves were obtained from the derivatives of the Lennard-Jones 6–12 potentials for aromatic $C_8\cdots C_8$ (solid line), carbonyl $C_7\cdots C_7$ (long-dashed line), and aliphatic $C_6\cdots C_6$ (short-dashed line) interactions, respectively. The solid triangles are values for both the Thomas-Fermi-Dirac and Hartree-Fock force constant data,[51,52] which are nearly identical with each other for C$\cdots$C interactions.

$H_3\cdots H_3$ and $H_3\cdots C_8$ types of interactions, respectively. The agreement with the force constants (obtained here from the second derivative with respect to distance of the 6–12 non-bonded potential for $H_3\cdots H_3$ interactions) is very good (see Figure 7). The $H_3\cdots C_8$ force constants of Harada and Shimanouchi[53,54] lie between (and are in good agreement with) the curves (Figure 8) which we obtained for the aromatic and aliphatic force constants. Since no $C_8\cdots C_8$ interaction force constants were obtained from the study of the crystal vibrations,[53,54] no comparison can be made for these quantities. Instead, we show in Figure 9 the repulsive force constants of Bonham, et al.,[51,52] which were obtained by fitting Hartree-Fock (HF) and Thomas-Fermi-Dirac (TFD) repulsive potentials with analytical functions and calculating the force constant curves from these functions. The HF and TFD results (for neutral atoms) compare quite favorably with our results for aromatic $C_8\cdots C_8$ interactions over the range (3.2–3.6 Å) of interactions which can be considered to apply to our parameters (i.e., only over the range of close contact distances found in the molecular crystals studied here). In particular, the repulsive potential energy at interatomic contact distances shorter than the intermolecular contact distances in the crystals studied here would not be expected to be well represented by the r^{-12} term used here. This point will be discussed in a future paper.[29]

E. Carboxylic Acids. The CNDO/2 (ON) partial charges and structures of the acids considered in this section are shown in Figure 2. The acidic unit (i.e., –COOH) is treated as four different atoms, the carbonyl oxygen (O_{17}), the hydroxyl oxygen (O_{18}), the carbonyl carbon (C_7), and the acidic hydrogen (H_4). The repulsive coefficients A^{kk} for each of these four atoms were derived using crystal data from both acetic[79] and succinic[80] acids. The coefficients of the potentials for the methyl and methylene groups (i.e., those involving C_6 and H_1) were fixed at one of the two sets of values (see below) found from the aliphatic crystals, and the general hydrogen-bond potential ($H_4\cdots O_{17}$) was initially taken as that found by McGuire, et al.[14c] The H_4 atom was held fixed cis to the carbonyl oxygen throughout the
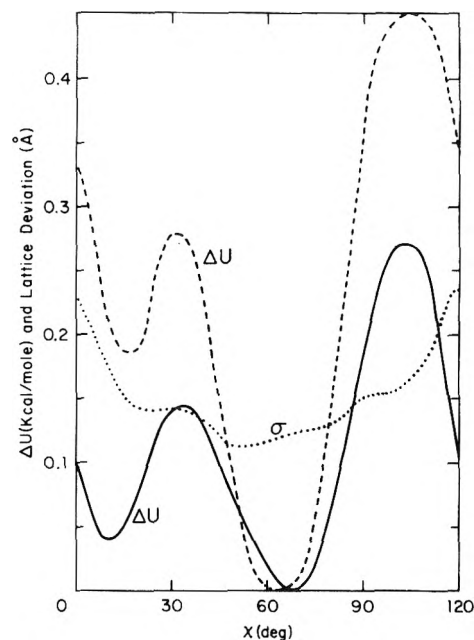
Figure 10. Dependence of crystal binding energy and deviation, σ (i.e., the square root of the sum of the squares of the deviations), of the lattice constants on dihedral angle for rotation of the methyl group of acetic acid. The solid curve is the binding energy (normalized to zero at the lowest energy value) after one cycle of energy minimization (with respect to the lattice constants) for each $10°$ rotational position of the methyl group, and for a 111 cell index. The dashed curve was obtained by computing the binding energy as a function of methyl rotation (without minimization), with the molecular structure and lattice constants fixed at their experimental values, and for a 111 cell index (also normalized to zero at the lowest energy value). The dotted curve is the deviation, σ, of the lattice constants, *a*, *b*, and *c*.

calculations, and was chosen *initially* to have the same value of $A^{H_4\cdots H_4}$ as had been found for $H_3\cdots H_3$ interactions. After refinement of the parameters, rotation of this hydrogen atom led to no improvement in either the binding energy or the lattice fit. The initial estimates of A^{kk} for the O$\cdots$O nonbonded interactions were taken from Ooi, et al.,[59] and the repulsive term was increased by $\sim20\%$ to compensate for the cell contraction observed with the parameters of Ooi, et al.[59] The initial values of A^{kk} for the $C_7\cdots C_7$ interactions were taken to be those obtained for C_8 type atoms from the aromatic crystals. The value of A^{kk} for $C_7\cdots C_7$ was varied around the starting value only after the parameters for O_{17} and O_{18} were optimized using both acetic and succinic acid crystals, and subsequently fixed at the starting value because no close (sensitive) contacts of the $C_7\cdots C_7$ type (or those derived from cross terms) occur in these crystals (i.e., the crystal packing patterns of the molecules of carboxylic acids are relatively insensitive to the C_7 parameter). However, there is a close $C_7\cdots C_7$ contact in oxamide, formamide, and succinamide, and these amides (in particular oxamide) served to determine the A^{kk} coefficient for C_7 (see section IVF1). The A^{kk} parameter for $H_4\cdots H_4$ interactions was also found to remain near that for $H_3\cdots H_3$, and was adjusted after the parameters for the oxygens had been determined in the calculations.

The two acids, acetic and succinic, were chosen to determine the parameters for the atoms of the acid group because they have different hydrogen-bonding arrangements in their crystal lattices. Acetic acid has a linear hydrogen-bond network with a single O–H$\cdots$O hydrogen bond to each of two molecules. On the other hand, succinic acid forms a

cyclic hydrogen-bond complex at each end of the monomer. The atomic framework of the succinic acid molecule is nearly planar, and the axis from the first carboxyl carbon to the second one on the other end of the molecule lies roughly in the direction of the c axis. We expect the general hydrogen bond term to dominate the crystal packing along this direction. However, the two perpendicular axes should be sensitive to changes in the A^{kk} coefficients. This expectation is borne out by the sensitivity of the a and b lattice constants of succinic acid to changes in the A^{kk} coefficients for the O_{17} and O_{18} atoms [because of close $H_1 \cdots O_{17}$ contacts (2.6 Å), $H_1 \cdots O_{18}$ contacts (2.7 Å), and $H_1 \cdots H_4$ contacts (2.75 Å)].

As indicated in section IVA, two sets of values of $A^{C_6 \cdots C_6}$ and $A^{H_1 \cdots H_1}$ were obtained from the hydrocarbon crystals, and a choice between them could not be made on the basis of the hydrocarbon crystals alone. The acetic acid data helped to make this choice unambiguous (and also to determine the A^{kk} coefficients for O_{17}, O_{18}, and H_4) because of the following short contact distances: $H_1 \cdots O_{17}$ (2.5 Å), $H_1 \cdots H_4$ (2.4 Å), $H_4 \cdots C_7$ (2.6 Å), $H_1 \cdots O_{18}$ (2.65 Å), and $H_1 \cdots C_6$ (2.85 Å). N-Methylacetamide and adipamide also helped to remove the ambiguity about the choice of the $A^{C_6 \cdots C_6}$ and $A^{H_1 \cdots H_1}$ coefficients. In the acetic acid crystal, the $H_4 \cdots C_7$ interaction is directed across the hydrogen bond, and σ is not very sensitive to variation in the repulsive coefficient for this interaction; thus, the acetic acid crystal was not a suitable one for determining the $C_7 \cdots C_7$ repulsive coefficient. The final parameters for the atoms of the carboxyl group are a best fit for both acetic and succinic acids, with oxamide (in particular) serving to further define A^{kk} for the C_7 atom.

The positions of the methyl hydrogens of acetic acid were not well defined in the crystal data, although Nahringbauer[79] suggested that a methyl hydrogen is cis to the carbonyl oxygen in acetic acid. This result also agrees with some semiempirical molecular orbital calculations[81] on the rotation of the methyl group in acetic acid. However, for the initial and final sets of values of A^{kk}, we found that the best fit and lowest crystal energy was obtained with a methyl hydrogen trans to the carbonyl oxygen; it is shown in this conformation in Figure 2B, and was maintained in this way in the computations. The dependence of the crystal lattice binding energy (for the final set of A^{kk} parameters and for a 111 cell index) on the dihedral angle χ (for $H_1 C_6 - C_7 O_{17}$) is shown in Figure 10, along with the deviation σ (viz., the square root of the sum of the squares of the deviations) of the lattice constants. In accordance with the arguments presented in section IIA4, no intramolecular energy or torsional terms were included when χ was varied. Although the difference in intermolecular energy between $\chi \sim 10°$ and $\sim 60°$ is only 0.04 kcal/mol in favor of $\sim 60°$ (see Figure 10), the fit of the energy-minimized lattice constants is better at 60°, as indicated by the value of σ. The existence of an apparent sixfold rotational potential (i.e., two minima per 120°) arising from the intermolecular interactions in the crystal is interesting, since one might have expected a similar potential to arise from the intramolecular forces. Indeed, the maximum barrier to rotation found here from calculations of the crystal energy [~ 0.45 kcal/mol without energy minimization (dashed curve) and ~ 0.30 kcal/mol with energy minimization (solid curve); see Figure 10] is nearly the same as that (0.48 kcal/mol[82]) arising from intramolecular forces, as found in a gas-phase microwave[82] study of acetic acid (where the cis conformation was found

to be favored). From the experimental crystal data,[79] it is quite possible that the intramolecular energy is more important than the intermolecular crystal lattice energy in determining the average positions of the methyl hydrogens, and it tends to keep the methyl hydrogen cis. We report the results of the fitting for the trans conformation in Table VII (and the corresponding carboxyl group parameters in Table IV); the difference in fit is only slightly different for the cis conformation, and will not have any significant effect on the values of A^{kk} for the H_4, O_{17}, and O_{18} atoms.

Before discussing the results obtained from the calculations of the energies of the carboxylic acids (given in Table VII), we consider for the first time the contribution of the electrostatic energy of the polar atoms to the total interatomic potential (the electrostatic contribution to the lattice binding energy in the hydrocarbons was small, and played only a minor role in the determination of the parameters of the potential function there). In section IIA5,[33] we argued that the shortest contact distances between atoms should have repulsive nonbonded forces, since the attractive dispersion (and some electrostatic) forces of the surroundings compress the molecules together, and that the first interatomic contacts hold the molecules in the observed orientations. When many different types of atoms are present in a crystal, it is imperative (in order to be able to compute parameters with good precision) that the important close contacts be those related to the A^{kk} parameters which are being determined in the minimization procedure. Only then will the energy and packing of molecules in the crystal be sensitive to those particular interactions. The effect that the electrostatic and nonbonded contributions have in determining the total interatomic potential is shown for selected interatomic interactions in Figure 11.

In Figure 11A, the various energy contributions to the total interatomic potential between two carbonyl oxygens is shown. The distance of closest contact for these atoms (i.e., distance between O_{17} of the 0th molecule and O_{17} of molecule 1) for the carboxylic acids is shown as short lettered vertical strokes on the figure. Although these contact distances lie to the right of the position of the minimum of the curve for the nonbonded potential, both the force ($+1.85$ kcal mol^{-1} Å^{-1} at $r_{O \cdots O} = 3.3$ Å, but not shown) and force constants (shown on the calculated f_r curve) are positive, i.e., repulsive. This is a result of the large positive (repulsive) electrostatic contribution to the total interatomic energy (the charges on both the carbonyl oxygens of acetic acid being -0.362). The computed force constant curve f_r lies between those obtained from the Hartree–Fock (HF) and Thomas–Fermi–Dirac (TFD) potentials[51,52] in the range of contact distances considered here.

In Figure 11B, showing the contributions of the different components of the energy to the interatomic potential for $H_1 \cdots O_{17}$ interactions, we see a reversal of the above effect. Now, because of the negative (attractive) electrostatic energy (the charge on each hydrogen of acetic acid being $+0.063$ and that on O_{17} being -0.362), some of the contact distances are found to the left of the minimum in the curve for the nonbonded potential; in fact, in the case of the molecules formic acid[83] (a), acetic acid[79] (b), and succinic acid[80] (c), the nonbonded energy has become positive at the distances observed in the crystals. The curve for the nonbonded energy is shifted to the right because of the negative electrostatic energy, and the force ($+2.1$ kcal mol^{-1} Å^{-1} at 2.5 Å, and -0.3 kcal mol^{-1} Å^{-1} at 3.0 Å, but not shown) is repulsive at the close contacts (i.e., ~ 2.5 Å), as
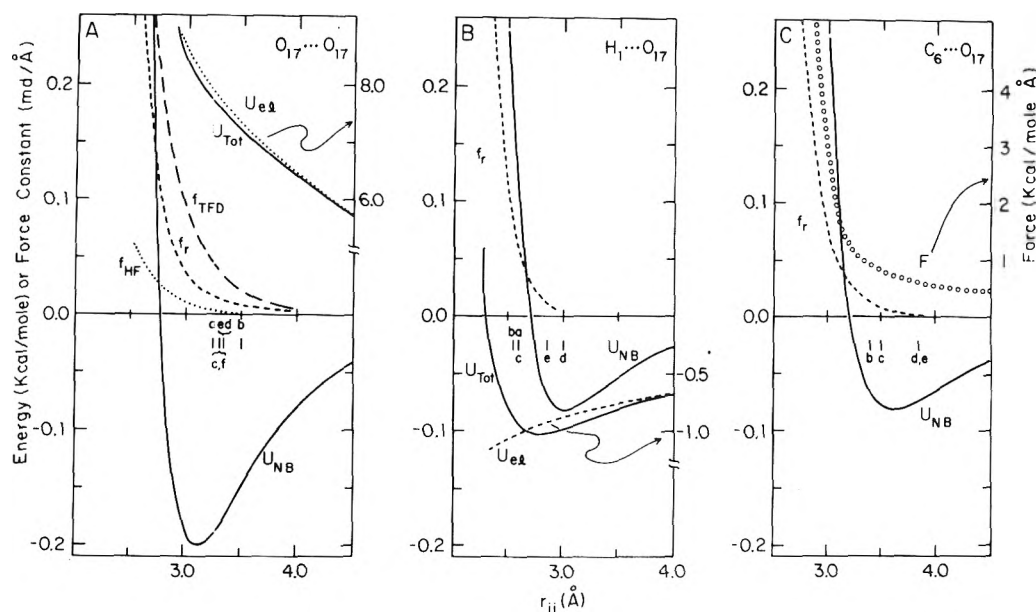
Figure 11. Energy, force, and force constant curves as a function of interatomic distance. (A) U_{Tot} (total interatomic energy) = U_{el} (electrostatic energy) + U_{NB} (nonbonded energy) for the interaction of two O_{17} atoms. f_r is the force constant curve obtained from U_{Tot}. f_{HF} and f_{TFD} are the Hartree–Fock and Thomas–Fermi–Dirac force constant curves obtained from the data of Bonham, et al.[51,52] (B) Same as in A except for the $H_1 \cdots O_{17}$ interaction. (C) U_{NB}, f_r, and F for the $C_6 \cdots O_{17}$ interaction. F is the force curve obtained from U_{Tot} for $C_6 \cdots O_{17}$. In A, B, and C, a signifies the shortest intermolecular (contact) distance for the particular atom types in formic acid; b, in acetic acid; c, in succinic acid; d, in suberic acid; e, in sebacic acid; and f, in oxalic acid.

expected for interactions of this type. The $H_1 \cdots O_{17}$ interactions are very important for determining the value of A^{kk} for $O_{17} \cdots O_{17}$ in acetic acid, since we have held A^{kk} for H_1 constant and varied A^{kk} for $O_{17} \cdots O_{17}$ for this molecule.

The 6–12 nonbonded interaction between C_6 (methyl carbon) and O_{17} is shown in Figure 11C, along with the force (F) and force constant curves. As in Figure 11A, the electrostatic repulsive terms make the force repulsive over the whole range of $C_6 \cdots O_{17}$ distances (since the C_6 and O_{17} charges of acetic acid are −0.163 and −0.362, respectively).

From Figure 11, it is clear why acetic and succinic acids were excellent choices for determination of the A^{kk} parameters for the atoms of the carboxyl group. In two types of interactions (viz., $C_6 \cdots O_{17}$ and $H_1 \cdots O_{17}$), both acetic and succinic acids have the shortest, and thus most important, contact distances for determining A^{kk}. For example, for acetic acid, the $H_1 \cdots O_{17}$ and $C_6 \cdots O_{17}$ interactions lead to the largest positive force constants among those of the carboxylic acids treated here. The $O_{17} \cdots O_{17}$ contact distance is longest for acetic acid because of the extended (rather than cyclic) hydrogen-bond arrangement. It should be pointed out that the contribution of the electrostatic terms to the total lattice binding energy is only ~10% (i.e., the 6–12 nonbonded and GHB contributions make up most of the energy). Thus, even though the charges of two particular atoms may interact strongly (with either positive or negative electrostatic energy), these interactions are always counterbalanced by other electrostatic energies of opposite sign to give a net electrostatic contribution to the lattice binding energy which is relatively quite small.

Further refinement of the A^{kk} coefficients for the atoms of the COOH group was achieved using formic acid, oxalic acid, and suberic acids.

1. Acetic Acid. As mentioned earlier, acetic and succinic acids were used to obtain the parameters of the carboxyl group. The optimized lattice parameters of acetic acid

(using the parameters of Table IV) are given in Table VII. The excellent fit (i.e., ~1% deviation) obtained for this molecule is found for most of the other acids except oxalic and formic (which will be discussed in sections 4 and 5, respectively). In order to assess the dependence of the lattice constants on the A^{kk} coefficients, we first examine the effect of temperature on the observed lattice constants. If one compares the lattice constants at the two temperatures +5 and −190° at which the cell dimensions were obtained,[79] it is observed that the parameter a (viz., 13.31 at +5° and 13.21 at −190°) is larger by ~0.10 Å at the higher temperature. The parameter b also increases by ~0.16 Å, while the parameter c is relatively independent of temperature (viz., 5.77 Å at both temperatures). The volume change, between these two temperatures, is ~15 Å³, which is quite large. The hydrogen-bonding network is complicated, but is directed to some extent along the c axis, and is probably responsible for the fact that c is relatively independent of temperature, but that a and b vary with temperature. The temperature independence of the lattice constant in the direction of the hydrogen-bonded networks is also observed for other crystals studied here. With the temperature dependence as a guide, i.e., with the observation that a and b do vary with temperature (and are less influenced than c by the hydrogen bonding), we see that the A^{kk} coefficients for the atoms of the carboxylic acids can be determined with precision, in terms of the good fits to the experimental values of a and b (i.e., a and b are sensitive to changes in the A^{kk} coefficients). Further, the $A'_{H_4 \cdots O_{17}}$ coefficient of the GHB function was allowed to vary but was found to remain very close to the value found[14c] by fitting CNDO/2 energies for dimers.

Table VII also shows the small deviation in the distance between hydrogen-bonded atoms (viz., $\Delta r_{H_4 \cdots O_{17}}^{calcd}$) in the energy-optimized crystal from that in the observed structure.[79] The origin of the deviation between the calculated binding energy and experimental[84] sublimation energy

(*viz.*, −14.3 kcal/mol compared to +9.96 kcal/mol) is not clear, especially since the energy of dimerization for acetic acid in the gas phase[85] has been found to be ∼−14.4 kcal/mol. Since we find that the calculated lattice binding energies (for the energy-minimized cell) of all the other carboxylic acids studied here agree within ∼10% of the reported sublimation energies, we can only surmise that either experimental difficulties (*e.g.*, dimer formation which might have influenced the reported sublimation energy) or large quantum effects (such as large changes in zero-point energy in going from the solid to the gas phase) may be partially responsible for the discrepancy observed here.

2. β-Succinic Acid. The CNDO/2 (ON) partial charges and structure of succinic acid[80] are shown in Figure 2E. This molecule was also used in the refinement of the parameters of the carboxyl group, as mentioned earlier. The results of the energy minimization (using the potential coefficients of Table IV) are given in Table VII. A head-to-tail aspect of association (involving cyclic hydrogen bonds) is observed with a zig-zag aliphatic chain configuration. In the computations, the H_4 atoms were held fixed cis to the carbonyl oxygen, because the cyclic hydrogen-bond network makes this position the only reasonable one. The hydrogen bonds are directed primarily along the *c* axis, and this axis exhibits a very small deviation from the observed value in the calculations carried out here. The calculated binding energy is very close (*i.e.*, ∼3% deviation) to the experimental value,[86] and the deviation of the length of the hydrogen bond in the energy-minimized lattice from the experimental value is very small (0.02 Å).

3. Butyric Acid. The CNDO/2 (ON) partial charges and structure of butyric acid[87] are shown in Figure 2C. The final optimized lattice parameters (using the potential coefficients of Table IV) are given in Table VII. The end methyl group was found to be best positioned in a staggered conformation (*i.e.*, χ = 60°), similar to the alkanes. The molecule lies in the *b* = 0 plane and forms cyclic hydrogen-bonded dimers. From Table VII, it can be seen that, even though the energy optimized lattice constants *a* and *c* differ slightly from those obtained from the X-ray data, these deviations do not affect the length of the hydrogen bond; *i.e.*, the asymmetric units (*viz.*, the dimers) have shifted ever so slightly with respect to one another, but the operator defining the inversion center maintains the observed lengths of the hydrogen bonds. A rough estimate of the structural inaccuracy is obtained by comparing the lattice constants determined by two different groups of workers. For example, Strieter and Templeton[87] found *a* = 8.01 ± 0.08, *b* = 6.82 ± 0.02, and *c* = 10.14 ± 0.03 Å; β = 111° 27′ ± 15′ (at *t* = −43°), while Scheuerman and Sass[88] found the values *a* = 8.08 ± 0.02, *b* = 6.83 ± 0.02, *c* = 10.10 ± 0.02 Å; β = 111° 9′ ± 12′ (at −30°). These discrepancies are too large to arise from the small difference in temperature, and are not much less than the deviations of our computed lattice constants from those observed by Strieter and Templeton.[87]

4. α-Oxalic Acid. The CNDO/2 (ON) partial charges and structure of oxalic acid[89] are shown in Figure 2D. The crystalline form considered here was α-oxalic acid, and the structure determination[89] is rather old. The hydrogen-bonded chain system is extended (rather than the cyclic dimer type of succinic and butyric acids), and links the molecules together to form a puckered layer structure throughout the crystal. The results of minimization of the lattice energy are given in Table VII. The deviations in the

lattice constants for this crystal are the largest observed for the carboxylic acids. There are no unusually small contact distances in the observed structure. We find a significant shrinkage in both the *a* and *b* lattice constants and an expansion in the *c* lattice constant. The result is a crystal structure which is much less puckered than the original, with a hydrogen-bond length (*viz.*, 1.68 Å for $H_4 \cdots O_{17}$ instead of 1.8 Å in the observed structure) more in line with those of other carboxylic acids. The binding energy calculated for the optimized structure is in good agreement with experimental data;[90] finally, the volume of the calculated unit cell is nearly identical with that found from the X-ray cell dimensions. Rotation of the H_4 atom away from the position cis to the carbonyl oxygen and minimization of the lattice energy produced no significant improvement in the fit. It is clear that anhydrous oxalic acid (which packs as an extended chain with the molecules linked in a puckered layer structure) does not take up a structure similar to the other (hydrated) oxalic acids[91] (which pack in a cyclic head-to-tail structure similar to succinic acid), and this may be an indication of some anomalies in the structure. No explanation for the deviations found here is available at this time.

5. Formic Acid. The X-ray structure and CNDO/2 (ON) partial charges of formic acid[83] are shown in Figure 2A. The hydrogen-bonding network is similar to that of acetic acid, being extended rather than cyclic. The standard deviation from the experimental results is given in Table VII. The fit to the lattice constants (*i.e.*, σ = 0.25) is not particularly good in this case, and it was decided to investigate the effect of varying the position of the hydrogen, H_4, as a function of the dihedral angle for rotation about the C–OH bond. The results of this study (*i.e.*, minimization of the lattice energy as a function of lattice constants for each position of H_4) were not clear cut. For example, the lattice binding energy was most negative for H_4 cis to the carbonyl oxygen, but the lattice fit was poor (this is the result presented in Table VII). As H_4 was rotated, the fit to the lattice parameters improved (the standard deviation became approximately half of that for the cis conformation) but the lattice binding energy became less negative (by ∼20%). Since the position of H_4 was not found in the X-ray study, we expect it to be cis to the carbonyl oxygen as found in the gas phase by microwave spectroscopy.[92] The high experimental barrier to rotation[92] of 17 kcal/mol also indicates that the conformation should be planar. The experimental sublimation energy[93] is in good agreement with our calculated binding energy. It is possible that errors in the X-ray structure[83] itself may be responsible for the large deviations found here. For example, the gas-phase electron diffraction data[94] on monomeric formic acid give a C_7–O_{18} bond length of 1.36 Å (1.32 Å in the dimer) compared to 1.26 Å found[83] in the crystal data considered here. The other bond lengths and bond angles are nearly the same in each study. Further, an X-ray study of a 1:1 addition complex of formic acid and formamide[95] gave a C_7–O_{18} bond length of 1.32 Å, in agreement with the gas-phase dimer value. It is also of interest that the hydrogen-bond distance between oxygens in the gas-phase dimer[94] was found to be 2.70 Å, compared to 2.5 Å in the crystal. Our energy-minimized hydrogen-bond distance was 2.67 Å, in good agreement with the gas-phase dimer result.

6. Suberic Acid. The CNDO/2 (ON) partial charges and structure of suberic acid[96] are shown in Figure 2F, and the results of the energy minimization are given in Table VII.

The packing arrangement is similar to that of succinic acid, but the molecules are somewhat less rigidly held (i.e., there are larger vibrational amplitudes as indicated by the X-ray thermal parameters perpendicular to the direction of hydrogen bonding) because of the longer aliphatic section of the molecule. The molecules lie in the a–c plane. Thus, the observed deviation in the c axis is difficult to interpret in terms of large vibrational amplitudes. The binding energy is ~7% smaller than the experimental value[86] and the dicarboxylic acid cyclic hydrogen bonding arrangement was very well maintained.

7. Sebacic Acid. The CNDO/2 (ON) partial charges and molecular structure of sebacic acid[97] are the same as those of suberic acid, and are not shown in Figure 2. The molecular packing is similar to that of succinic acid, except that the hydrogen bond is directed along the a axis. The results of the optimization of the lattice are given in Table VII. The fit of the energy-minimized lattice to the X-ray one is nearly equivalent to that of suberic acid (i.e., the c axis deviates somewhat more than a or b. It is not clear why the value for the sublimation energy[86] is ~12% lower than the calculated lattice binding energy. Since only one cell was taken in both the a and c directions, it may be that some (~10%) energy was lost. This marginally small cell size was used to simplify the computations for this large molecule. The length of the hydrogen bond is again in excellent agreement with the starting (i.e., X-ray) result. As in the case of suberic acid, no reason can be proposed for the expansion in the c axis upon minimization.

8. Conclusion from Calculations on Carboxylic Acids. The results on the carboxylic acids are on the whole very good (with the exception for oxalic and formic acids noted above), even though there are two different types of hydrogen-bonding arrangements, viz., cyclic dimer and noncyclic. The exceptions, formic and oxalic acids, are both unusual molecules, being the smallest members of the mono- and dicarboxylic acid groups, respectively. It is desirable that their crystal structures be reinvestigated, using the more refined X-ray and neutron diffraction techniques available today; the difference found for formic acid in the addition compound with formamide[95] supports the suggestion that the structure of formic acid should be reinvestigated.

The transference of the parameters, A^{kk}, found from aliphatic hydrocarbons to the long-chain dicarboxylic acids seems to be acceptable, with no appearance of large deviations which are easily related to these coefficients. The positions of hydrogens which must be rotated in order to find minimum-energy positions, and the resultant barriers to rotation from intermolecular interactions in the crystal, are found to be in agreement with the limited available experimental data.

The fact that several crystals have hydrogen-bonding networks which are directed along a single axis, and that small deviations are observed in the lattice constant in this direction, provides a good indication that the GHB parameters correctly reproduce the observed hydrogen-bond lengths. The fact that, in these cases, the other two lattice constants are also fit very well indicates that the total potential is correct to within the uncertainty cited.

F. Amides and Amine. The CNDO/2 (ON) partial charges and structures of some amides and methylamine[98] are shown in Figure 3. Suberamide[99] and adipamide[100] are not shown in Figure 3, but their charges for equivalent atoms are the same as those of succinamide, whose structure[101] is

shown. In determining the A^{kk} coefficients of the atoms of the amide unit, $-CONH_2$, the coefficients of the atoms of the carbonyl group ($C_7=O_{17}$) were initially taken to be the same as in the COOH group and the A^{kk} parameters for these atoms were varied only later. This approximation was used and found to be satisfactory until oxamide was examined, at which time the $A^{C_7\cdots C_7}$ coefficient was refined further, and all previous calculations were then repeated with the new $A^{C_7\cdots C_7}$ coefficient. Initially, then, the repulsive parameters for only two new atoms [nitrogen (N_{13}) and hydrogen (H_2)] and that for the $H_2\cdots O_{17}$ general hydrogen bond potential remain to be determined from the crystals of the amides. The $H_2\cdots O_{17}$ interaction was reconsidered here since it had not been adjusted to experimental data on amides in our earlier paper.[14c] Initially, crystal data for the molecules oxamide[102] and adipamide[100] were chosen to determine the potentials of the amide group, and later formamide and N-methylacetamide were included because of the sensitivity of their structures to the parameters of the amide atoms, which was observed when the crystal energy of these molecules was minimized. Methylamine was chosen for the determination of the $N_{14}-H_2\cdots N_{14}$ hydrogen-bond parameter. The H_1, C_6, C_7, and O_{17} interatomic potentials were fixed at the values found previously from the combined results for the aliphatic hydrocarbons and carboxylic acids. The amide group was always maintained planar even though the positions of the amide hydrogens were not determined precisely in the experimental data. An initial estimate of A^{kk} for the $N_{13}\cdots N_{13}$ nonbonded interaction was taken from Ooi, et al.[59] (by increasing this repulsive term by ~20% over the original value reported by Ooi, et al.[59]), and of A^{kk} for $H_2\cdots H_2$ from the results obtained here for the carboxyl hydrogen (H_4). An initial value of the $A'_{H_2\cdots O_{17}}$ coefficient was obtained by adjusting it (holding the A^{kk} parameters fixed for all the other interactions involved) until a gas-phase formamide cyclic dimer resulted, with a total energy minimum at an $H_2\cdots O_{17}$ distance of 1.9 Å. This GHB term, together with all other amide A^{kk} coefficients, was refined further on the crystals of formamide, oxamide, and adipamide.

Before presenting the results of the energy minimization, the choice of molecules (by the near-neighbor contact criteria) must be considered. As was previously argued for the carboxylic acids, the shortest contact distances are the most sensitive to the repulsive parameters which are being varied. In Figure 12 are shown the shortest contact distances, found in the crystals of the amides studied here, for the $N_{13}\cdots N_{13}$, $N_{13}\cdots O_{17}$, and $N_{13}\cdots H_1$ interactions. These three interactions are simply examples for illustrative purposes only; the other types of contacts (e.g., $N_{13}\cdots C_7$, etc.) are also important, and it must be remembered that the complete potential from all interatomic interactions contributes to the packing and energetics of these crystals. In Figure 12A, the closest $N_{13}\cdots N_{13}$ contacts are seen to be those for oxamide and adipamide, and the most distant, that in N-methylacetamide. In sections 1 and 3 on oxamide and formamide, respectively, we will see that molecular stacking in planes (i.e., parallel planes of dimers in a non-hydrogen-bonding direction) plays a significant role in determining this parameter. On the other hand, the $N_{13}\cdots O_{17}$ contact across the hydrogen bond is closest for N-methylacetamide, but clustered about 2.9 Å for all the other amide $N_{13}\cdots O_{17}$ distances. Since this interaction distance is crucial to the formation of a hydrogen bond (i.e., the $H_2\cdots O_{17}$ GHB term depends on the $N_{13}\cdots O_{17}$ distance), it is not surprising
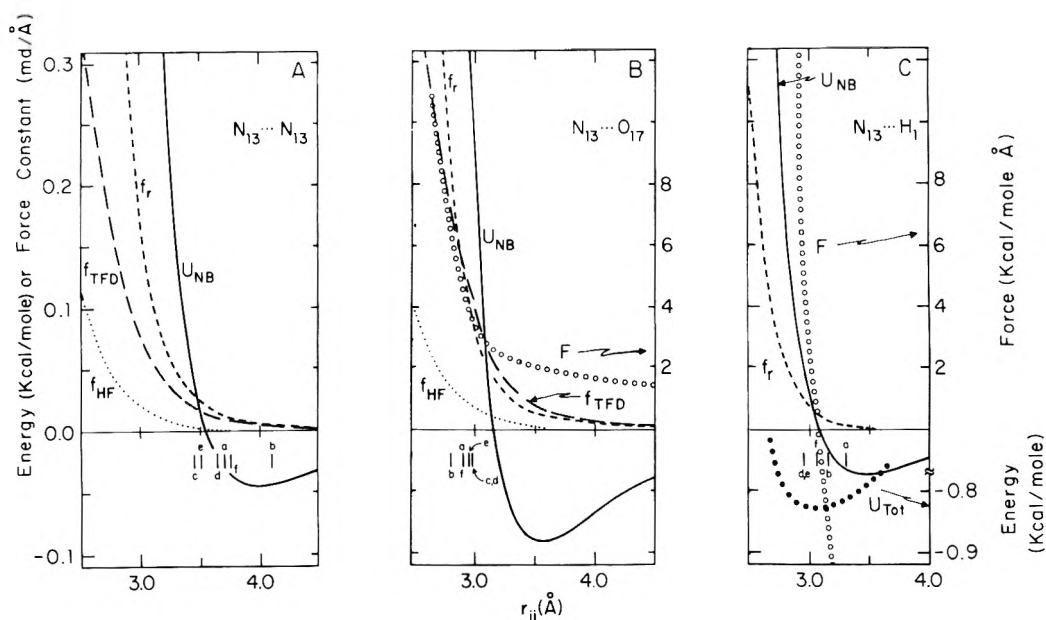
Figure 12. The same as Figure 11, but for interactions involving nitrogen: (A) $N_{13}\cdots N_{13}$ interaction; (B) $N_{13}\cdots O_{17}$ interaction; (C) $N_{13}\cdots H_1$ interaction. In A, B, and C, a signifies the shortest intermolecular (contact) distance for the particular atom types in formamide; b, in N-methylacetamide (NMA); c, in oxamide; d, in succinamide; e, in adipamide; and f, in suberamide.

to find the small spread in $N_{13}\cdots O_{17}$ distances. The closest $N_{13}\cdots H_1$ contacts are those for succinamide and adipamide, again making these appear to be good choices for determining the parameters of the amide group. The curves shown in Figure 12 for U_{NB} and f_r for interatomic interactions are obtained from the final coefficients given in Table IV, which are a best fit to the amides, oxamide, adipamide, formamide, and N-methylacetamide, for which the A^{kk} coefficients were varied. The $N_{13}\cdots N_{13}$ interactions are repulsive (i.e., the force, not shown in Figure 12, is $+2.4$ kcal mol^{-1} $Å^{-1}$ at 3.5-Å separation) at the observed contact distances, and the force constant curve compares favorably with the Thomas–Fermi–Dirac curve, but not so favorably with the Hartree–Fock curve, in this range. The $N_{13}\cdots O_{17}$ contacts are even more repulsive (i.e., the force, not shown in Figure 12, is $+6.0$ kcal mol^{-1} $Å^{-1}$ at 2.9-Å separation), with the force constant curve fitting closely to the Thomas–Fermi–Dirac curve. Since the $N_{13}\cdots O_{17}$ nonbonded energy terms are repulsive at the hydrogen-bond contact distance, the stability of a hydrogen bond (i.e., $H_2\cdots O_{17}$) must arise primarily from a slightly net negative electrostatic energy, with a negative energy contribution from the GHB term of the 10–12 potential for the $H_2\cdots O_{17}$ interaction. The hydrogen-bond potential will be discussed in section 2 on adipamide, and in the Discussion section (V) in more detail. Thus, oxamide, adipamide, formamide, and N-methylacetamide were chosen for the determination of the relevant parameters here, and these were then tested on succinamide and suberamide.

1. Oxamide. The CNDO/2 (ON) partial charges and structure of the oxamide molecule[102] are shown in Figure 3C. There is a distinct difference in the crystal packing of oxamide from the packing of the other amides. The molecule lies very nearly in the *b–c* plane, and the stacking in the *a* direction is such that the carbonyl group of the molecule in the *a* = 0 plane is antiparallel to the carbonyl group of the molecule in the next layer up along the *a* axis in the *b–c* plane. This alignment has the unique feature of making the $C_7\cdots O_{17}$ and $C_7\cdots C_7$ contact distances shorter (i.e., 3.1

and 3.3 Å, respectively) than is found in the other amides. The properties of the $C_7\cdots C_7$ contact, which is much shorter for oxamide than for any of the other amides, are illustrated in Figure 13. Indeed, it was found that the $C_7\cdots C_7$ repulsive interaction plays an important role in oxamide, and placed a limitation on the A^{kk} parameter for C_7 which was not found in either the carboxylic acids or the other amides. For this reason, it was necessary to repeat the previous calculations on the carboxylic acids, using the $C_7\cdots C_7$ parameter determined for oxamide, and recomputing the other A^{kk} values. The results reported previously (in Tables VI and VIII) were all obtained with the final refined parameter set (of Table IV) and so have already had this refinement included (as mentioned in section IVE, the energies of the carboxylic acids are relatively insensitive to the C_7 parameter; therefore, the carboxylic acid data changed very little in this recalculation).

While the A^{kk} parameters for $N_{13}\cdots N_{13}$ and $H_2\cdots H_2$ were being varied, it was found that σ was sensitive to changes in $\langle r_g{}^{N_{13}\cdots N_{13}}\rangle$ of the magnitude of ± 0.1 Å. This sensitivity arises from the close planar packing between molecules. On the other hand, σ was insensitive to changes in $\langle r_g{}^{H_2\cdots H_2}\rangle$ of the order of ± 0.3 Å. This sensitivity enables us to determine the value of $A^{N_{13}\cdots N_{13}}$ very precisely, but the value of $A^{H_2\cdots H_2}$ less so. The GHB coefficient for $H_2\cdots O_{17}$ was found to vary only slightly (i.e., ~ 0.03 Å in the position of the minimum of the GHB potential) from the adjusted value selected initially using the formamide dimer, and was refined further using adipamide. In Figure 14, we show the total GHB function, the 6–12 nonbonded energy for $H_2\cdots C_7$ and $N_{13}\cdots O_{17}$, the electrostatic energy for $H_2\cdots O_{17}$ interaction, and the force for the total (i.e., GHB plus electrostatic) $H_2\cdots O_{17}$ interaction. It can be seen that the force rises very steeply near the minimum of the $H_2\cdots O_{17}$ curve, and will dominate the forces in the direction along the hydrogen bond. The total energy of any hydrogen-bonded molecular system is made up of contributions from all the near-neighbor atoms, and is not completely dependent on the GHB term.
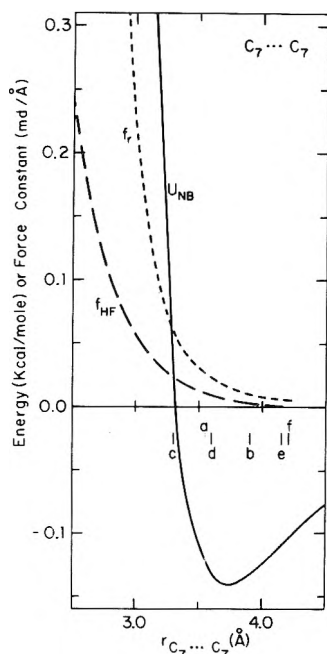
Figure 13. The same as Figure 11, but for $C_7 \cdots C_7$ interactions in amides. The small letters designate the same molecules listed in Figure 12.

Figure 14. Dependence of various energy contributions U, and force F, on distance r_{ij}.

The resulting fit to the lattice constants of oxamide is given in Table VIII. It can be seen from Table VIII that the calculated binding energy (~ -20 kcal/mol) is considerably less than the experimental value[103] (~ -27 kcal/mol). It is not clear why this discrepancy exists. The volume and hydrogen-bond lengths are very close to the experimental values.

2. Adipamide. The CNDO/2 (ON) partial charges of adipamide are the same (for equivalent atoms) as those of succinamide shown in Figure 3D. Unlike succinamide and suberamide (see section IVF5), whose crystals contain eight hydrogen bonds per molecule, adipamide packs in the crystal with only six hydrogen bonds per molecule. The amide hydrogens on one end of the molecule link two other molecules through hydrogen bonds to their carbonyl oxygens, while the carbonyl oxygen on the same end hydrogen bonds to yet a third molecule. This same bonding also appears at the other end. Thus, each adipamide molecule is surrounded by, and linked through hydrogen bonds to, six other molecules. The molecules lie nearly flat in the b-c plane, with the hydrogen-bonding network directed along the b and c axis. The stacking interactions between planes influences the c axis primarily, which in turn is relatively insensitive to the hydrogen-bond interactions. Adipamide has some close contacts between atoms such as $H_1 \cdots O_{17}$ (2.65 Å), $H_1 \cdots N_{13}$ (2.95 Å), $H_1 \cdots H_2$ (2.65 Å), and $H_1 \cdots C_7$ (2.85 Å) which helped in the refinement of the $H_1 \cdots H_1$, $C_6 \cdots C_6$, $H_2 \cdots H_2$, $N_{13} \cdots N_{13}$, and $O_{17} \cdots O_{17}$ parameters. The fit to the lattice constants (using the final parameters of Table IV) is given in Table VIII, and is seen to be excellent. The calculated binding energy is of the correct order of magnitude (by considering the successive addition of methylene groups to oxamide) if one takes a contribution of ~ 1.8–1.9 kcal/mol per methylene group to the binding energy for each methylene group added to oxamide. The value of ~ 1.8 kcal/mol for each methylene group also agrees with that computed from the differences in binding energies between crystalline hexane and octane.

3. Formamide. The final optimized lattice constants of
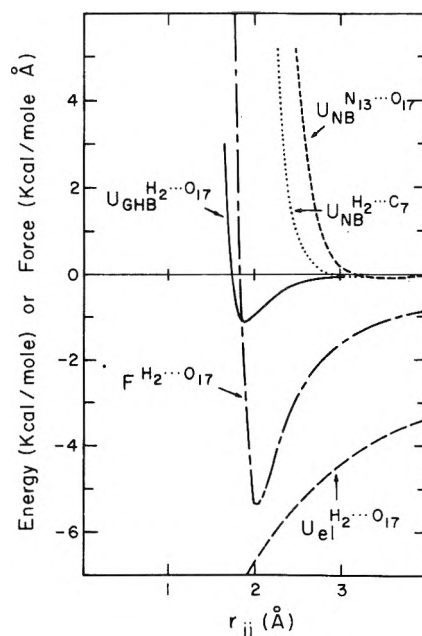
formamide[104] are given in Table VIII (using parameters of Table IV). Although the lattice fit (*i.e.*, $\sigma = 0.13$) is not as good as for some of the other amides, the contraction in the a and c axis, together with the expansion in the b axis, nearly cancel; hence the computed volume of the unit cell is close to the observed one. In fact, the computed hydrogen-bond lengths (two of which are given in Table VIII) agree very well with the experimental values. It was found that this structure was the most sensitive of all the amides to variation in the $A^{H_2 \cdots H_2}$ coefficient. The $H_2 \cdots H_2$ contact at 2.55 Å and other related cross terms, were helpful in reducing the uncertainty in this parameter. We have examined other packing arrangements of formamide by changing the positions of the carbonyl hydrogen (*i.e.*, by changing the N–C–H bond angle) as well as those of the amide hydrogens (*i.e.*, the C'–N–H bond angle), and find that minor improvement in the lattice fit is possible. However, in order to maintain consistency throughout, the positions of the hydrogens given in Table III were retained for this and all of the other amide crystals. The relatively large value of σ may be due to possible uncertainties in the molecular geometry, but no attempt was made here to alter the heavy-atom geometry. The binding energy reported in Table VIII is derived from data for acetamide,[105] with a group increment for –CH_3 subtracted away (*i.e.*, $\Delta H_{acetamide} = -18.5$ kcal/mol, and $\Delta H_{-CH_3} \approx -1.5$ kcal/mol), and is not a reliable value.

4. N-Methylacetamide. N-Methylacetamide[106] has two methyl groups which must be rotated in order to achieve the lowest lattice binding energy and the corresponding conformation. In Figure 15, the lattice binding energy (computed with the final parameters of Table IV, and with the experimental heavy-atom geometry and lattice constants), normalized to zero at the lowest value found in a $10°$ ϕ,ψ grid (see Figure 3B for definition of ϕ and ψ), is plotted as a function of ϕ^1 and ψ^1. The minimum is near $\phi^1 = 60°$; $\psi^1 = 45°$, and these values of the dihedral angles for rotation of the methyl groups were chosen for the final minimization of the lattice energy, the results of which are given in Table VIII and compared to the experimental sub-
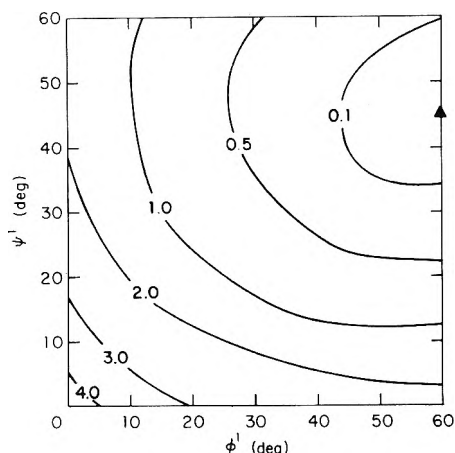
Figure 15. Energy contour diagram for the binding energy of a 111 cell index crystal of N-methylacetamide, as a function of the dihedral angles for rotation of the two methyl groups. The energies are in kcal/mol, scaled to zero at the minimum (▲) of ϕ^1 and ψ^1 equal to 60 and 45°, respectively. The heavy-atom X-ray geometry and the lattice parameters were the experimental values, and were held fixed as ϕ^1 and ψ^1 were varied.

limation energy.[107] It can be seen from Figure 15 that each methyl group passes over a barrier, around 0° in either ϕ^1 or ψ^1, of ~2.5 kcal/mol, and that the highest energy region (at $\phi^1 = 0°$; $\psi^1 = 0°$) is one with a barrier of approximately twice the individual barriers (i.e., ~4.5 kcal/mol at $\phi^1 = 0°$; $\psi^1 = 0°$). This implies that, in the crystal, the rotation of the methyl groups is only moderately strongly coupled, and that the barrier to rotation is sufficiently high so that it cannot be easily overcome by thermal energy; thus, the methyl hydrogens will be locked (i.e., with methyl hydrogen oscillations of ~±30°) into the conformation shown in Figure 3B. The conformation of the methyl groups of N-methylacetamide can be compared to that obtained by molecular orbital and ab initio calculations on the isolated molecule.[14a,108] The molecular orbital calculations (i.e., EHT,[14a] CNDO/2,[14a] and ab initio[108]) gave the conformation of lowest internal energy at $\phi^1 = 60°$; $\psi^1 = 0°$. However, the energy difference upon varying ψ^1 from 0 to 60° (for $\phi^1 = 60°$) is only 0.18 kcal/mol by EHT,[14a] 0.30 kcal/mol by CNDO/2,[14a] and 1.1 kcal/mol by ab initio calculations.[108] The energy difference upon varying ϕ^1 from 0 to 60° (for $\psi^1 = 0°$) is 0.30, 0.24, and 0.7 kcal/mol, respectively, for the three methods. From Figure 15, it can be seen that the intermolecular interactions in the crystal will probably dominate in determining the conformation of the methyl groups, these energies being somewhat larger than the intramolecular terms, with the intramolecular energy serving to make ψ^1 approach 30°.

Table VIII shows the final fit to the lattice constants, using the coefficients of Table IV. It is not clear from an examination of the crystal packing why the a axis expands and the b axis contracts. The plane of the N-methylacetamide molecule is that defined by the a–c axes, with the hydrogen bond directed nearly parallel to the a axis. One possible reason for expansion along the a direction may be the close $H_1\cdots H_1$ contact (viz., 2.15 Å) between the N-methyl group of one molecule with the C'-methyl group of a second molecule in the a–c plane, or possibly the $H_1\cdots O_{17}$ contact (viz., 2.85 Å) between adjacent molecules. These close contacts helped resolve the uncertainty arising from the appearance of two sets of repulsive coefficients for the $H_1\cdots H_1$ and $C_6\cdots C_6$ interactions, as described in section IVA. It was

apparent from our study of this molecule that the parameters $A^{H_1\cdots H_1}$ and $A^{C_6\cdots C_6}$ are sensitive to the packing, and helped define the limit of uncertainty in these coefficients. The fit to the lattice constants (using the final parameters of Table IV) is given in Table VIII, and is seen to be good.

5. Succinamide and Suberamide. The molecules succinamide[101] and suberamide[99] are diamides, and form similar end-to-end arrangements of their hydrogen-bonding network. The CNDO/2 (ON) partial charges and structure are shown for succinamide in Figure 3D. The partial charges of suberamide are the same as those of succinamide for equivalent atoms, with only slightly different charges for the two extra methylene groups in suberamide (viz., −0.10 for C_6 and 0.050 for H_1). In all respects, the energy-minimized fits (using parameters of Table IV) to the lattice constants, as given in Table VIII, are excellent. The deviations in hydrogen-bond lengths are very small, and the volume is very close to the observed value. It should be noted that the uncertainty in the X-ray lattice constants of these molecules is given[99,101] as several hundredths of an ångström, which is not as good as for some other crystals considered here. No variation of A^{kk} coefficients were allowed for these molecules.

6. Methylamine. The CNDO/2 (ON) partial charges and structure for methylamine[98] are shown in Figure 3E. This molecule, being an amine rather than an amide, was included as a check on the parameters for the hydrogen-bonding nitrogen (N_{14}), which is considered to be equivalent to the ring nitrogen in pyrazine, but (in this paper) is allowed to hydrogen bond to type H_2 hydrogen atoms. Thus, the $N_{14}\cdots H_2$ GHB repulsive parameter was determined with this molecule. Since the coordinates of only the heavy atoms are available from the X-ray data, there is considerable ambiguity as to the position of both amine and methyl hydrogens. We have chosen tetrahedral geometry for the methyl hydrogens, and have considered two different geometries for the amine hydrogens. Although it seemed reasonable to assume that the amine hydrogens should be tetrahedral, or nearly so, we studied the planar amine group first. In this case, the methyl group was rotated about the N–C axis (for a particular –NH_2 orientation), and the crystal energy calculated (by initially fixing the $A'_{H_2\cdots N_{14}}$ GHB repulsive coefficient at the value found previously for $A'_{H_2\cdots O_{17}}$), maintaining the experimental values for the positions of the N and C atoms and for the lattice constants.[98] It was found that the maximum difference in energy between the lowest and highest value for methyl rotation (independent of the –NH_2 orientation), not shown in Figure 16, was only 0.3 kcal/mol. We next fixed the methyl group at its lowest-energy conformation, and rotated the planar amine group. The lattice binding energy was very sensitive to rotation of the amine group, and is shown by the solid curve in Figure 16. [This curve was obtained after the $H_2\cdots N_{14}$ GHB term had been adjusted (see below) for the tetrahedral configuration of the amine group]. The lowest binding energy found for the planar amine was −4.6 kcal/mol at $\chi = 130$ and −50°. We next placed the two amine hydrogens in the tetrahedral configuration, and again repeated the calculation of the binding energy upon rotation of the amine group. The results were similar to the dashed curve of Figure 16; the dashed curve was obtained only after variation of the $A'_{H_2\cdots N_{14}}$ coefficient. When a minimum was found in the U_{bind} vs. χ curve, we optimized the $H_2\cdots N_{14}$ GHB term, holding all other A^{kk} values constant. Both curves shown in Figure 16 are for the optimized coefficients. There are two
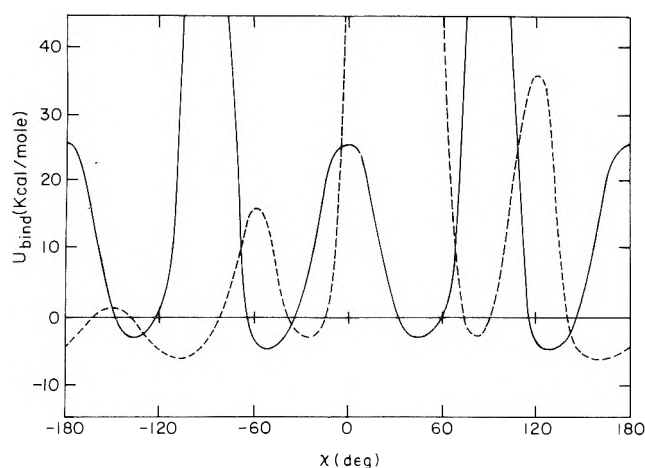
Figure 16. Crystal binding energy of methylamine, calculated as a function of the dihedral angle for rotation of the $-NH_2$ group. The solid curve corresponds to a planar arrangement of the hydrogens on the nitrogen. The dashed curve corresponds to a tetrahedral configuration of the hydrogens. The dihedral angle χ is taken to be zero when H_1^1 is cis to H_2^1 (see Figure 3E).

minima in the dashed curve of equal depth at $\chi = 160°$ and $\chi = -100°$, with energies of -6.1 kcal/mol. It is apparent in Figure 16, both from the lower energy and the lower intermolecular barrier to rotation of the amine group, that the puckered amine group (i.e., tetrahedral arrangement of two hydrogens) is the preferred configuration. While the positions of the hydrogens are not very well defined in the X-ray structure,[98] the observed positions appear to be closer to our minimum-energy one at $-100°$ rather than $160°$. For $\chi = -100°$, the hydrogens of the amine and the methyl group are staggered with respect to one another, and hydrogen bonds are formed between the amine hydrogens and two nitrogens of neighboring molecules. The high barrier to rotation of the amine group [~ 8 kcal between $\chi = -100°$ and $\chi = 160°$ (see Figure 16)] suggests that two different orientations should be expected to be observed in the methylamine crystal. With tetrahedral arrangements of the hydrogens at both the methyl and amine groups, the energy-minimized fit to the observed lattice constants is excellent (see Table VIII).

V. Discussion

From the results presented in Tables VI, VII, and VIII for 23 molecular crystals, several conclusions can be drawn. It is apparent that the procedure used here results in an interatomic potential which is applicable to a number of different types of molecules, and gives values of σ upon energy minimization which are, on the whole, remarkably small. The few structures, where agreement with experimental data is outside the average value of σ for the remaining crystals studied, are those whose atomic coordinates may possibly contain some errors, although we cannot rule out the possibility that the omission of noncentral forces from our potential functions may be the origin of the discrepancies in these few cases. It appears that there is no need to include components of the potential, other than those used here, to determine crystal lattice constants and lattice binding energies to the precision reported here. The calculated binding energies are generally in good agreement with observed sublimation energies, implying (in particular for the hydrocarbons where the partial charges and their contribution to the energy are negligible) that our use of the

London (Slater–Kirkwood) formulation to obtain the attractive $(1/r^6)$ coefficients of the nonbonded potential (instead of determining these coefficients from the crystal data) is reasonable. At this time, we have no explanation for the large deviation between the lattice binding energy and the experimental sublimation energy of oxamide, since the agreement is excellent for N-methylacetamide and reasonably good for formamide when the same potentials are used.

The relative sizes of the contributions to the lattice binding energy from various components of the potentials (i.e., the 6–12 nonbonded, electrostatic, and general hydrogen bond terms) are of interest since, if, e.g., the GHB term dominated the total energy, the remaining terms would not be sensitive to variations in the lattice constants in the direction of the hydrogen-bonding atoms. In this respect, it can be seen in Figure 14 that the GHB term [for the optimum GHB position (~ 1.9 Å) of the $H_2 \cdots O_{17}$ hydrogen bond] is only ~ -1.1 kcal/mol. In the case of formamide, there are three such hydrogen bonds per molecule in the crystal; thus, the contribution of the GHB term to the lattice binding energy (i.e., including only close contacts) is one-half of ~ -3.3 kcal/mol or ~ -1.7 kcal/mol out of the total lattice binding energy of ~ -19 kcal/mol. The contribution of the total electrostatic energy to the energy of the crystal of formamide was found here to be -3.8 kcal/mol. Thus, even for this small molecule, the 6–12 nonbonded energy is ~ -13.5 kcal/mol. For N-methylacetamide, there are two $H_2 \cdots O_{17}$ hydrogen bonds per molecule in the crystal, giving a GHB contribution to the binding energy of -1.1 kcal/mol. Since the total electrostatic contribution for the crystal is -1.6 kcal/mol, there is a net 6–12 nonbonded energy of ~ -8.6 kcal/mol (out of a total of -11.3 kcal/mol computed for the energy-minimized lattice).

Partitioning the total energy into component parts in the case of the carboxylic acids is also possible in the same way. Here, the $H_4 \cdots O_{17}$ GHB term is ~ -5.9 kcal/mol at the optimum GHB position of ~ 1.66 Å. Then, applying the above procedure to succinic acid, where there are four such hydrogen bonds per molecule in the crystal, the total GHB contribution to the binding energy is ~ -12 kcal/mol. Since the total electrostatic contribution to the binding energy is -2.3 kcal/mol, there is a 6–12 nonbonded energy contribution of -14.7 kcal/mol to the computed binding energy of ~ -29 kcal/mol. Of course, errors arise in this approach from the omission of the small nonbonded repulsive terms for the $O_{17} \cdots O_{18}$ and $H_4 \cdots C_7$ contacts across the hydrogen bond. However, it appears that this approximate treatment is applicable to a variety of crystals. It is clear from the above analyses that one can partition the total energy into its various components, but one must consider the total potential as being self-consistent, and not any one component independent of the other contributions. It should be emphasized here that no angle-dependent terms are included either in the GHB potential or in any of the other components of the total potential energy. Yet the hydrogen-bonding network is maintained very closely to that observed. Thus, it does not appear that angle-dependent terms are required if all interactions of the type described here are included.

Although a direct comparison of this work with that of other authors is difficult, because of differing functional forms, etc., we can comment to some extent on the major differences in technique and relate them to the results presented in Table VI. For example, Williams[8] studied many

TABLE IX: Comparison of Values of ϵ and $\langle r_g \rangle$ with Those of Other Authors

Parameters	This work	Ref 12[a]	Ref 9[b]	Ref 7a[c]	Ref 8d[d]	Ref 112	Ref 110
$-\epsilon_{H_1\cdots H_1}$[e]	0.037	0.0045 (0.0025)[f]	0.033	0.060	0.010	0.027[i]	
$\langle r_g^{H_1\cdots H_1}\rangle$	2.92	2.936 (3.548)[f]	3.36	2.80	3.37	3.08[i]	
$-\epsilon_{C_6\cdots C_6}$	0.038	0.196 (0.185)[f]	0.049	0.060	0.095		
$\langle r_g^{C_6\cdots C_6}\rangle$	4.12	4.228 (3.616)[f]	4.16	3.80	3.88		
$-\epsilon_{C_8\cdots C_8}$	0.073		0.095		0.095		
$\langle r_g^{C_8\cdots C_8}\rangle$	3.70		3.90		3.88		
$-\epsilon_{O_{17}\cdots O_{17}}$	0.200	0.230[g]	0.325	0.124[h]		0.106[i]	
$\langle r_g^{O_{17}\cdots O_{17}}\rangle$	3.12	3.00[g]	3.10	3.25[h]		3.32[i]	
$-\epsilon_{N_{14}\cdots N_{14}}$	0.107	0.194[g]	0.165			0.076[i]	0.081
$\langle r_g^{N_{14}\cdots N_{14}}\rangle$	3.51	3.60[g]	3.52			3.80[i]	3.60
$-\epsilon_{S_{20}\cdots S_{20}}$	0.043		0.361	0.333[j]			
$\langle r_g^{S_{20}\cdots S_{20}}\rangle$	3.78		3.91	3.90[j]			

[a] Data used in this work were determined primarily from *intra*molecular interactions. [b] Assumed short interatomic cutoff distances of 7.0, 6.5, and 6.0 Å for C$\cdots$C, C$\cdots$H, and H$\cdots$H interactions; these could influence the attractive coefficients. [c] The values of ϵ for C$\cdots$C and H$\cdots$H types of interactions were *assumed* to be the same. [d] Moved repulsion center 0.03 Å into the C–H bond, and used cutoff distances of 6.0, 5.5, and 5.0 Å for C$\cdots$C, C$\cdots$H, and H$\cdots$H interactions. [e] Only those interactions comparable to the work of other authors are listed. ϵ is the depth of the potential at the minimum, $\langle r_g^{kk}\rangle$. [f] Reference 12b; parameters for a 9–6 potential. [g] Reference 12c. [h] Reference 7e; parameters determined from CO_2 crystals. [i] Midpoint values of maximal and minimal sets of coefficients, derived from virial coefficients. [j] Reference 111.

hydrocarbons (both aromatic and aliphatic) and obtained several sets of attractive and repulsive coefficients (using an exponential repulsive term which contained two variable parameters instead of the one-parameter function used here), all of which gave reasonable fits to the lattice constants and binding energy upon energy minimization. It seems that the procedure adopted here is nearly as good, even though we allow only the repulsive coefficients to vary. By using short artificial interatomic distance cutoffs (as both Williams[8] and Ferro and Hermans[9] have done), the attractive forces become asymmetric with respect to the 0th molecule (see Figure 4), and could lead to errors in the computed lattice constants. We have taken care to balance the interactions with the complete molecules interacting with the 0th one (by translational operators), and in this way have avoided errors which might have arisen from arbitrary cutoff distances. Because of electrostatic contributions to the potential of polar molecules,[109] we have retained interactions with *whole* molecules which are at least 10 Å or greater from the 0th one.

The application of the molecular orbital (CNDO/2) method to obtain reasonable electronic distributions of partial atomic charges has enabled us to extend the treatment beyond the hydrocarbons, and study polar and hydrogen-bonding molecules. Ferro and Hermans,[9] using Del Re σ charges and molecular orbital π charges, also studied some non-hydrogen-bonding polar molecules but, to our knowledge, no one has systematically studied hydrogen-bonding systems by the methods described here. Tables VII and VIII give the deviations in the computed hydrogen bond lengths from the experimental values (with our hydrogen positions) for energy-minimized crystals of acids and amides. It can be seen that the deviations are very small, and the hydrogen-bonding network (whose distance dependence is related to the GHB term) is maintained closely in every case.

A further test of the parameters derived here was the comparison of the force constants, f_r, for H$\cdots$H and C$\cdots$H interactions with those obtained by Harada and Shimanouchi[53,54] by fitting the crystal lattice frequencies. The agreement is excellent in light of the different approaches, suggesting that our nonbonded parameters will correctly reflect the crystal properties which depend on the second derivative of the energy. It is not yet clear that the hydrogen-bonding terms of our potential will be as successful in

fitting spectra, but this problem is very complicated, and will require further study.

Further, we have compared the parameters obtained here with those obtained by other authors,[7–9,12,110–112] and these results are presented in Table IX. The depth, ϵ, and position of the minimum, $\langle r_0 \rangle$, can often be compared directly with those of other authors, but the shape (or curvature) at the minimum will depend on the function used. One must also be cautious about comparing these terms if the centers of repulsion and attraction have been moved into the bonds. In our case, having fixed the dispersion coefficients, we have adjusted only one parameter in the nonbonded function. Thus, if different (*e.g.*, attractive) coefficients are used by other authors, or if they determine them in some way from crystal data, then the values of ϵ and $\langle r_0 \rangle$ will again be different. In general, the values of $\langle r_0 \rangle$ vary, with some coefficients seeming to be similar in magnitude from author to author and others deviating to a greater degree. The values of ϵ are significantly different from author to author, and it is difficult to find a trend for a given pair interaction. While we have not extrapolated our crystal data to 0°K, and have assumed theoretical [CNDO/2 (ON)] values for charges and a 10–12 type hydrogen-bond functional form, it appears that th parameters that we have obtained, when used in the context of the *total* set of interatomic potentials, give very good values of σ and binding energies for a large number of different molecular crystals. It must be emphasized that it is the *total* potential which determines the properties of the crystals computed here; therefore, one should not mix individual parts of our total potential with the complementary parts of the total potential of other authors.

The application of these potentials to the calculation of conformational energy in macromolecules (*e.g.*, polypeptides and proteins) will be presented elsewhere.[29] Care must be exercised in using these potentials found from crystal data for the polypeptide conformational problem, and the reader is referred to ref 29 for an examination of this problem.

Miniprint Material Available. Full-sized photocopies of the miniprinted material from this paper only or micro-

fiche (105 × 148 mm, 24× reduction, negatives) containing all of the miniprinted and supplementary material for the papers in this issue may be obtained from the Journals Department, American Chemical Society, 1155 16th St., N.W., Washington, D. C. 20036. Remit check or money order for $3.00 for photocopy or $2.00 for microfiche, referring to code number JPC-74-1595.

References and Notes

(1) This work was supported at Cornell University by research grants from the National Institute of General Medical Sciences of the National Institutes of Health, U. S. Public Health Service (GM-14312), from The National Science Foundation (GB-28469X3), and from Walter and George Todd.

(2) (a) Special Fellow of the National Institute of General Medical Sciences, National Institutes of Health, 1968–1969. (b) NIH Postdoctoral Trainee, 1968–1969; Postdoctoral Fellow of the National Institute of General Medical Sciences, National Institutes of Health, 1969–1971. (c) To whom requests for reprints should be addressed at Cornell University.

(3) H. A. Scheraga, Advan. Phys. Org. Chem., 6, 103 (1968).

(4) H. A. Scheraga, Symmetry Funct. Biol. Syst. Macromol. Level, Proc. Nobel Symp., 11th, 1968, 43 (1969).

(5) G. N. Ramachandran and V. Sasisekharan, Advan. Protein Chem., 23, 283 (1968).

(6) H. A. Scheraga, Chem. Rev., 71, 195 (1971).

(7) (a) A. I. Kitajgorodskij, "Advances In Structure Research by Diffraction Methods," Brunswick, Vol. 3, R. Brill and R. Mason, Ed., Braunschweig, Vieweg, 1970, p 173; (b) Acta Crystallogr., 18, 585 (1965); (c) J. Chim. Phys., 63, 6 (1966); (d) A. I. Kitaigorodsky and K. V. Mirskaya, "Molecular Crystals and Liquid Crystals," Vol. 6, Gordon and Breach, New York, N. Y., 1970, p 339; (e) A. I. Kitaigorodski, K. V. Mirskaya, and V. V. Nanchitel, Sov. Phys. Crystallogr., 14, 769 (1970).

(8) (a) D. E. Williams, J. Chem. Phys., 43, 4424 (1965); (b) Science, 147, 605 (1965); (c) J. Chem. Phys., 45, 3770 (1966); (d) ibid., 47, 4680 (1967); (e) Acta Crystallogr., Sect. A, 28, 84 (1972); (f) ibid., 28, 629 (1972).

(9) D. R. Ferro and J. Hermans, Jr., in "Liquid Crystals and Ordered Fluids," J. F. Johnson and R. S. Porter, Ed., Plenum Press, New York, N. Y., 1970, p 259; Biopolymers, 11, 105 (1972).

(10) (a) D. P. Craig, R. Mason, P. Pauling, and D. P. Santry, Proc. Roy. Soc., Ser. A, 286, 98 (1965); (b) D. P. Craig, P. A. Dobosh, R. Mason, and D. P. Santry, Discuss. Faraday Soc., 40, 110 (1965).

(11) (a) F. A. Momany, G. Vanderkooi, and H. A. Scheraga, Proc. Nat. Acad. Sci. U. S., 61, 429 (1968), paper I of this series; (b) R. F. McGuire, G. Vanderkooi, F. A. Momany, R. T. Ingwall, G. M. Crippen, N. Lotan, R. W. Tuttle, K. L. Kashuba, and H. A. Scheraga, Macromolecules, 4, 112 (1971), paper II of this series.

(12) (a) S. Lifson and A. Warshel, J. Chem. Phys., 49, 5116 (1968); (b) A. Warshel and S. Lifson, ibid., 53, 582 (1970); (c) A. Warshel, M. Levitt, and S. Lifson, J. Mol. Spectrosc., 33, 84 (1970).

(13) (a) E. Giglio and A. M. Liquori, Acta Crystallogr., 22, 437 (1967); (b) A. Di Nola and E. Giglio, Acta Crystallogr. Sect. A, 26, 144 (1970); (c) G. Capaccio, P. Giacomello, and E. Giglio, ibid., 27, 229 (1971).

(14) (a) J. F. Yan, F. A. Momany, R. Hoffmann, and H. A. Scheraga, J. Phys. Chem., 74, 420 (1970); (b) F. A. Momany, R. F. McGuire, J. F. Yan, and H. A. Scheraga, ibid., 74, 2424 (1970); (c) R. F. McGuire, F. A. Momany, and H. A. Scheraga, ibid, 76, 375 (1972).

(15) R. G. C. Arridge and C. G. Cannon, Proc. Roy. Soc., Ser. A, 278, 91 (1964).

(16) J. O. Hirshfelder, C. F. Curtiss, and R. B. Bird, "Molecular Theory of Gases and Liquids," Wiley, New York, N. Y., 1954.

(17) (a) J. E. Williams, P. J. Stang, and P. v. R. Schleyer, Ann. Rev. Phys. Chem., 19, 531 (1968); (b) C. Schlier, ibid., 20, 191 (1969); (c) A. D. Buckingham and B. D. Utting, ibid., 2ᵀ, 287 (1970).

(18) H. Margenau and N. R. Kestner, "Theory of Intermolecular Forces," 2nd ed, Pergamon Press, Elmsford, N. Y., 1971, p 412.

(19) P. R. Certain and L. W. Bruch, MTP (Med. Tech. Publ. Co.) Int. Rev. Sci.: Phys. Chem., Ser. One, 1972–1973, 113 (1973).

(20) R. Mason, "Perspectives in Structural Chemistry," Vol. III, J. Dunitz and J. Ibers, Ed., Wiley, New York, N. Y., 1970, p 59.

(21) I. M. Torrens, "Interatomic Potentials," Academic Press, New York, N. Y., 1972.

(22) The problem is difficult even for molecules of two types of atoms (such as benzene) because the solutions of the equations of static equilibrium occasionally yield negative coefficients of the $1/r^6$ term, and are particularly sensitive to very slight changes in position of the interaction potential.

(23) The subscripts on the atoms in Figures 1–3 indicate different types of atoms. The reason for considering several different types of atoms is primarily that their electronic environments and atomic mobility differ, and this may be reflected in different repulsive coefficients for atoms of the same atomic number. Thus, aliphatic and aromatic hydrogens are designated as types 1 and 3, respectively. These designations are arbitrary, and are used to distinguish between types of atoms. The numbering scheme adopted is as follows: 1–5, hydrogens; 6–12, carbons; 13–16, nitrogens; 17–19, oxygens; and 20–21, sulfurs. These numbers do not necessarily imply that the energy parameters differ. The different types of atoms are described in Table I.

(24) F. A. Momany, L. M. Carruthers, and H. A. Scheraga, J. Phys. Chem., 78, 1621 (1974).

(25) The crystals were treated in selected sets as indicated, instead of by a simultaneous least-squares treatment of all of them, because the former procedure allows some introduction of chemical intuition, which can be used when anomalous results appear, and which might reduce the computer time.

(26) M. J. Huron and P. Claverie, Chem. Phys. Lett., 4, 429 (1969).

(27) J. Baran, Acta Phys. Pol., A37, 709 (1970).

(28) A brief discussion of the observed structure of a molecular crystal is given in paragraph 6 of section IIA.

(29) F. A. Momany, R. F. McGuire, and H. A. Scheraga, J. Phys. Chem., to be submitted for publication.

(30) We assume here that the inter- and intramolecular free energies are separable at 0°K, and that the kinetic energy is also separable and small.

(31) For crystals such as ice,³² where the combination of hydrogen motion and stiff hydrogen bond potential leads to large zero-point energies, this approximation is very seriously in error. However, the contribution of the intermolecular zero-point energy to the intermolecular binding energy is generally small (i.e., ~0.5 kcal/mol) for hydrocarbons⁷ compared to their binding energies of ~ −10 to −30 kcal/mol. In the case of crystals containing hydrogen-bonded networks (as in many of the crystals studied here), the intermolecular zero-point energy may contribute significantly to the total binding energy.³² At this stage, it is difficult to assess this contribution to the energy and its effect on the computed repulsive 6–12 nonbonded coefficients. However, if we assume that, in first order, the change in zero-point energy with change in repulsive coefficient is small (i.e., that the first derivatives are small), which appears to be the case even for ice,³² then we need not include this contribution to the energy in our computations. Similar arguments may be made for the intramolecular zero-point contributions,³² which are not included here in any event.

(32) (a) L. L. Shipman and H. A. Scheraga, J. Phys. Chem., 78, 909 (1974); (b) ibid., submitted for publication.

(33) In general, the equilibrium positions of those atoms in closest contact with one another will occur on the repulsive side of the interatomic potential for the particular pair of atoms. These repulsive contacts must exist to balance the long-range attractive (6–12) forces between all other pairs of atoms (i.e., the electrostatic forces are very nearly balanced between repulsion and attraction, while the $1/r^6$ potential term is always attractive at large interatomic distances). The result is that, for the crystals studied here, each pair interatomic 6–12 nonbonded potential will have a minimum at an interatomic distance which is in general larger than the observed contact distance in the crystal (van der Waals distance). In contrast to a crystal (and probably in solution), the equilibrium separation of two isolated atoms in the gas phase does occur at the minimum of the pair interatomic potential since the compressive effect of other nearby atoms is not present.

(34) J. O. Hirschfelder, J. Chem. Phys., 43, S199 (1965).

(35) A point that is sometimes ignored when comparing lattice binding energies to sublimation energies is that the sublimation energy includes contributions from any conformational changes which may occur in going from the solid to the gas phase (e.g., the normal hydrocarbons are trans in the solid state, but become mixtures of various conformers in the gas phase³⁶). Since we use the experimental sublimation energies only as an indication of the validity of the calculations, and not as input data to scale our parameters, we do not correct the sublimation data to 0°K, nor do we include changes in zero-point energy upon going from the solid to the gas phase. Also, we do not consider the possibilities that there may be a mixture of conformers, and also association, in the gas phase, and their effect on the observed sublimation energy.

(36) L. S. Bartell and D. A. Kohl, J. Chem. Phys., 39, 3097 (1963).

(37) The 10-Å cutoff is a compromise between computational expediency and theoretical considerations. We have found that smaller microcrystals (viz., those with a ~7-Å cutoff) are required for computational feasibility when the repulsive coefficients are determined by the procedure described in section III. However, in order to obtain ~90% or better of the lattice binding energy of an infinite crystal, we must select a large enough microcrystal to include interactions out to ~10 Å or greater, when computing the interactions with the 0th molecule. While the ~7-Å cutoff was used in determining the repulsive coefficients, the final energy minimization with these parameters (and the resulting lattice constants and binding energies reported here) was carried out with a ~10-Å cutoff. See footnote 56 for further discussion of this point.

(38) R. A. Scott and H. A. Scheraga, J. Chem. Phys., 45, 2091 (1966).

(39) A. Dalgarno, Advan. Phys., 11, 281 (1962).

(40) In the calculations reported here, the bond lengths and bond angles are held fixed. Thus, any change in the conformational energy of the molecule would have appeared in the variation of dihedral angles. This intramolecular energy will be discussed in a later paper.²⁹

(41) P. K. Ponnuswamy, R. F. McGuire, and H. A. Scheraga, Int. J. Peptide Protein Res., 5, 73 (1973).

(42) A. W. Burgess, F. A. Momany, and H. A. Scheraga, Proc. Nat. Acad. Sci. U. S., 70, 1456 (1973).

(43) P. N. Lewis, F. A. Momany, and H. A. Scheraga, Isr. J. Chem., 11, 121 (1973).

(44) R. A. Bonham and L. S. Bartell, J. Amer. Chem. Soc., 81, 3491 (1959).

(45) L. S. Bartell, K. Kuchitsu and R. J. DeNeui, J. Chem. Phys., 35, 1211 (1961).

(46) J. E. Worsham, Jr., H. A. Levy, and S. W. Peterson, *Acta Crystallogr.*, **10**, 319 (1957).

(47) H. C. Freeman and G. L. Paul, *Acta Crystallogr.*, *Sect. B*, **26**, 925 (1970).

(48) M. S. Lehmann, T. F. Koetzle, and W. C. Hamilton, *J. Amer. Chem. Soc.*, **94**, 2657 (1972).

(49) T. F. Koetzle and W. C. Hamilton, *Acta Crystallogr.*, *Sect. B*, **28**, 2083 (1972).

(50) P. Jönsson and A. Kvick, *Acta Crystallogr.*, *Sect. B*, **28**, 1827 (1972).

(51) R. A. Bonham and T. G. Strand, *J. Chem. Phys.*, **39**, 2200 (1963); *ibid.*, **40**, 1686 (1964).

(52) R. A. Bonham, *J. Mol. Spectrosc.*, **14**, 404 (1964).

(53) I. Harada and T. Shimanouchi, *J. Chem. Phys.*, **44**, 2016 (1966).

(54) I. Harada and T. Shimanouchi, *J. Chem. Phys.*, **46**, 2708 (1967).

(55) For example, in a cubic crystal $a = b = c$ and $\alpha = \beta = \gamma = 90°$. Hence, there is only *one* independent variable (*i.e.*, α, β, and γ are fixed, since an alteration of any one of them from 90° would change the crystal symmetry; therefore, $\Delta a = \Delta b = \Delta c$ is the only allowed variable, where the Δ's indicate deviations between observed and computed quantities).

(56) In practice, we have tested the energy convergence by including several unit cells in each (both positive and negative) direction, and looked for an asymptotic approach to the limiting compression and limiting binding energy by adding more cells. The results of this test (carried out on pentane and formamide) were that, after 7–8 Å distance from the 0th molecule, no observable change in compressive effects could be detected, and at a cutoff of ~10 Å, the binding energy converged to ~90% of the limiting value.[37]

(57) The two minimization cycles are coupled and nested so that each time a repulsive coefficient, A^{kk} or $A'_{H\cdots X}$, is incremented, all other cross terms (*i.e.*, A^{kl} coefficients) related to that particular A^{kk} are recalculated using eq 4–7. The binding energy of the crystal is then reminimized for this new set of coefficients, a new σ obtained, and the cycle started over again. In this way, repulsive coefficients are obtained which give an energy minimized lattice which has a low root-mean-square deviation from the experimentally observed values. Since many crystals are treated in this way, the σ value for any one crystal may not be the lowest that can be obtained for that crystal, but is a result for composite parameters derived for all crystals used in the minimization procedures.

(58) R. A. Scott, G. Vanderkooi, R. W. Tuttle, P. M. Shames, and H. A. Scheraga, *Proc. Nat. Acad. Sci. U. S.*, **58**, 2204 (1967).

(59) T. Ooi, R. A. Scott, G. Vanderkooi, and H. A. Scheraga, *J. Chem. Phys.*, **46**, 4410 (1967).

(60) N. Norman and H. Mathisen, *Acta Chem. Scand.*, **18**, 353 (1964).

(61) N. Norman and H. Mathisen, *Acta Chem. Scand.*, **15**, 1755 (1961).

(62) N. Norman and H. Mathisen, *Acta Chem. Scand.*, **15**, 1747 (1961).

(63) T. P. Das, *J. Chem. Phys.*, **27**, 763 (1957).

(64) J. P. Lowe, *Progr. Phys. Org. Chem.*, **6**, 1 (1968).

(65) G. E. Bacon, N. A. Curry, and S. A. Wilson, *Proc. Roy. Soc., Ser. A*, **279**, 98 (1964).

(66) E. G. Cox, D. W. J. Cruickshank, J. A. S. Smith, *Proc. Roy. Soc., Ser. A*, **247**, 1 (1958).

(67) G. Milazzo, *Ann. Chim.*, **46**, 1105 (1956).

(68) A. Bondi, *J. Chem. Eng. Data*, **8**, 371 (1963).

(69) R. S. Bradley and T. G. Cleasby, *J. Chem. Soc.*, 1690 (1953).

(70) R. Mason, *Acta Crystallogr.*, **17**, 547 (1964).

(71) A. I. Kitaigorodskii, K. V. Mirskaya, and A. B. Torbis, *Sov. Phys. Crys-*

tallogr., **13**, 176 (1968).

(72) K. V. Mirskaya and I. E. Koslova, *Sov. Phys. Crystallogr.*, **14**, 339 (1969).

(73) P. J. Wheatley, *Acta Crystallogr.*, **10**, 182 (1957).

(74) L. L. Merritt, Jr., and E. D. Schroeder, *Acta Crystallogr.*, **9**, 801 (1956).

(75) H. Lynton and E. G. Cox, *J. Chem. Soc.*, 4886 (1956).

(76) F. L. Hirshfeld and G. M. J. Schmidt, *J. Chem. Phys.*, **26**, 923 (1957).

(77) A. Bondi, *J. Phys. Chem.*, **68**, 441 (1964).

(78) M. Tasumi and T. Shimanouchi, *J. Chem. Phys.*, **43**, 1245 (1965).

(79) I. Nahringbauer, *Acta Chem. Scand.*, **24**, 453 (1970).

(80) J. S. Broadley, D. W. J. Cruickshank, J. D. Morrison, J. M. Robertson, F. R. S. Shearer, and H. M. M. Shearer, *Proc. Roy. Soc.*, *Ser. A*, **251**, 441 (1959).

(81) W. C. Herndon and J. Feuer, *Tetrahedron Lett.*, **22**, 2625 (1968).

(82) W. J. Tabor, *J. Chem. Phys.*, **27**, 974 (1957).

(83) F. Holtzberg, B. Post, and I. Fankuchen, *Acta Crystallogr.*, **6**, 127 (1953).

(84) E. W. Johnson and L. K. Nash, *J. Amer. Chem. Soc.*, **72**, 547 (1950).

(85) J. O. Halford, *J. Chem. Phys.*, **10**, 582 (1942).

(86) M. Davies and G. H. Thomas, *Trans. Faraday Soc.*, **56**, 185 (1960).

(87) F. J. Strieter and D. H. Templeton, *Acta Crystallogr.*, **15**, 1240 (1962).

(88) R. G. Scheuerman and R. L. Sass, private communication, cited in ref 87.

(89) E. G. Cox, M. W. Dougill, and G. A. Jeffrey, *J. Chem. Soc.*, 4854 (1952).

(90) W. A. Noyes, Jr., and D. E. Wobbe, *J. Amer. Chem. Soc.*, **48**, 1882 (1926).

(91) F. R. Ahmed and D. W. J. Cruickshank, *Acta Crystallogr.*, **6**, 385 (1953).

(92) R. G. Lerner, B. P. Dailey, and J. P. Friend, *J. Chem. Phys.*, **26**, 680 (1957).

(93) A. S. Doolidge, *J. Amer. Chem. Soc.*, **52**, 1874 (1930).

(94) A. Almenningen, O. Bastiansen, and T. Motzfeldt, *Acta Chem. Scand.*, **23**, 2848 (1969).

(95) I. Nahringbauer and G. Larsson, *Ark. Kemi*, **30**, 91 (1969).

(96) J. Housty and M. Hospital, *Acta Crystallogr.*, **18**, 753 (1965).

(97) J. Housty and M. Hospital, *Acta Crystallogr.*, **20**, 325 (1966).

(98) M. Atoji and W. N. Lipscomb, *Acta Crystallogr.*, **6**, 770 (1953).

(99) M. Hospital and J. Housty, *Acta Crystallogr.*, **20**, 368 (1966).

(100) M. Hospital and J. Housty, *Acta Crystallogr.*, **20**, 626 (1966).

(101) D. R. Davies and R. A. Pasternak, *Acta Crystallogr.*, **9**, 334 (1956).

(102) E. M. Ayerst and J. R. C. Duke, *Acta Crystallogr.*, **7**, 588 (1954).

(103) R. S. Bradley and T. G. Cleasby, *J. Chem. Soc.*, 1681 (1953).

(104) J. Ladell and B. Post, *Acta Crystallogr.*, **7**, 559 (1954).

(105) M. Davies, A. H. Jones, and G. H. Thomas, *Trans. Faraday Soc.*, **55**, 1100 (1959).

(106) J. L. Katz and B. Post, *Acta Crystallogr.*, **13**, 624 (1960).

(107) M. Davies and A. H. Jones, *Trans. Faraday Soc.*, **55**, 1329 (1959).

(108) L. L. Shipman and R. E. Christoffersen, *J. Amer. Chem. Soc.*, **95**, 1408 (1973).

(109) Williams[8] did not introduce charges on the hydrocarbon molecules, and we have also found their contribution to these molecules to be insignificant.

(110) N. C. Parsonage and R. C. Pemberton, *Trans. Faraday Soc.*, **63**, 311 (1967).

(111) V. V. Nanchitel and K. V. Mirskaya, *Sov. Phys. Crystallogr.*, **16**, 891 (1972).

(112) M. Oobatake and T. Ooi, *Progr. Theor. Phys.*, **48**, 2132 (1972).

Intermolecular Potentials from Crystal Data. IV. Application of Empirical Potentials to the Packing Configurations and Lattice Energies in Crystals of Amino Acids[1]

F. A. Momany,[2a] L. M. Carruthers, and H. A. Scheraga*[2b]

Department of Chemistry, Cornell University, Ithaca, New York 14850, and Department of Biophysics, Weizmann Institute, Rehovoth, Israel (Received December 11, 1973)

Previously derived empirical intermolecular potentials are used to compute the minimum-energy packing configurations and binding energies of crystals of various amino acids. The total potential energy function includes contributions from electrostatic, dispersion, nonbonded repulsion, and hydrogen-bonding interactions. The heavy atoms of the individual molecules in the unit cell are treated as rigid bodies, with no internal degrees of freedom. The positions of hydrogens on methyl, amino, hydroxyl, and carboxyl groups were allowed to vary by rotating each of these groups about the bond connecting it to the rest of the molecule. The intermolecular barriers to such rotations are computed and compared with experimental data. The positions of all other hydrogens were obtained by the procedure of the previous paper. The minimum-energy lattice constants are in good agreement with experimental values. The results indicate that these intermolecular potentials will be applicable to the computation of the conformations of polypeptides and proteins.

I. Introduction

In the previous paper[3] (paper III), the parameters of an empirical potential energy function were obtained; they were used to compute energy-minimized lattice constants and binding energies, and the results were compared to experimental data for crystals of aliphatic and aromatic hydrocarbons, heterocyclic compounds, carboxylic acids, amines, and amides. In this paper, we test this empirical energy function further, by using it to carry out similar calculations on crystals of amino acids. The molecules treated here were selected on the basis of the following three criteria. (1) The crystals should not contain halogen atoms (e.g., hydrobromides, etc.) or water (hydrates) since, in both cases, these additional moieties would have to be treated as independent bodies, thereby complicating the computations unnecessarily. (2) Zwitterion structures could be included, with the assumption (subsequently found here to be a valid one) that the nonbonded potentials obtained previously[3] from uncharged molecular species could be transferred to molecules having charged groups, and that the electrostatic interactions could be computed from the molecular orbital partial atomic charges [CNDO/2 (ON)] for all atoms, including the charged groups. (3) The geometry obtained from the experimental X-ray (or neutron) diffraction data had to be reasonable, the same criterion applied earlier;[3] i.e., there should be no abnormal[4] bond lengths or bond angles (suggesting strain or poor crystal refinement) in the crystal structure. A number of different amino acids satisfied these conditions, and were chosen for study here. They are α-, β-, and γ-glycine, perdeuterio-α-glycylglycine, N-acetylglycine, L-alanine, L-glutamine, L-glutamic acid, L-aspartic acid, L-threonine, L-tyrosine ethyl ester, N-acetyl-N'-methyl-L-prolineamide, glycyl-L-asparagine, and diketopiperazine. While this group does not include an example of each type of amino acid, it is felt that it contains sufficient diversity to enable us to verify that our empirical intermolecular potentials[3] are applicable to amino acid crystals.

A preliminary report on calculations similar to these has already been presented.[5] Ferro and Hermans[6,7] have also carried out computations on several heteroatomic molecular crystals[6] to obtain parameters for empirical energy functions, and have applied their parameters to study the crystal packing of two dipeptides.[7] Their results will be compared with ours in the Discussion section.

II. Procedure

The potential functions, parameters, positions of hydrogen atoms, and the procedure for minimizing the energy of a crystal are the same as those of paper III.[3] Rotatable groups containing hydrogen atoms (viz., $-NH_3^+$, $-CH_3$, and $-OH$) were rotated or placed in their conformations of lowest crystal energy (keeping the heavy-atom geometry and lattice constants fixed at their experimental values) prior to the minimization of the energy of the crystal. Then, the lattice constants were varied, with the rotatable groups fixed in their predetermined intermolecular minimum-energy conformations. The molecules were treated as rigid bodies, except for the rotations of hydrogens mentioned above.

The nonbonded and general hydrogen bond (GHB) parameters are those given in Tables IV and V, respectively, of paper III.[3] The atom types (designated by subscripts) are described in Table I of paper III.[3] In particular, N_{15} in the $-NH_3^+$ group is treated as an N_{13} type nitrogen, while atom types C_9, C_{10}, C_{11}, and O_{19} were assumed to be similar to types C_6, C_8, C_7, and O_{18}, respectively. The use of separate designations of these new atom types (N_{15}, C_9, C_{10}, C_{11}, and O_{19}) was based on the possibility that they might differ in atomic polarizability or in repulsive interactions from N_{13}, C_6, C_8, C_7, and O_{18}, respectively. However, during the course of this study, such differences did not emerge, and we retained the nomenclature of Table I of paper III[3] simply to call attention to the chemical differences in these atoms.

The partial atomic charges are those obtained from the CNDO/2 (ON) molecular orbital method; they were computed for the molecules studied here, using the experimental heavy-atom coordinates, together with the positions of hydrogens which were determined as described in paper

TABLE I: Parameters for $H_2 \cdots O_{18}$ General Hydrogen Bond Potential[a]

Donor and acceptor atoms	$A'_{H_2 \cdots O_{18}}$, kcal $Å^{12}$/mol	$B_{H_2 \cdots O_{18}}$, kcal $Å^{10}$/mol	r_{min},[b] Å	U_{min},[c] kcal/mol
$H_2 \cdots O_{18}$	5890	2624	1.64	-3.09

[a] The crystals used to test this set of parameters were L-threonine and L-aspartic acid. [b] $r_{min} = (1.2 \, A'/B)^{1/2}$, and is the value of $r_{H_2 \cdots O_{18}}$ at which U_{min} occurs. [c] $U_{min} = -0.067 \, B^6/A'^5$; it is the lowest value of the GHB energy, and occurs at r_{min}.

III.[3] The CNDO/2 (ON) partial charges of the isolated glycine molecule (obtained by rotating the $-NH_3^+$ and COO^- groups) were examined in order to investigate the effect of conformation on the partial charges of the atoms of these groups; an average charge for each atom (averaged over several conformations) was assigned.[8,9]

Aside from the partial charges for the dipolar ions (zwitterions), the only required parameters not given previously in paper III[3] are the repulsive term, $A'_{H_2 \cdots O_{18}}$, and the attractive term, $B_{H_2 \cdots O_{18}}$, of the GHB potential of eq 8 of paper III[3] for the $H_2 \cdots O_{18}$ interaction. The parameters for this potential were taken directly from McGuire, et al.,[10] and are reported in Table I. Since small variations in $A'_{H_2 \cdots O_{18}}$ did not improve the fit to the experimental lattice constants of threonine or aspartic acid, the parameters of the $H_2 \cdots O_{18}$ GHB potential (which indicate that this hydrogen bond is a relatively weak one) were kept at those shown in Table I.

The reader is referred to the original X-ray and neutron diffraction papers for discussion of the atoms in closest contact in each crystal; these play an important role in determining the crystal configuration and the binding energy.

The nomenclature used here is that recommended by an international commission.[11]

III. Results

A. α-, β-, and γ-Glycine. Three polymorphic forms of crystalline glycine are known, and have been studied by X-ray diffraction methods. The ordinary form, α, crystallizes readily by slow evaporation of neutral aqueous solutions.[12] The β form[13] crystallizes by adding ethyl alcohol to a concentrated aqueous solution of glycine; these crystals readily transform into the α form in moist air, and must be kept in a dry atmosphere in order to obtain diffraction patterns. The third form, γ-glycine,[14] is crystallized by slow cooling of aqueous solutions of glycine made acidic with acetic acid or basic with ammonium hydroxide; the γ form is also obtainable by appropriate treatment of the β form with water. The γ-glycine crystal is strongly piezoelectric along the c axis and has trigonal (i.e., P_{3_2}) crystal symmetry. Glycine is in the zwitterion form in all three crystals, and the bond lengths and bond angles in the three molecules are nearly identical. The differences between these three crystalline forms of glycine are primarily in the three-dimensional frameworks of their hydrogen bonds, there being differences of only several degrees in their internal conformations (dihedral angles).

The CNDO/2 (ON) partial charges and the molecular structures of the three polymorphic forms of glycine are shown in Figure 1 (A-C). In order to position the tetrahedrally arranged $-NH_3^+$ hydrogens, the heavy-atom coordinates and the lattice constants were held fixed at their experimental values, and the binding energy of the crystal of each polymorphic form was calculated at 10° intervals in
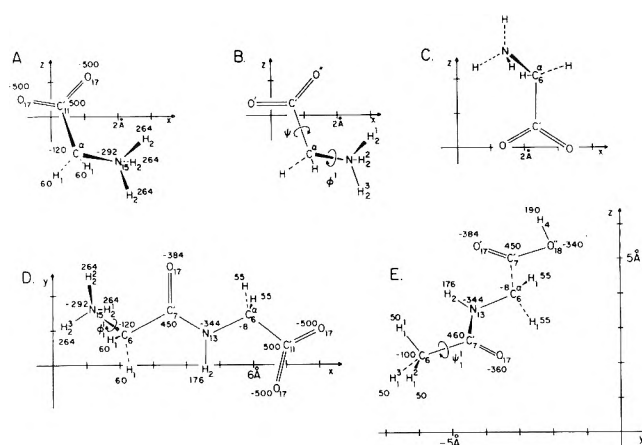
Figure 1. The CNDO/2 (ON) partial charges (in electronic units × 1000) for α-glycine (A) [β- and γ-glycine (B and C) have the same charges], glycylglycine (D), and N-acetylglycine (E).
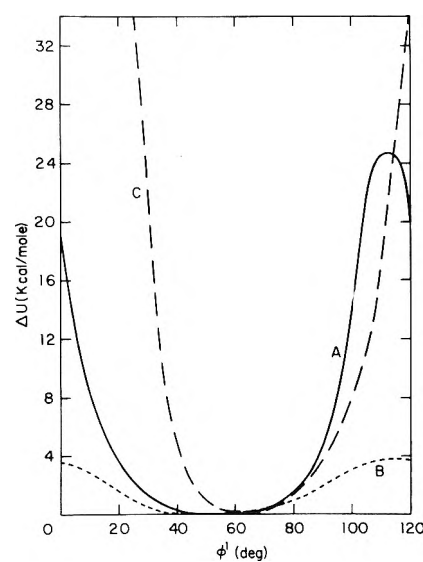
Figure 2. Dependence of the binding energy of the crystal on ϕ^1 (see Figure 1B for definition of ϕ^1) for fixed positions of all other atoms of α-, β-, and γ-glycine (curves A, B and C, respectively). The energy was normalized to zero at the lowest value for each crystal.

the dihedral angle ϕ^1 (defined in Figure 1B) for rotation of only the $-NH_3^+$ hydrogens about the $C'C^\alpha-NH_3^+$ bond. The calculated dependence of the binding energy on ϕ^1 is shown in Figure 2. All three glycine crystals show broad low-energy regions in ϕ^1 with the minimum near 60° (i.e., the staggered conformation). This minimum-energy position of the $-NH_3^+$ group agrees with a recent neutron-diffraction result for α-glycine[15] in which a nearly perfect staggered conformation for the $-NH_3^+$ protons was found. The differences between the polymorphic forms manifest themselves as the $-NH_3^+$ is rotated out of the minimum-energy region. For example, α-glycine appears to have an intermolecular barrier to rotation of ~25 kcal/mol, while the β form has one of only ~4 kcal/mol. The computed barrier of the β form may be compared with some experimental values[16] (viz., 8.0 and 6.1 kcal/mol) found for the rotation of the $-NH_3^+$ group in crystals of β-alanine and glycine, respectively, from nmr measurements of line width at various temperatures. However, the value for α-glycine agrees more closely with the barrier obtained from neutron

TABLE II: Intermolecular Hydrogen Bond Lengths in Glycine Crystals

| | Bond length,[a] Å | | | | | |
| | $r_{H_2}{}^1 \cdots O$ | | $r_{H_2}{}^2 \cdots O$ | | $r_{H_2}{}^3 \cdots O$ | |
Crystal	Exptl[b]	Calcd[c]	Exptl[b]	Calcd[c]	Exptl[b]	Calcd[c]
α-Glycine[d]	1.793	1.899	1.867	1.891	2.137	2.137
β-Glycine	2.177	2.198	1.846	1.866	1.775	1.885
γ-Glycine[e]	1.986	1.969	1.896	1.919	1.813	2.023

[a] $r_{H_2}{}^1 \cdots O$ is the distance from the H^1 atom of the $-NH_3{}^+$ group to its nearest oxygen in the crystal for $\phi^1 = 60°$. Similarly for $r_{H_2}{}^2 \cdots O$ and $r_{H_2}{}^3 \cdots O$. (H^1 is the hydrogen having the smallest positive dihedral angle ψ.) [b] From the X-ray data for the heavy atoms (with our hydrogen geometry) and the experimental lattice constants. [c] Computed by minimizing the energy of the crystal as a function of lattice constants; these are the minimum-energy values. [d] These distances differ slightly (i.e., by ~0.04 Å) from those found in ref 15 because of our choice of an N–H distance of 1.00 Å, and the tetrahedral geometry about the $-NH_3{}^+$ group. [e] In γ-glycine, the nitrogen atom is surrounded by five oxygen atoms at short distances. We have listed only three distances for comparison with the α and β structures, which have a fourth close oxygen that is not considered by us as a hydrogen-bonding oxygen.

scattering librational frequencies (viz., 20 ± 7 kcal/mol for rotation of the $-NH_3{}^+$ group in crystalline L-alanine[17]).

It is not clear why these differences in barriers to rotation in the α and β forms occur, since the environment of the oxygens surrounding the $-NH_3{}^+$ group is somewhat similar in each polymorphic form (see Figure 5 of ref 14 for a stereoscopic representation of the hydrogen-bond projections). In Table II, where the hydrogen bond lengths (H⋯O) for $\phi^1 = 60°$ are listed, it appears that there are two short and one slightly longer hydrogen bonds in each crystal, the two shortest being nearly linear with respect to the N–H⋯O atoms (see Table 6 of ref 13). The longer the H⋯O distance, the weaker is the hydrogen bonding. A fourth oxygen is located near the $-NH_3{}^+$ group, but we do not consider it to be involved in the hydrogen bonding because of its small N–H⋯O angle. Both the experimental and calculated values indicate that there are hydrogen bonds of nearly the same length in each crystal, but this does not account for the difference in barrier to rotation of the $-NH_3{}^+$ group between crystals. The answer must lie in the total packing arrangement, and not just in the hydrogen-bonding environment. In fact, in both α- and β-glycine, the two shortest hydrogen bonds hold the nearly flat molecules [the O'O''C'C$^\alpha$N atoms being nearly coplanar, and ψ (defined in Figures 1B) being ~19° in α-glycine and 25° in β-glycine] together to form extended sheets (see Figure 7 of ref 13). On the other hand, γ-glycine, although having bond lengths and bond angles that are nearly identical with those of the α and β structures, packs very differently in the crystal. For example, the dihedral angle ψ is slightly smaller (viz., 13° in γ-glycine), making the molecule flatter, and the environment of the oxygens around the $-NH_3{}^+$ group is nearly tetrahedral for three oxygens, but two other oxygens are also close to the $-NH_3{}^+$ group. Table II shows the near equivalence of the hydrogen-bond lengths of the three closer oxygens. The packing arrangement of γ-glycine (i.e., P_{32} crystal symmetry) shows a threefold screw axis parallel to the c axis with the successive molecules being held together by lateral hydrogen bonds, rather than the sheets found for the α and β forms. These packing differences must be the cause of the differences in barrier heights shown in Figure 2.

Experimentally, γ-glycine crystals change irreversibly into α-glycine crystals upon heating to ~165°,[18] and the estimated[18] heat of transition is ~600 cal/mol. The β form changes into the α form by heating to ~100° or by grinding or mechanical shock, and may change into the γ form in the presence of water vapor. The experimental results on the α and β forms correlate well with our calculated binding energies (see Table III) where we find the difference in energy between the α and β forms to be ~1.5 kcal/mol. However, the difference in binding energy between the β

and γ forms is found to be ~13 kcal/mol. This large difference arises from electrostatic interactions in the γ form. The total contribution to the binding energy from the nonbonded and GHB interactions is very close for the α, β, and γ forms. However, the electrostatic contribution of the γ form is ~12 kcal less negative than that of the α and β forms. The origin of this large difference is not understood, but may arise from the manner in which the threefold screw-axis packing brings five oxygen atoms together (at O⋯O distances of 3.20, 3.33, 3.47, 3.99, and 4.01 Å, respectively) leading to a large repulsive electrostatic contribution, which is not compensated for by the three close $H_2 \cdots O_{17}$ attractive electrostatic interactions.

The reasonableness of the CNDO/2 (ON) partial charges of the glycine molecule is indicated by the fact that the calculated dipole moment of glycine [computed here from CNDO/2 (ON) charges to be 10 D] agrees moderately well with that found from experimental data for glycine in water, viz., 13 D.[19]

Table III shows that the energy-minimized lattice constants and volumes are in excellent agreement with the experimental values for the three glycine crystals, being at most ~5% larger in volume. In minimizing the energy of the γ-glycine crystal, the lattice constants a and b were allowed to vary independently. However, it can be seen in Table III that they did not deviate to any great extent from the experimental values; thus, the P_{32} symmetry was retained very closely. This is the only crystal treated in these two papers,[3] for which this relaxation of the crystal symmetry requirement was allowed in the energy minimization process.

At first sight, our computed binding energy of -26 kcal/mol for α-glycine seems to be much smaller than the value of -103 kcal/mol, computed by Shimura[20] using data on the free energy of hydration of glycine. Shimura's value[20] would be a reasonable one if unit positive and negative charges were located on the N and O atoms, respectively, giving rise to a large electrostatic contribution to the binding energy. However, as shown in Figure 1A, the results of the CNDO/2 method suggest that unit charges are not localized on the N and O atoms; instead, the charges are spread out over the molecule in such a way as to reduce the electrostatic contribution to the binding energy. Thus, our value of -26 kcal/mol (for a process in which a molecule in the gas phase, carrying the charge distribution of Figure 1A, is transferred to the crystal, without a change in the charge distribution) might be expected to be closer to the value expected if uncharged molecules were transferred from the gas phase to the crystal, where they remain uncharged. While we cannot calculate the change in energy for such a process because we do not know how uncharged molecules would pack in a crystal, we cite the estimate of

TABLE III: Results for Amino Acids

| Molecule	Author	Space group	Discrepancy index R,[a] %	No. of molecules per unit cell	Cell[b] index	a, Å / Δa[c], Å	b, Å / Δb[c], Å	c, Å / Δc[c], Å	α deg / Δα[c] deg	β deg / Δβ[c] deg	γ deg / Δγ[c] deg	V, Å³ / ΔV[c], Å³	σ,[d] Å	Binding energy U_calcd, kcal/mol	r_H...O[exptl,e], Å / Δr_H...O[calcd], Å	r_H...O[exptl,e], Å / Δr_H...O[calcd], Å
α-Glycine	Exptl[f]	$P2_1/n$	6.3	4	212	5.10	11.97	5.46	90.0	111.7	90.0	309			1.86	2.14
	This work					0.03	0.13	0.12		−0.6		13	0.10	−25.8	0.03	0.00
β-Glycine	Exptl[g]	$P2_1$	4.6	2	222	5.08	6.27	5.38	90.0	113.2	90.0	157			1.85	2.17
	This work					0.02	0.06	0.14		−1.4		8	0.09	−24.3	0.03	0.03
γ-Glycine	Exptl[h]	$P3_2$	10.8	3	222	7.04	7.04	5.48	90.0	90.0	120.0	235			1.81	1.99
	This work					0.02	0.06	0.21				9	0.13	−11.2	0.21	−0.02
Glycylglycine	Exptl[i]	$P2_1/c$	6.0	2	222	9.43	9.56	7.83	90.0	124.9	90.0	580			1.85	2.03
	This work					0.08	0.18	−0.07		0.2		8	0.12	−38.9	0.08	0.05
N-Acetylglycine	Exptl[j]	$P2_1/c$	6.5	4	311	4.86	11.54	14.63	90.0	138.2	90.0	542			1.57	2.09
	This work					−0.10	−0.25	0.21		0.0		−8	0.20	−23.8	0.12	−0.12
L-Alanine	Exptl[k]	$P2_12_12_1$	4.9	4	212	6.03	12.34	5.78	90.0	90.0	90.0	430			1.94	1.84
	This work					0.03	0.00	0.14				14	0.08	−26.0	0.02	0.04
L-Glutamine	Exptl[l]	$P2_12_12_1$	12.0	4	122	16.01	7.76	5.10	90.0	90.0	90.0	634			1.94	2.12
	This work					0.11	0.04	0.14				17	0.10	−31.1	0.03	0.03
L-Glutamic acid	Exptl[m]	$P2_12_12_1$	16.0	4	212	5.17	17.34	6.95	90.0	90.0	90.0	624			1.93	1.58
	This work					0.02	0.24	0.09				18	0.18	−35.1	0.02	0.11
L-Aspartic acid	Exptl[n]	$P2_1$	4.0	2	222	7.62	6.98	5.14	90.0	99.8	90.0	269			1.90	1.58
	This work					0.08	0.11	0.05		1.1		9	0.08	−33.4	0.00	0.09
L-Threonine	Exptl[o]	$P2_12_12_1$	11.2	4	122	13.61	7.74	5.14	90.0	90.0	90.0	541			1.92	1.72
	This work					−0.13	0.07	0.02				7	0.09	−29.1	0.01	−0.04
L-Tyrosine ethyl ester	Exptl[p]	$P2_12_12_1$	14.1	4	212	12.79	16.98	5.28	90.0	90.0	90.0	1145			1.80	
	This work					0.04	−0.15	0.14				25	0.12	−30.3	0.02	0.15
Ac-Pro-amide	Exptl[q]	$P2_12_12_1$	9.8	4	212	9.74	13.20	7.17	90.0	90.0	90.0	922			1.90	
	This work					−0.13	−0.04	0.29				21	0.18	−19.1	0.04	
Gly-L-asn	Exptl[r]	$P2_12_12_1$	16.3	4	311	4.81	12.85	13.52	90.0	90.0	90.0	837			1.89	2.15
	This work					0.08	−0.07	−0.15				−3	0.11	−35.9	0.06	0.02
Diketopiperazine	Exptl[s]	$P2_1/a$	7.2	2	213	5.23	11.55	3.98	90.0	98.0	90.0	238			1.85	1.85
	This work					0.02	0.21	0.10		−0.4		11	0.12	−19.7	0.08	0.08

[a] The discrepancy index (taken from the experimental papers) is defined as $R(\%) = \{\Sigma|F_o - F_c|/\Sigma|F_o|\}100$ where the F's are the experimentally observed and calculated structure factors. [b] The cell index describes the number of unit cells taken in our calculation (in addition to the cell containing the 0th molecule) along the unit cell axis, a, b, and c, respectively. [c] The Δ's are defined as $\Delta l = l_{calcd} - l_{obsd}$, where $l = a$, b, c, α, β, γ, and V (volume of a unit cell). [d] σ is defined as $\sigma = [(1/N)\Sigma_{i=1}^{N}(l_i^{calcd} - l_i^{obsd})^2]^{1/2}$ where the l_i's run over the N lattice parameters, a, b, and c and the angles that have been varied. [e] The values listed are for $H_2\cdots O_{11}$ distances, except for N-acetylglycine, L-glutamic acid, and L-aspartic acid, where the smallest value of $r_{H\cdots O}$ is for an $H_4\cdots O_{11}$ distance. [f] Reference 12. [g] Reference 13. [h] Reference 14. [i] Reference 22. [j] Reference 26. [k] Reference 28. [l] Reference 29. [m] Reference 30. [n] Reference 31. [o] Reference 32. [p] Reference 33. [q] Reference 34. [r] Reference 35. [s] Reference 36.

−21 to −25 kcal/mol, made by Takagi, *et al.*,[21] for this process. Takagi, *et al.*,[21] also report a value of 31 kcal/mol for the heat of sublimation of glycine, and they attribute this value to the transfer of a zwitterion in the crystal to the uncharged state in the gas phase. While one might question the charge distribution reported in Figure 1A, we would not expect it to be so much different from the one shown there so as to lead to a very large electrostatic energy and hence a very large binding energy, as found in ionic crystals. The relatively low binding energy, computed here for glycine, is compatible with similar values found for the other crystals listed in Table III.

B. Perdeuterio-α-glycylglycine. The structure of perdeuterio-α-glycylglycine[22] was chosen because both X-ray[23,24] and neutron[22,25] diffraction results are available for this molecular crystal. The deuterium atoms were treated as normal hydrogens in the calculations reported here since the structure is the same in both cases,[22-25] *i.e.*, the calculations were performed for the hydrogenated rather than the deuterated molecule. The CNDO/2 (ON) partial charges and molecular structure (for the zwitterion form) are shown in Figure 1D. As found for the glycine crystals, the staggered conformation of the $-NH_3^+$ group was found to be the one of lowest energy. This result is shown in Figure 3 together with the variation in the lengths of two hydrogen bonds (*i.e.*, $H_2^1 \cdots O_{17}$ and $H_2^2 \cdots O_{17}$) with dihedral angle. The third hydrogen bond distance follows curve B very closely, and is not shown. The calculated barrier to rotation (for ϕ_1^1) in this crystal is only ~2.5 kcal/mol, somewhat lower than that found experimentally (8.0 kcal/mol) for β-alanine[16] and considerably lower than that (20 kcal/mol) found by neutron scattering.[17] The position at which the energy is a minimum corresponds to a conformation in which the hydrogen-bond lengths are of nearly equal value. The results of the neutron diffraction work[22,25] indicate that the $-NH_3^+$ group ($-ND_3^+$ in their studies) has nearly tetrahedral geometry (the CNH bond angles being 106–111°), and a conformation[25] with $\phi_1^1 \approx 72°$. The difference between this observed value and our calculated value of 60° may be due to some intramolecular interactions not included here. This result confirms our use of tetrahedral geometry for the $-NH_3^+$ group.

The energy-minimized lattice constants are in excellent agreement with experimental results, as given in Table III. The computed binding energy of −39 kcal/mol is ~13 kcal/mol more negative than that for α-glycine, suggesting that the $CONHCH_2$ moiety contributes ~−13 kcal/mol to the binding energy.

C. N-Acetylglycine. The CNDO/2 (ON) partial charges and molecular structure of *N*-acetylglycine[26] are shown in Figure 1E. In the crystal structure analysis,[26] the hydrogen atoms of the methyl group of the acetyl moiety were found to be in a disordered or random conformation (*i.e.*, they exhibited large thermal amplitudes of libration). The other hydrogens were partially observed in the X-ray study, and the carboxyl hydrogen was found to be in the trans (*i.e.*, H trans to C^α) position as shown. Before minimizing the energy of this structure, the rotation of the methyl group was examined to see if it had a preferred conformation. Figure 4 (curve A) shows how the binding energy of the crystal varies with the dihedral angle for rotation of the methyl group. The dihedral angle ψ_1^1 is that for rotation about the $H^1C-C'N$ bond (see Figure 1E), and thus the energy minimum at 60° corresponds to a conformation in which a hydrogen is cis to the carbonyl oxygen. This result is in excel-
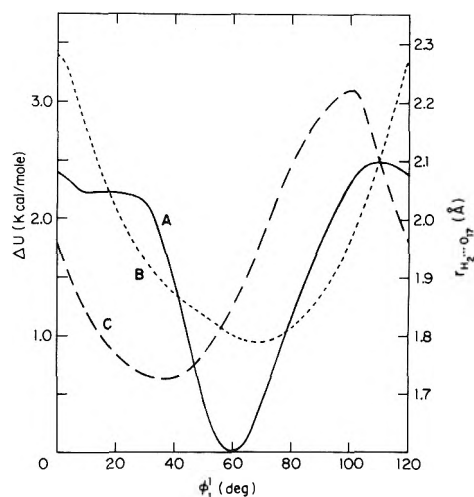
Figure 3. Dependence of the binding energy of the crystal and hydrogen-bond distance on ϕ_1^1 for fixed positions of all other atoms of α-glycylglycine. The energy (solid line, curve A) was normalized to zero at the lowest value. Curves B and C represent the variation of the $H_2^1 \cdots O_{17}$ and $H_2^2 \cdots O_{17}$ distances, respectively, with ϕ_1^1 (see Figure 1D).
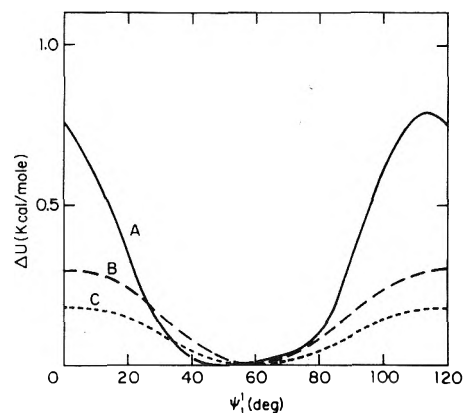
Figure 4. Dependence of the binding energy of the crystal (curve A) on ψ_1^1 for fixed positions of all other atoms of *N*-acetylglycine. Curve B is an extended Hückel energy for the same rotation but for the isolated molecule. Curve C is the same as B but from a CNDO/2 calculation. The energy was normalized to zero at the lowest value for each curve.

lent agreement with those of previous molecular orbital calculations on *isolated* model amides,[27] which are also shown in Figure 4 (curves B and C). The barrier to rotation about the $H^1C-C'N$ bond is small, both for the isolated molecule (~0.25 kcal/mol, intramolecular[27]) and for the molecule in the crystal (~0.75 kcal/mol, intermolecular). This implies that there is probably a very large librational motion of the methyl group at room temperature, and agrees with the X-ray observations and conclusions[26] that the methyl groups are in a random array at room temperature.

The energy-minimized lattice constants and binding energy are given in Table III. The fit to the observed lattice constants is reasonably good, even though the hydrogen-bond lengths increased to 1.69 Å for the $H_4 \cdots O_{17}$ interaction and decreased to 1.97 Å for the amide $H_2 \cdots O_{17}$ interaction. The binding energy of ~−24 kcal/mol can again be used to estimate the contribution of a glycine peptide group to the total energy, by subtracting out the value for acetic acid (*viz.*, ~−14 kcal/mol[3]). The result, ~−10 kcal/mol contribution to binding from the $CONHCH_2$ moiety, is in reasonable agreement with the value (~13 kcal/mol) found

above from α-glycylglycine, considering that the energy depends on the different packing patterns for the different molecules.

To conclude the consideration of glycine residues, it can be seen that the data obtained by energy minimization techniques are in agreement with the experimental lattice constants, hydrogen bonding, hydrogen positions, and intermolecular torsional barriers, and the zwitterion can be treated equally as well as the uncharged species by this technique.
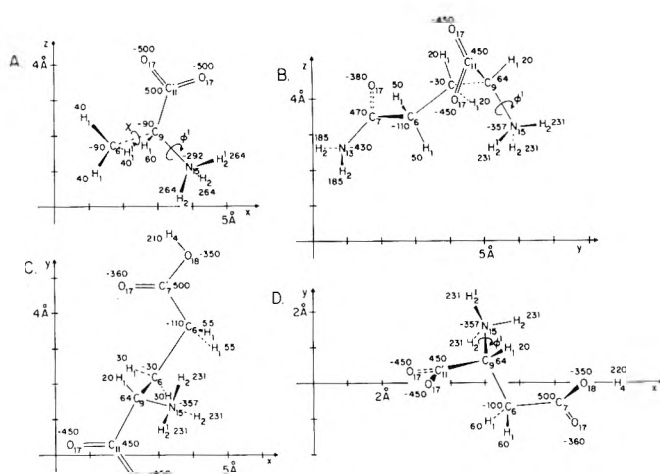
D. L-Alanine. The CNDO/2 (ON) partial charges and molecular structure of L-alanine[17,28] are shown in Figure 5A. In this structure,[28] both the side-chain methyl group and the $-NH_3^+$ end group must be rotated about their respective bonds defined by the pertinent heavy atoms in order to find the best packing arrangement. The binding energy of the crystal was calculated in 10° increments between $\phi^1 = 40$–$90°$ and $\chi = 40$–$80°$, holding the coordinates of the heavy atoms and the lattice constants fixed at the observed X-ray values. The low energy positions were found to be $\phi^1 \approx 50$–$60°$ and $\chi \approx 60$–$70°$. Since the complete ϕ^1, χ space was not examined, it was not possible to compare the barriers to rotation with those found by neutron scattering.[17] The computed torsional angles do, however agree with those found by Lehmann, *et al.*[17] ($\phi^1 = 58°$; $\chi = 58°$), and values of $\phi^1 = 50°$ and $\chi = 70°$ were used in the energy minimization.

The energy-minimized lattice constants, binding energy, and hydrogen bond lengths are given in Table III; these agree well with the observed values.[28] The calculated binding energy of L-alanine is only ~ 0.2 kcal/mol lower than that of α-glycine. Since the volume of the unit cell is larger for L-alanine, it appears that the added methyl side chain interferes with the very closely packed arrangement found in α-glycine, and tends to make the packing between molecules somewhat looser. For this reason, the additional nonbonded contribution to the energy, resulting from the methyl group, is compensated for by a reduction in binding energy because of the more loosely packed structure.

E. L-Glutamine. The CNDO/2 (ON) partial charges and molecular structure of L-glutamine[29] are shown in Figure 5B. This molecule has one rotatable $-NH_3^+$ group; the side-chain amide hydrogens were placed in the plane defined by the heavy atoms (N–C(=O)C) and were not rotated in this study, because of the high barrier to rotation about the amide bond.[27] The value of ϕ^1 of lowest energy was $\phi^1 \approx 80°$, and the barrier to rotation was only ~ 5 kcal/mol in this case.

The energy-minimized lattice constants and binding energy are given in Table III. The fit to the observed lattice parameters is again very good. The binding energy (-31 kcal/mol) is only 5 kcal/mol more negative than that of alanine, and would appear to be somewhat less than would be expected for the increased number of possible hydrogen-bonding atoms. However, the hydrogen bond lengths (shown in Table III) of L-glutamine appear to be somewhat longer and weaker than those found in alanine (which is consistent with the low barrier to rotation of the NH_3^+ group), indicating a looser packing arrangement and, consequently, a lower crystal energy than might otherwise be expected.

F. L-Glutamic Acid. The CNDO/2 (ON) partial charges and molecular structure of L-glutamic acid[30] are shown in Figure 5C. As described previously, the $-NH_3^+$ group was rotated in 10° increments to its position of minimum lat-

Figure 5. The CNDO/2 (ON) partial charges (in electronic units $\times$ 1000) for L-alanine (A), L-glutamine (B), L-glutamic acid (C), and L-aspartic acid (D).

tice energy, which is $\phi^1 \approx 40°$ in this molecule. The barrier to rotation was ~ 3.2 kcal/mol in this crystal.

The side-chain acid group was taken to be uncharged, in accordance with the experimental conclusions,[30] and the carboxyl hydrogen was taken to be in the trans conformation (*i.e.*, H trans to C^γ).[30] The carboxyl hydrogen forms a short hydrogen bond (*i.e.*, $r_{H_4\cdots O_{17}}^{\text{exptl}} = 1.58$ Å) to a C-terminal COO^- oxygen, while the side-chain carboxyl oxygen forms a hydrogen bond to the $-NH_3^+$ group of another molecule with a normal amide hydrogen bond length ($r_{H_2\cdots O_{17}}^{\text{exptl}} = 1.93$ Å). The two other amide hydrogens form normal hydrogen bonds to different C-terminal COO^- oxygens. The energy-minimized crystal (with lattice constants and crystal energy given in Table III) has an $H_4\cdots O_{17}$ hydrogen-bond length of 1.69 Å, which is in agreement with other carboxylic acids,[3] but is somewhat longer than that (*i.e.*, 1.58 Å) found in the X-ray results used here for L-glutamic acid. The expansion of the energy-minimized cell along the *b* axis probably arises from the elongation of this hydrogen bond, and might possibly be reduced by allowing the side-chain carboxyl hydrogen to be slightly out of the plane of the carboxyl group. However, we have not adjusted the position of this hydrogen.

The overall fit to the observed lattice constants is fairly good. The difference in binding energy between L-glutamine (-31 kcal/mol) and L-glutamic acid (-35 kcal/mol) is primarily due to the more attractive hydrogen-bond energy of the side-chain carboxyl group compared to that of the side-chain amide group.

G. L-Aspartic Acid. The CNDO/2 (ON) partial charges and molecular structure of L-aspartic acid[31] are shown in Figure 5D. The $-NH_3^+$ group was again rotated in 10° increments and the energy of the crystal plotted, as shown in Figure 6. The minimum in the energy was found near $\phi^1 \approx 60°$, with a barrier to rotation of ~ 4 kcal/mol. Two of the intermolecular $H_2\cdots O_{17}$ distances, shown in Figure 6 as a function of ϕ^1, also are shortest near $\phi^1 \approx 70°$ and are nearly equal in $H_2\cdots O_{17}$ length. In the nonstaggered conformation (*i.e.*, $\phi^1 \sim 0°$), an intermolecular $H_2\cdots H_1$ contact distance (H_2 from the 0th molecule, and H_1 from a neighboring molecule) is quite short (2.04 Å), contributing a repulsive energy of ~ 3 kcal/mol which nearly accounts for the value of the barrier near $\phi^1 \sim 0°$.
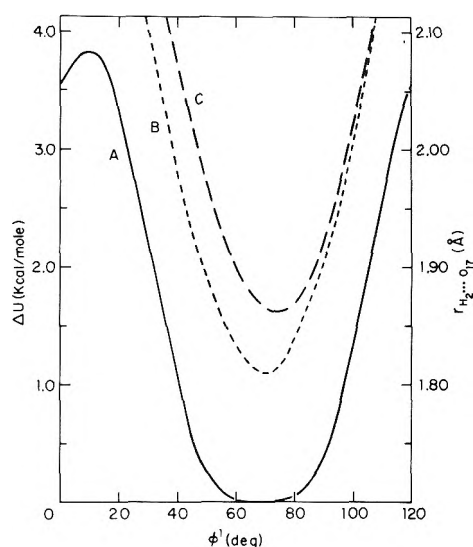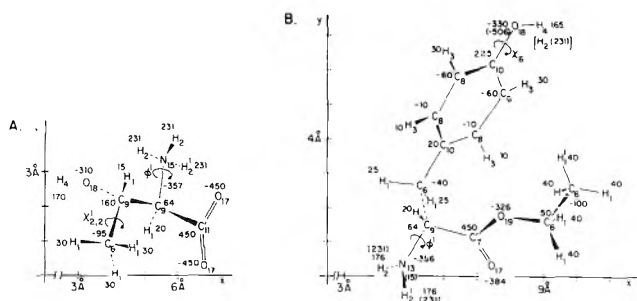
Figure 6. Dependence of the binding energy of the crystal on ϕ^1 for fixed positions of all other atoms of L-aspartic acid. The energy (solid line, curve A) was normalized to zero at the lowest value. Curves B and C represent the variation of $H_2^1 \cdots O_{17}$ and $H_2^2 \cdots O_{17}$ distances, respectively, with ϕ^1 (see Figure 5D).
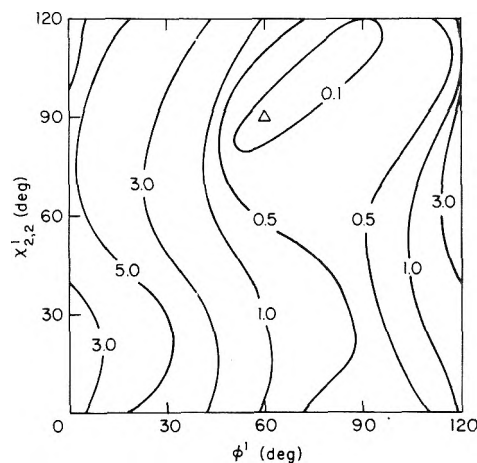

Figure 7. The CONDO/2 (ON) partial charges (in electronic units X 1000) for L-threonine (A) and L-tyrosine ethyl ester (B). The partial charges in parentheses in (B) are for the charged $-NH_3^+$ hydrogen atoms and the O^- of the tyrosyl group. The third $-NH_3^+$ hydrogen (H_2) is attached to the nitrogen, but is shown here near the H_4 hydrogen of the phenolic $-OH$ group.

Figure 8. Dependence of the binding energy of the crystal on ϕ^1 and $\chi_{2,2}^1$ (calculated at 15° intervals in these dihedral angles for fixed positions of all other atoms of L-threonine). The energy was normalized to zero at the minimum, indicated by the triangle. The lines are contours of constant energy, in units of kcal/mol.

The uncharged[31] side-chain carboxyl hydrogen was held in the trans conformation (i.e., H trans to C^β).[31] In this position the calculated length of the intermolecular carboxyl ($H_4 \cdots O_{17}$) hydrogen bond is 1.58 Å, which increases to 1.67 Å when the energy of the crystal is minimized. The energy-minimized data are listed in Table III. The fit to the observed lattice constants is very good. The binding energy is only slightly less than that of L-glutamic acid, indicating that the contribution of the extra side-chain methylene group of glutamic acid is ~1.5 kcal/mol in excellent agreement with trends in methylene energies observed for hydrocarbons and carboxylic acids in paper III.[3]

H. L-Threonine. The CNDO/2 (ON) partial charges and molecular structure of L-threonine[32] are shown in Figure 7A. The two rotatable groups in threonine are the $-NH_3^+$ and side-chain methyl. The hydroxyl hydrogen is taken to be in the extended conformation (i.e., HO trans to $C^\beta C^\alpha$) which allows it to make a very good hydrogen bond (with $r_{H_4 \cdots O_{17}} = 1.74$ Å) to a carboxyl oxygen of another molecule in the crystal (see ref 32). Figure 8 shows the energy of the crystal (with the heavy-atom coordinates and lattice constants held fixed at their experimental values) calculated as a function of both ϕ^1 and $\chi_{2,2}^1$. The position of minimum crystal energy was found at $\phi^1 \sim 60°$, $\chi_{2,2}^1 \sim 90°$. There is a distinct coupling between the two rotating groups, and the energy contours of Figure 8 show some asymmetry, but the coupling energy is relatively weak (the energy would increase by only 0.5 kcal/mol in passing from the minimum-energy conformation to that for which $\phi^1 = 60°$ and $\chi_{2,2}^1 = 60°$). Examination of Figure 8 also shows that the barrier to rotation (along the path of lowest energy for ϕ^1) for the $-NH_3^+$ group is ~5 kcal/mol, while that for rotation of the side-chain methyl group is much less (being only ~0.5 kcal/mol). The conformations found here for these two rotatable groups (viz., $\phi^1 = 60°$ and $\chi_{2,2}^1 = 90°$) correspond to positions of the hydrogen atoms which agree with those estimated from the X-ray data, even though the intramolecular energy could shift the dihedral angles (in particular the methyl group) slightly away from these positions.

The energy-minimized lattice constants and binding energy are given in Table III. The fits to the observed quan-

tities are very good, and the lengths of the hydrogen bonds remain close to the values observed in the X-ray study.

I. L-Tyrosine Ethyl Ester. The CNDO/2 (ON) partial charges and molecular structure of L-tyrosine ethyl ester[33] are shown in Figure 7B. The X-ray diffraction study[33] could not determine whether the amino and side-chain hydroxyl groups are charged or uncharged. The molecular packing is such that the phenolic hydroxyl oxygen of one molecule is very near the amino nitrogen of another molecule, and the positioning of the hydrogens thus becomes crucial. The following procedure was, therefore, used to obtain the positions of the hydrogens. First, the CH_2 hydrogens of the ethyl ester group were positioned by the coordinates of the heavy atoms (as described for methylene hydrogens in paper III[3] of this series), leaving the methyl hydrogens to be placed. The methyl group was then rotated through 120° about the C–C bond, and the binding energy calculated at each 10° in dihedral angle. The position of the hydrogens which had the lowest crystal energy was found to be the staggered conformation (i.e., the dihedral angle for rotation around the $O_{19}C_6–C_6H_1^1$ bond being $\approx 60°$), the barrier to rotation being ~4 kcal/mol. This result was independent of the positions of the $-OH$ or $-NH_3^+$ hydrogens. Second, the phenolic hydroxyl hydrogen was positioned in either of two conformations in the plane of

the phenyl ring (at $\chi_6 = 0$ and $180°$)[9] (the hydrogen was kept in the plane of the ring, since conjugation effects would make this the favored position). For each conformation, the NH_2 group (chosen, in this step, to be planar and with the angle $H-N-C = 120°$) was rotated through $180°$ about the $N-C^\alpha$ bond (*i.e.*, ϕ^1 was varied), and the crystal energy calculated. It was immediately found that the hydroxyl hydrogen had to be positioned as shown in Figure 7 (*i.e.*, at $\chi_6 = 0°$), the second position ($\chi_6 = 180°$) being of very high energy because of steric contacts between the hydroxyl hydrogen and the $-NH_2$ group. It was also obvious that the planar configuration of the amino group was not the preferred one in the crystal, giving a negative, but relatively weak binding energy (*viz.*, -18 kcal/mol) for the conformation shown in Figure 7. The energy-minimized lattice parameters also showed large deviations (*viz.*, $\Delta a = 0.27$, $\Delta b = 0.63$, and $\Delta c = -0.08$ Å) from the experimental data, and it was concluded from this that either the amino group was nonplanar, with the nitrogen forming a hydrogen bond to the hydroxyl hydrogen, or the amino group was charged (*i.e.*, $-NH_3^+$, with the phenolic hydroxyl hydrogen being placed on the amino group). Considering first the possibility that the amino group might be nonplanar, the tetrahedral $-NH_2$ was rotated about the $N-C^\alpha$ bond, but the binding energy and fit to the lattice parameters improved only slightly. Next, the hydroxyl hydrogen was removed, making the phenolic oxygen more negatively charged, and transferred to form the tetrahedral $-NH_3^+$ group [and the CNDO/2 (ON) partial atomic charges were recalculated]. When the $-NH_3^+$ and methyl groups were subsequently rotated, a decided improvement in both the binding energy and fit to the lattice parameters (compared to the previous configurations) was obtained. It thus seems clear that the hydroxyl and amino groups of this crystal are charged. The partial charges shown in parentheses in Figure 7 pertain to the molecule with charged hydroxyl and amino groups. The hydrogen-bonding arrangement is shown in ref 33 and, with the charged groups described above, all three hydrogens on the $-NH_3^+$ group point toward three tyrosyl ring oxygens of other molecules. The energy-minimized lattice constants given in Table III pertain to the charged states of these two groups. The fit to the observed lattice constants is excellent.

J. N-Acetyl-N'-methyl-L-prolineamide. The CNDO/2 (ON) partial charges and molecular structure of N-acetyl-N'-methyl-L-prolineamide[34] are shown in Figure 9. There are no ionizable groups in this molecule. The pyrrolidine ring is puckered, with the γ-carbon atom displaced in the direction of the carbonyl carbon atom of the proline residue. This molecule contains two rotatable methyl groups. The packing arrangement is such that the intermolecular methyl contacts are important, the one weak [*i.e.*, relatively long ($r_{H...O}^{exptl} = 1.90$ Å)] intermolecular amide hydrogen bond being somewhat less important in the crystal packing than in the case of the zwitterion crystals, where extensive hydrogen-bond networks are encountered.

The rotation of the two methyl groups is represented as an energy contour plot in Figure 10. The minimum shown is the lowest-energy position for ϕ_2^1 and ψ_1^1 taken in $30°$ increments. It is clear that the staggered conformations of these methyl groups is favored for ϕ_2^1 (the low-energy path for rotation having a barrier height of ~ 2.0 kcal/mol) and for ψ_1^1 (the barrier height being ~ 1.0 kcal/mol, and the energy difference between $\psi_1^1 = 60°$ and $90°$ being small). This broad low-energy range of ϕ_2^1, ψ_1^1 values implies that
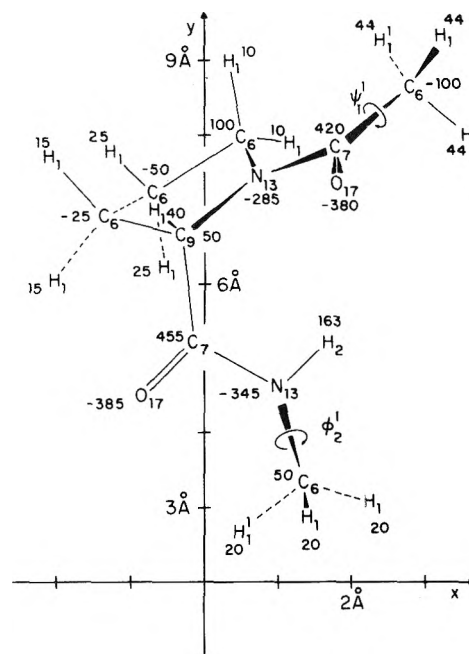

Figure 9. The CNDO/2 (ON) partial charges (in electronic units $\times$ 1000) for N-acetyl-N'-methyl-L-prolineamide.
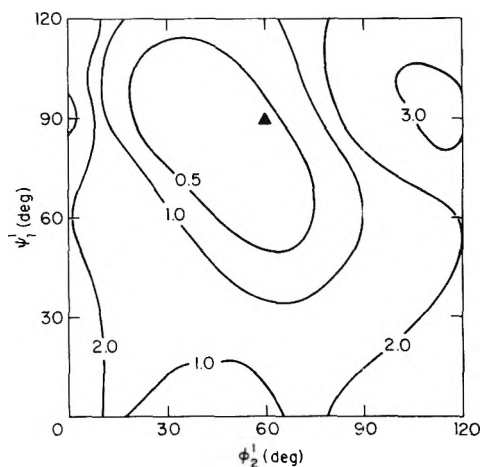

Figure 10. Dependence of the binding energy of the crystal on ϕ_2^1 and ψ_1^1 for fixed positions of all other atoms of N-acetyl-N'-methyl-L-prolineamide. The energy was normalized to zero at the minimum, indicated by the solid triangle. The lines are contours of constant energy in units of kcal/mol.

considerable librational motion should be observed, with the methyl groups preferentially in a staggered conformation (with respect to the backbone atoms).

The energy-minimized lattice constants and binding energy are given in Table III. The fit to the experimental data is fairly good, and the length of the hydrogen bond is maintained close to the observed value.

K. Glycyl-L-asparagine. The CNDO/2 (ON) partial charges and molecular structure of glycyl-L-asparagine[35] are shown in Figure 11. The zwitterionic form is found,[35] the neutral side chain being held in the planar amide conformation, as described for L-glutamine. The $-NH_3^+$ group was allowed to rotate to find the conformation of lowest crystal energy, this being a staggered one with $\phi_1^1 \approx 40°$ and a barrier to rotation of only ~ 2 kcal/mol. The aspara-
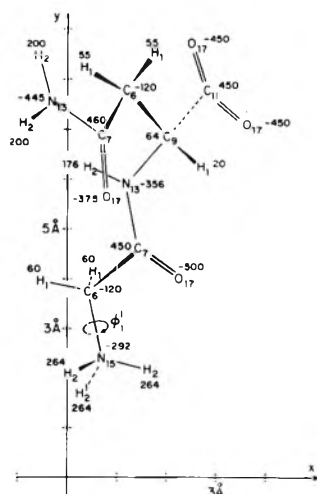
Figure 11. The CNDO/2 (ON) partial charges (in electronic units × 1000) for glycyl-L-asparagine.

gine side chain $-NH_2$ group was fixed by the planar heavy-atom positions and was not allowed to rotate.

The hydrogen-bonding network is extensive in this crystal (the $-NH_3^+$ group having three oxygen neighbors, the amide $-NH$ having one, and the side-chain $-NH_2$ having two), and the $H_2\cdots O_{17}$ distances are all near 1.9 Å. The energy-minimized lattice constants and crystal energy are given in Table III. The fit to the experimental data is very good; in particular the volumes agree exceptionally well. All hydrogen-bond lengths are found to be within 0.1 Å of the values determined with the experimental lattice parameters and our hydrogen geometry.[3]

L. Diketopiperazine. The CNDO/2 (ON) partial charges and molecular structure of diketopiperazine[36] are shown in Figure 12. This cyclic anhydride of glycylglycine is of interest here since its molecular packing has been investigated by computational methods by other authors.[37] Unfortunately, these authors used atomic coordinates which differ from those found experimentally,[36] and they calculated the crystal energy by allowing only for rigid body translation of the molecules, but did not allow the lattice constants to vary; thus, we cannot compare their results directly with ours which are shown in Table IV. Our binding energy of ≈-20 kcal/mol is close to that found by Giacomello and Giglio[37] (viz., -23.6 kcal/mol), and gives ~-10 kcal/mol for the $CONHCH_2$ moiety, in agreement with the results in sections IIIB and C.

We may obtain some indication of the magnitudes of the errors in these calculations on diketopiperazine crystals by comparing the cartesian coordinates (and bond lengths computed therefrom) obtained from the X-ray data with those computed from the unit cell coordinates (converted to cartesian coordinates using the lattice constants of the energy-minimized crystal). The deviations between the experimental and calculated coordinates and bond lengths are given in Table IV, and reflect the deviations in the energy-minimized lattice constants. The interesting point is that the calculated bond lengths agree with the experimental ones within the limits of precision of the X-ray data, and are nearly the same as those given by Giacomello and Giglio[37] in their calculations with different geometry. The values of Δr_{ij} in Table IV (which is an alternative measure of the RMS deviation, $\sigma = 0.12$, of Table III) represent the
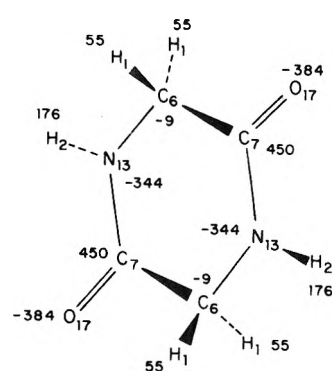

Figure 12. The CNDO/2 (ON) partial charges (in electronic units × 1000) for diketopiperazine.

TABLE IV: Comparison of Experimental and Calculated Cartesian Coordinates and Bond Lengths for Diketopiperazine Crystals

Atom	Deviations in cartesian coordinates,[a] Å			
	$\Delta x \times 10^4$	$\Delta y \times 10^4$	$\Delta z \times 10^4$	Δd^b
C_7	+58	+145	+211	0.026
C_6	+8	−257	−15	0.026
N_{13}	+63	−90	+185	0.021
O_{17}	+108	+276	+394	0.049

Bond length	Bond lengths and deviations, Å			
	r_{ij}^c (obsd)	r_{ij}^d (calcd)	Δr_{ij}^e	Δr_{ij}^f
C_7–C_6	1.499	1.508	0.009	0.030
C_7–O_{17}	1.239	1.253	0.014	0.001
C_7–N_{13}	1.326	1.344	0.018	−0.006
C_6–N_{13}	1.448	1.468	0.020	0.022

[a] Deviation (calculated − observed) between X-ray cartesian coordinates and those obtained using unit cell coordinates and lattice constants found after energy minimization. [b] $\Delta d = (\Delta x^2 + \Delta y^2 + \Delta z^2)^{1/2}$. [c] Reference 36. [d] Calculated using the lattice constants found after energy minimization, and the unit cell coordinates given in ref 36. [e] $\Delta r = r_{ij}$ (calcd) − r_{ij} (obsd). [f] Calculated as in d using data and results of ref 37.

limit of precision that one can expect to obtain from calculations of intermolecular interactions between amino acids, using the potentials presented here.

IV. Discussion

The agreement between the experimental and energy-minimized lattice constants and the initial and final hydrogen-bond lengths and orientations for the amino acid crystals studied here is excellent. Thus, this test of the parameters derived in paper III[3] indicates that they may be used with confidence in conformational energy calculations on long-range interactions in polypeptides and proteins.

We have seen that, by allowing groups such as $-CH_3$ and $-NH_3^+$ to rotate and thereby position their hydrogen atoms, we are able to fit the energy-minimized crystal structures very well without moving any heavy atoms. It was necessary to adjust the positons of the hydrogens since their coordinates are generally not obtained very precisely from the X-ray data. However, we have not altered the positions of the heavy atoms even though we most probably would have obtained even better fits to the observed lattice constants if these extra degrees of freedom had been allowed.

In each case in which the $-NH_3^+$ group was rotated, the maximum number of hydrogen bonds and shortest $H\cdots O$ distance were generally found at the minimum of the crystal energy. The reproduction of the hydrogen-bond lengths

was excellent, indicating that the "general hydrogen-bond" potential used in paper III[3] is satisfactory for both charged and uncharged groups, the differences in hydrogen-bond strength arising only from the different partial atomic charges.

The magnitudes of the binding energies for all of the amino acids studied might appear, at first sight, to be much too low (for ionic type species, such as zwitterions). However, the charge migration into the heavy atoms near the charged group makes the *net* excess charge on an $-NH_3^+$ or $-COO^-$ group about ±0.5 electronic units (by the CNDO/2 (ON) method), rather than a full charge unit, *i.e.*, the charge is spread out over many atoms and is not localized on any one. This diffuseness tends to make zwitterions behave in the crystal much like any other uncharged species, and results in values for binding energies close to those found[3] for carboxylic acids and amides. The partial charges obtained in the CNDO/2 (ON) calculations give fair agreement with dipole moment data for these molecules. It is conceivable that, by including a polarization energy term (for induced charge redistribution in these ionic species), the binding energy will become more negative; however, we would expect an increment in binding energy of only a few kilocalories at most, leading to values which are still much lower than the binding energies in ionic crystals.

There are no other data on these molecules, obtained by other authors, with which we may compare our results. However, Ferro and Hermans[7] have carried out a similar calculation on the crystal packing of D,L-acetylleucine-N'-methylamide and D,L-acetylamino-n-butyric acid N'-methylamide, in which they allowed for intramolecular rotations about single bonds as well as for translational and rotational degrees of freedom of the molecules and for variation in the lattice constants. The partial charges which they used are in general agreement with those presented here, and the fits to the crystal lattice were generally good. It is clear that the parameters used in this work have given excellent fits to crystals without these extra degrees of freedom. It appears that the potentials obtained in paper III[3] can be applied in conformational energy calculations on polypeptides and proteins. The use of these potentials for this purpose will be published elsewhere.[9] However, two points must be emphasized very strongly here. (1) It is the *total* potential, and not simply a portion of it, which must be used; *i.e.*, whereas individual components of the total potential (*e.g.*, the partial charges or the general hydrogen bond potential) need not correspond to similar components of other authors, it is the *total* potential which yielded the fit to experimental data, as reported here. (2) The adaptation of this total potential (obtained from *inter*molecular interactions in crystals) to conformational energy calculations on polypeptides and proteins (which involve, among other things, some *intra*molecular interactions between nearby atoms in the chain, and some torsional potentials)

requires some additional treatment which will be presented elsewhere.[9]

References and Notes

(1) This work was supported at Cornell University by research grants from the National Institute of General Medical Sciences of the National Institutes of Health, U. S. Public Health Service (GM-14312), from the National Science Foundation (GB-28469X3), and from Walter and George Todd.

(2) (a) Special Fellow of the National Institute of General Medical Sciences, National Institutes of Health, 1968–1969. (b) To whom requests for reprints should be addressed at Cornell University.

(3) F. A. Momany, L. M. Carruthers, R. F. McGuire, and H. A. Scheraga, *J. Phys. Chem.*, **78**, 1595 (1974).

(4) "Abnormal" means deviations of more than several hundredths of ångströms in the bond lengths or several degrees in bond angles of heavy atoms, when compared to the many similar amino-acid structures which have been determined in recent years.

(5) H. A. Scheraga, *Symmetry Funct. Biol. Syst. Macromol. Level, Proc. Nobel Symp., 11th, 1968*, 43 (1969).

(6) D. R. Ferro and J. Hermans, Jr., in "Liquid Crystals and Ordered Fluids," J. F. Johnson and R. S. Porter, Ed., Plenum Press, New York, N. Y., 1970, p 259.

(7) D. R. Ferro and J. Hermans, Jr., *Biopolymers*, **11**, 105 (1972).

(8) The variation in charge with a change in conformation will be discussed in a future paper.[9]

(9) F. A. Momany, R. F. McGuire, and H. A. Scheraga, manuscript in preparation.

(10) R. F. McGuire, F. A. Momany, and H. A. Scheraga, *J. Phys. Chem.*, **76**, 375 (1972).

(11) IUPAC-IUB Commission on Biochemical Nomenclature, *Biochemistry*, **9**, 3471 (1970).

(12) R. E. Marsh, *Acta Crystallogr.*, **11**, 654 (1958).

(13) Y. Iitaka, *Acta Crystallogr.*, **13**, 35 (1960).

(14) Y. Iitaka, *Acta Crystallogr.*, **14**, 1 (1961).

(15) P. G. Jönsson and A. Kvick, *Acta Crystallogr., Sect. B*, **28**, 1827 (1972).

(16) T. P. Das, *J. Chem. Phys.*, **27**, 763 (1957).

(17) M. S. Lehmann, T. F. Koetzle, and W. C. Hamilton, *J. Amer. Chem. Soc.*, **94**, 2657 (1972).

(18) Y. Iitaka, *Proc. Jap. Acad.*, **30**, 109 (1954).

(19) A. D. Buckingham, *Aust. J. Chem.*, **6**, 323 (1953).

(20) K. Shimura, *Nippon Nogei Kagaku Naishi*, **24**, 4-2 (1951).

(21) S. Takagi, H. Chihara, and S. Seki, *Bull. Chem. SOC/ Jap.*, **32**, 84 (1959).

(22) H. C. Freeman, G. L. Paul, and T. M. Sabine, *Acta Crystallogr., Sect. B*, **26**, 925 (1970).

(23) A. B. Biswas, E. W. Hughes, B. D. Sharma, and J. N. Wilson, *Acta Crystallogr., Sect. B*, **24**, 40 (1968).

(24) E. W. Hughes, *Acta Crystallogr., Sect. B*, **24**, 1128 (1968).

(25) T. F. Koetzle, W. C. Hamilton, and R. Parthasarathy, *Acta Crystallogr., Sect. B*, **28**, 2083 (1972).

(26) J. Donohue and R. E. Marsh, *Acta Crystallogr.*, **15**, 941 (1962).

(27) J. F. Yan, F. A. Momany, R. Hoffmann, and H. A. Scheraga, *J. Phys. Chem.*, **74**, 420 (1970).

(28) H. J. Simpson, Jr., and R. E. Marsh, *Acta Crystellogr.*, **20**, 550 (1966).

(29) W. Cochran and B. R. Penfold, *Acta Crystallogr.*, **5**, 644 (1952).

(30) S. Hirokawa, *Acta Crystallogr.*, **8**, 637 (1955).

(31) J. L. Derissen, H. J. Endeman, and A. F. Peerdeman, *Acta Crystallogr., Sect. B*, **24**, 1349 (1968).

(32) D. P. Shoemaker, J. Donohue, V. Schomaker, and R. B. Corey, *J. Amer. Chem. Soc.*, **72**, 2328 (1950).

(33) A. F. Pieret, F. Durant, M. Griffe, G. Germain, and T. Debaerdemaeke, *Acta Crystallogr., Sect. B*, **26**, 2117 (1970).

(34) T. Matsuzaki and Y. Iitaka, *Acta Crystallogr., Sect. B*, **27**, 507 (1971).

(35) R. A. Pasternak, L. Katz, and R. B. Corey, *Acta Crystallogr.*, **7**, 225 (1954).

(36) R. Degeilh and R. E. Marsh, *Acta Crystallogr.*, **12**, 1007 (1959).

(37) P. Giacomello and E. Giglio, *Acta Crystallogr., Sect. A*, **26**, 324 (1970).

Programmed Temperature Dehydration Studies of Octacalcium Phosphate

C. William Anderson, Ralph A. Beebe, and J. S. Kittelberger*[1]

Department of Chemistry, Amherst College, Amherst, Massachusetts 01002 (*Received January 4, 1974*)

Publication costs assisted by the National Institutes of Health

Thermal dehydration spectra of octacalcium phosphate (OCP) are obtained with a mass spectrometric technique at linear heating rates. Infrared spectra of vacuum-pyrolyzed OCP are obtained, as well as BET surface areas and pyrolysis weight-loss measurements *in vacuo*. Infrared results indicate a growth of OH^- and HPO_4^{2-} concentrations at temperatures above $\sim 200°$, growth of $P_2O_7^{4-}$ concentration at higher temperatures reaching a maximum near 500° and falling off near 700°, and a concommitant loss of OH^- and $P_2O_7^{4-}$ in the 600-800° region. Six discrete processes are identified in the thermal dehydration spectra. One of these, occurring near 200°, is interpreted as the disappearance of the OCP lattice, accompanied by a large loss of water and growth of OH^- and HPO_4^{2-} concentrations. The activation energy for this process is measured to be 59 ± 5 kcal/mol. A second, occurring about 700°, accompanied by simultaneous loss of OH^- and $P_2O_7^{4-}$, is probably the reaction $Ca_{10}(PO_4)_6(OH)_2 + Ca_2P_2O_7 \rightarrow 4Ca_3(PO_4)_2 + H_2O$. The activation energy for this process is found to be 122 ± 11 kcal/mol.

Introduction

This is one in a series of studies of the state of water associated with bone mineral and various synthetic calcium phosphates. In previous work, Dry and Beebe measured heats of adsorption of water on an organic bone and a synthetic hydroxyapatite (HA), and found values ranging from 22 to 11 kcal/mol.[2a] Holmes and Beebe found evidence for considerable internal water in synthetic amorphous calcium phosphate (ACP) but for only surface water in HA.[2b] Sedlak and Beebe[3] recently studied the internal water in ACP by an extension of the programmed temperature desorption (TPD) method developed by Cvetanović and Amenomiya.[4] Sedlak has established the validity of the TPD technique for obtaining approximate activation energies for bulk-dehydration processes in solids.[5] Prior to the work in this laboratory the use of TPD had been confined to surface desorption phenomena. The intention in the present work was to apply these methods to octacalcium phosphate (OCP) in order to learn more about the decomposition processes and binding energy of water in this highly hydrated material.

Fowler, Moreno, and Brown[6] have reviewed the literature on OCP, which indicates the occurrence of this substance in association with other calcium phosphates both *in vitro* and *in vivo*. These authors have studied the pyrolysis of OCP using ir spectroscopy, weight loss, and chemical analysis to characterize the pyrolysis products up to 900°. Weight loss up to 700° approximates that expected from the formula for OCP: $Ca_8H_2(PO_4)_6 \cdot 5H_2O$, on the assumption that water is the sole gaseous pyrolysis product.

In the present study we follow the dehydration of OCP by the mass spectrometric thermal analysis (MTA) technique which is closely related to TPD or to the original flash desorption method.[7] In MTA the sample is heated *in vacuo*, so that (in our apparatus) the temperature rises at a linear rate. Gaseous decomposition products are monitored with a mass spectrometer, most of the interest in this work being in H_2O. It has been shown[4,7] that in a first-order desorption, under conditions obtained in our apparatus, the shift in the temperature of a peak (T_M) in the MTA spectrum, with heating rate β, obeys the equation

$$\ln (T_M^2/\beta) = E_A/RT_M + \ln (E_A/AR)$$

where E_A is the activation energy for the desorption, A is the Arrhenius frequency factor, and R is the gas constant. Thus, if the results of a series of experiments at different heating rates are plotted in the form $\ln (T_M^2/\beta$ *vs.* $1/T_M$, a straight line is obtained with slope E_A/R. Recently Lord and Kittelberger have shown[8] that the same graphical method can be used to obtain activation energies in second (and probably higher) order processes. For fixed β, the position of a peak (T_M) is sensitive to the initial concentration of reagent in higher order, but not in first-order reactions; this phenomenon can be used to determine reaction order.[9] Wightman has shown that in a situation where a distribution of activation energies exists, a rather broad, flat-topped desorption peak occurs.[10]

The present work, therefore, extends the earlier work of Fowler, Moreno, and Brown,[6] and allows the measurement of the activation energies of the discrete dehydration processes.

Experimental Section

The MTA runs were carried out in a two-chamber high-vacuum system shown in Figure 1. The sample chamber is a 36-l. aluminum cube with Viton-A O-ring seals. This chamber is pumped by a 7-in. oil diffusion pump (CVC) baffled by a liquid nitrogen cooled trap (Granville-Phillips), and the estimated pumping speed at the throat of the sample chamber is 400 l./sec in the 10^{-7} Torr range. The sample chamber walls are partially shrouded by an additional liquid nitrogen trap to reduce background pressure. Base pressure in this chamber is 1×10^{-8} Torr from a Bayard-Alpert gauge, and rises to a typical maximum of 5×10^{-7} Torr during a run.

The sample chamber is separated from the detector chamber by a 2-in. bore "butterfly" valve (Edwards High Vacuum). This chamber is a 3-l. copper-brazed stainless steel cylinder sealed with Conflat flanges and OFHC copper gaskets (Varian), and pumped by an 8 l./sec ion pump (Varian). This chamber houses a quadrupole mass spectrometer (EAI Model 250) equipped with a copper-beryllium particle multiplier. With all settings optimized,
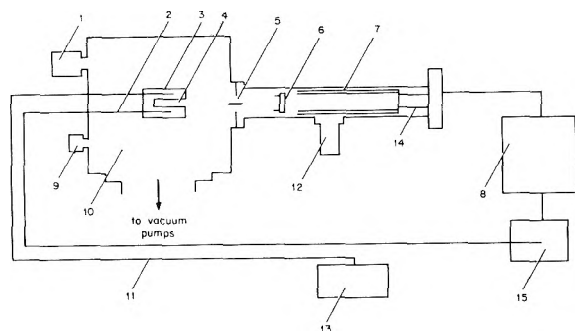
Figure 1. MTA apparatus: 1, ionization gauge; 2, monitor thermocouple; 3, oven; 4, sample compartment; 5, butterfly valve; 6, ionizer assembly; 7, quadrupole filter; 8, mass spectrometer control panel; 9, thermocouple gauge; 10, vacuum chamber; 11, sensing and power cables; 12, ion pump; 13, temperature programmer; 14, detector/multiplier; 15, two-channel recorder.

Figure 2. MTA spectra of H_2O lost from OCP.

this instrument is capable of detecting a partial pressure of N_2 of 10^{-14} Torr.

The sample oven is a cylinder 3.7 cm in diameter by 6.3 cm long made of OFHC copper with a 1.0-cm diameter sample cavity bored 3.0 cm deep on the oven axis. The heater consists of 12 spirals of 0.38-mm tantalum wire in series, mounted in longitudinal holes around the sample cavity, and insulated by thin-walled alumina tubes. Operating at maximum temperature ($\sim 1800°K$) and 120 V ac, this heater dissipates more than 300 W. The oven is positioned within a stainless steel radiation shield by four thin stainless screws; the whole oven assembly is mounted on an adjustable stainless arm so that the sample cavity is coaxial with the mass spectrometer ionizer axis. Temperature measurement and control are achieved with two chromel–alumel thermocouples screwed into the copper oven, which agreed, after calibration, to within the precision of the measuring equipment, $\pm 0.2°$. In order to determine the magnitude of any thermal lag which may exist between the copper oven and the powdered sample, about 10 mg of which is spread thinly directly on the oven floor in a typical run, we have compared dehydration peak temperatures obtained in this apparatus with those obtained in a TPD apparatus[11] for the same sample and heating rates. In TPD, the sample is heated in a stream of helium which is preheated in a baffle at the front of the oven; no thermal lag exists with this arrangement.[11] Peak temperatures obtained by the two methods at identical heating rates agree within $\pm 1°$ at the highest heating rates, ensuring, we believe, that any thermal lag which may exist between oven and sample in our MTA apparatus is no greater than the least uncertainty in locating the peak maxima, which is shown below to be $\pm 1°$.

Ten heating rates between 0.5 and 30°/min are provided by a Hewlett-Packard Model 240 temperature programmer. In this unit a voltage derived from a motor-driven potentiometer is opposed to the output from one of the thermocouples; the amplified error is used to gate an SCR which powers the oven heaters. The limiting source of error in sample heating rate appears to be the nonlinearity in the emf vs. temperature curve for chromel–alumel. This has a very slight S-shape in the temperature region studied, with a variation in slope of $\pm 3\%$, which is the variation we find in sample heating rate during the course of a run. The actual heating rate is obtained for each peak as the tangent to the thermocouple emf vs. time plot at the exact time of the peak.

In order to facilitate this determination of heating rate,
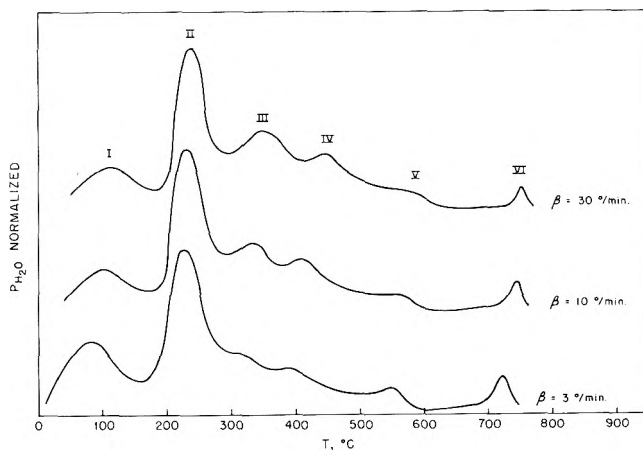
the mass spectrometer signal and the signal from the second thermocouple are simultaneously plotted on a two-pen recorder. During each run the temperature pen is calibrated frequently against a Leeds & Northrup potentiometer. The overall uncertainty in determining the temperature of a peak depends on a number of factors, sharpness of peak, spectrum noise, recorder scale, etc., but for no peak reported here does this exceed $\pm 2°$, and it drops to $\pm 1°$ in favorable cases.

The OCP sample studied here was prepared by the slow hydrolysis of $CaHPO_4 \cdot 2H_2O$ in 1 M sodium acetate at 38°.[12] Chemical analysis of the sample gives 30.7 wt % Ca (EDTA titration[13]), 55.5 wt % PO_4^{3-} (spectrophotometric phosphomolybdate method[14]), or a Ca/P molar ratio of 1.37 ± 0.04; the expected ratio for stoichiometric OCP is 1.33. No carbonate analysis was performed, but the ir spectrum shows no detectable carbonate or bicarbonate bands.

Infrared spectra were obtained on samples dispersed to about 5 wt % in dried KBr, and pressed in a small hand press. Where H_2O is of special importance, an identical pellet of pure KBr can be used in the reference beam. Spectra were recorded on a Perkin-Elmer Model 237.

The ir spectrum of the unheated OCP samples is shown below in Figure 3, and is identical with spectra reported previously by Fowler, Moreno, and Brown.[6] Our sample shows shoulders at 3570 and 633 cm^{-1}, suggesting the presence of traces of HA.

X-Ray powder diffraction patterns of the sample also confirm its identity as OCP. In particular, the 18.7-Å reflection[15] most characteristic of OCP is very strong in the X-ray patterns of the OCP studied here. To complement the MTA spectra obtained here, the surface area of the OCP has been determined by BET nitrogen adsorption.[16] The samples were outgassed at 10^{-5} Torr overnight at the temperatures indicated in Table I, which summarizes the results.

Results

a. MTA Studies. The dehydration spectrum of OCP obtained with the mass spectrometric apparatus is shown in Figure 2. We have reproduced here runs at heating rates of 3, 10, and 30°/min in order to show how the peaks shift with heating rate. Background spectra of the empty oven are featureless except for a burst of water from the heaters and another from the alumina insulators which occur immediately after starting the run (at temperatures below 100°); these have been suppressed in Figure 2. The peaks
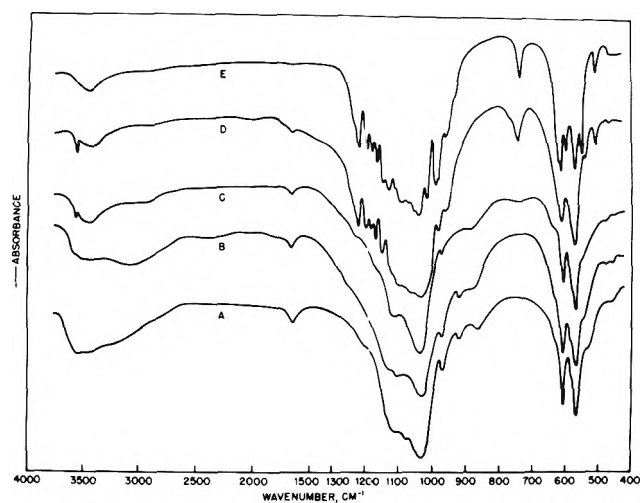
Figure 3. Infrared spectra of OCP heated to various temperatures *in vacuo*: A, unheated; B, 157° C, 271°; D, 625°; E, 800°. The absorbance scale is logarithmic.

TABLE I: Effect of Degassing Temperature on Surface Area of OCP as Measured by BET Method

Outgassing temp, °C	Surface area, m^2/g
22	4.7
100	3.6
200	5.2
300	5.4, 5.7
500	7.0, 6.5

are numbered in order of appearance from low to high temperature as I through VI. The spectra in Figure 2 have been normalized to the height of peak II, not to unit sample weight. The spectra, thus, do not allow observation of changes in the area of peak II with β.

We find that the area under peak I decreases somewhat with increasing evacuation time before the start of the run, and the position of the maximum is also sensitive to these prepumping conditions.

Peaks III and IV are least pronounced at low β, and increase in area as β increases. Peak VI appears with smaller area at the greatest heating rates. No quantitative measure of the areas under the overlapped peaks was attempted; while curve shapes for simple, single-step desorption processes are understood,[8,9] there is no *a priori* reason to suppose that the processes under investigation are simple and single step.

b. Weight Loss. Samples of the OCP studied here lost $10 \pm 1\%$ in weight during the course of a run to 850°, essentially all of which was H_2O, since the mass spectrometer detected negligible amounts of other gaseous effluents (such as CO_2) during a run. An unknown fraction of the weight loss can easily occur during pumpdown before the start of heating. Thus, the spectra in Figure 2 cannot be assumed to record *all* of the water lost from the sample; very loosely-bound water will not be recorded by this high-vacuum technique. For reference, however, a stoichiometric OCP contains 9.16% water of hydration, with additional loss possible *via* pyrophosphate formation and desorption of surface water.

c. Infrared Studies. To assist the interpretation of the dehydration spectra, we have recorded, at room temperature, infrared spectra of samples heated under high vacuum to various temperatures in the sample oven of the MTA apparatus. All of the spectra shown in Figure 3 are of samples held at the temperature indicated for 7–8 hr
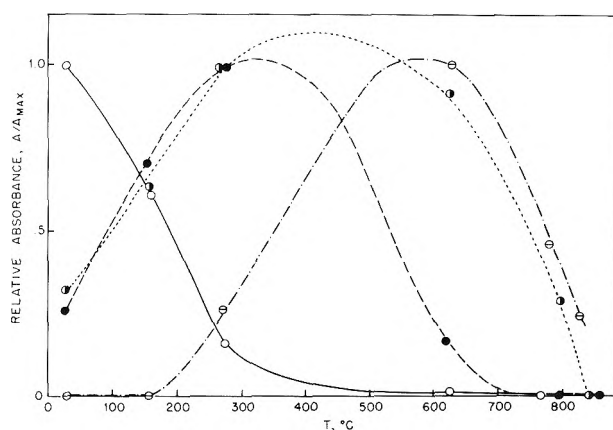

Figure 4. Infrared band intensities of OCP samples heated to various temperatures; H_2O, O; HPO_4^{2-}, ●; OH^-, ◑; $P_2O_7^{4-}$, ◒.

and heated to this temperature at 15°/min. These spectra are in essential agreement with those reported by Fowler, Moreno, and Brown.[6]

We have monitored the concentrations of four species during the course of these pyrolyses: H_2O, OH^-, $P_2O_7^{4-}$, and HPO_4^{2-}. To do so we have measured the intensities of the ir bands at 1630 cm^{-1} for H_2O, at 3570 cm^{-1} for OH^-, at 725 cm^{-1} for $P_2O_7^{4-}$, and at 870 cm^{-1} for HPO_4^{2-}. The band assignments have been discussed.[6,17,18] The reported band intensities were measured with a planimeter and normalized either to unit sample weight or to unit area under the phosphate ir band between 500 and 700 cm^{-1}. The two methods of normalization agree within the reliability expected for this kind of procedure. Before reporting our findings here, we caution the reader that this method of determining ion concentrations in a pyrolysis experiment is beset with several difficulties, and cannot be regarded as completely quantitative. For example, extinction coefficients vary with environment, a well-known problem for the 3570-cm^{-1} OH^- line.[19] The qualitative trends indicated by the ir intensities in Figure 4, however, are certainly meaningful. Other bands could have been used to monitor the ion concentrations. As a check, we have measured the intensities of the 633-cm^{-1} OH^- libration. For all spectra, $OD(3570)/OD(633) = 0.26 \pm 0.06$. The errors, we feel, can be due entirely to the area measurement.

This figure shows a simultaneous increase in both HPO_4^{2-} and OH^- in OCP samples heated to 157°, and to 271°. OH^- then remains reasonably constant to 625° and falls off in samples heated above 625°. HPO_4^{2-} falls off above 271° in the region where $P_2O_7^{4-}$ rises. H_2O falls off steadily, and is nearly absent from samples held for 8 hr at 450° or higher.

Since the heating time in all the above ir pyrolysis studies ($\sim$8 hr) was considerably longer than the duration of a typical MTA run ($\sim$1 hr at $\beta = 15°/min$), we have conducted two ir experiments in which the total heating time was approximately 1 hr.

In the first a sample was heated at 15°/min to 359° and cooled immediately to room temperature. The ir spectrum of this sample showed significant increases in OH^- and HPO_4^{2-} over the amount present in the original material and less of these ions than found in samples heated to 271° for 8 hr. In this same experiment no $P_2O_7^{4-}$ was found.

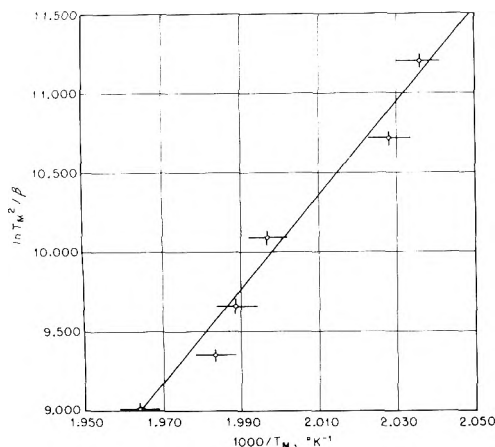In the second experiment a sample was heated to 800°

Figure 5. $Ln(T_M^2/\beta)$ vs. $1000/T_M$ for peak II in the MTA spectrum of OCP.

Figure 6. $Ln(T_M^2/\beta)$ vs. $1000/T_M$ for peak VI in the MTA spectrum of OCP.

TABLE II

| β, deg/min	Peak II T_M, °C	Peak VI T_M, °C
3.3	218	721
5.4	220	
10.4	228	743
10.5	228	742
13.8		746
16.2	230	
18.3		747
22.1	231	
24.6		752
31.6	236	

at 15°/min and cooled immediately. The resulting ir showed more of both OH⁻ and $P_2O_7^{4-}$ than in the sample heated for 8 hr at 800°, but significantly less than in the sample heated at 625° for 8 hr. The loss of OH⁻ and $P_2O_7^{4-}$ between 600 and 800° would thus appear to be coupled.

In comparing our results with those found in other pyrolysis studies, the reader should bear in mind that our samples were heated *in vacuo* at 10⁻⁷ Torr.

d. Activation Energies. Attempts were made to determine E_A for all six peaks appearing in the MTA spectrum of OCP by plotting ln (T_M^2/β) vs. $1/T_M$. Only for peaks II and VI are these plots satisfactory; for the others there is such a large standard deviation in the slope of the line that we feel the results are meaningless. The data for peaks II and VI are recorded in Table II. The plots for peaks II and VI are presented in Figures 5 and 6. The slope of the least-squares line gives an activation energy of 59 kcal/mol with a standard deviation of 5 kcal for peak II. For peak VI E_A = 122 kcal/mol with a standard deviation of 11 kcal.

Discussion

The infrared studies show that at fairly mild temperatures (150–350°) the concentrations of HPO_4^{2-} and OH⁻ increase. This suggests that the simultaneous increases in both may arise from a single chemical reaction

$$H_2O + PO_4^{3-} = HPO_4^{2-} + OH^-$$
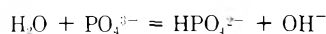
in which some of the water of hydration is consumed. This could arise from the formation of separate phases of $CaHPO_4$ and hydroxyapatite

$$Ca_8H_2(PO_4)_6 \cdot 5H_2O \longrightarrow \tfrac{1}{2}Ca_{10}(PO_4)_6(OH)_2 + 3CaHPO_4 + 4H_2O$$
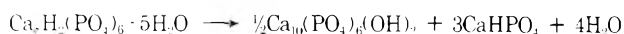
$CaHPO_4$ has been found as a pyrolysis product of OCP in

this temperature region in some studies,[12] but not in others.[6] This may be due to different experimental conditions such as partial pressure of water and duration of pyrolysis. Our results indicate no discrete $CaHPO_4$ phase; the doublet at 1350–1400 cm⁻¹ characteristic of $CaHPO_4$[6] never appears in our ir spectra. It is worth noting that those studies which found $CaHPO_4$ used X-ray diffraction,[12] while no conclusive ir evidence has been found for $CaHPO_4$ in a pyrolysis study.[12]

Another possibility, favored by some authors,[20] is the formation of a defect, or calcium-deficient apatite; for example

$$Ca_8H_2(PO_4)_6 \cdot 5H_2O \longrightarrow Ca_8H_3(PO_4)_6OH \cdot 4H_2O$$
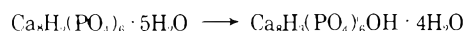
Since the MTA technique is a nonequilibrium technique, and since we have no X-ray patterns of pyrolyzed samples, we cannot draw much information from our data on the question of what solid products are formed in this temperature range. With the infrared results in mind, we propose the following assignment of the MTA spectrum. Peak I is the first step in the loss of water of hydration. Given the sizable area under this peak together with the fact that some loosely held water is lost during pumpdown, we can state that at least 20% of the total dehydration is associated with this step. Fowler, *et al.,* found roughly 50% of the weight loss occurred below 150°.[6] The tendency of T_M to shift to higher temperatures with greater prepumping time is due, we conclude, to the fact that a distribution of values of E_A exists for this process. Loss of water with low E_A during pumpdown would shift T_M to a higher value.

Peak II, the largest in the spectrum, occurs near 220°; HPO_4^{2-} and OH⁻ are being formed in the same temperature range. OCP heated to 200° begins to lose its structural identity, and HA and $CaHPO_4$ have been reported to appear near this temperature.[12] We assign this peak as the loss of the bulk of the water of hydration in OCP. The activation energy associated with this process, 59 kcal, is considerably greater than the 20–30 kcal activation energies found for desorption of water from HA surfaces,[21] so that we believe peak II cannot be due to a desorption process.

Peaks III and IV grow in area as the heating rate is increased. This fact suggests that the water lost here can also be removed by a competitive chemical reaction; at low heating rates more of the water is removed by the competitive mechanism, while at high heating rates more

of it is lost in peaks III and IV. We note that peaks V and VI decrease in area as β increases suggesting that reactions V and VI are the terminal steps in the alternate mechanism. Our proposed assignments for peaks III and IV are two additional stages in the loss of water of hydration. The greater the heating rate the more undecomposed OCP remains at these elevated temperatures. Peak V we assign as the water loss associated with the formation of pyrophosphate
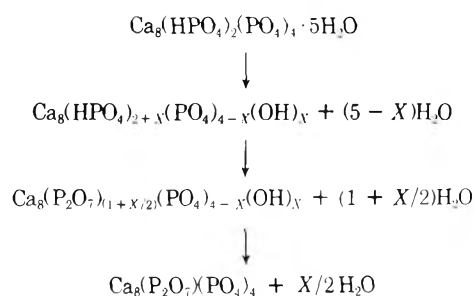
$$2HPO_4{}^{2-} \longrightarrow P_2O_7{}^{4-} + H_2O$$
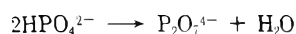
which is known to occur in this temperature region.[6,22] Fowler, et al., for example, find a maximum yield of pyrophosphate in OCP samples pyrolyzed at 550°,[6] very nearly the temperature of peak V at low β. Peak VI occurs in a temperature region where the present infrared study and earlier work[6] indicate losses of $P_2O_7{}^{4-}$ and OH^-. Fowler, et al.,[6] have suggested that the reaction

$$Ca_{10}(PO_4)_6(OH)_2 + Ca_2P_2O_7 \longrightarrow 4Ca_3(PO_4)_2 + H_2O$$
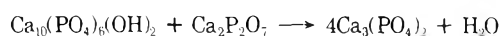
accounts for weight loss near 700°. In the present study we find a simultaneous decrease in $P_2O_7{}^{4-}$ and OH^- in samples heated to 800°; if peak III were due to simple dehydroxylation no decrease in $P_2O_7{}^{4-}$ would be expected. In addition the ir spectrum of samples heated to 800° shows bands at 1120, 972, 950, 602, 589, 550, and 541 cm^{-1} which have been reported in β-Ca$_3$(PO$_4$)$_2$.[6] We find an activation energy of 122 kcal for this reaction which is known to be very slow.[6] Our assignment of peaks III-VI is consistent with the observation that peaks III and IV increase in area with increasing β, while peaks V and VI decrease with increasing β. Quantitative measure of the areas of these peaks is not possible, but it is worth noting that the weight loss during a complete MTA run seems independent of β.

Our weight-loss studies give a 10% decrease in weight on heating to 850°, which corresponds to about 5.5 mol of water per mole of OCP. This finding is in essential agreement with data reported by Fowler, et al.[6] From Table I, the specific surface area of the OCP is on the order of 5 m^2/g. Using 11 Å^2 as the cross sectional area of the water molecule,[2] a close-packed monolayer of adsorbed water on the OCP would represent less than 0.01 mol of H$_2$O per mole of OCP. Adsorbed water, thus, represents a negligible fraction of the 10% weight loss. We suggest that this dehydration can be understood by the following set of reactions, consistent with the above assignment of peaks

$$Ca_8(HPO_4)_2(PO_4)_4 \cdot 5H_2O$$

$$\downarrow$$

$$Ca_8(HPO_4)_{2+X}(PO_4)_{4-X}(OH)_X + (5 - X)H_2O$$

$$\downarrow$$

$$Ca_8(P_2O_7)_{1+X/2}(PO_4)_{4-X}(OH)_X + (1 + X/2)H_2O$$

$$\downarrow$$

$$Ca_8(P_2O_7)(PO_4)_4 + X/2\,H_2O$$

for a total loss of 6 mol of water. Since $1 + X/2 + X/2$ or $1 + X$ of the 6 mol of water are lost in the last, slow steps, we can readily see how only the 4 mol of water of hydration plus approximately 1 of the 2 mol of water available for

loss in the last two (slow) steps would show up in our weight loss measurements, in which the total heating time was $\leq$6 hr. Fowler, et al., also observed 10% weight loss[6] in pyrolyses of much longer duration but heated their samples in a muffle furnace at atmospheric pressure.

Not much is said in this discussion about the crystalline phases formed in the decomposition of OCP. Our experiments were not designed to produce maximum yields of the decomposition products, and we have limited structural information. There is evidence for HA in the parent sample, and increasing amounts of it above 200°. There is evidence for β-Ca$_3$(PO$_4$)$_2$ at the highest temperatures reached in our experiments. Evidence on the formation of discrete phases of CaHPO$_4$ and Ca$_2$P$_2$O$_7$ is less clear in the present study.

Note Added in Proof. In preparing the manuscript, we overlooked a relevant reference on this subject.[23] Newesely cites evidence for one of the five water molecules being held rather loosely in the OCP lattice, so that its loss may be reversible. The loss of such a loosely held water molecule would either be complete during the prepumping stages of our MTA experiments, or it could account for peak I in the MTA spectrum. Additionally, Newesely finds $P_2O_7{}^{4-}$ formation has a threshold temperature near 150° in pyrolyzed OCP. This is in essentially perfect agreement with our findings (see Figure 4).

References and Notes

(1) Address correspondence to Xerox Corp., Bldg. 114, 800 Phillips Road, Webster, N. Y. 14580.
(2) (a) M. E. Dry and R. A. Beebe, *J. Phys. Chem.*, **64**, 1300 (1960); (b) J. M. Holmes and R. A. Beebe, *Calcif. Tissue Res.*, **7**, 163 (1971).
(3) J. M. Sedlak and R. A. Beebe, *J. Colloid Interface Sci.*, submitted for publication.
(4) R. J. Cvetanović and Y. Amenomiya, *J. Phys. Chem.*, **67**, 144 (1963).
(5) J. M. Sedlak and R. A. Beebe, *Thermochim. Acta*, submitted for publication.
(6) B. O. Fowler, E. C. Moreno, and W. E. Brown, *Arch. Oral Biol.*, **11**, 477 (1966).
(7) G. Ehrlich, *Advan. Catal.*, **14**, 256 (1963).
(8) F. M. Lord and J. S. Kittelberger, *Surface Sci.*, **43**, 173 (1974).
(9) P. A. Redhead, *Vacuum*, **12**, 203 (1962).
(10) Wightman's results are unpublished but cited extensively by R. J. Cvetanović and Y. Amenomiya, *Catal. Rev.*, **6**, 21 (1972).
(11) J. M. Sedlak, unpublished results. The spectrometer and temperature measurement in it is described in ref 3.
(12) W. E. Brown, J. R. Lehr, J. P. Smith, and A. W. Frazier, *J. Amer. Chem. Soc.*, **79**, 5318 (1957). The sample used here was supplied by Dr. A. S. Posner, Cornell Medical College.
(13) R. G. Yalman, W. Bruegemann, P. T. Baker, and S. M. Garn, *Anal. Chem.*, **31**, 1230 (1959).
(14) F. J. Welcher, Ed., "Standard Methods of Chemical Analysis," Vol. IIb, 6th ed, Van Nostrand, New York, N. Y., 1963, p 2467.
(15) W. E. Brown, *Nature (London)*, **196**, 4859 (1962). X-Ray patterns were run by Dr. A. S. Posner.
(16) Surface areas were determined by Professor J. M. Holmes, Carleton University, Ottawa, Canada. For a description of the BET technique as applied to calcium phosphate systems, see ref 2b.
(17) See S. H. Joris and C. H. Amberg, *J. Phys. Chem.*, **75**, 3167, 3172 (1971), for a discussion of the assignment of this band.
(18) W. E. Klee and G. Engel, *J. Inorg. Nucl. Chem.*, **32**, 1837 (1970).
(19) N. C. Blumenthal and A. S. Posner, *Calcif. Tissue Res.*, in press.
(20) E. E. Berry and S. A. Leach, *Arch. Oral Biol.*, **12**, 171 (1967).
(21) C. W. Anderson and J. S. Kittelberger, manuscript in preparation.
(22) A. Gee and V. R. Dietz, *J. Amer. Chem. Soc.*, **77**, 2961 (1955).
(23) H. Newesely, *Monatsh. Chem.*, **98**, 379 (1967).

Isothermal Compressibility of Aqueous Sodium Chloride, Magnesium Chloride, Sodium Sulfate, and Magnesium Sulfate Solutions from 0 to 45° at 1 Atm[1a]

Frank J. Millero,* Gary K. Ward,[1b] Fred K. Lepple, and Edward V. Hoff

University of Miami, Rosenstiel School of Marine and Atmospheric Science, Miami, Florida 33149 (Received December 7, 1973)

The isothermal compressibilities (β's) of aqueous NaCl, Na_2SO_4, $MgSO_4$, and $MgCl_2$ solutions have been measured at 0, 15, 30, and 45° by a piezometric technique. The compressibilities were determined at applied pressures P = 8.7, 16.8, and 25.7 bars and the data were extrapolated to 1 atm. The β's have been fitted to an equation of the form, $\beta = \beta^0 + A_K c + B_K c^{3/2}$, where β^0 is the compressibility of pure water, c is the molar concentration, and A_K and B_K are temperature-dependent parameters. The equation fits the compressibility data to $\pm 0.07 \times 10^{-6}$ bar^{-1} for all the salts. The apparent molal compressibilities, ϕ_K, have been calculated from the compressibility data. At high concentrations the concentration dependence of the (ϕ_K)'s were found to follow the equation, $\phi_K = \phi_K{}^0 + S_K{}^* I_V{}^{1/2}$, where $\phi_K{}^0$ and $S_K{}^*$ are empirical constants and I_V is the molar ionic strength. To obtain reliable infinite dilution ($\phi_K{}^0$)'s (that agree with values derived from sound velocity measurements) it was necessary to use the equation, $\phi_K = \phi_K{}^0 + S_K I_V{}^{1/2} + b_K I_V$, where $\phi_K{}^0$ is the infinite dilution apparent molal compressibility, S_K is the Debye–Hückel limiting law slope, and b_K is a temperature-dependent parameter related to deviations from the limiting law. The ($\phi_K{}^0$)'s from all the electrolytes increase with increasing temperature and appear to go through a maximum between 40 and 50°. The deviations from the limiting law, b_K, are all positive at low temperature and decrease with increasing temperatures for all the salts. The (ϕ_K)'s are briefly discussed in terms of the ion–water and ion–ion interactions responsible for the observed behavior. The (ϕ_K)'s for $MgSO_4$ solutions have been analyzed by assuming the ion pair, $MgSO_4{}^0$, is formed. The $\Delta\phi_K$ for the formation of the ion pair and the ϕ_K of $MgSO_4{}^0$ have been calculated at various concentrations and temperatures. The results are used to examine the structure of the ion pair.

Introduction

Although the isothermal compressibilities have been measured for various electrolytes by a number of workers,[2,3] the results are at high pressures ($P > 100$ bars) and for concentrated solutions ($m > 1.0$). The pressure dependence of the compressibility, β, is such that β decreases most rapidly at low pressures, where it is most difficult to obtain accurate experimental results. The usual measurements involve determining the volume change due to an increase in pressure of the order of 200 to 1000 atm. The apparent molal compressibilities, ϕ_K, which are calculated from the compressibility data extrapolated to 1 atm, vary a good deal between different studies.[2,3] Thus, there is a need for accurate 1-atm compressibilities for aqueous solutions of various electrolytes at low concentrations ($m < 1.0$). Although ϕ_K's derived from sound speed data are normally more reliable than those derived from direct measurements, the heat capacities and expansibilities necessary to convert the adiabatic to isothermal values are not readily available.

This study deals with the precise determination of the isothermal compressibilities for four electrolytes, NaCl, $MgSO_4$, Na_2SO_4, and $MgCl_2$, which were chosen because they are the four major sea salts in the oceans. The basic thermodynamic properties of these salts are of prime importance for various thermodynamic calculations in oceanography.

One of the applications of the data obtained is the study of ion pair formation of $MgSO_4{}^0$. Although the compressibility changes for the ionization of weak acids and bases have been studied by a number of workers,[4] little attention has been paid to the compressibility changes associated with the ion pair formation

$$M^+ + A^- = MA^0 \qquad (1)$$

where M^+ and A^- are the free ions, and MA^0 is the ion pair.

From the compressibility data in this study, one can calculate the $\Delta\phi_K$ for the formation of the $MgSO_4{}^0$ ion pair and the ϕ_K for the ion pair by applying a method recently used to study the volume change for the formation of the ion pair using apparent molal volume data.[5]

Experimental Section

The isothermal compressibility apparatus used in this study was originally described by Millero, Curry, and Drost-Hansen.[6] The apparatus has been shown[6,7] to yield results for the compressibility of water that agree with the results of Kell and Whalley[8] and Kell[9] to $\pm 0.07 \times 10^6$ bar^{-1} from 0 to 65°.

The apparatus consists of three basic units, a piezometer, a pressure cell, and a constant temperature bath. A precision bore capillary is fitted to the bottom of the glass piezometer vessel, which has a volume of approximately 410 ml. The capillary is calibrated by weighing various lengths of mercury (measured with a cathetometer), yielding a cross-sectional area of 0.03246 ± 0.00001 cm^2. The piezometer is contained inside a pressure cell constructed of nickel-plated brass and a glass boiler tube which allows the viewing of the capillary stem. The boiler tube restricts

the measurements to a maximum of 35 bars. The pressure inlet is fitted with a stainless steel Swagelok tee, and also serves as the mercury exchange port. The chamber between the capillary and the boiler tube is open to the main pressure cell, thus allowing equalization of the pressure inside and outside the piezometer. The interior of the main pressure cell area is filled with ethylene glycol which is circulated by a magnetic stirring bar. The entire pressure cell is submerged in a constant temperature bath, regulated to ±0.001° with a Hallikainen Thermotrol.

The temperature inside the cell is monitored with a Hewlett-Packard quartz crystal thermometer, which was calibrated with a platinum resistance thermometer (traceable to the National Bureau of Standards) and a G-2 Mueller bridge. The quartz crystal thermometer can detect temperature changes of ±0.0001° with an accuracy of ±0.001° after calibration. The inside temperature fluctuates less than ±0.0002° after thermal equilibrium is reached before and after compression, and it is expected that the fluctuations within the piezometer are even smaller than this value.

The pressure changes are measured with a Texas Instrument Company's fused quartz precision gauge to a precision of ±0.001 bar and an accuracy of ±0.005 bar (traceable to the National Bureau of Standards) at the highest pressure differences measured. Since we are only concerned with pressure differences, the accuracy of the instrument is not a limiting factor. The change in volume of the solution in the piezometer, caused by a given pressure change (ΔP), was determined by measuring the change in height, Δh, of the mercury in the attached capillary. This height change was measured to ±0.01 mm (±0.001%) with a Gaertner cathetometer. The height measurements were made at 0, 17, and 34 bars applied pressure.

The piezometric compressibility apparatus was calibrated with water using the sound derived compressibilities of Kell.[9] The water used for both the calibration and the test solutions was ion exchange (Millipore Super Q) 18 megohm water.

The densities of the solutions (used in some of the calculations) were measured on a magnetic float densimeter[10] and are given elsewhere.[11]

The sodium chloride and magnesium sulfate were anhydrous Baker analyzed reagents, while the sodium sulfate was anhydrous Fisher Certified ACS grade. The solutions of these salts were made up by weight without further purification and analyzed by a quantitative evaporation technique. The magnesium chloride, MgCl·6H₂O, was a Mallinckrodt Analytical reagent, and the test solutions were analyzed by a gravimetric chloride titration. All the solutions were analyzed after each run to eliminate errors due to possible changes in concentration occurring during degassing of the samples prior to each experiment.

Results and Calculations

The isothermal compressibility, β, of a liquid is defined by the equation

$$\beta = -\frac{1}{V}\left(\frac{\partial V}{\partial P}\right)_T \qquad (2)$$

The total volume of the interior of the glass piezometer, V_g, is given by

$$V_g = V_{liq} + V_{Hg} + Ah \qquad (3)$$

where V_{liq} is the volume of the test solution, and $V_{Hg} + Ah$ is the total volume of mercury, A represents the cross-

sectional area of the capillary, and h is the height of mercury in the capillary measured from the reference mark. If eq 3 is differentiated with respect to pressure and we include the effect of pressure on glass,[12,13a] we obtain

$$\beta = -\beta_{Hg}\left(\frac{V_{Hg}}{V_{liq}}\right) +$$
$$\beta_G\left(1 + \frac{V_{Hg}}{V_{liq}} + \frac{A\Delta h}{3V_{liq}}\right) + \frac{A\Delta h}{V_{liq}\Delta P} \qquad (4)$$

where β_G is the isothermal compressibility of glass, β_{Hg} is the compressibility of mercury, β is the compressibility of the test solution, and Δh is the change in height of the mercury in the capillary for a given change in applied pressure, ΔP.

Since the volumes of liquid and mercury used in the test solution runs and the water calibration run were nearly equal, the differences between β of the test solution and β^0 (compressibility of pure water) can be calculated in a manner which is independent of the values selected for β_G and β_{Hg}. By subtracting eq 4 for water from eq 4 for the test solution, we obtain

$$(\beta - \beta^0) = (A\Delta h/V\Delta P)_{liq} - (A\Delta h/V\Delta P)_{H_2O} \qquad (5)$$

when $(V_{Hg})_{H_2O} \simeq (V_{Hg})_{liq}$, $V_{H_2O} \simeq V_{liq}$, and $(\Delta h/\Delta P)_{H_2O}$ and $(\Delta h/\Delta P)_{liq}$ are compared at the same applied pressure. The precision of the term, $(A\Delta h/V_{liq}\Delta P)$, is ±0.025 × 10⁻⁶ bar⁻¹ and, therefore the precision of β, determined by our apparatus, is ±0.05 × 10⁻⁶ bar⁻¹ with an accuracy of ±0.07 × 10⁻⁶ bar⁻¹.

The quantity $(\beta - \beta^0)$ for various concentrations of aqueous NaCl, MgSO₄, Na₂SO₄, and MgCl₂ solutions at 0, 15, 30, and 45° is given in Table I.[13b] The values of $(\beta - \beta^0)$ given in Table I are the average values determined from the compressions $(A\Delta h/\Delta P)$ at the average pressures of 8.9 (Δh from 0 to 17 bars), 16.8 (Δh from 0 to 34 bars), and 25.7 (Δh from 17 to 34 bars). We have reported the average value of $(\beta - \beta^0)$ since there appears to be no regular pressure dependence of the $(\beta - \beta^0)$ term and deviations from the average are within our experimental error.[14] Since the pressure dependence of $(\beta - \beta^0)$ is small, we have equated the average values to the 1-atm values. Thus, we are assuming that the compressibilities of salt solutions have the same pressure dependence as water (i.e., within the experimental error).

The compressibilities of the solutions have been fitted to equations of the form[2a]

$$\beta = \beta^0 + A_K c + B_K c^{3/2} \qquad (6)$$

where A_K and B_K are temperature-dependent parameters and c is the molar concentration, $c = 1000d^0m/(1000 + \phi_V md^0)$ [d^0 is the density of pure water, m is the molality, and ϕ_V is the apparent molal volume[11]]. The A_K term is related to infinite dilution ion-water interactions ($10^3A_K = \phi_K^0 - \beta^0\phi_V^0$) and the B term is related to ion-ion interactions ($10^3B_K = S_K^* - \beta^0S_V^*$). Plots of $(\beta - \beta^0)/c$ vs. $c^{1/2}$ for the various salts are given in Figures 1-4.[13b] The constants A_K and B_K for the salts at various temperatures are given in Table II.[13a] The average deviations between the experimental values and those calculated from eq 6 are within ±0.07 × 10⁻⁶ bar⁻¹ over the entire temperature and concentration range (which represents our experimental error). An attempt was made to fit the data to an equation similar to eq 6 by using molal concentrations (which are more convenient to use); however, the errors were much larger (±0.15 × 10⁻⁶ bar⁻¹) and required an

additional term. The compressibility of all the solutions decreases with increasing concentration. If we assume that the size of the ion is not pressure dependent and the electrostricted water is already compressed to its maximum extent by the charge on the ions, we can assume (as will be discussed later) that the compressibility of a solution is mainly due to the effect of pressure on the bulk (unhydrated) water molecules. As the concentration of the electrolyte increases and a larger portion of the water molecules are electrostricted, the amount of bulk water decreases causing the compressibility to decrease. For electrolytes with large hydration numbers, such as $MgSO_4$ and Na_2SO_4, one would expect $\partial\beta/\partial c$ to be much more negative than electrolytes such as NaCl with small hydration numbers. This would indicate that the concentration dependence of β becomes greater as the number of water molecules affected by the ions increase. As predicted, our data indicate that $-(\partial\beta/\partial c)$ is directly related to the hydration number of the salts. The magnitude of $\partial\beta/\partial c$ at $0°$ follows the order $Na_2SO_4 > MgSO_4 > MgCl_2 > NaCl$ which holds for the hydration numbers (determined later in the paper).

The temperature dependence of β, $\partial\beta/\partial T$, is also negative for all the solutions studied below $25°$. The compressibility of water also decreases with temperature to a minimum β value near $46°$. A number of workers[6,13a,15,16] have postulated that this is due to the existence of two structural types of water aggregates at a given temperature (a structured form and a nonstructured or less-structured form). The $\partial\beta/\partial T$ term for the structured form is negative, while it is positive for the less-structured form. At low temperatures, this structured form is the predominant species while at high temperatures, the nonstructured form predominates. In dilute electrolyte solutions (Figure 5),[13b] the compressibility decreases with temperature to a minimum also near $46°$. The value of $\partial\beta/\partial T$, however, is much less negative in dilute solutions than in water, indicating an increasing importance of a structure-breaking effect due to the presence of ions. As concentration increases, $\partial\beta/\partial T$ becomes less negative and the minimum occurs at lower and lower temperatures (Figure 5). In a 4 m NaCl solution, the minimum occurs at $29°$. One possible explanation is that the ions enhance the nonstructured form causing this form to become the predominant factor at increasingly lower temperatures.

The apparent molal compressibility is defined as

$$\phi_K = -(\partial\phi_V/\partial P)_T \tag{7}$$

where ϕ_V is the apparent molal volume of the electrolyte. The ϕ_K of an electrolyte can be calculated from the isothermal compressibility, β, and the density data from the following relations

$$\phi_K = \frac{1000}{md^0}(\beta - \beta^0) + \beta\phi_V \tag{8}$$

or

$$\phi_K = \frac{1000}{c}(\beta - \beta^0) + \beta^0\phi_V \tag{9}$$

where β^0 is the compressibility of water,[9] m is the molality, ϕ_V is the apparent molal volume[5,11] at m or c, and d^0 is the density of water.[17] The ϕ_K's of aqueous NaCl, $MgSO_4$, Na_2SO_4, and $MgCl_2$ solutions, calculated by eq 8, are given in Table I for various molalities and temperatures.

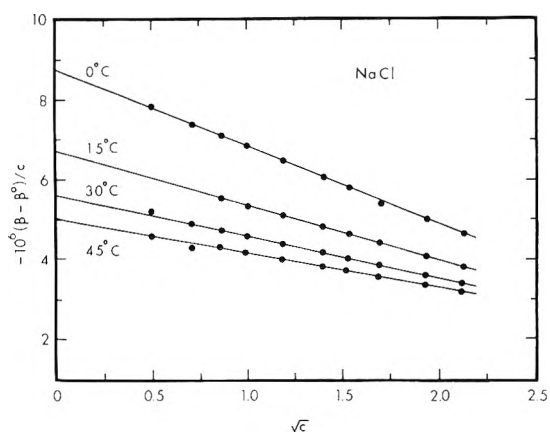The ionic strength dependence of the ϕ_K of electrolytes

Figure 1. Plot of $-10^6(\beta - \beta^0)/c$ vs. $c^{1/2}$ for NaCl solutions at 0, 15, 30, and $45°$.

TABLE III: Values for ϕ_K^0, $S_K{}^*$, and b_K from Eq 10 and 11 for NaCl, $MgSO_4$, Na_2SO_4, and $MgCl_2$ at Various Temperatures

Temp, °C	$-10^4\phi_K^0$	$10^4 S_K{}^*$	$10^4 b_K$	Av deviation
		NaCl		
0	81.4[a](75.6)[b]	21.0[a]	13.9[b]	±0.3[c]
15	60.1(55.6)	14.9	6.7	0.2
30	48.5(42.2)	11.3	2.0	0.2
45	42.4(39.0)	9.5	1.2	0.2
		$MgCl_2$		
0	147.8(129.4)	26.6	5.9	0.6
15	113.9(103.6)	19.0	2.4	0.5
30	96.2(93.7)	14.7	0.3	0.6
45	88.6(89.9)	12.5	−1.0	0.8
		Na_2SO_4		
0	230.8(191.1)	54.2	15.5	0.4
15	168.4(153.5)	33.3	9.4	0.4
30	139.2(121.5)	25.8	1.6	0.7
45	122.1(114.9)	19.4	−1.6	0.8
		$MgSO_4$		
0	183.4(169.6)	26.1	7.6	0.3
15	151.3(145.8)	21.0	3.9	0.5
30	129.6(130.5)	16.6	0.1	0.5
45	118.2(125.6)	14.3	−1.6	0.4

[a] The values of ϕ_K^0 (cm^3 mol^{-1} bar^{-1}) and $S_K{}^*$ determined by using eq 10 over the entire concentration range. [b] The values of ϕ_K^0 and b_K determined by using eq 11 below 1 m. [c] The average deviations between the measured ϕ_K's and those determined using the fitted values for eq 10.

in concentrated solutions is expected to follow the form of the equation[18]

$$\phi_K = \phi_K{}^0 + S_K{}^* I_V{}^{1/2} \tag{10}$$

where ϕ_K^0 is the apparent molal compressibility at infinite dilution, $S_K{}^*$ is the experimental slope, and I_V is the volume ionic strength, $I_V = \frac{1}{2}\Sigma\gamma_i Z_i{}^2 c$ (where c is the molarity, γ_i is the number of ions of charge, Z_i, formed from 1 molecule of electrolyte). The values of ϕ_K^0 and $S_K{}^*$, along with the average deviations from eq 10, for NaCl, $MgSO_4$, Na_2SO_4, and $MgCl_2$ solutions at 0, 15, 30, and $45°$ are given in Table III. The ϕ_K's are plotted vs. $I_V{}^{1/2}$ for NaCl, $MgSO_4$, Na_2SO_4, and $MgCl_2$ solutions in Figures 6-9.[13b]

Although eq 10 holds for the higher concentrations, the ϕ_K's of an electrolyte should approach the Debye-Hückel theoretical limiting law slope in dilute solutions. Therefore, the concentration dependence of ϕ_K can be expressed by

$$\phi_K = \phi_K{}^0 + S_K I_V{}^{1/2} + b_K I_V \qquad (11)$$

where $\phi_K{}^0$ is the apparent molal compressibility at infinite dilution, S_K is the theoretical limiting law slope, and b_K is the deviation from the theoretical slope. The theoretical limiting law slope can be calculated from

$$S_K = -[(\partial S_V/\partial P)_T + \beta^0 S_V/2] \qquad (12)$$

where S_V is the theoretical limiting law slope for the partial molal volume of the electrolyte.[4]

Using the high pressure $\partial \ln D/\partial P$, and D data of Owen, et al.,[19] and the high-pressure β data of Kell and Whalley,[8] we obtain[20,21] $10^4 S_K = 1.4$, 2.9, 4.2, and 5.3, respectively, at 0, 15, 30, and 45° for a 1–1 electrolyte. Values of the limiting law slope for polyvalent electrolytes can be calculated from these S_K's by multiplying by the valence factor, w (where $w = \frac{1}{2}\Sigma\gamma_i Z_i{}^2$).

Since extrapolation to infinite dilution from high concentrations using eq 10 may be in error, eq 11 can be used to more accurately extrapolate the partial molal compressibility to infinite dilution from data where $c \leq 1\ M$. The infinite dilution value, $\phi_K{}^0$, and the deviation constant, b_K, representing the deviation from the theoretical slope, can be found by plotting $[\phi_K - S_K I_V{}^{1/2}]$ vs. I_V. This relationship was found to be linear for these electrolytes when $c \leq 1.5\ M$. The $\phi_K{}^0$'s and b_K's, calculated by a least-squares fit, are given in Table III for aqueous NaCl, MgSO₄, Na₂SO₄, and MgCl₂ solutions. The $\phi_K{}^0$'s estimated in this manner differ by as much as 39×10^{-4} cm³ mol⁻¹ bar⁻¹ from the $\phi_K{}^0$'s extrapolated with eq 10. The $\phi_K{}^0$'s of NaCl solutions at various temperatures, determined by using eq 10 and 11 are compared in Table IV to the values determined from sound velocity data in dilute solutions.[2a] The results using eq 11 for extrapolation to infinite dilution are in good agreement with the sound velocity data. Thus, the $\phi_K{}^0$'s estimated by eq 11 are more reliable than those using eq 10. The internal consistency of the infinite dilution $\phi_K{}^0$'s for NaCl, MgCl₂, Na₂SO₄, and MgSO₄ can be examined by using the additivity principle, $\phi_K{}^0(\text{MgSO}_4) = \phi_K{}^0(\text{MgCl}_2) + \phi_K{}^0(\text{Na}_2\text{SO}_4) - 2\phi_K{}^0(\text{NaCl})$. Using the $\phi_K{}^0$'s obtained from eq 11, we obtain by additivity $-10^4 \phi_K{}^0(\text{MgSO}_4) = 169.3$, 145.9, 130.8, and 126.8 cm³ mol⁻¹ bar⁻¹, respectively, at 0, 15, 30, and 45°. These additivity estimates are in good agreement with the experimental values.

The $\phi_K{}^0$'s of NaCl, MgCl₂, Na₂SO₄, and MgSO₄ have been determined at 25° from sound velocity and direct high-pressure measurements by a number of workers[2,22-24] in concentrated solutions. A comparison of our $\phi_K{}^0$'s interpolated to 25° and those obtained by other workers[2,22-24] is given in Table V. The sound-derived (high concentration) results of Allam and Lee[2b] are in good agreement with our results (from eq 10) for NaCl, MgCl₂, and MgSO₄. The values given by Owen and Brinkley[22] for MgSO₄ and Na₂SO₄ appear to be too high when compared to our values. The low concentration sound-derived[3,23,24] ($\phi_K{}^0$)'s for NaCl are in good agreement with our values obtained from eq 11.

The temperature behavior of the $\phi_K{}^0$'s of NaCl, MgCl₂, Na₂SO₄, and MgSO₄ appears to be similar to that found for the $\phi_V{}^0$ in that the $\phi_K{}^0$'s increase with increasing temperature and appear to go through a maximum between 40 and 50°.

The b_K's for all of the electrolytes are positive at low temperatures and become smaller as the temperature is increased (i.e., $\partial b_K/\partial T$ is negative). This behavior is similar to the behavior of b_V, the deviation constant for the ϕ_V of the electrolytes.[4] The b_K's at various temperatures determined in this study have been found to be linearly related to b_V

$$b_K = a_1 + a_2 b_V \qquad (13)$$

where $10^4 a_1 = 3.14$, 2.72, -1.80, and 0.53; $10^4 a_2 = 8.098$, 1.242, 1.570, and 0.343, respectively, for NaCl, MgCl₂, Na₂SO₄, and MgSO₄ solutions. Since the b_K is directly related to b_V, the ion–ion interactions responsible for the magnitude and temperature dependence of b_K are related to the b_V behavior. A discussion of how b_V (and thus b_K) for electrolytes is related to ion–ion interactions is given elsewhere[4] and will not be repeated here.

The apparent molal compressibilities of aqueous MgSO₄ solutions can be used to estimate the apparent molal compressibility of the MgSO₄⁰ ion pair, $\phi_K(\text{MgSO}_4{}^0)$, and the apparent molal compressibility change, $\Delta\phi_K$, for the formation of the ion pair. Recently, general methods of examining molal volume data of electrolyte solutions in terms of ion-pair formation have been developed. Millero and Masterton[5] have applied these methods to determine the apparent molal volume of the MgSO₄⁰ ion pair, and the volume change for the formation of the ion pair. These methods may also be applied to compressibility data.

If Young's rule[25] is applied to the compressibility components of the solution (Mg²⁺, SO₄²⁻, and MgSO₄⁰), we obtain

$$\phi_K(\text{obsd}) = \alpha\phi_K(\text{Mg}^{2+},\ \text{SO}_4{}^{2-}) + (1 - \alpha)\phi_K(\text{MgSO}_4{}^0) \qquad (14)$$

where α is the fraction of free ions, $\phi_K(\text{obsd})$ is the observed apparent molal compressibility at total molality m_T, $\phi_K(\text{Mg}^{2+},\ \text{SO}_4{}^{2-})$ is the apparent molal compressibility of the free ions at $I = 4\alpha m_T$, and $\phi_K(\text{MgSO}_4{}^0)$ is the apparent molal compressibility of the ion pair.

TABLE IV: Comparison of the $\phi_K{}^0$'s of Aqueous NaCl Solutions Determined from Piezometric and Sound Velocity Data

Temp, °C	$-\phi_K{}^0 \times 10^4$, cm³ mol⁻¹ bar⁻¹	
	Present study[a]	Sound velocity[b]
0	75.6 (81.4)	75.7 ± 0.5
15	55.6 (60.1)	55.7 ± 0.8
30	42.2 (48.5)	42.5 ± 2.0
45	39.0 (42.4)	36.3 ± 2.9

[a] The $\phi_K{}^0$ values are those extrapolated from eq 11. The values in parentheses are those extrapolated from eq 10. [b] From ref 2a.

TABLE V: Comparison of the $\phi_K{}^0$'s of NaCl, MgCl₂, Na₂SO₄, and MgSO₄ Obtained by Various Workers at 25°

Salt	$-\phi_K{}^0 \times 10^4$, cm³ mol⁻¹ bar⁻¹	
	This study[a]	Other workers
NaCl	51.3 (45.9)	51.6[b,c] 52.0[d], 46.3[e], 46.7[f]
MgCl₂	100.4 (95.3)	101.7[b]
Na₂SO₄	145.4 (130.3)	154[d]
MgSO₄	135.7 (134.6)	134.5,[b] 153[d]

[a] The $\phi_K{}^0$'s, obtained from eq 10 and 11 at 0, 15, 30, and 45°, have been fitted to quadratic functions of temperature (to within $\pm 0.7 \times 10^{-4}$) and interpolated to yield these 25° values. The values in parentheses are those obtained from eq 11. [b] From ref 2b. [c] From ref 2a. [d] From ref 22. [e] From ref 3. [f] From ref 23 and 24.
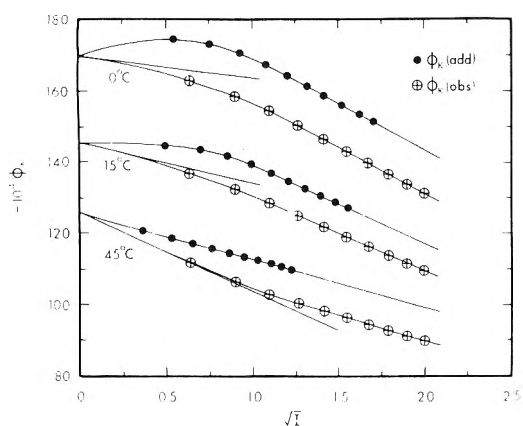
Figure 10. The observed and additivity ϕ_K for $MgSO_4$ vs. $I_V^{1/2}$ at 0, 15, and 45°. The straight lines are the limiting law slopes.

The apparent molal compressibility change for the formation of the ion pair, $\Delta\phi_K$, is given by the relation

$$\Delta\phi_K = \phi_K(MgSO_4^0) - \phi_K(Mg^{2+}, SO_4^{2-}) \quad (15)$$

By rearranging eq 14 and combining with eq 15, we obtain

$$\phi_K(MgSO_4^0) =$$
$$[\phi_K(obsd) - \alpha\phi_K(Mg^{2+}, SO_4^{2-})]/(1 - \alpha) \quad (16)$$

and

$$\Delta\phi_K(MgSO_4^0) =$$
$$[\phi_K(obsd) - \phi_K(Mg^{2+}, SO_4^{2-})]/(1 - \alpha) \quad (17)$$

The fraction of free ions, α, is determined from the work of Millero and Masterton,[5] who calculated α at 0, 25, and 50° from the following relation

$$\alpha = 1 - K_A\gamma_\pm^2 m_T \quad (18)$$

where K_A is the known association constant,[26,27] $\gamma_\pm$ is the stoichiometric activity coefficient of $MgSO_4$ solutions, and m_T is the total molality. The values of α used in this study at 15, 30, and 45° were interpolated from the results of Millero and Masterton.[5]

The $\phi_K(obsd)$ for $MgSO_4$ determined from eq 10 and 11 at 0, 15, and 45° are plotted vs. the square root of the volume ionic strength ($I_V^{1/2}$) and are shown in Figure 10. The ϕ_K's for the free ions Mg^{2+}, SO_4^{2-}, also given in Figure 10, were calculated from the additivity principle

$$\phi_K(Mg^{2+}, SO_4^{2-}) = \phi_K(MgCl_2) +$$
$$\phi_K(Na_2SO_4) - 2\phi_K(NaCl) \quad (19)$$

As discussed elsewhere,[5] we feel that the additivity estimate for the $\phi_K(Mg^{2+}, SO_4^{2-})$ is more reliable than values estimated using the Debye–Hückel limiting law (or its extensions). Since ion-pair formation may be important in Na_2SO_4 solutions, the ϕ_K for Na_2SO_4 used in eq 19 may be too high. This would result in a $\Delta\phi_K(MgSO_4^0)$ that would be too large.

The values for $\phi_K(MgSO_4^0)$, calculated from eq 16, are shown plotted vs. $I_V^{1/2}$ in Figure 11. The infinite dilution $\Delta\phi_K^0$ and ϕ_K^0 at various temperatures are given in Table VI. Since no studies have been made on the $\Delta\phi_K^0$ for the formation of $MgSO_4^0$, these results cannot be directly compared to other work. Fisher[28] has directly determined ΔV^0 for $MgSO_4^0$ from high-pressure conductance data; however his ΔV^0's do not appear to be pressure dependent (i.e., within his experimental error).
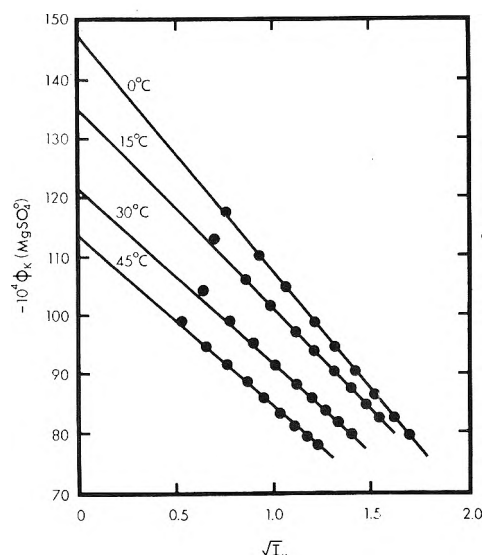
Figure 11. The ϕ_K for the $MgSO_4^0$ ion pair vs. $I_V^{1/2}$ at 0, 15, 30, and 45°.

TABLE VI: The $\bar{K}^0$ of $MgSO_4^0$ and the $\Delta\bar{K}^0$ for the Formation of $MgSO_4^0$ at Various Temperatures

Temp, °C	$-10^4\bar{K}^0(MgSO_4^0)^a$	$10^4\Delta\bar{K}^0(MgSO_4^0)$
0	146.3	23.3
15	134.1	11.7
30	120.3	10.2
45	115.2	10.4

^{a} The values of $\bar{K}^0$ and $\Delta\bar{K}^0$ are in units of $cm^3 \, mol^{-1} \, bar^{-1}$.

The $\phi_K^0(MgSO_4^0)$, like the electrolytes studied, appear to go through a maximum when plotted vs. temperature. This behavior is similar to the ϕ_V^0 of $MgSO_4^0$ determined by Millero and Masterton.[5]

The concentration dependence of ϕ_K and $\Delta\phi_K$ of $MgSO_4^0$ appear to increase with increasing ionic strength, which is similar to the ϕ_V behavior.[5] Since we cannot be certain that the concentration dependence of $\phi_K(Mg^{2+}, SO_4^{2-})$ obtained by additivity is correct, we cannot be sure that the concentration dependence of either ϕ_K or $\Delta\phi_K$ is correct.

Discussion

The infinite dilution compressibility data may be examined by using the simple model for hydration[4,29]

$$\bar{V}^0(ion) = \bar{V}^0(int) + \bar{V}^0(elect) \quad (20)$$

where $\bar{V}^0(int)$ is the intrinsic partial molal volume of the ion (the crystal volume, $2.52r^3$, and the void space volume) and $\bar{V}^0(elect)$ is the electrostriction partial molal volume. By differentiating eq 20 with respect to pressure, we obtain

$$\bar{K}^0(ion) = \bar{K}^0(int) + \bar{K}^0(elect) \quad (21)$$

where $K^0(int) = -\partial\bar{V}^0(int)/\partial P$ is the intrinsic partial molal compressibility and $\bar{K}^0(elect) = -\partial\bar{V}^0(elect)/\partial P$ is the electrostriction partial molal compressibility. Since the effect of pressure on the volume of crystals is small, one would expect $K^0(int)$ to be positive and close to zero.[30] Thus $K^0(ion)$ is due mainly to $\bar{K}^0(elect)$. The electrostriction $\bar{V}^0$ and $\bar{K}^0$ of ions can be examined by using a hydration model or by using the continuum model for ion–water interactions.

TABLE VII: Ionic Partial Molal Compressibilities of Some Ions at Various Temperatures

Ion	$-10^4 \bar{K}^0(\text{ion})$, cm³ mol⁻¹ bar⁻¹			
	0°	15°	30°	45°
Na⁺	49.6	36.5	27.7	25.6
Mg²⁺	77.4	65.3	64.3	63.0
Cl⁻	26.0	19.1	14.5	13.4
SO₄²⁻	91.9	80.6	66.2	63.8

If we use the continuum model, the $\bar{K}^0(\text{elect})$ is given by[30]

$$\bar{K}^0(\text{elect}) = B(Z^2/r) \tag{22}$$

where B is a constant related to the effect of pressure on the dielectric constant of pure water ($B = 6.946 \times 10^6[(1/D)(\partial^2 \ln D/\partial P^2) - (1/D)(\partial \ln D/\partial P)^2]$), Z is the charge on the ion, and r is the radius. Using the dielectric constant data of Owen, et al.,[19] we obtain $B = -5.3_5 \times 10^{-4}$, -8.3×10^{-4}, and $-11.2_5 \times 10^{-4}$ cm³ mol⁻¹ bar⁻¹, respectively, at 0, 25, and 50°. Using the value for B at 25°, we obtain $-10^4 K^0 = 8.7$, 51.1, 4.6, and 16.2, respectively, for Na⁺, Mg²⁺, Cl⁻, and SO₄²⁻. To compare these values with our values for the salts it is necessary to separate the $\bar{K}^0(\text{salt})$ into ionic values. Various estimates for the $\bar{K}^0$ of Cl⁻ have ranged from -6.1×10^{-4} to -39×10^{-4} cm³ mol⁻¹ bar⁻¹. Laliberté and Conway[31] obtained $\bar{K}^0(\text{Cl}^-) = -13 \times 10^{-4}$, based on an extrapolation of the $\bar{K}^0$ of R₄N⁻ halides to zero molecular weight of the cation. Noyes[30] obtained $\bar{K}^0(\text{Cl}^-) = -39 \times 10^{-4}$, based on an extrapolation using the continuum model with $\bar{K}^0(\text{int}) = 2.5 \times 10^{-4}r^3$. Glueckauf[32] obtained $\bar{K}^0(\text{Cl}^-) = -17.5 \times 10^{-4}$ by taking into account dielectric saturation effects. Since $\bar{K}^0(\text{ion}) \simeq \bar{K}^0(\text{elect}) \propto 1/r$ as a first approximation, we have divided the $\bar{K}^0$ of NaCl by assuming $\bar{K}^0(\text{Na}^+)/\bar{K}^0(\text{Cl}^-) = r(\text{Cl}^-)/r(\text{Na}^+)$. Using this simple assumption we obtain $10^4 K^0(\text{Cl}^-) = -26.0$, -19.1, -14.5, and -13.4 cm³ mol⁻¹ bar⁻¹ respectively, at 0, 15, 30, and 45°. The interpolated value of $10^4 K^0(\text{Cl}^-) = -16.0$ at 25° is in reasonable agreement with the value estimated by other workers. The ionic $\bar{K}^0$'s for Na⁺, Mg²⁺, Cl⁻, and SO₄²⁻ determined from our estimates of $\bar{K}^0(\text{Cl}^-)$ are given in Table VII.

Although the values of $\bar{K}^0(\text{ion}) = \bar{K}^0(\text{elect})$ calculated from the continuum model are of the same order of magnitude as the measured values, the theoretical values are too high and the temperature dependence incorrect. This is similar to what one finds when one compares the $\bar{V}^0(\text{elect})$ calculated from the continuum model. The smaller measured values of $\bar{V}^0(\text{elect})$ and $\bar{K}^0(\text{elect})$ (i.e., more negative) for ions can be attributed to dielectric saturation effects or to water structure effects.[2a,29]

Some workers[2a,5,33] have related $\bar{V}^0(\text{elect})$ to the hydration number, n_H, of an ion or electrolyte

$$\bar{V}^0(\text{elect}) = n_H(\bar{V}_E^0 - \bar{V}_B^0) \tag{23}$$

where $\bar{V}_E^0$ is the molar volume of the electrostricted water molecules and $\bar{V}_B^0$ is the molar volume of the bulk water molecules. If $\bar{V}^0(\text{int})$ and n_H are assumed to be independent of pressure, we obtain from eq 23

$$\frac{\partial \bar{V}^0(\text{ion})}{\partial P} = \frac{\partial \bar{V}^0(\text{elect})}{\partial P} = -n_H \frac{\partial \bar{V}_B^0}{\partial P} \tag{24}$$

Upon rearranging and substituting $\bar{K}^0(\text{ion}) = -\partial \bar{V}^0(\text{ion})/\partial P$ and $\beta_B^0 = -(1/\bar{V}_B^0)(\partial \bar{V}_B^0/\partial P)$, we obtain

$$n_H = -\bar{K}^0(\text{ion})/\beta_B^0 \bar{V}_B^0 \tag{25}$$

TABLE VIII: Hydration Numbers for Various Salts, Ion Pairs, and Ions Calculated from Partial Molal Compressibility Data at Various Temperatures

	0°	15°	25°	30°	45°
Salt					
NaCl	8.2	6.6	5.6	5.2	4.9
MgCl₂	14.1	12.3	11.7	11.5	11.2
Na₂SO₄	20.8	18.2	15.9	14.9	14.3
MgSO₄	18.5	17.3	16.5	16.0	15.6
Ion Pair					
MgSO₄⁰	15.9	15.9	15.2	14.9	14.3
Ion					
Na⁺	5.4	4.3	3.7	3.4	3.2
Mg²⁺	8.4	7.7	7.7	7.9	7.8
Cl⁻	2.8	2.3	2.0	1.8	1.7
SO₄²⁻	10.0	9.6	8.6	8.1	7.9

where β_B^0 is the isothermal compressibility of bulk water. Values of n_H calculated from eq 25 for the salts and ions are given in Table VIII. Our results are in good agreement with the hydration numbers obtained by Kaulgud[34] who used adiabatic compressibilities and workers who used other experimental methods.[35] Since $\bar{K}^0(\text{int})$ may not be equal to zero (possibly due to the effect of pressure on void space or packing), one can question the n_H values derived from the $\bar{K}^0$'s. Although many workers[35-37] have derived n_H's from compressibility data at high concentrations, we do not feel that these values are reliable due to interference from ion-ion interactions.[38]

The hydration numbers for all the salts decrease with increasing temperature (from 0 to 45°), which is what we would expect from molal volume data.[2a,29] Our n_H results for the individual ions also decrease with increasing temperature. The n_H for Mg²⁺ does not appear to change much with temperature.

If we use the compressibility derived hydration numbers with eq 20 and 23, it is possible to estimate $\bar{V}_E^0$. Using the semiempirical[29] $\bar{V}^0(\text{int}) = 4.48r^3$ and the $\bar{V}^0$ for the salts,[11] we obtain $\bar{V}_E^0 - \bar{V}_B^0 = -2.5$, -2.6, -2.7, and -2.8 (± 0.5) cm³/mol, respectively, at 0, 15, 30, and 45°. These values are in reasonable agreement with the -2.1 cm³/mol estimated by Padova.[33] The value of $\bar{V}_E^0 = 15.5 \pm 0.2$ cm³/mol for the molar volume of water in the electrostricted region is quite a lot larger than the crystal volume of water (6.6 cm³/mol) and the intrinsic volume corrected for packing effects (11.8 cm³/mol). These results indicate that the hydrated water molecules are not as tightly packed as one might expect. Since the n_H calculated from $\bar{K}^0$ data may include water molecules in outer hydration shells, the $\bar{V}_E^0$ cannot be equated to only the first layer or primary hydration.

Both the continuum model and the hydration model indicate the $\bar{V}^0(\text{elect})$ is directly proportional to $\bar{K}^0(\text{elect})$

$$\bar{V}^0(\text{elect}) = k\bar{K}^0(\text{elect}) \tag{26}$$

For the continuum model, k is given by

$$k = \frac{(\partial \ln D/\partial P)}{(\partial^2 \ln D/\partial P^2) - (\partial \ln D/\partial P)^2} \tag{27}$$

and for the hydration model

$$k = (\bar{V}_E^0 - \bar{V}_B^0)/\bar{V}_B^0 \beta_B^0 \tag{28}$$

At 25° the continuum model yields $k = 5.0 \times 10^3$ bars. A plot of $\bar{V}^0(\text{elect}) = \bar{V}^0(\text{salt}) - 4.48r^3$ vs. $\bar{K}^0(\text{salt})$ calculated from $\bar{K}^0(\text{salts})$ obtained by various workers[2,22-24] is shown
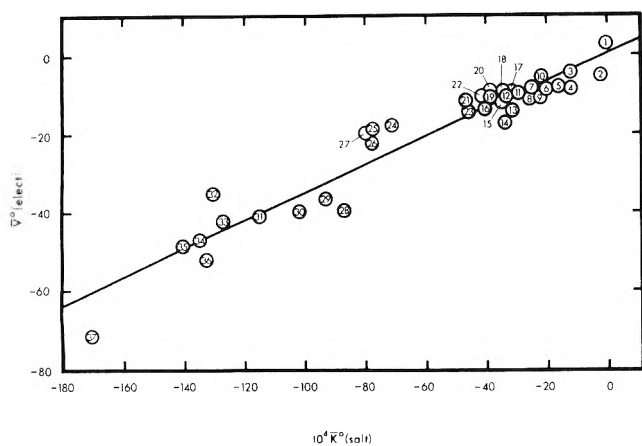
Figure 12. The $\bar{V}^0$(elect) vs. $\bar{K}^0$(elect) $\simeq \bar{K}^0$(salt) at 25° for various salts: (1) $C_2H_4O_2$; (2) NH_4I; (3) NH_4Br, NH_4NO_3; (4) HCl; (5) HNO_3; (6) NH_4Cl; (7) CsBr; (8) KI; (9) LiI; (10) KSCN; (11) KNO_3; (12) LiBr, KBr; (13) NaI; (14) $AgNO_3$; (15) $KHCO_3$; (16) NaBr, $NaNO_3$; (17) $LiNO_3$; (18) CsCl; (19) LiCl; (20) RbCl; (21) $KC_2H_3O_2$; (22) KCl; (23) NaCl; (24) NaF; (25) LiOH; (26) NaOH; (27) KOH; (28) $CaCl_2$; (29) $BeSO_4$; (30) $MgCl_2$; (31) $BaCl_2$; (32) Na_2SO_4; (33) $CdSO_4$; (34) $MgSO_4$; (35) $ZnSO_4$; (36) $CuSO_4$; (37) $LaCl_3$.

in Figure 12. As is quite apparent from this figure, $\bar{V}^0$(elect) does appear to be proportional to K^0(elect) $\simeq K^0$(ion). The slope, k, is found to be 3.6×10^3 which is in good agreement with the value obtained from the continuum model.

The volume and compressibility change for ion pair formation can also be examined by using the electrostatic theory and the hydration theory. Using the Fuoss methods,[39] the volume change for ion pair formation is given[5,40] by

$$\Delta \bar{V}_A^{\,0} = \frac{Z_+ Z_- Ne^2}{aD} \left(\frac{\partial \ln D}{\partial P} \right) - \beta RT \quad (29)$$

where a is the ion size parameter and the other symbols have their normal meaning. The βRT term (equal to 1.11 cm^3/mol at 25°) is needed because the Fuoss K_A is expressed in molar units. If we assume that a is not pressure dependent, we obtain

$$\Delta \bar{K}_A^{\,0} = \frac{-\partial \Delta \bar{V}_A^{\,0}}{\partial P} = \frac{-Z_+ Z_- Ne^2}{aD} \left[\frac{1}{D} \left(\frac{\partial^2 \ln D}{\partial P^2} \right) - \frac{1}{D} \left(\frac{\partial \ln D}{\partial P} \right) \right] + RT \left(\frac{\partial \beta}{\partial P} \right) \quad (30)$$

Using the dielectric constant data of Owen, et al.,[19] and the compressibility data of Kell and Whalley,[8] we obtain $10^4 \Delta K_A^0 = 7.2$, 13.8, and 19.5 cm^3 mol^{-1} bar^{-1}, respectively, at 0, 25, and 50°. As for the $\Delta \bar{V}_A^0$,[40] the $\Delta \bar{K}^0$'s predicted from the continuum model are in reasonable agreement with measured values ($10^4 \bar{K}^0 = 10.3$ at 25°). The continuum model predicts that $\Delta \bar{K}^0$ (as well as $\Delta \bar{V}^0$)[5] should increase with increasing temperature. The experimental ion pairing ΔK^0's (as well as the $\Delta \bar{V}^0$'s)[5] decrease with increasing temperature between 0 and $\sim 40°$ and appear to increase at higher ($>50°$) temperatures. This experimental behavior is similar to that observed for the formation of weak acids or bases.[4,41] Therefore, although the continuum model predicts reasonable values for the electrostriction volume and compressibility changes at a given temperature, it fails to predict the correct temperature dependence. This failure also holds for the temperature dependence of the electrostriction of ions.[4,29] If one assumes the electrostriction is inversely proportional to the

compressibility of the water, one arrives at the proper temperature dependence.[4,42] The inclusion of a compressibility term in the $\bar{V}^0$(elect) has been made by a number of workers.[4,42-48] At present it is not possible to state with certainty that the failure of the continuum model to predict the temperature dependence of $\bar{V}^0$(elect) or $\bar{K}^0$(elect) is due to the unique nature of water (between 0 and 50°) or an improper form for the electrostriction. Studies of the temperature dependence of $\bar{K}^0$ of electrolytes in other solvent systems (with different compressibilities and dielectric constants) could yield data to test the relationship of electrostriction to β of the solvent.

The hydration numbers for the ion pair, $MgSO_4^0$, calculated from eq 25 at various temperatures are given in Table VIII. The values at 0 and 25° are in reasonable agreement with those calculated from molal volume data using eq 23. For example, using $\bar{V}^0$(elect) = -48.2 and -38.2 cm^3/mol, respectively, at 0 and 25°, we obtain (using $\bar{V}_E^0 - \bar{V}_B^0 = -3$ cm^3/mol) $n_H = 16.1$ and 12.7 for the ion pair.

The large hydration numbers for $MgSO_4^0$ yield small values (1.3 to 2.5) for the Δn_H for ion pair formation (where Δn_H is the difference between the n_H for the products and reactants). Since the $MgSO_4^0$ ion pair exists in a number of forms (i.e., $Mg^{2+}[H_2O]_2SO_4^{2-}$; $Mg^{2+}[H_2O]$-SO_4^{2-}; $Mg^{2+}SO_4^{2-}$),[5,28,48] it is difficult to fully interpret the ΔK^0 or Δn_H in great detail.[5,48] The large n_H for $MgSO_4^0$ or small Δn_H for the formation of $MgSO_4^0$ is what one would expect if the pair is predominately an outer-sphere type. If the ion pair were a nonhydrated inner-sphere or contact type, one might assume that $\bar{K}^0(MgSO_4^0)$ or $n_H(MgSO_4^0) \simeq 0$. This would give $\Delta n_H = n_H(Mg^{2+} + SO_4^{2-}) = 16.3$ at 25°. By comparing these values for the formation of a contact ion pair with the actual values (1.3–2.5) one can estimate that 8–15% of the $MgSO_4^0$ exists in the contact form. This estimate is in reasonable agreement with values (10%) estimated from ultrasonic[48-50] and Raman spectral studies.[51]

The hydration model predicts that ΔK^0 for an ion pairing (or acid and base) formation should be proportional to $\Delta n_H \beta_B^0 \bar{V}_B^0$ and $\Delta \bar{V}^0$.[52] Thus the correlation of $\Delta \bar{V}^0$ vs. ΔK^0 that occurs for the ionization of weak acids and bases[53] also appears to hold for ion pairing processes.[54] A plot of $\Delta \bar{V}^0$ vs. $\Delta \bar{K}^0$ for the formation of ion pairs determined from direct equilibrium constant[28,55-57] measurements at various pressures are shown in Figure 13. The $\Delta \bar{V}^0$'s and ΔK^0's have been determined by fitting the equilibrium constants K_m at various applied pressures, P, to

$$RT \log \frac{K_m^P}{K_m^0} = -\Delta \bar{V}^0 P + 0.5 \Delta \bar{K}^0 P^2 \quad (31)$$

The $\Delta \bar{K}^0$ for the formation of $MgSO_4^0$ used in Figure 13 is the value determined in this study. As is quite apparent from this figure, $\Delta \bar{V}^0$ is linearly related to $\Delta \bar{K}^0$ for ion pair formation. The slope is equal to 3.7×10^3 bars, which is smaller than the value of 4.7×10^3 determined for the ionization of weak acids and bases.[53] Both values are in reasonable agreement with the values of k determined from the continuum model and the hydration model (eq 27 and 28). The ion pairing k is closer to the hydration model while the acid and base formation k is closer to the continuum model. Since the hydration model k is strongly dependent upon the value of $(\bar{V}_E^0 - \bar{V}_B^c)$, one cannot use these results to strongly support or not support the two models. For example, the experimental value[53] of $k = 4.6_7$
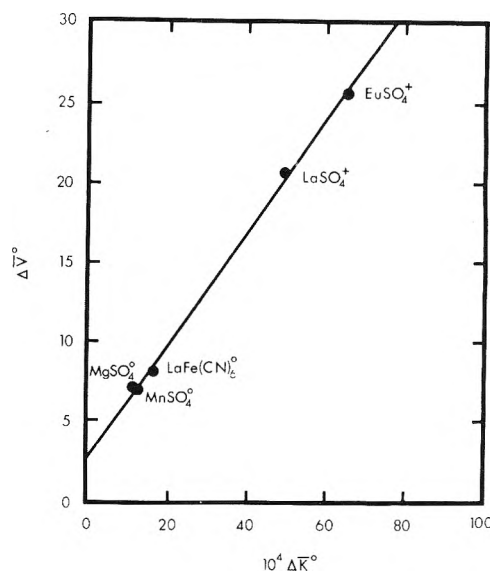
Figure 13. The ΔV^0 vs. ΔK^0 for the formation of various ion pairs at 25°.

$\times 10^3$ bars for the acids and bases gives $(\bar{V}_E{}^0 - V_B{}^0) = -3.8$ cm^3/mol, which is in reasonable agreement with the value of -3.0 cm^3/mol determined from the k from Figure 12.

To summarize our results, the infinite dilution K^0's for ions and the formation of ion pairs can be examined by using a hydration model or the continuum model. Both appear to give reasonable estimates for the electrostriction at a given temperature; however, the continuum model fails to predict the correct temperature dependence. The $\bar{K}^0$ of salts has been used to estimate the decrease in volume $(-3.0$ cm^3/mol) of transferring a water molecule from the bulk phase to the electrostriction region. From the hydration numbers for the formation of MgSO$_4{}^0$, we have estimated that 8–15% of MgSO$_4{}^0$ exists as a contact ion pair. The ΔK^0 for ion pair formation has been found to be proportional to ΔV^0 as predicted by both the hydration model and the continuum model. At present it is not possible to state which model is perferred.

In future work we plan to determine the K^0 for a number of ions (of various charges and radii) so that we can attempt to determine the importance of $\bar{K}^0(\mathrm{int})$ and further test the continuum and hydration models.

Supplementary Material Available. Tables I and II and Figures 2–9 will appear following these pages in the microfilm edition of this volume of the journal. Photocopies of the supplementary material from this paper only or microfiche (105 × 148 mm, 24× reduction, negatives) containing all of the supplementary material for the papers in this issue may be obtained from the Journals Department, Americal Chemical Society, 1155 16th St., N.W., Washington, D. C. 20036. Remit check or money order for $4.00 for photocopy or $2.00 for microfiche, referring to code number JPC-74-1636.

References and Notes

(1) (a) Scientific Contribution No. 1764 from the University of Miami, Rosenstiel School of Marine and Atmospheric Science, Miami, Florida 33149. (b) Taken in part from a thesis submitted by G. K. Ward in partial fulfillment of the requirements of the Master of Science degree, University of Miami.
(2) (a) H. S. Harned and B. B. Owen, "The Physical Chemistry of Electrolyte Solutions," ACS Monograph Series, No. 137, Reinhold, New York, N. Y., 1958; (b) D. S. Allam and W. H. Lee, *J. Chem. Soc. A*, 5 (1966).
(3) B. B. Owen and P. L. Kronick, *J. Phys. Chem.*, **65**, 84 (1961).
(4) F. J. Millero, *Chem. Rev.*, **71**, 147 (1971).
(5) F. J. Millero and W. L. Masterton, *J. Phys. Chem.*, submitted for publication.
(6) F. J. Millero, R. W. Curry, and W. Drost-Hansen, *J. Chem. Eng. Data*, **14**, 422 (1969).
(7) F. K. Lepple and F. J. Millero, *Deep-Sea Res.*, **18**, 1233 (1971).
(8) G. S. Kell and E. Whalley, *Phil. Trans. Roy. Soc.*, **258**, 565 (1965).
(9) G. S. Kell, *J. Chem. Eng. Data*, **15**, 119 (1970).
(10) F. J. Millero, *Rev. Sci. Instrum.*, **38**, 1441 (1967).
(11) F. J. Millero and J. H. Krox, *J. Chem. Eng. Data*, **18**, 407 (1973).
(12) M. Diaz-Peña and M. L. McGlashan, *Trans. Faraday Soc.*, **55**, 2018 (1959).
(13) (a) F. J. Millero and F. K. Lepple, *J. Chem. Phys.*, **54**, 946 (1971). (b) See paragraph at end of paper regarding supplementary material.
(14) G. K. Ward, Masters Thesis, University of Miami, 1973.
(15) L. Hall, *Phys. Rev.*, **73**, 775 (1948).
(16) F. S. Feates and D. J. G. Ives, *J. Chem. Soc.*, 2798 (1956).
(17) G. S. Kell, *J. Chem. Eng. Data*, **12**, 66 (1967).
(18) A. F. Scott and R. W. Wilson, *J. Phys. Chem.*, **38**, 951 (1934).
(19) B. B. Owen, R. C. Miller, C. E. Milner, and H. L. Cogan, *J. Phys Chem.*, **65**, 2065 (1961).
(20) F. J. Millero, *J. Solution Chem.*, **2**, 1 (1973).
(21) F. J. Millero in "The Sea," Vol. 5, E. Goldberg, Ed., Wiley-Interscience, New York, N. Y., in press.
(22) B. B. Owen and S. R. Brinkley, *Chem. Rev.*, **29**, 461 (1941).
(23) B. B Owen and H. L. Simmons, *J. Phys. Chem.*, **61**, 479 (1957)
(24) R. Garnsey, R. J. Boe, R. Mahoney, and T. A. Litovitz, *J. Chem. Phys.*, **50**, 5222 (1969).
(25) T. F. Young and M. B. Smith, *J. Phys. Chem.*, **58**, 716 (1954).
(26) V. S. K. Nair and G. N. Nancollas, *J. Chem. Soc.*, 3706 (1958).
(27) E. C. Righellato and C. W. Davies, *Trans. Faraday Soc.*, **26**, 592 (1930).
(28) F. H. Fisher, *J. Phys. Chem.*, **66**, 1607 (1962).
(29) F. J. Millero in "Water and Aqueous Solutions," R. A. Horne, Ed., Wiley-Interscience, New York, N. Y., 1972, Chapter 13.
(30) R. M. Noyes, *J. Amer. Chem. Soc.*, **86**, 971 (1964).
(31) L. H. Laliberité and B. E. Conway, *J. Phys. Chem.*, **74**, 4116 (1970).
(32) E. Glueckauf, *Trans. Faraday Soc.*, **64**, 2423 (1968).
(33) J. Padova, *J. Chem. Phys.*, **39**, 1552 (1963); **40**, 691 (1964).
(34) M. V. Kaulgud, *Z. Phys. Chem.*, **47**, 24 (1965).
(35) J. O. M. Bockris and P. P. S. Saluja, *J. Phys. Chem.*, **76**, 2140 (1972).
(36) R. H. Stokes and R. A. Robinson, "Electrolyte Solutions," Butterworths, London, 1953.
(37) A. Passynski, *Acta Physicochim. USSR*, **8**, 385 (1938).
(38) J. E. Desnoyers, *J. Phys. Chem.*, **77**, 567 (1973).
(39) R. M. Fuoss, *J. Amer. Chem. Soc.*, **80**, 5059 (1958).
(40) P. Hemmes, *J. Phys. Chem.*, **76**, 895 (1972).
(41) F. J. Millero, E. V. Hoff, and L. Kahn, *J. Solution Chem.*, **1**, 309 (1972).
(42) T. J. Webb, *J. Amer. Chem. Soc.*, **48**, 2589 (1926).
(43) L. G. Hepler, *J. Phys. Chem.*, **61**, 1426 (1957).
(44) S. W. Benson and C. J. Copeland, *J. Phys. Chem.*, **67**, 1194 (1963).
(45) H. M. Evjen and F. Zwicky, *Phys. Rev.*, **33**, 860 (1929).
(46) F. Zwicky, *Phys. Z.*, **26**, 664 (1925); **27**, 271 (1926); *Proc. Nat. Acad. Sci. U. S.*, **12**, 86 (1926).
(47) W. L. Marshall, *J. Phys. Chem.*, **74**, 346 (1970).
(48) M. Eigen and K. Tamm, *Z. Elektrochem.*, **66**, 93, 107 (1962).
(49) F. H. Fisher, *J. Acoust. Soc.*, **38**, 805 (1965).
(50) G. Atkinson and S. Petrucci, *J. Phys. Chem.*, **70**, 3122 (1966).
(51) A. R. Davis and B. G. Oliver, *J. Phys. Chem.*, **77**, 1315 (1973).
(52) N. A. North, *J. Phys. Chem.*, **77**, 931 (1973).
(53) D. A. Lown, H. R. Thirsk, and Lord Wynne-Jones, *Trans. Faraday Soc.*, **64**, 2073 (1968).
(54) R. T. Emmet and F. J. Millero, Paper presented at American Chemical Society Meeting-In-Minature, Gainesville, Fla., May, 1971, ABSTRACT No. 53, F.L.A.C.S., Vol. XXIV.
(55) F. H. Fisher and D. F. Davis, *J. Phys. Chem.*, **69**, 2595 (1965); **71**, 819 (1967).
(56) C. F. Hale and F. H. Spedding, *J. Phys. Chem.*, **76**, 2925 (1972).
(57) S. D. Hamann, P. J. Pearce, and W. Strauss, *J. Phys. Chem.*, **68**, 375 (1964).

Measurement and Interpretation of Activity Coefficients for Aromatic Solutes at Infinite Dilution in *n*-Octadecane and *n*-Hexadecyl Halide Solvents

G. M. Janini and D. E. Martire*

Department of Chemistry, Georgetown University, Washington, D. C. 20007 (Received January 21, 1974)

Activity coefficients in the range 30–60° are obtained by gas–liquid chromatography for *n*-heptane (N) and eleven homonuclear aromatic solutes (Z) at infinite dilution in *n*-octadecane (R) and three *n*-hexadecyl halide solvents (Y): chloride, bromide, and iodide. From these data interaction parameter differences $\Delta\chi$ (= $\chi_{RZ} - \chi_{YZ} - \chi_{RN} + \chi_{YN}$) are determined and are related to molecular energetic parameters through a first-order perturbation treatment. Comparison with experiment verifies the predicted (a) linear relation between $\Delta\chi$ and ϵ_{ZZ} (pairwise potential energy well depth per segment) in a given solvent Y, (b) linear relation between $\Delta\chi$ and ϵ_{YY} for a given solute Z, and (c) temperature dependence of $\Delta\chi$. The nature of these aromatic–haloalkane interactions is discussed and it is concluded that they are predominantly electrostatic in nature.

Introduction

Elution gas–liquid chromatography (glc) is a rapid and accurate technique for determining infinite dilution solute activity coefficients (γ_2^{∞}) in high molecular weight solvents.[1,2] In recent years glc has provided much of the necessary excess free energy data for testing current theories of nonelectrolytic solutions of molecules of different size.[2-10] This paper represents a further contribution to the study of molecular interactions between unlike molecules in binary mixtures through glc. γ_2^{∞} values are reported for *n*-heptane (the reference solute) and eleven aromatic solutes in four solvents: the reference solvent *n*-octadecane, *n*-hexadecyl chloride, *n*-hexadecyl bromide, and *n*-hexadecyl iodide. The results are interpreted by utilizing a corresponding states approach for mixtures of molecules of different size[10] in conjunction with a first-order perturbation treatment of the energetic terms.[7]

Theoretical

Recently, a refined version of Prigogine's[11] corresponding states theory of chain molecule mixtures was successfully employed in the prediction of the excess properties of *n*-alkane mixtures.[10] In its most general form, the resulting expression for γ_2^{∞} is given by[8,10]

$$\ln \gamma_2^{\infty} = \ln \gamma_2^{c} + \ln \gamma_2^{e} + \ln \gamma_2^{s} \quad (1)$$

where the superscripts c, e, and s refer to, respectively, the combinatorial, energetic, and structural contributions to $\ln \gamma_2^{\infty}$. The combinatorial part is given by

$$\ln \gamma_2^{c} = \ln \frac{V_2}{V_1} + \left(1 - \frac{V_2}{V_1}\right) \quad (2)$$

where V_k is the hard-core volume of component k (1 = solvent, 2 = solute). The sum of the energetic and structural terms is usually referred to as the interaction parameter χ, *i.e.*

$$\ln \gamma_2^{e} + \ln \gamma_2^{s} = \chi^{e} + \chi^{s} = \chi \quad (3)$$

Combining eq 1–3 and dropping the superscript ∞, we have

$$\ln \gamma_2 = \ln \frac{V_2}{V_1} + \left(1 - \frac{V_2}{V_1}\right) + \chi^{e} + \chi^{s} \quad (4)$$

Thus, if it is one's intention to examine the energetics of solute–solvent interactions in a given system, account must be taken of the structural (or "free volume"[8,9,12]) contribution χ^{s}. Unfortunately, a quantitative evaluation of χ^{s} requires quite accurate values for the temperature dependence of the solute and solvent densities,[8,12,13] information which may not be available. One way of circumventing this problem is to also study the solute of interest in a "reference" solvent (R) which is closely related and similar in size, shape, and structure to the solvent of interest (Y), so that the thermal expansion coefficients of R and Y are approximately equal and, hence, $\chi_Y^{s} \approx \chi_R^{s}$.[8,9,12,13] For example, if Y is di-*n*-octyl ether, R might be *n*-heptadecane. Then, from eq 4

$$\ln \left(\frac{\gamma_2^{R}}{\gamma_2^{Y}}\right) = \ln \frac{V_Y}{V_R} + V_2\left(\frac{1}{V_Y} - \frac{1}{V_R}\right) + \chi_R^{e} - \chi_Y^{e} \quad (5)$$

A further useful simplification, from the points of view of both experimental accuracy (see later) and treatment of the energetic terms (see below), is to introduce a nonpolar reference solute (N) belonging to the same homologous series as R (*e.g.*, *n*-hexane) which is studied along with the solute of interest (Z) in solvents R and Y. Then, from eq 5

$$\ln \left(\frac{\gamma_Z^{R}\gamma_N^{Y}}{\gamma_Z^{Y}\gamma_N^{R}}\right) = (V_Z - V_N)(V_Y^{-1} - V_R^{-1}) + \chi_{RZ}^{e} - \chi_{YZ}^{e} - \chi_{RN}^{e} + \chi_{YN}^{e} \quad (6)$$

where χ_i^{e} is the energetic contribution to the interaction parameter of solute j in solvent i. Finally, if $V_Z \approx V_N$ and/or $V_Y \approx V_R$, eq 6 yields

$$\ln \left(\frac{\gamma_Z^{R}\gamma_N^{Y}}{\gamma_Z^{Y}\gamma_N^{R}}\right) \approx \Delta\chi \approx \Delta\chi^{e} \quad (7)$$

where $\Delta\chi^{e} \equiv \chi_{RZ}^{e} - \chi_{YZ}^{e} - \chi_{RN}^{e} + \chi_{YN}^{e}$. Again, it is assumed in eq 7 that $\Delta\chi^{s} \approx 0$, by virtue of a proper choice for the reference solvent.

To relate $\Delta\chi^{e}$ to molecular energetic parameters, we take[7,10,14]

$$\chi_{ij}^{e} = (U_N/RT)d_{ij} \quad (8)$$

TABLE I: Hard-Core Volumes (V_k) and Molecular Energetic Parameters (δ_k) for Solutes and Solvents

Solvents	V_k, cm³ mol⁻¹	δ_k
n-Octadecane (R)	377.1	0.0316
1-Chlorohexadecane	349.7	0.1546
1-Bromohexadecane	354.5	0.1718
1-Iodohexadecane	366.6	0.1952
n-Heptane (N)	152.2	0.0000
Benzene	93.75	0.2233
Toluene	113.7	0.2085
Ethylbenzene	132.7	0.1957
o-Xylene	131.4	0.2263
m-Xylene	133.0	0.1957
p-Xylene	133.7	0.1917
n-Propylbenzene	153.0	0.1789
Isopropylbenzene	152.4	0.1680
Mesitylene	151.7	0.1818
Chlorobenzene	111.3	0.2974
Bromobenzene	116.5	0.3587

where U_N is the configurational internal energy of N and d_{ij} is given by

$$d_{ij} = \frac{2\epsilon_{ij} - \epsilon_{ii} - \epsilon_{jj}}{\epsilon_{NN}} \qquad (9)$$

where the ϵ's refer to pairwise potential energy well depths *per segment* (or *per unit hard core volume*).[10,11] Combining eq 7–9, one obtains

$$\ln\left(\frac{\gamma_Z{}^R\gamma_N{}^Y}{\gamma_Z{}^Y\gamma_N{}^R}\right) \approx \Delta\chi^e =$$
$$\frac{2U_N}{RT}\left(\frac{\epsilon_{RZ} - \epsilon_{RN} + \epsilon_{YN} - \epsilon_{YZ}}{\epsilon_{NN}}\right) \qquad (10)$$

Since N is chosen to belong to the same homologous series as R (and, thus, is closely related to Y), the usual geometric mean combining rule will be assumed for ϵ_{RN} and ϵ_{YN}, *i.e.*

$$\epsilon_{ij} = (\epsilon_{ii}\epsilon_{jj})^{1/2} \qquad \text{(with } j = N) \qquad (11)$$

However, since Z might be chemically dissimilar to R and Y, allowance should be made for possible deviations from eq 11. Hence, we take

$$\epsilon_{ij} = \zeta_i(\epsilon_{ii}\epsilon_{jj})^{1/2} \qquad \text{(with } j = Z) \qquad (12)$$

where ζ_i is close to unity. Combining eq 10–12, expanding $(\epsilon_{ii}/\epsilon_{NN})^{1/2}$ and $(\epsilon_{jj}/\epsilon_{NN})^{1/2}$ and keeping first-order terms only,[7] we obtain

$$\Delta\chi^e = \frac{2U_N}{RT}\left[\left(1 + \frac{\delta_R}{2}\right)\left\{\zeta_R\left(1 + \frac{\delta_Z}{2}\right) - 1\right\} - \right.$$
$$\left.\left(1 + \frac{\delta_Y}{2}\right)\left\{\zeta_Y\left(1 + \frac{\delta_Z}{2}\right) - 1\right\}\right] \qquad (13)$$

where

$$\delta_R \equiv (\epsilon_{RR}/\epsilon_{NN}) - 1$$
$$\delta_Y \equiv (\epsilon_{YY}/\epsilon_{NN}) - 1 \qquad (14)$$
$$\delta_Z \equiv (\epsilon_{ZZ}/\epsilon_{NN}) - 1$$

and all the δ's are small compared to unity.

Experimental Section

The solvents n-hexadecyl chloride (HC) and n-hexadecyl bromide (HB) were obtained from Humphrey Chemical Co., as was the reference solvent (R) n-octadecane (OD). The solvent n-hexadecyl iodide (HI) was obtained

TABLE II: Comparison of Experimental Activity Coefficients $(\gamma_2{}^\infty)$

System	T, °C	This study[a]	Bristol group	Ref
n-C₇–n-C₁₈	35	0.903[b]	0.896	3
Benzene–n-C₁₈	30	1.001	1.001	4
	40	0.961	0.966	4
	50	0.930	0.927	4

[a] Data listed in microfilm edition. [b] Interpolated value.

from Eastman Kodak. OD had a stated purity in excess of 99.5% and was not purified further. HC and HB were purified by vacuum distillation, while traces of iodine were removed from HI by drying in a vacuum oven at 60° for 10 hr. High-temperature glc analysis of OD and the three purified solvents indicated purities in excess of 99.5%. The nonpolar reference solute (N) n-heptane and the eleven homonuclear aromatic solutes chosen for this study (see Table I) were used without further purification (solute purity is not an important consideration in these glc studies).

The method of column preparation and analysis, the glc apparatus used, and the procedure followed for obtaining specific retention volumes $(V_g{}^0)$ are described elsewhere.[2] $V_g{}^0$'s were measured for the 48 binary systems at 30, 40, 50, and 60° (see the microfilm edition for values). The uncertainty in $V_g{}^0$ is estimated to be about 0.5%.[2]

Results and Data Reduction

Infinite dilution activity coefficients (γ_2) for the twelve solutes in each of the four solvents were calculated at 30, 40, 50, and 60° from the $V_g{}^0$ data using the usual procedure and equations[2] (see the microfilm edition for values). The uncertainty in $\ln\gamma_2$ is estimated to be ±0.007.[2] Some of our results are compared with available literature values[3,4] in Table II, where the excellent agreement (±0.004 in $\ln\gamma_2$, on the average) is evident. $V_g{}^0$ values were also determined at 45° by interpolation of the linear $V_g{}^0$ *vs.* reciprocal temperature plots, and are listed in Table III along with the corresponding γ_2 values.

Hard-core volumes (V_k) were found through Kreglewski's procedure[15] of determining molar volumes at $T = 0.6T^c$, where T^c is the critical temperature. The necessary densities[16] and critical temperatures[17] were obtained from available compilations. For the haloalkane solvents the contribution of the halogen group to V_k was determined by applying Kreglewski's method to the lower molecular weight homologs for which the necessary data are available.[16,17] The contributions of methylene and methyl groups to V_k are known.[10] The V_k values are listed in Table I.

The total interaction parameter χ was calculated through eq 4 for each binary system at 30, 40, 50, 60 (values listed in the microfilm edition), and 45° (see Table III). From these, the $\Delta\chi$ values $(\chi_{RZ} - \chi_{YZ} - \chi_{RN} + \chi_{YN})$ were determined for the aromatic (Z)–alkyl halide (Y) systems at each temperature and are listed for 45° in Table IV. Alternatively, $\Delta\chi$ could have been directly computed through eq 6 (or, with minimal error, eq 7), where it is assumed that $\Delta\chi \approx \Delta\chi^e$, *i.e.*, that $\Delta\chi^s \approx 0$. Note that, since[2]

$$\ln\left[\frac{\gamma_Z{}^R\gamma_N{}^Y}{\gamma_N{}^R\gamma_Z{}^Y}\right] = \ln\left[\frac{(V_g{}^0)_N{}^R(V_g{}^0)_Z{}^Y}{(V_g{}^0)_Z{}^R(V_g{}^0)_N{}^Y}\right] = \ln\left[\frac{\beta_Y}{\beta_R}\right] \qquad (15)$$

where β_i (the retention time of Z relative to that of N on a

TABLE III: Solute Specific Retention Volumes $(V_g{}^0)$ in cm³ g⁻¹, Infinite Dilution Activity Coefficients $(\gamma_2{}^\infty)$, and Interaction Parameters (χ) at 45°

Solute	Solvent	$V_g{}^0$				$\gamma_2{}^\infty$				χ			
		OD	HC	HB	HI	OD	HC	HB	HI	OD	HC	HB	HI
n-Heptane		661.5	545.0	457.9	378.3	0.893	1.057	1.075	1.128	0.198	0.324	0.347	0.415
Benzene		321.7	390.9	339.5	289.2	0.944	0.587	0.746	0.759	0.584	0.308	0.302	0.343
Toluene		996.8	1186	1031	871.4	0.914	0.749	0.736	0.755	0.410	0.159	0.152	0.200
Ethylbenzene		2449	2912	2541	2150	0.994	0.816	0.799	0.818	0.390	0.144	0.132	0.177
o-Xylene		3531	4301	3762	3176	0.957	0.767	0.749	0.769	0.359	0.089	0.074	0.122
m-Xylene		2990	3522	3061	2571	0.922	0.764	0.751	0.774	0.314	0.077	0.069	0.121
p-Xylene		2953	3469	3004	2519	0.892	0.741	0.731	0.756	0.278	0.044	0.039	0.093
n-Propylbenzene		6031	7059	6163	5206	1.020	0.850	0.832	0.853	0.328	0.102	0.088	0.133
Isopropylbenzene		4491	5230	4538	3804	1.040	0.871	0.858	0.887	0.349	0.128	0.121	0.174
Mesitylene		8771	10170	8850	7448	0.935	0.787	0.773	0.796	0.246	0.029	0.019	0.067
Chlorobenzene		1875	2424	2119	1799	1.056	0.797	0.779	0.795	0.570	0.236	0.222	0.267
Bromobenzene		4245	5727	5102	4443	1.209	0.874	0.838	0.834	0.673	0.298	0.265	0.288

TABLE IV: $\Delta\chi$ $(\approx \Delta\chi^e)$ Values at 45°

Solute	Solvent	HC	HB	HI
Benzene		0.402	0.431	0.458
Toluene		0.377	0.407	0.427
Ethylbenzene		0.372	0.403	0.430
o-Xylene		0.396	0.419	0.454
m-Xylene		0.363	0.394	0.410
p-Xylene		0.360	0.388	0.402
n-Propylbenzene		0.352	0.389	0.412
Isopropylbenzene		0.347	0.377	0.392
Mesitylene		0.343	0.376	0.396
Chlorobenzene		0.460	0.497	0.520
Bromobenzene		0.501	0.557	0.607

column containing solvent i is known to within ±0.2%, the experimental uncertainty in $\Delta\chi$ is estimated to be ±0.003.

In order to assess the magnitude of $\Delta\chi$, the following expression[10,18] was employed

$$\chi_{ij}{}^s = \frac{C_{p_j}}{2R}\left(1 - \frac{T_j{}^*}{T_i{}^*}\right)^2 \qquad (16)$$

where $\Delta\chi^s \equiv \chi_{RZ}{}^s - \chi_{YZ}{}^s - \chi_{RN}{}^s + \chi_{YN}{}^s$, R is the gas constant, C_{pj} is the solute configurational heat capacity, and $T_j{}^*/T_i{}^*$ is the ratio of temperature reduction parameters. Assuming that our set of solutes and solvents follows the same corresponding states behavior, the T^* ratios were roughly approximated from available temperature dependence of liquid density data[16] by the Patterson–Bardin[13] approach. Briefly, the T^* ratios were taken to be the ratios of the temperatures at which the components have the same αT value $(1/3)$, where α is the thermal expansion coefficient. The C_{pj}'s were approximated from enthalpies of vaporization (ΔH),[16] through the expression

$$C_{p_j} \approx -\frac{d\Delta H_j}{dT} + R \qquad (17)$$

Typically, $\Delta\chi^s$ was found to be of the order of +0.03, thus verifying the assumption utilized in eq 6 and 7. Hence, the $\Delta\chi$ values in Table IV will be referred to as $\Delta\chi^e$ terms, and will be analyzed via eq 13.

Treatment of $\Delta\chi^e$ Values Through Eq 13

The configurational internal energy (U_N) of the reference solute n-heptane is -32.76 kJ/mol at 45°.[10,16] δ_R and the δ_Z's listed in Table I were evaluated through Kreglewski's[15] successful semiempirical approach, where ϵ_{kk} is shown to be proportional to $T_k{}^c/(V_k)^{1/3}$. Accordingly, from eq 14
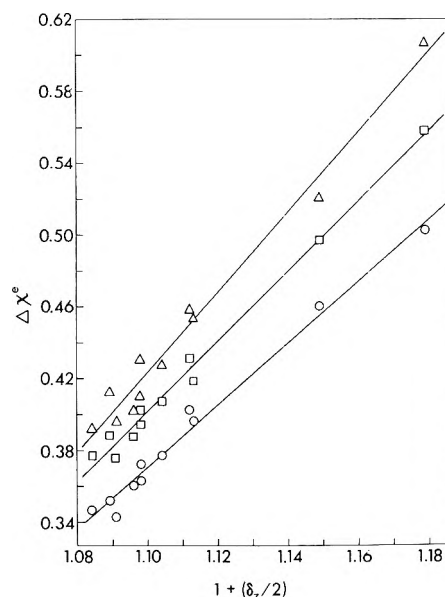
Figure 1. Plots of $\Delta\chi^e$ (at 45°) against $1 + (\delta_Z/2)$. See eq 19 and Table V: O, HC; □, HB; △, HI.

$$\delta_k = \frac{\epsilon_{kk}}{\epsilon_{NN}} - 1 = \frac{T_k{}^c/(V_k)^{1/3}}{T_N{}^c/(V_N)^{1/3}} - 1 \qquad (18)$$

where $T_N{}^c/(V_N)^{1/3}$ is 101.2 deg/cm mol$^{1/3}$. Rearranging eq 13 we have

$$\Delta\chi^e = \frac{2U_N}{RT}\left[\left\{\zeta_R\left(1 + \frac{\delta_R}{2}\right) - \zeta_Y\left(1 + \frac{\delta_Y}{2}\right)\right\}\left\{1 + \frac{\delta_Z}{2}\right\} + \left\{\frac{\delta_Y - \delta_R}{2}\right\}\right] \qquad (19)$$

which is of the form $\Delta\chi^e = A + B\{1 + (\delta_Z/2)\}$. Thus, eq 19 suggests that a plot of $\Delta\chi^e$ vs. $[1 + (\delta_Z/2)]$ for a given solvent Y should be linear, with δ_Y determinable from the intercept and a relationship between ζ_Y and ζ_R obtainable from the slope. Plots of $\Delta\chi^e$ vs. $[1 + (\delta_Z/2)]$ are shown in Figure 1 for HC, HB, and HI, and the least-squares intercepts and slopes are given in Table V. The deviation of the experimental data points from the best straight line is, on the average, ±0.007 in $\Delta\chi^e$. The values of δ_Y determined from the intercepts A are listed in Table I. Taking $\zeta_Y = \zeta_R + \Delta$ (where $\Delta \ll 1$) and assuming that ζ_Y is constant for all YZ pairs studied here, the following equations are obtained from eq 19 and the observed slopes (Table V)

$$HC \quad 0.06054\zeta_Y + \Delta = 0.06846$$

$$HB \quad 0.06901\zeta_Y + \Delta = 0.07725 \qquad (20)$$

$$HI \quad 0.08053\zeta_Y + \Delta = 0.08850$$

Least-squares analysis of eq 20 yields values of $\zeta_Y = 1.001$ and $\Delta = +0.008$; hence $\zeta_R = 0.993$. This implies aromatic-haloalkane segmental interactions marginally stronger than the geometric mean values and aromatic-alkane segmental interactions somewhat weaker, both being reasonable possibilities,[15,19] as is the trend in unlike interaction ϵ_{ij}: HI > HB > HC > OD (see Table I, and eq 11, 12, and 14).

According to eq 13 a plot of $\Delta\chi^e$ vs. $[1 + (\delta_Y/2)]$ for a given solute Z should yield a straight line, from which ζ_Y can be determined from the slope and ζ_R from the intercept. Utilizing the δ values in Table I, such plots were made and least-squares slopes and intercepts were obtained for each solute. Average values of $\zeta_Y = 1.003$ and $\zeta_R = 0.995$ were found, in excellent agreement with those reported above. Also, the deviation of the $\Delta\chi^e$ data points from the best straight line averaged ±0.004.

To further test the applicability of eq 13 and the validity of the determined molecular parameters, the temperature dependence of $\Delta\chi^e$ was examined. Least-squares values of $d\Delta\chi/dT^{-1}$ were calculated for each aromatic-haloalkane system from the experimental $\Delta\chi$ values in the temperature range 30–60°. (The χ results are tabulated in the microfilm edition.) Typically, $\Delta\chi$ decreases by about 0.023 units for a 10° increase in temperature, and the experimental uncertainty in $d\Delta\chi/dT^{-1}$ is substantial (about ±15%). Accordingly, the experimental values for a given solvent (listed in Table V along with the corresponding standard deviations) were determined by taking the average value of $d\Delta\chi/dT^{-1}$ over all eleven aromatic solutes. The large standard deviations are due in part to experimental error and in part to systematic solute-to-solute differences. The predicted values were computed as follows. The molar heat of vaporization of N is given by

$$\Delta H_N = D_N - E_N t \qquad (21)$$

where D_N and E_N are tabulated constants[16] and t is the temperature in °C. Thus, the configurational internal energy of N can be written as

$$U_N = -\Delta H_N + RT = -(D_N + 273.2E_N) + (E_N + R)T \qquad (22)$$

where T is the temperature in K. Combining eq 13 and 22, and differentiating with respect to T^{-1}, we obtain

$$\frac{d\Delta\chi^e}{dT^{-1}} \text{ (Kelvin)} = -\frac{2(D_N + 273.2E_N)}{R} \ [\ ]$$

$$= -1.384 \times 10^4 \ [\ ] \qquad (23)$$

where [ ] is the term in square brackets on the right-hand side of eq 13. Choosing $\zeta_Y = 1.002$ and $\zeta_R = 0.994$, and using the δ's given in Table I, $d\Delta\chi^e/dT^{-1}$ values were computed through eq 23 and are listed in Table V. The excellent agreement with experiment is evident. Note that the tabulated predicted values were also determined by averaging over all solutes in a given solvent, and that the standard deviations here reflect only systematic solute-to-solute differences. A mixture-by-mixture comparison (33 systems in all) of the experimental and predicted values indicates agreement to within ±36 K or 15% (on the average). This corresponds to a difference of about ±0.0035 between the predicted and observed increment of

TABLE V

1. Intercepts (A) and Slopes (B) of Plots of $\Delta\chi^e$ vs. $1 + (\delta_z/2)$. (See Figure 1.)

Solvent	$-A$	B
HC	1.5239	1.7224
HB	1.7363	1.9437
HI	2.0261	2.2267

2. Experimental and Predicted Values of $d\Delta\chi/dT^{-1}$ in Kelvin. (See Eq 23.)

Solvent	Exptl	Predicted
HC	220 ± 50	220 ± 27
HB	230 ± 50	234 ± 30
HI	250 ± 70	252 ± 34

$\Delta\chi$ with a 10° decrease in temperature, a number which is comparable to the experimental error.

Discussion

It is clear that the proposed energetic interpretation of $\Delta\chi$ through eq 13 produces quantitative agreement with experiment and that the values of the derived molecular parameters are physically reasonable. Since these aromatic-alkane interactions involve dispersion forces predominantly, the finding that ζ_Y is slightly larger than ζ_R suggests that small additional forces are involved in aromatic-haloalkane interactions. These could be electrostatic interactions (e.g., halide dipole-aromatic quadrupole, halide dipole-aromatic induced dipole, or, in some cases, halide dipole-aromatic dipole) or, less likely (see below), charge-transfer interactions. However, given that the dipole moments of the n-butyl halides are approximately equal (handbook values of 2.08 ± 0.03 D), it follows that those of the three hexadecyl halides should be roughly the same. Thus the observed trend (HI > HB > HC) in aromatic-haloalkane interactions (ϵ_{YZ}), which is governed by the trend in ϵ_{YY} (eq 12) or δ_Y, most likely follows the trend in haloalkane dispersion forces. Support for this contention can be found by comparing molar refractions[16] per unit hard-core volume (proportional to molecular polarizability per unit volume), which are 0.243, 0.237, 0.232, and 0.227 for HI, HB, HC, and OD, respectively. Note also that $\epsilon_{YZ} > \epsilon_{RZ}$, because $\zeta_Y > \zeta_R$ and $\delta_Y > \delta_R$.

At present there is no direct evidence of charge-transfer interaction between these homonuclear aromatic compounds and n-alkyl halides. We have scanned the uv-visible spectral region of a benzene-iodohexadecane mixture. No charge-transfer band was observed. A few workers[20,21] have carried out nmr and uv-visible studies on polar aliphatic-aromatic systems. They found a small amount of complex formation and concluded that the complexes were stabilized by electrostatic, rather than charge-transfer, interactions.

One cannot categorically eliminate the possibility that molecular complexes are present in our systems. In fact, a procedure formally related to that used here for obtaining $\Delta\chi$ has been employed for determining association constants in systems with known complex formation.[22,23] In the present notation, the 1:1 association constant K (in liters per mole) is related to $\Delta\chi$ by the approximate (uncorrected for solution nonideality) expression[22,23]

$$\Delta\chi \approx \ln (1 + KC_Y) \qquad (24)$$

where C_Y is the pure solvent concentration in moles/liter. From the tabulated $\Delta\chi$'s, we calculate K values in the range 0.1 to 0.3 and "enthalpies of association" in the

range −4 to −8 kJ/mol. Thus, at best, these would correspond to very weak complexes. Also, given the excellent correlation between the $\Delta\chi$'s and the electrostatic energy parameters (δ_Z) of the aromatic solutes (Figure 1), it seems unlikely that charge-transfer forces are important. If they were, one would expect a trend of increasing $\Delta\chi$ with increasing methylation of the aromatic ring (or decreasing "donor" ionization potential), which is not observed. Note the low value for mesitylene and the high values for the halobenzenes in Table IV. It is concluded, therefore, that the interactions present in these systems, whether they lead to long-lived complexes or short-lived contact interactions,[23] are predominantly electrostatic in nature.

Supplementary Material Available. Tables VI-IX will appear following these pages in the microfilm edition of this volume of the journal. These tables contain specific retention volumes ($V_g{}^0$), infinite dilution activity coefficients ($\gamma_2{}^\infty$), and interaction parameters (χ) at 30, 40, 50, and 60° for the 48 binary systems found in Table III. Photocopies of the supplementary material from this paper only or microfiche (105 × 148 mm, 24× reduction, negatives) containing all of the supplementary material for the papers in this issue may be obtained from the Journals Department, American Chemical Society, 1155 16th St., N.W., Washington, D. C. 20036. Remit check or money order for $3.00 for photocopy or $2.00 for microfiche, referring to code number JPC-74-1644.

References and Notes

(1) A. J. B. Cruickshank, M. L. Windsor and C. L. Young, *Proc. Roy. Soc., Ser. A*, **295**, 259, 271 (1966).
(2) Y. B. Tewari, D. E. Martire, and J. P. Sheridan. *J. Phys. Chem.*, **74**, 2345, 3263 (1970), and pertinent references therein.
(3) A. J. B. Cruickshank, B. W. Gainey, and C. L. Young, *Trans. Faraday Soc.*, **64**, 337 (1968).
(4) B. W. Gainey and C. L. Young, *Trans. Faraday Soc.*, **64**, 349 (1968).
(5) C. L. Young, *Trans. Faraday Soc.*, **64**, 1537 (1968).
(6) C. P. Hicks and C. L. Young, *Trans. Faraday Soc.*, **64**, 2675 (1968).
(7) G. R. Luckhurst and D. E. Martire, *Trans. Faraday Soc.*, **65**, 1248 (1969).
(8) D. Patterson, Y. B. Tewari, and H. P. Schreiber, *J. Chem. Soc., Faraday Trans. 2.* **68**, 885 (1972).
(9) H. P. Schreiber, Y. B. Tewari, and D. Patterson, *J. Polym. Sci.*, **11**, 15 (1973).
(10) G. M. Janini and D. E. Martire, *J. Chem. Soc., Faraday Trans. 2.* **70**, 837 (1974).
(11) I. Prigogine (with the collaboration of V. Mathot and A. Bellemans), "The Molecular Theory of Solutions," North Holland Publishing Co., Amsterdam, 1957, Chapters 16 and 17.
(12) R. A. Orwoll and P. J. Flory, *J. Amer. Chem. Soc.*, **89**, 6814, 6822 (1967).
(13) D. Patterson and J. M. Bardin, *Trans. Faraday Soc.*, **66**, 321 (1970).
(14) H. C. Longuet-Higgins, *Discuss. Faraday Soc.*, **15**, 73 (1953).
(15) A. Kreglewski, *J. Phys. Chem.*, **71**, 2860 (1967); **72**, 1879, 2280 (1968); **73**, 3359 (1969).
(16) R. R. Dreisbach, *Advan. Chem. Ser.*, **No. 15** (1955); **No. 22** (1959); **No. 29** (1961).
(17) A. P. Kudchadker, G. H. Alani, and B. J. Zwolinski, *Chem. Rev.*, **68**, 659 (1968).
(18) D. Patterson, *Macromolecules*, **1**, 279 (1969).
(19) J. S. Rowlinson. "Liquids and Liquid Mixtures," 2nd ed, Plenum Press, New York, N. Y., 1969, Chapters 7 and 9.
(20) J. Homer and M. C. Cooke, *J. Chem. Soc. A*, 773, 777, 1984, 2862 (1969).
(21) R. Sahai and S. H. Lin, *Can. J. Chem.*, **49**, 1771 (1971).
(22) D. E. Martire and P. Riedl, *J. Phys. Chem.*, **72**, 3478 (1968).
(23) J. P. Sheridan, D. E. Martire, and Y. B. Tewari, *J. Amer. Chem. Soc.*, **94**, 3294 (1972).

Structure and Reactions of Some Mercaptans on a Nickel Surface

Laurence D. Neff* and Stanley C. Kitching

The Department of Chemistry, East Texas State University, Commerce, Texas 75428 (*Received March 5, 1974*)

Publication costs assisted by the Robert A. Welch Foundation

Infrared spectra of *n*-propyl, isopropyl, *n*-butyl, isobutyl, and *tert*-butyl mercaptans adsorbed on evaporated nickel films were recorded over the range of 4000 to 300 cm^{-1}. Absorption bands corresponding to mercaptide structures (R–S–Ni) were observed. Subsequent addition of CO resulted in the formation of nickel tetracarbonyl. Heating to 80° decomposed the mercaptide with the formation of the corresponding olefin. The sulfided nickel surface did not react with hydrogen, but reacted readily with oxygen at 80°.

Introduction

Poisoning of catalytic surfaces by compounds containing unshielded sulfur atoms, *e.g.*, mercaptans, is of widespread interest.[1] Garland[2] studied the effect of poisoning by carbon disulfide on the spectra of carbon monoxide chemisorbed on nickel. Blyholder and coworkers[3,4] have reported spectra for methyl and ethyl mercaptan adsorbed on silica supported and evaporated nickel films. They

concluded the surface species is of a mercaptide type, although no direct evidence for the carbon–sulfur nor nickel–sulfur bonds was reported.

The work presented herein is concerned with the infrared spectra of several mercaptans adsorbed on evaporated nickel films. The spectral range investigated is from 4000 to 300 cm^{-1}. This region permits careful investigation of all spectra for evidence of carbon–sulfur and possibly nickel–sulfur bonds. Spectra are shown of stable sur-

face species formed at 25 and 80° by the interaction of the various mercaptans with finely divided nickel particles. Also reported are the interactions of the surface species with carbon monoxide and oxygen.

Experimental Section

The metal films used in this study were prepared in such a manner so as to give good transmission characteristics over a wide spectral range. Details of the experimental technique[5] and cell design[6] have been described elsewhere. Preparation of the film is accomplished by evaporating the metal of interest from a resistively heated tungsten filament in the presence of a small pressure of helium. The metal particles formed in the gas phase are deposited in a hydrocarbon oil film on the windows of the *in situ* cell. The role of the oil serves to reduce the rate at which the films sinter and therefore scattering of the incident radiation. Films prepared in this manner are not to be considered "clean." However, materials which may be adsorbed on contact with the oil are apparently weakly held to the surface since many gases have been found to readily chemisorb on the metal. Therefore one might describe the oil as a solvent having weak interactions with the systems of interest. Spectra were also recorded after evacuation of the gas phase in order to establish which absorption bands can be attributed to chemisorbed species. A 15-min evacuation period proved sufficient to remove all of the unadsorbed mercaptans from the ir spectra. All spectra of chemisorbed mercaptans reported in this study were recorded after evacuation of the cell for at least 1 hr at 10^{-6} Torr.

In general the cell was equipped with KBr windows, although in certain cases CsBr windows were used for their extended transmission characteristics. Infrared spectra were recorded on a Beckman Model IR-10 spectrophotometer. Useful spectra were obtained over the spectral range of 4000 to 400 cm^{-1} (300 cm^{-1} in the case of the CsBr windows). The instrument is equipped with an external recorder (Rikadenki Model B-14) and an ordinate scale expander. The nickel and tungsten were obtained in the form of high-purity wire from A. D. Mackay, Inc. The CO was supplied by the Air Reduction Co. as CP grade. The H$_2$ and He were supplied by Big 3 Industries. The H$_2$ and He were purified by passing over hot copper turnings at 420°, then through two traps cooled with liquid nitrogen. The second trap contained activated charcoal. The CO was purified by passage through a charcoal trap immersed in liquid nitrogen. The mercaptans were supplied by Eastman Organic Chemicals (1-propanethiol) and Aldrich Chemical Co. These were subjected to several freeze–thaw cycles with pumping and stored in glass vessels on the vacuum system.

Results

The experimental results of the adsorption of the various mercaptans on the evaporated nickel films are presented in Table I. For each adsorbate the length of exposure was at least 2 hr, although experiments have shown that 30 min was sufficient in most cases to assure the mercaptan had diffused into the oil film. The column listed as observed frequencies corresponds to the bands that are due to the chemisorbed species. These bands were recorded after the adsorbate was evacuated from the cell and the cell pumped at 10^{-6} Torr for at least 1 hr. Absorption bands listed under model compound frequencies are the frequencies reported in the literature for the re-

spective material. The last column is used for the various vibrational assignments.

It should be noted that many absorption peaks observed for the adsorbates used are not listed in the table. Generally only those peaks are listed which are observed to occur in the region where the surface species gives rise to absorptions that are not present in the background spectrum. Thus the regions listed generally are below 1300 cm^{-1}. Absorption bands ascribed to C–H stretching or deformation modes are obscured by corresponding bands due to the oil and are present in all background spectra. These bands are located in the general region of 2900, 1460, and 1370 cm^{-1}, respectively. Although the adsorption of gas samples result in an increase in the band intensities in these regions, the changes are difficult to interpret with any sense of assurance and generally are not discussed. The band near 700 cm^{-1} is attributed to a methylene rock mode and obscures the band due to the C–S stretching vibration of certain thiols. Also, only those absorptions that correspond to the more intense bands of the mercaptan are noted. The other bands are not observed apparently because the surface concentrations are relatively low. This has been reported before and is not unexpected.[6,7] Considering this, the spectra of the adsorbed species are in good agreement with those of the particular thiols in question.

All adsorption processes were performed at about 25°, which is the average temperature of the laboratory. Absorption bands designated as "added CO" resulted from exposure of the sample to about 3 cm CO pressure after the adsorption of the mercaptan in question.

Figure 1 shows typical spectra that result when a mercaptan is adsorbed on an evaporated metal surface. These spectra were recorded when *tert*-butyl mercaptan was added to a freshly prepared nickel surface. The absorption bands shown in the spectra are listed in the table along with the corresponding vibrational assignments. The band at 580 cm^{-1} is attributed to the C–S stretching mode while the other bands are assigned to vibrations of the rest of the molecular skeleton. Although the spectra shown in Figure 1 do not cover the total recorded spectral range, careful investigation of the region near 2600 cm^{-1} using a 10× ordinate scale expansion indicates the absence of any observable absorption band attributed to the S–H moiety. This is consistent with the absence of a band near 860 cm^{-1}.

Absorption bands that are observed when iso- and *n*-butyl mercaptan are adsorbed on freshly prepared nickel surfaces are also presented in Table I. The band corresponding to the C–S stretch is not observed in the spectrum for adsorbed *n*-butyl mercaptan and may be due to the fact that the amount of adsorbed thiol is too small for it to be detected. For the spectra of the adsorbed *n*- and isopropyl mercaptan, absorption bands correspond closely with those of the free mercaptan. The bands of the adsorbed isopropyl mercaptan are relatively strong, while those bands due to the adsorbed *n*-propyl mercaptan are less intense. Both spectra display absorption bands that have been attributed to the C–S bond. The position of these bands is slightly shifted to lower energy when compared to the free thiols.

Effect of Carbon Monoxide. Addition of 3 cm pressure of CO to the samples containing a preadsorbed mercaptan resulted in some rather curious observations. A strong band developes at 2040 cm^{-1} accompanied by the formation of a band at 420 cm^{-1}. The intensity of these bands

TABLE I: Frequencies and Assignments for Adsorbed Species on Nickel

Adsorbate	Observed frequencies, cm^{-1}	Model compound frequencies, cm^{-1}	Assignments
n-Propyl mercaptan[a]	1270	1298 s	CH$_2$ wag
		1246 s	CH$_2$ wag
		1225 sh	CH$_2$ twist
	1200	1208 sh	
		1105 s	CH$_2$ rock
	1065	1088 s	CC stretch (skew)
	1035	1060 sh	CH$_3$ rock
	1005	1032 w	CC stretch (trans)
		961 m	CH$_3$ rock
		925 w	CC stretch
		897 s	CC stretch
		883 m	CSH bend (trans)
		793 s	CH$_2$ rock (skew)
	760	763 sh	CH$_2$ rock (trans)
	725	719 m	Combination of CS stretch and CCC bend for trans
	620	655	CS stretch (skew)
	2040		CO stretch of gas phase Ni(CO)$_4$
	2020		CO stretch of adsorbed carbon monoxide
	1860		NiC stretch of gaseous
	420		Ni(CO)$_4$[b]
Isopropyl mercaptan[c]	1385	1385	CH$_3$ sym bend character-
	1368	1368	istic of (CH$_3$)$_2$CH$^-$
	1298		
		1250	CH wag
	1220		
		1161	CH$_3$ rock
	1132		
		1085	CC stretch
	1030	1063	CH$_3$ rock
		929	CH$_3$ rock
		894	CC stretch
		861	CSH bend
	585	617	CS stretch
	360		NiS stretch
	2040		CO stretch of gas-phase Ni(CO)$_4$
	420		NiC stretch of Ni(CO)$_4$[b]
n-Butyl mercaptan[d]	1290	1290 s	CH$_2$ wag
	1260	1240 m	CH$_2$ wag
	1210	1200 sh	
		1110 m	CH$_2$ rock
	1090		
		1060 vw	CH$_3$ rock
		1020 vw	CC stretch
		960 w	CH$_3$ rock
		380 vw	CSH bend
	820		CH$_3$ rock
		770 w	
		750 w	
		740 m	
		710 sh	
		650 w	CS stretch
	2040		CO stretch of gas-phase Ni(CO)$_4$
	420		Ni–C stretch of Ni(CO)$_4$[b]
Isobutyl mercaptan[d,e]	1380	1380 s	CH$_3$ sym bend charac-
	1365	1365 s	teristic of (CH$_3$)$_2$CH–
		1330 m	
	1310	1325 m	CH wag
	1260 (1235)	1255 s	CH$_2$ wag
	1225 (1210)	1225 sh	CH$_2$ twist
	1165	1170 m	CC stretch
	1130 (1105)		
		1100 m	CH$_3$ rock
		1020 vw	CC stretch
		955 sh	
	920 (940) (920)	925 m	CH$_3$ rock

TABLE I *(Continued)*

Adsorbate	Observed frequencies, cm^{-1}	Model compound frequencies, cm^{-1}	Assignments
Isobutyl mercaptan *(continued)*	840	820 sh	CH$_3$ rock
	800	800 m	CH$_2$ rock
	710	710 m	CS stretch
	630	665 w	CS stretch
	2040		C–O stretch of gas phase Ni(CO)$_4$
	420		NiC stretch of Ni(CO)$_4$[b]
tert-Butyl mercaptan[d]	1300		
	1250		
		1210 sh	CC stretch
	1150	1168 vs	CH$_3$ rock
	1020	1030	CH$_3$ rock
		860 m	CSH bend
	800	820 m	CC stretch
	580	590 m	CS stretch
	2040		CO stretch of gas phase Ni(CO)$_4$
	1990		CO stretch of chemisorbed CO
	1860		
	402		NiC stretch of gaseous Ni(CO)$_4$[b]

[a] Reference 8. [b] Reference 9. [c] Reference 10. [d] Reference 11. [e] Reference 12.

increases with time indicating that the species giving rise to them is being produced as a result of a chemical reaction. Evacuation of the gas phase caused these bands to disappear and it was possible to effect their disappearance by freezing the gas phase using liquid nitrogen. In no case did the presence of the CO influence the intensity of the absorption bands attributed to the preadsorbed mercaptan species.

No evidence for chemisorbed CO was noted except for the cases using *n*-propyl and *tert*-butyl mercaptans. For these two, absorption bands that developed in the spectra upon exposure to CO indicate some of the surface was free to chemisorb a limited amount of CO. This can be seen in Figure 1. The appearance of the two bands at 1990 and 1860 cm^{-1} are observed immediately upon introduction of the CO. For *n*-propyl mercaptan the high wave number band occurs at a frequency that is more nearly "normal," however, the other absorption is at a frequency lower than expected. The intensities of these bands are distinctly smaller (up to 5% T) than those observed when CO is added to a freshly evaporated metal surface.

If the order of addition of the mercaptan and the CO are reversed, that is the CO is preadsorbed and then the mercaptan added to the resulting surface, the CO is displaced as expected. However the spectra indicate that the chemisorbed carbon monoxide is never completely displaced no matter which mercaptan is used, since all spectra retain a small absorption band in the 1850-cm^{-1} region. The preadsorbed CO does not change the position of the bands attributed to the adsorbed mercaptan. This effect was noted for all the mercaptans studied.

Effect of Added Oxygen. A series of experiments were conducted in which 2 cm of oxygen was admitted to the cell containing the nickel film and the preadsorbed mercaptan in question. Spectra were recorded at room temperature and after heating the sample to 80° for a period of 2 hr. Exposure of the samples to oxygen at room temperature results in no change in the spectra even after extended periods (up to 56 hr). However, when the samples are subsequently heated to 80° the spectra change significantly. The absorption bands that correspond to the car-
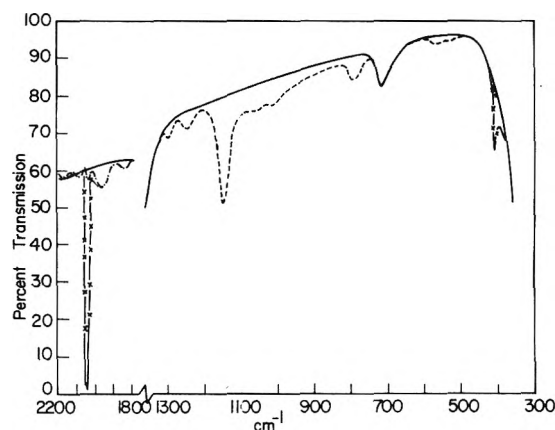

Figure 1. Spectrum of *tert*-butyl mercaptan adsorbed on nickel: (——) background; (- - -) chemisorbed *t*-C$_4$H$_9$SH; (– – –) with 3 cm of CO; (- × -) after 10 hr exposure to 3 cm of CO.

bon skeleton of the thiol disappear and new peaks appear at 1140, 1030, 960, and 920 cm^{-1}. This is observed for each of the mercaptans.

Effect of Heating with and without Oxygen Present in the Cell. A series of experiments were performed in which the primary purpose was to identify the gaseous products resulting from the thermal desportion of the mercaptan. Analysis of these products was accomplished using gas chromatography and mass spectral data. In addition to the excess oxygen present, the primary product was an olefin, with trace quantities of other materials. For certain of the mercaptans the products of the thermal desorption were dependent upon whether oxygen was present or not during the desorption period. Specifically for the *n*- and isopropyl mercaptans the primary product was propene, while that of the *tert*-butyl mercaptan was 2-methylpropene. These products were observed whether or not oxygen was present in the cell during the desorption process. For *n*- and isobutyl mercaptan if the cell was heated in the absence of oxygen the primary gaseous product was 1-butene whereas if the heating was performed in the presence of oxygen the product was *trans*-2-butene.

An additional experiment was performed in which 1-butene and oxygen were heated in the presence of a sulfided nickel catalyst and in the absence of such a surface. In the absence of the sulfided surface no reaction was observed however when a sulfided nickel surface is present 1-butene is converted to *trans*-2-butene.

Discussion

Mercaptan. A few infrared studies[3,4] have been directed to the elucidation of the structure of the surface species formed when a mercaptan is adsorbed on a nickel surface. These studies indicated the surface species formed is bonded to the nickel through the formation of a sulfur-nickel bond in which the thiol hydrogen is replaced by the metal. The presence of the C–S bond was assumed in that no spectral evidence was observed that could be directly attributed to this structure (the spectra contained no absorption bands due to this structure). As reported in Table I, an absorption band that is attributed to the C–S stretching mode of the surface mercaptide was noted for all the mercaptans used except *n*-butyl mercaptan. For each of the mercaptans employed in this study, the surface structure most consistent with the observed spectra is that of a mercaptide, *i.e.*, a single point attachment of the mercaptan to the surface through the sulfur atom. In the spectra that were recorded using isopropyl mercaptan as the adsorbate, a small band was observed at 360 cm^{-1}. This band is attributed to the Ni–S stretch and is in agreement with those reported for certain sulfur chelates.[13,14] The fact that this band is so elusive is not unexpected. In general it is found that the spectra of chemisorbed molecules do not contain an absorption band that can be attributed to the adsorbate–adsorbent bond.[15,16] Why this is so, is not understood.

Effect of Added Carbon Monoxide. The absorption bands observed at 2040 and 420 cm^{-1} in spectra corresponding to the addition of CO to a nickel sample containing preadsorbed mercaptan are attributed to vibrations of nickel tetracarbonyl.[9] Production of nickel tetracarbonyl upon addition of CO is in marked contrast with the result of CO exposure to a fresh nickel surface. In the latter case, the spectra indicate the CO is strongly chemisorbed without the production of observable quantities of nickel tetracarbonyl. These observations are consistent with the practice of introducing small amounts of mercaptan to enhance the commercial production of nickel tetracarbonyl. Apparently the mercaptan causes a change in the distribution of the surface atoms thereby exposing new nickel atoms while simultaneously making it easier for these to react with the CO forming the gaseous carbonyl. Such rearrangements of surface structures are not new[17] and it would seem that a nickel catalyst subjected to both mercaptan and carbon monoxide would experience rapid erosion of the metal by the formation of nickel tetracarbonyl.

The chemisorption of CO by a nickel surface previously exposed to *n*-propyl or *tert*-butyl mercaptan is surprising. This behavior contradicts the work of earlier authors[4] but may be due to the experimental conditions used in this study.

Blyholder[18] suggests that the strength of the adsorbate–adsorbent bond for chemisorbed CO could be related to the position of the carbon–oxygen stretching frequency. Van Hardeveld and Hartog[19] have correlated the position of the CO stretching vibration with various types of metallic clusters on the metal surface reaching essentially the same conclusion as Blyholder. It is known[20] that the position of the absorption band shifts from lower to higher energy as the surface coverage increases. Assuming the more energetic adsorption sites are covered first implies band positions at the lower wave number correspond to the most tightly held CO. This should also be the most difficult to displace by another adsorbent such as a mercaptan which will compete for the surface.

The results indicate that not all the CO can be displaced by the mercaptan under the experimental conditions. The position of the absorption maximum shifts to lower energy as the intensity of the band decreases. When the band no longer decreases upon addition of mercaptan, the position of the peak (near 1850 cm^{-1}) implies the remaining CO is very strongly held to the surface as would be expected using this model. The intensity of the absorption band shows that the amount of CO remaining on the surface is very small, probably about 1% or less than originally present. It is felt that this last CO is bonded to the surface in what Blyholder[21] calls a "multicenter bond." This species could possibly account for the fact that the remaining CO is so strongly attached to the surface that the mercaptan is incapable of displacing it.

Effect of Added Oxygen and Heating. Many attempts made to remove sulfur from mercaptans have involved the use of catalysts.[22] Generally hydrogen sulfide is split off at around 300°.[23,24] The primary products are the olefin and hydrogen sulfide under the experimental conditions reported. In the presence of Rainey Nickel, the products are the parent hydrocarbons, with carbon–carbon cleavage occurring as an important side reaction in certain cases.[25]

In this study it was found that the adsorbed mercaptan underwent decomposition at a temperature significantly lower (80°) than that normally observed.[22] Since the gaseous products resulting from the decomposition are olefins, and not the present hydrocarbons, it appears the nickel films employed for this study are more nearly related to a bare nickel catalyst rather than Rainey Nickel.

A sulfided surface results when the mercaptan decomposes on the adsorbent. No evidence is observed for the hydrogenation of this sulfide species, although experiments were performed where hydrogen was added to the sulfided surface, both at room temperature and 80°. At the elevated temperature the results indicate a reaction does occur upon addition of oxygen to the cell. The spectra which are observed are very similar to those noted for the addition of SO$_2$ to a fresh nickel film. Blyholder[4] has reported spectra of SO$_2$ on iron and nickel films. He finds his spectra are best interpreted in terms of the formation of a Ni–SO$_4$ structure. Therefore when oxygen is added to one of the sulfided nickel surfaces, the sulfur is oxidized with the subsequent formation of a sulfate ion on the surface. The exact nature of this species is difficult to discern because the spectral bands are weak. However, a comparison of the evidence with spectra of known sulfato[26] complexes indicates the surface species formed in these experiments is most likely a unidentate complex having C_{3v} symmetry.

References and Notes

(1) E. B. Maxted in "Advances in Catalysis," Vol. 3, Academic Press, New York, N. Y., 1951, p 129.
(2) C. W. Garland, *J. Phys. Chem.*, **63**, 1423 (1959).

(3) G. D. Blyholder and D. O. Bowen, *J. Phys. Chem.*, **66**, 1288 (1962).

(4) G. D. Blyholder and G. W. Cagle, *Environ. Sci. Techol.*, **5**, 158 (1971).

(5) G. D. Blyholder, *J. Chem. Phys.*, **36**, 2036 (1962).

(6) R. W. Sheets and R. S. Hanson, *J. Phys. Chem.*, **76**, 972 (1972).

(7) L. D. Neff, Ph.D. Dissertation, University of Arkansas, Fayetteville, Arkansas, 1964.

(8) M. Hayashi, Y. Shirs, and H. Murata, *Bull. Chem. Soc. Jap.*, **39**, 112 (1966).

(9) L. H. Jones, *J. Chem. Phys.*, **28**, 1215 (1958).

(10) D. Smith, J. P. Devlin, and D. W. Scott, *J. Mol. Spectrosc.*, **25**, 174 (1968).

(11) I. F. Trotter and H. W. Thompson, *J. Chem Soc.*, 481 (1946).

(12) D. W. Scott, J. P. McCullough, J. F. Messerly, R. E. Pennington, I. A. Hossenlopp, H. L. Finke and G. Waddington, *J. Amer. Chem. Soc.*, **80**, 55 (1958).

(13) K. Nakamoto, "Infrared Spectra of Inorganic and Coordination Compounds," Wiley, New York, N. Y., 1970, p 257.

(14) J. P. Fackler and D. Coucouvanis, *J. Amer. Chem. Soc.*, **88**, 3913 (1966).

(15) M. L. Hair, "Infrared Spectroscopy in Surface Chemistry," Marcel Dekker, New York, N. Y., 1967.

(16) L. H. Little, "Infrared Spectra of Adsorbed Species," Academic Press, New York, N. Y., 1966, p 404.

(17) J. W. May in "Advances in Catalysis," Vol. 21, Academic Press, New York, N. Y., 1970, p 210.

(18) G. D. Blyholder, *J. Phys. Chem.*, **68**, 2772 (1964).

(19) R. Van Hardeveld and F. Hartog in "Advances in Catalysis," Vol. 22, Academic Press, New York, N. Y., 1972, p 75.

(20) R. P. Eischens, S. A. Francis, and W. A. Pliskin, *J. Phys. Chem.*, **60**, 194 (1956).

(21) G. D. Blyholder, private communication.

(22) E. Emmett Reid, "Organic Chemistry of Bivalent Sulfur," Vol. I, Chemical Publishing Co., New York, N. Y., 1958, p III.

(23) M. G. Rudenko and V. N. Gromoua, *Dokl. Akad. Nauk SSSR*, **81**, 207 (1951).

(24) H. S. Taylor, *Refiner Natur. Gasoline Mfr.*, **9**, 83 (1930).

(25) H. R. Snyder and G. W. Cannon, *J. Amer. Chem. Soc.*, **66**, 1955 (1944).

(26) K. Nakamoto, J. Fujita, S. Tamaka, and M. Kobayashi, *J. Amer. Chem. Soc.*, **79**, 4904 (1957).

Transition Metal Ions on Molecular Sieves. II. Catalytic Activities of Transition Metal Ions on Molecular Sieves for the Decomposition of Hydrogen Peroxide

Isao Mochida* and Kenjiro Takeshita

Research Institute of Industrial Science, Kyushu University, Fukuoka, Japan 812   (*Received December 27, 1973*)

The catalytic activities of Y molecular sieves ion exchanged with transition metal ions were observed for the decomposition of hydrogen peroxide, in order to develop a novel catalytic utilization of isolated metal ions dispersed on the sieve, where the nature of the metal ions can be easily modified by coordination of ligands. Their activities were in order of Pd(II) < Fe(III) < Ni(II) < Ag(I) > Mn(II) > Co(II) > Co(III) > Hg(II) > Cu(II) > Tl(I) > Cr(III) > Zn(II). This bell-shaped activity pattern is correlated with the transition metal redox potentials in basic solution. The catalytic activities of Mn(II), Ag(I), and Cu(II) were improved markedly by coordination with diamine ligands, as observed in homogeneous systems, whereas those of Ni(II) and Co(II) were suppressed. Based on studies of the rate dependence on hydrogen ion concentration in addition to the trend of catalytic activities, the decomposition mechanism of hydrogen peroxide is concluded to contain the redox steps for the metal ion, either of which is rate determining, depending on the redox potential of the catalyst.

Introduction

Isolated transition metal ions attached to a molecular sieve would be expected to behave as their homogeneous analogs, even though they are located on a solid surface, because they are isolated from one another on the fixed sites of the molecular sieve. Although molecular sieve-bonded metal ions have been extensively studied[1] and their catalytic activities have been reported for the oxidation of olefins,[2] cyclohexane,[3] and carbon monoxide[1] as well as for acid–base reactions,[1] there is little work in which the metal-ion on the sieve is expected to have a chemical nature similar to that of homogeneous catalysts such as metal complexes. We have reported that bidentate ligands such as ethylenediamine formed chelated complexes with an isolated cupric ion on a molecular sieve.[4]

In the present study, catalytic activities of transition metal ions and their complexes on the sieve were observed for the decomposition of hydrogen peroxide, which has been investigated extensively as a homogeneous reaction catalyzed by transition metal ions and their complexes as well as by enzymes such as catalase.[5] It may be of value to try to develop a novel catalytic utilization of the isolated metal ions dispersed on the sieve, taking advantage of the possibility that the nature of such a catalyst may be easily modified by ligands as in the case of homogeneous transition metal systems.[6] The present study is one of such trials.

Experimental Section

Chemicals. Hydrogen peroxide (30% aqueous solution) was obtained from Wako Pure Chemical Industry. Ligands obtained from Tokyo Kasei Co. were used without purification.

Catalysts. The ion-exchanged molecular sieves examined are listed in Table I. They were prepared by ion exchange of Y molecular sieves (Linde), Na(I)-Y, with aqueous solutions of metal sulfates or nitrates, except for Cu(II), Pd(II), and Co(III) ions. Ammine complexes of the first two and ethylenediamine complexes of the latter

TABLE I: Catalytic Activities of Metal Ions and Their Ethylenediamine Chelates on Y Sieve for the Decomposition of H_2O_2

		Activity[a]	Activity of ethylenediamine chelate[a]	ΔG_1,[b] kcal/mol	ΔG_2,[c] kcal/mol
1	Ag(I)	4.8×10^3	Increase		
2	Mn(II)	6.8×10^2	1.3×10^3		
3	Co(II)	2.8×10^2	3.5	7	43
4	Co(III)	1.4×10^2			
5	Hg(II)	1.9×10			
6	Cu(II)	7.0	1.0×10^2	46	6
7	Fe(III)	6.8	1.3×10	30	20
8	Tl(I)[d]	4.9×10^{-1}			
9	Ni(II)	3.8	2.8×10^{-1}		
10	V(IV)	4.9×10^{-1}			
11	Cr(III)	3.7×10^{-1}	1.3	58	−8
12	Zn(II)	3.3×10^{-1}	2.5×10		
13	Pd(II)	1.4×10^{-1}			

[a] Rate of decomposition at 24.5° and pH 10.15 (cm/g min). [b] Free-energy change of the reaction $M^{n+} + H_2O_2 \rightarrow M^{(n-1)+} + HOO + H^+$. [c] Free-energy change of the reaction $M^{(n-1)+} + H_2O_2 \rightarrow M^{n+} + HO + OH^-$. [d] 10% exchange.

Figure 1. A bell-shaped activity pattern for metal ions on a sieve correlated with redox potential. Numbers refer to catalysts in Table I.

were used for ion exchange. A sufficient amount of metal ions was passed through the cylindrically shaped Na(I)-Y in a column, except for Fe(III)-Y, preparation of which was described by Delgass, et al.[7] The ion-exchanged sieves were then washed and dried at 100°, followed by calcination at 400° for 7 hr in air. Approximately 90–100% of sodium ions were exchanged, except for Tl(I), where only 10% was exchanged.[2a]

To yield the chelate-impregnated materials, the ion-exchanged sieves were stirred for 2 days in an aqueous or ethanolic solution of ligand, washed with ethanol, and dried in a desiccator.

Apparatus and Procedure. After a reaction flask (containing 50 ml of basic aqueous solution, pH 6–11, and the catalyst) was immersed in a constant-temperature bath (24.5°) for 1 hr, 1 ml of H_2O_2 was added. The reaction mixture was stirred by a magnetic stirrer, and the evolution of oxygen during the course of H_2O_2 decomposition was followed as a function of time with a manometer connected to the reaction flask. Although the reaction seemed first order in H_2O_2,[4] observed rates of H_2O_2 decomposition, V, in cm/g min were obtained from the initial slopes of plots of increasing pressure (cm) of O_2 evolved *vs.* time, which were divided by the weight of catalyst used. The pressures observed were corrected to those at 25°. Because the pH of the reaction solution changed as H_2O_2 decomposition progressed, pH of the solution at the initial stage of reaction was measured with a Hitachi-Horiba pH meter immediately after the addition of H_2O_2 to the reaction systems.
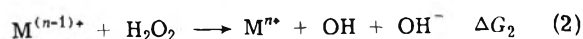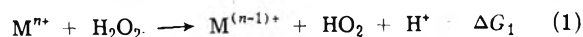
Results

Catalytic Activities of Y Molecular Sieves Ion Exchanged with Transition Metal Ions. Catalytic activities of ion-exchanged sieves for H_2O_2 decomposition in an aqueous NaOH solution of pH 10.15 are summarized in Table I together with some properties of the metal ions. Ag(I)-, Mn(II)-, Co(II)-, and Co(III)-Y as well as their oxides were excellent catalysts for this reaction.[8] The redox potential of the metal ion has been considered as one of critical factors for determining the catalytic activity of the catalyst containing the metal ion for the redox reaction, because the reaction appears to involve the
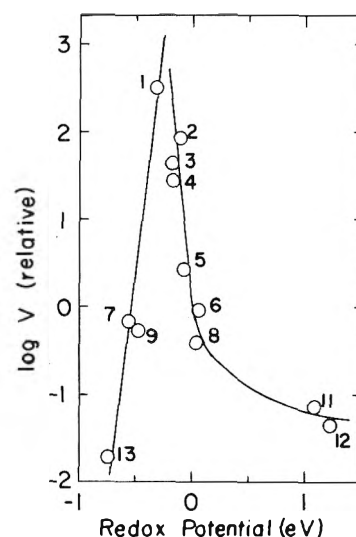
redox steps of the metal ion in any form. The catalytic activities of the sieve catalysts are compared with the redox potentials of the metal ions exchanged in Figure 1, where the catalytic activity relative to that of Cu(II)-Y was corrected by the ion-exchanged ratio, and the values of the redox potentials in a basic solution[9] are plotted because the reaction was carried out in a basic solution. The problem of which oxidation states of the metal ions are involved in the catalysis under the reaction conditions is quite fundamental, however, it may be rather difficult to define this quantity for all metal ions, although couples of oxidation states for some metal ions are obviously involved or have been established as being involved.[5,10] At the present stage, couples of the following oxidation states are assumed to be important in the present reaction: $Ag^{0,I}$, $Mn^{II,III}$, $Co^{II,III}$, $Hg^{0,II}$, $Cu^{I,II}$, $Fe^{II,III}$, $Tl^{I,III}$, $Ni^{II,IV}$, $Cr^{II,III}$, $Zn^{0,II}$, and $Pd^{II,IV}$. Black deposits of silver metal were observed during the reaction so that the assumed couple of $Ag^{0,I}$ may be correct. The bell-shaped relation shown in Figure 1 is thought to indicate the presence of redox reactions of the catalyst, and its explanation will be discussed later in connection with the reaction mechanism. Similar activities of Co(II)- and Co(III)-Y may support this assumption.

The free-energy changes of the following reactions are reported for Co, Cu, Fe, and Cr ions[11]

$$M^{n+} + H_2O_2 \longrightarrow M^{(n-1)+} + HO_2 + H^+ \quad \Delta G_1 \quad (1)$$

$$M^{(n-1)+} + H_2O_2 \longrightarrow M^{n+} + OH + OH^- \quad \Delta G_2 \quad (2)$$

If the H_2O_2 decomposition proceeds through these elementary steps as assumed by Von Bertlan,[12] the greatest difference between ΔG_1 and ΔG_2 should be related to the rate-determining step of this catalysis and related to the activities of the metal ions, however, no reasonable relation was observable.

The rate limits for exchange of methanol coordinated to metal ions repoted for Mn(II), Co(II), Cu(II), and Ni(II)[13] are related to the respective catalytic activities for the present reaction, however, data are too scarce to be discussed further.

Ligand Effects on the Catalytic Activity. The effects of ethylenediamine on the catalytic activities of some metal

TABLE II: Effects of Ligands on the Catalytic Activities

Ligand	Catalytic activity[m]		
	Mn at pH 7.6	Co at pH 8.6	Cu at pH 11.4
Aquo	143	82	30
1,2pn[a]	850	1.9	36
dien[b]	445		62
en₃[c]	278	1.9	
en₂[d]			450
en[e]		15	110
trien[f]	426	2.8	18
1,3pn[g]	420		48
Pyperizine	354		45
(Et₂en)₃[h]	200		
(CN-en)[i]	8.9		
Ph₂en[j]	4.3		
dmg[k]	4.4	3.5	
dip[l]		3.6	32

[a] 1,2-Propylenediamine. [b] Diethylenetriamine. [c] Tris(ethylenediamine). [d] Bis(ethylenediamine). [e] Ethylenediamine. [f] Triethylenetetramine. [g] 1,3-Propylenediamine. [h] N,N-Diethylethylenediamine. [i] Ethylenedicyanide. [j] N,N′-Diphenylethylenediamine. [k] Dimethylglyoxime. [l] Dipyridyl. [m] H_2O_2 decomposition rate at 24.5°, cm/g min. Except for bis- and monoethylenediamine, excess ligands were added during synthesis of the chelates.

ions for the hydrogen peroxide decomposition reaction are summarized in Table I. The ligand enhanced the activities of Ag, Mn, Cu, Fe, Cr, and Zn, whereas it depressed those of Co and Ni. Effects of other chelating reagents on the activities of Mn, Cu, and Co ions are shown in Table II. In the case of Mn ion, 1,2-propylenediamine (1,2pn) was the best ligand, increasing the catalytic activity by more than a half-order of magnitude in comparison with that of the aquo ion on the sieve. Amines without other functional groups in the molecule enhanced the activity regardless of coordination number, whereas substitution in the amine molecule by cyanide or phenyl group decreased the activity. The enhancement of the activity was provoked by a particular pairing of metal ion and ligand, and was not due solely to the existence of ligand molecules in the reaction system.

In the case of cupric ion, ethylenediamine is the best ligand and improved the activity by more than one order of magnitude. In contrast to the enhancement of the activity of Mn ion by coordination with triethylenetetramine (a tetradentate ligand), the activity of the cupric ion on the sieve was depressed by this ligand. These features are common to those in a homogeneous system,[14] although some discrepancies were also observed. Sigel, et al.,[15] and Sharma and Schubert[10] reported that the catalytic activity of the cupric ion was depressed when more than three of the coordination sites were occupied by ligands, as shown by the fact that bis(ethylenediamine)-, tris(imidazole)-, or triethylenetetraminecopper chelates had little activity for this reaction. However, bis(ethylenediamine) chelate on molecular sieve, which was identified in a previous study,[1] showed much higher activity than the monoethylenediamine chelate on the sieve which was blue in color, and the diethylenetriamine (tridentate chelating reagent) copper chelate on the sieve showed a larger activity than the aquo ion.

It is interesting that the ligands observed in the present study depressed the activity of the cobalt ion.

Dependence of Decomposition Rate on Proton Concentration of the Reaction Solution. The catalytic activities of some metal ions and their chelates on the sieve material were observed in aqueous NaOH solutions of different concentrations to study the influence of pH on the reac-
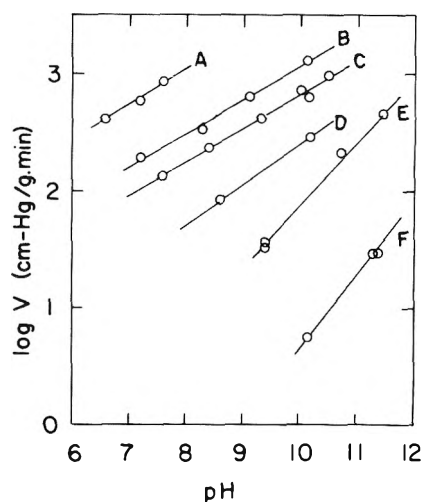
Figure 2. pH dependence of catalytic activity in aqueous NaOH: A, Mn(II)-1,2-pn-Y; B, Mn(II)-en-Y; C, Mn(II)-Y; D, Co(II)-Y; E, Cu(II)-en-Y; F, Cu(II)-Y.
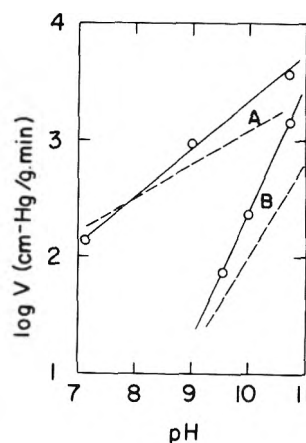
Figure 3. pH dependence of catalytic activity in aqueous ethylenediamine: A, Mn(II)-en-∨; B, Cu(II)-en-Y; dotted lines, activities at the same pH in aqueous NaOH.

tion rate. Results are shown in Figure 2. They are described by the following rate equation

$$V = k'(H^+)^{-n} \tag{3}$$

where the values of n were 0.30 for Mn(II) and its chelates on the sieve, 0.35 for Co(II), 0.54 for bis(ethylenediamine)-copper, and 0.62 for Cu(II). The reaction orders for proton which were observed in the present study are larger than those observed in homogeneous systems, where they were −1 in many cases.[5,10,15]

In the case where the pH was changed by varying the concentration of ethylenediamine, the dependence of the catalytic activity on pH is shown in Figure 3, using Mn(II)-en₃-Y and Cu(II)-en₂-Y as catalysts. In the high pH region, decomposition of H_2O_2 occurred without the metal ion catalyst, so the catalytic activity was estimated by subtracting the decomposition without catalyst from the rate observed in the presence of the catalyst. The dependence under such conditions is also described by eq 3, where values of n were 0.4 for the manganese chelate and 1.1 for the copper chelate. It should be noted that the catalytic activity and the absolute values of the reaction order with respect to the proton were larger in aqueous ethylenediamine than in aqueous NaOH.

Table III shows the catalytic activities of Mn and its

TABLE III: Effect of Anion on Catalytic Activity[a]

Catalyst	Mn–1,2-pn–Y	Mn–en–Y	Mn(II)–Y
$Na_2B_4O_7$	2.1×10^2	1.2×10^2	4.5×10
NaOH	1.2×10^3	3.0×10^2	1.8×10^2

[a] pH of the solution 8.0; reaction temperature 24.5°, catalytic activity cm/g min.

chelates on the sieve in aqueous $Na_2B_4O_7$ and in aqueous NaOH of the same pH, showing the effects of anions on the activity. Marked decreases in activities were observed in aqueous $Na_2B_4O_7$.

Discussion

Metal ions of aquo and complex forms are well known as catalysts of various reactions whose mechanisms involve an oxidation or reduction of the substrate.[16] It is also recognized that metal ions play essential roles in the catalytic activity of some enzymes in redox reactions.[17] Metal ion exchanged onto the molecular sieve showed excellent catalytic activity for H_2O_2 decomposition, by means of a redox cycle between two oxidation states of considerable stability in a manner similar to that observed in homogeneous systems. Furthermore, the catalytic activities were found to be modified by ligands to a considerable extent. Although some contradictory details were observed in comparison with homogeneous systems, the facts observed in the present study may indicate a similarity between metal ion catalysts bound to the sieve and those in homogeneous form. Thus, one may expect a new type of solid catalyst with merits of both homogeneous and heterogeneous systems.

Mechanism of the Catalytic Decomposition of H_2O_2 by Metal Ion on Molecular Sieve. On the basis of the activity pattern of metal ions on the sieve material, effects of ligands, and reaction orders in hydrogen peroxide and proton, a rather complicated mechanism of the H_2O_2 decomposition catalyzed by metal ions and their chelates on the sieve can be discussed. The information obtained in the present study is not enough to definitely establish the mechanism. Analogous aspects of this catalysis to that in homogeneous systems where the details of the reaction mechanism have been discussed for a long time, however, may help in proposing a tentative mechanism. Many possible mechanisms for this catalysis have been proposed. They may be principally classified into two categories. One is the radical chain mechanism in which the initiation reaction of HOO or OH radical production is catalyzed by metal ions,[18] and the other is reaction within the coordination sphere of the metal ion. The latter mechanism can be subdivided into two redox reactions of the metal ion which are involved in one mechanism[10,19] and not in the other.[15,20]

The peaked relationship shown in Figure 1 may suggest that catalysis on the sieve involves redox reactions of the metal ions. It would be of value to discuss what intermediates are involved. A stepwise mechanism as described by eq 1 and 2[12] should be abandoned, as discussed above.

Sharma and Schubert[10] preferred a reaction mechanism involving the HOO radical in light of negative tests for the OH radical. Their scheme is essentially the same as that proposed by Haggett, *et al.*, for ferric ion catalysis.[19] The reaction mechanism can be extended to the reaction catalyzed by other metal ions as follows

$$2H_2O_2 \longrightarrow 2HOO^- + H^+ \qquad (4)$$

$$2(LM)^{n+} + 2HOO^- \longrightarrow 2(LM)^{(n-1)+} + 2HOO \qquad (5)$$

$$2HOO \longrightarrow O_2 + H_2O_2 \qquad (6)$$

$$2(LM)^{(n-1)+} + H_2O_2 \longrightarrow 2(LM)^{n+} + 2OH^- \qquad (7)$$
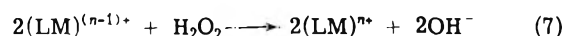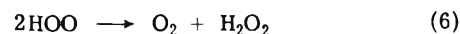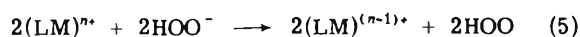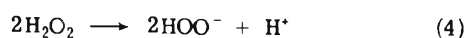
The most effective catalyst can be interpreted in terms of Balandin's theorem[21] assuming their reaction scheme and its thermodynamic data. A combination of reactions 5 and 7 cancels the catalyst term, giving

$$2HOO^- + H_2O_2 \longrightarrow 2HOO\cdot + 2OH^- \qquad (8)$$

The potential change for this reaction can be calculated as -0.389 eV, using the values of the potential changes of the related reactions previously described.[22] Thus, the most effective metal ion for this catalysis is the one for which the redox potential is -0.195 eV, one-half of the potential change of reaction 8. The rate-determining step of this catalysis may be reaction 5 or 7, depending on the rates of the steps which may be related to the redox potential of the catalyst. On a catalyst for which the higher oxidation state is much more stable than the lower one, that is, a large redox potential in Figure 1, reaction 5 may be rate determining, and reaction 7 may be rate determining in the case of a catalyst having a small redox potential. The catalytic activity of a metal ion increases as its redox potential decreases, within the range where the rate-determining step is reaction 5, however, a decreasing redox potential results in a decrease of catalytic activity of a metal ion if the rate-determining step is shifted to reaction 7. The transition of the rate-determining step may occur at a redox potential of -0.195 eV according to Balandin's theorem. The peaked curve of the catalytic activity pattern shown in Figure 1 is thus explained.

The reaction order for the hydrogen ion can be also explained in terms of the above scheme. On a catalyst where reaction 5 is rate determining (larger redox potential), the rate is first order in HOO$^-$, the concentration of which is proportional to $1/[H^+]$ ($n = 1$) during reaction, according to reaction 4. The rate of reaction 7 in the steady state is apparently independent of pH, although the rate constant may be influenced to a small extent by pH according to Le Chatelier's theorem. That is, the reaction order in $[H^+]$, n, is expected to decrease from unity to zero with decreasing redox potential of the metal ion catalyst, because reactions 5 and 7 may contribute to the rate-determining step according to their relative rates near the transition of the rate-determining step, which depends on the redox potential of the catalyst. The values of the reaction orders in $[H^+]$, n, for Mn(II)–, Co(II)–, and Cu(II)–Y are in the given order.

The effect of ligands on catalytic activity is not clearly delineated by the present study, although Sharma and Schubert[10] pointed out that the reduction of Cu(II) coordinated to two nitrogens is kinetically much faster than that of the aquo cupric ion, and Wang[14] ascribed the enhancement of catalytic activity to the strain around the metal ion catalyst provoked by the ligand molecules. As for Cu(II)–Y, the interpretation proposed by Sharma and Schubert may be true, and is consistent with the increase of reaction order in pH accompanying coordination with ethylenediamine. The depression of Co(II)–Y activity by ligands may be related to observed characteristic's of the electron transfer reaction between Co(II) and Co(III) which has been extensively studied.[23] At present, we can only point out the importance of the changes around the catalyst which are provoked by ligand coordination, par-

ticularly in the redox potential, substitution reactivity, and activation of the substrate in comparison with homogeneous catalysis by metal ions and their complexes.

Reference and Notes

(1) H. F. Leach, *Ann. Rep.*, **68A**, 195 (1971).
(2) (a) I. Mochida, S. Hayata, A. Kato, and T. Seiyama, *J. Catal.*, **15**, 314 (1969); **19**, 405 (1970); **21**, 31 (1971); *Bull. Chem. Soc. Jap.*, **44**, 2282 (1971); (b) J. Rouchand and J. Mokawa. *J. Catal.*, **19**, 172 (1970).
(3) I. Mochida, T. Jitsumatsu, A. Kato, and T. Seiyama, *Bull. Chem. Soc. Jap.*, **44**, 2595 (1971); *J. Catal.*, submitted for publication.
(4) I. Mochida, A. Kato, and T. Seiyama, *Bull. Chem. Soc. Jap.*, **45**, 2230 (1972).
(5) N. Uri, *Chem. Rev.*, **50**, 375 (1952); J. H. Baxendale, *Advan. Catal.*, **4**, 31 (1953); P. George, *ibid.*, **4**, 367 (1952).
(6) G. Herici-Olive and S. Olive, *Angew. Chem., Int. Ed. Engl.*, **10**, 105 (1971).
(7) W. N. Delgass, R. C. Garten, and M. Boudart, *J. Chem. Phys.*, **50**, 4603 (1969); *J. Catal.*, **18**, 90 (1970).

(8) H. M. Cota, *Nature (London)*, **203**, 1281 (1964); C. B. Roy, *J. Catal.*, **12**, 129 (1968).
(9) W. M. Latimer, "The Oxidation States of the Elements and their Relative Potentials in Aqueous Solution," Prentice Hall, New York, N. Y., 1952.
(10) V. S. Sharma and J. Schubert, *Inorg. Chem.*, **10**, 251 (1971).
(11) Y. Ogata and I. Tabushi, *Yuki Gosei Kagaku Shi*, **18**, 378 (1960).
(12) J. Von Bertlan, *Z. Phys. Chem.*, **A95**, 328 (1920).
(13) F. Basolo and R. G. Pearson, "Mechanisms in Inorganic Reactions," Wiley, New York, N. Y., 1967, p 226.
(14) J. H. Wang, *Account Chem. Res.*, **3**, 90 (1970); *J. Amer. Chem. Soc.*, **77**, 822, 4715 (1955); R. C. Jarnagin and J. H. Wang, *ibid.*, **80**, 6477 (1958).
(15) H. Sigel, *Angew. Chem., Int. Ed. Engl.*, **8**, 167 (1969), and references cited therein.
(16) M. L. Bender, "Mechanisms of Homogeneous Catalysis from Protons to Proteins," Wiley, New York, N. Y., 1971, Chapter 8.
(17) Reference 16, Chapters 12 and 13.
(18) F. Haber and J. Weiss, *Naturwissenschaften*, **20**, 948 (1932); *Proc. Roy. Soc., Ser. A*, **147**, 332 (1934); W. G. Barb, J. H. Baxendale, P. George, and K. R. Hargrave, *Nature (London)*, **163**, 692 (1949); *Trans. Faraday Soc.*, **47**, 591 (1951).
(19) M. L. Haggett, P. Jones, and W. F. K. Wynne-Jones, *Trans. Faraday Soc.*, **56**, 153 (1960).
(20) M. L. Kremer and G. Stein, *Trans. Faraday Soc.*, **55**, 595 (1959); M. L. Kremer, *ibid.*, **58**, 702 (1962); **59**, 2535 (1963).
(21) A. A. Balandin, *Advan. Catal.*, **19**, 1 (1969).
(22) Reference 9, Chapter 4.
(23) R. G. Link, in "Transition Metals in Homogeneous Catalysis," G. N. Schrauzer, Ed., Marcel Dekker, New York, N. Y., 1971, p 297.

Molecular Complexes of Iodine with Trioctylphosphine Oxide and Triethoxyphosphine Sulfide

Robert P. Lang

Department of Chemistry, Quincy College, Quincy, Illinois 62301 (Received April 10, 1974)

Absorption spectrophotometric studies have been made in the near-ultraviolet and visible spectral regions on the iodine complexes of trioctylphosphine oxide and triethoxyphosphine sulfide with *n*-heptane as solvent. For both complexes a "blue shift" of the visible iodine band was observed and isosbestic points obtained. Thermodynamic parameters were evaluated from the shifted visible iodine band data and the spectral characteristics for this band were determined. Also, for both complexes charge-transfer bands were located in the near-ultraviolet. The thermodynamic parameters were also evaluated from the charge-transfer band data and the spectral characteristics for this band were determined. Although the trioctylphosphine oxide-iodine complex was found to be significantly weaker than the trioctylphosphine sulfide-iodine complex the shift of the visible iodine band was the same, within experimental error, for both of these complexes. A solvent effect explanation has been offered for this unexpected experimental result. In contrast, the triethoxyphosphine sulfide-iodine complex has about the same strength as the structurally comparable tri-*n*-butoxyphosphine oxide-iodine complex, with essentially the same shift of the visible iodine band for both of these complexes.

Introduction

The thermodynamic parameters and the electronic spectral characteristics, for both the charge-transfer and the shifted visible iodine bands, have recently been determined for the trioctylphosphine sulfide-iodine complex in *n*-heptane.[1] The experimental results indicate that it is one of the strongest of known iodine complexes. A similar study of the iodine complexes of tetramethylurea and tetramethylthiourea indicates that the latter complex is sub-

stantially stronger than the former complex.[2] In addition, previous spectrophotometric work has shown that the diethyl sulfide-iodine complex[3] is significantly stronger than the diethyl ether-iodine complex.[4]

Furthermore, for both of these structurally comparable pairs of iodine complexes the stronger complex has its charge-transfer band absorption maximum located at the higher frequency and the stronger complex of the pair has the more intense charge-transfer band. These results are in agreement with the generally accepted charge-transfer

band theory predictions for a series of structurally similar molecular complexes.[5] In addition, for both of these pairs of iodine complexes the stronger complex has the greater "blue shift" of the visible iodine band and the stronger complex has the more intense shifted visible iodine band. Mulliken has proposed an explanation for the effect of complex formation on both the position and intensity of the visible iodine band.[5] Consequently, it would seem to be of considerable interest and value to determine both the thermodynamic and the electronic spectral characteristics of the trioctylphosphine oxide complex with iodine for comparison with the analogous properties of the trioctylphosphine sulfide–iodine complex.

Tsubomura and Kliegman have employed the shifted visible iodine band to determine the thermodynamic parameters of the tri-n-butoxyphosphine oxide (tri-n-butyl phosphate) complex with iodine in n-heptane.[6] The charge-transfer band of this complex was probably located at too short a wavelength to be detected under the usual experimental conditions. In connection with the above-mentioned thermodynamic and spectroscopic studies of structurally comparable pairs of iodine complexes involving oxygen and sulfur donor atoms, a comparison of the thermodynamic and spectroscopic data for the tri-n-butoxyphosphine oxide–iodine complex with those of the triethoxyphosphine sulfide–iodine complex would appear to be quite interesting and useful.

Experimental Section

Materials. Matheson Coleman and Bell spectroquality n-heptane and resublimed iodine were used without further purification. Eastman reagent grade trioctylphosphine oxide was recrystallized from absolute ethanol. Triethoxyphosphine sulfide (O,O,O-triethyl phosphorothioate), obtained from K & K Labs., Inc., was dried over Drierite and distilled under reduced pressure.

Spectrophotometric Determinations. Absorption spectra in the visible and near-ultraviolet spectral regions were measured by a Beckman double-beam (DB) ratio-recording spectrophotometer equipped with a Sargent linear-log (SRL) recorder. A pair of matched Beckman 1-cm silica U rectangular cells with ground-glass stoppers was employed for all the spectroscopic measurements. The Beckman DB spectrophotometer has a thermostatable cell compartment through which thermostated water was circulated from a Forma Scientific (Model 2095) refrigerated and heated bath and circulator. Measurements were made at 10, 20, 30, and 40° with the sample temperatures maintained constant to better than ±0.5°. Temperatures lower than 10° could not be employed because of the condensation of water vapor on the cell windows (a dry nitrogen purge kit cannot be used with the DB spectrophotometer).

The spectrophotometer wavelength scale was calibrated with a holmium oxide standard (Arthur H. Thomas Co.). For all the equilibrium constant determinations a series of solutions with a constant initial iodine concentration and variable initial donor concentrations was employed. The donor and acceptor concentrations were chosen so that all absorbance readings were in the range 0.30–0.95.

Calculation of K_c and ϵ_c. For both the visible and ultraviolet spectral studies of the trioctylphosphine oxide–iodine complex the following general equation for 1:1 molecular complex formation[1,7] was employed for the calculation of the molar concentration equilibrium constant, K_c, and the molar extinction coefficient of the complex, ϵ_c

$$\frac{D_0 I_0 b}{A'} = \left(D_0 + I_0 - \frac{A'}{b\epsilon_c'} \right) \frac{1}{\epsilon_c'} + \frac{1}{K_c \epsilon_c'} \quad (1)$$

where D_0 and I_0 are the initial molar concentrations of the donor and iodine, respectively, b is the path length of the spectrophotometer cell in centimeters, $A' = A - b\epsilon_I I_0$, and $\epsilon_c' = \epsilon_c - \epsilon_I$, where A is the total experimental absorbance and ϵ_I is the molar extinction coefficient of uncomplexed iodine. The actual calculations were performed by computer using an iterative standard least-squares treatment, with error limits at the 95% confidence level. Since the ϵ_I values varied randomly with temperature, for both the visible and ultraviolet regions, an average ϵ_I value was employed in the calculations. The computer program also took into account the change in density of the solution with temperature.

In the case of the triethoxyphosphine sulfide–iodine complex, for both the visible and ultraviolet studies, the experimental conditions were such that the initial concentration of the donor was always much greater than the initial concentration of iodine. Consequently, a modification of eq 1, in which the last two terms in the parentheses were dropped, was employed in the calculation of K_c and ϵ_c. The actual calculations were performed graphically by plotting $D_0 I_0 b/A'$ vs. D_0 and the error limits were estimated from the plots. Individual values of ϵ_I for each temperature were employed in the calculations and the variation of solution density with temperature was not taken into account.

Results

Trioctylphosphine Oxide. Solutions containing a constant initial iodine concentration and variable initial trioctylphosphine oxide concentrations showed an isosbestic point at about 485 nm in the visible spectral region. Some typical spectra are shown in Figure 1. The iodine concentration was about 6×10^{-4} M and the trioctylphosphine oxide concentrations varied from 1.0×10^{-3} to 6.3×10^{-3} M. The blue-shifted visible iodine band peak of the complex occurs at about 440 nm (see curve 4, Figure 1), and this wavelength was chosen for the determination of K_c. At this wavelength there was no absorption by the colorless trioctylphosphine oxide and there was a small absorption due to uncomplexed iodine which was corrected for by use of eq 1.

A rather interesting result of these visible spectral studies occurred as the concentration of trioctylphosphine oxide was increased above that mentioned in the previous paragraph, with the concentration of iodine remaining constant. These higher donor concentration spectral curves progressively missed the isosbestic point and two new absorption bands began to appear at shorter wavelengths. A very intense band appeared with absorption maximum at about 290 nm and a moderate intensity band with maximum around 370 nm. This pair of absorption bands has been attributed to the triiodide anion, I_3^-,[8] whose formation occurs as a frequent side reaction along with iodine molecular complex formation. However, in the author's past experience, simply reducing the donor concentration usually does not eliminate the triiodide formation.

In the near-ultraviolet the intense charge-transfer band of the trioctylphosphine oxide–iodine complex has an experimental absorption maximum at about 228 nm (see curve 3, Figure 2), and this wavelength was chosen for the determination of K_c. The initial iodine concentration was
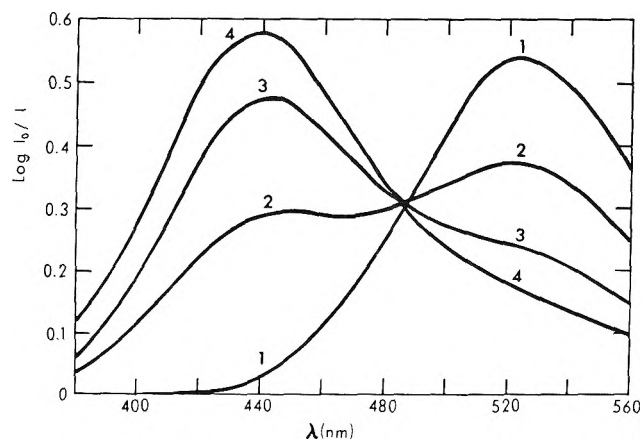
Figure 1. Visible absorption spectra of iodine–trioctylphosphine oxide solutions: solvent n-heptane, temperature 20°, cell 1 cm; curve 1, 6.0 × 10^{-4} M iodine; curve 2, 6.0 × 10^{-4} M iodine plus 1.0 × 10^{-3} M trioctylphosphine oxide; curve 3, 6.0 × 10^{-4} M iodine plus 3.2 × 10^{-3} M trioctylphosphine oxide; curve 4, 6.0 × 10^{-4} M iodine plus 5.2 × 10^{-3} M trioctylphosphine oxide.

maintained at about 6 × 10^{-5} M, a factor of ten less than for the visible spectral studies, and the donor concentration was in the range (3-11) × 10^{-4} M. At this wavelength there was a very small absorption due to trioctylphosphine oxide which was directly subtracted from the total experimental absorbance reading before the spectral data were employed in the calculation of K_c. In addition, there was a moderately large absorption due to uncomplexed iodine, attributed to the iodine–solvent "contact-charge-transfer" absorption band (see curve 2, Figure 2),[9] which was corrected for by use of eq 1.

Based on both the visible and ultraviolet data, the error limits for K_c are rather high (see Table I). Consequently, the standard enthalpy and entropy of complex formation were determined from the variation of log $K_c(\epsilon_c - \epsilon_I)$, rather than log K_c, with temperature.[10] The actual calculations were performed by computer using a standard linear least-squares treatment of log $K_c(\epsilon_c - \epsilon_I)$ as a function of $1/T$, with error limits at the 95% confidence level. The results are presented in Table I. There is a relatively large difference in the standard enthalpy and entropy values obtained from both the visible and the ultraviolet spectral data and the error limits are rather high. Also, the error limits for ϵ_c of the charge-transfer band, based on the least-squares treatment of the ultraviolet data, were very high. Consequently, the value of K_c determined from the visible data was employed to reduce the uncertainty in ϵ_c of the charge-transfer band.

The spectral data for the charge-transfer and shifted visible iodine bands are listed in Table II. The oscillator strength, f, and the transition dipole moment, D, were calculated from eq 2 and 3 of ref 1.[11] In order to obtain the integrated intensity data for both the charge-transfer and shifted visible iodine bands a correction was made, using K_c, for the overlap of the uncomplexed iodine absorption. For the shifted visible iodine band this correction did not result in a change in the absorption maximum wavelength position. However, for the charge-transfer band this correction resulted in a 2-nm shift in the absorption maximum from 228 to 230 nm (see Figure 2). Curve 4 of Figure 2 shows the charge-transfer band spectrum resulting from a small direct subtraction of the ab-
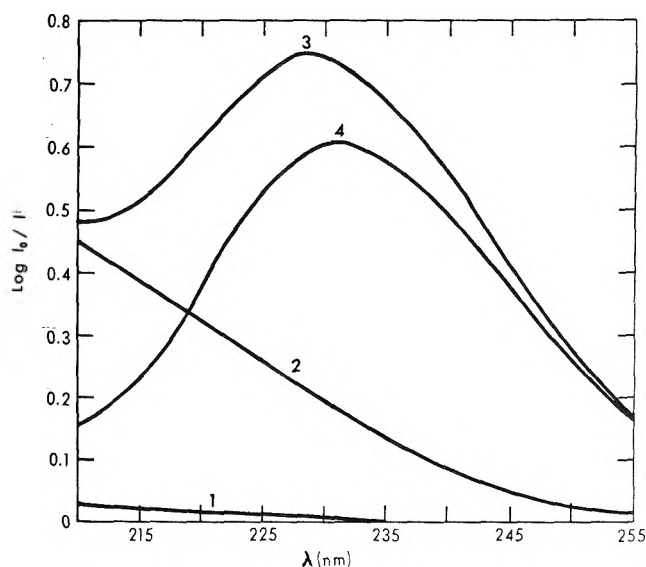
Figure 2. Ultraviolet absorption spectrum of the iodine–trioctylphosphine oxide complex: solvent n-heptane, temperature 20°, cell 1 cm; curve 1, 1.0 × 10^{-3} M trioctylphosphine oxide; curve 2, 6.0 × 10^{-5} M iodine; curve 3, 6.0 × 10^{-5} M iodine plus 1.0 × 10^{-3} M trioctylphosphine oxide; curve 4, the charge-transfer band of the trioctylphosphine oxide–iodine complex, obtained from curve 3 after correction for absorption due to trioctylphosphine oxide and uncomplexed iodine (see text for further explanation).

sorption due to the trioctylphosphine oxide and a moderate subtraction of the absorption due to uncomplexed iodine. These subtractions were made from curve 3 of Figure 2 to produce curve 4, Figure 2. It might be interesting to point out that for the solution concentrations employed in producing curve 3, Figure 2 about one third of the initial iodine concentration is in the complexed form so that the absorption due to uncomplexed iodine is approximately two thirds of curve 2, Figure 2. Resolved spectral curves were employed to obtain all the spectral data listed in Table II.

Triethoxyphosphine Sulfide. For the triethoxyphosphine sulfide–iodine complex an isosbestic point was obtained at about 500 nm for solutions containing a constant initial iodine concentration and a variable donor concentration. The spectra are similar to those shown in Figure 1. The iodine concentration was in the range (6.0-6.7) × 10^{-4} M and the triethoxyphosphine sulfide concentration varied from 0.05 to 0.6 M. The shifted visible iodine band experimental absorption maximum occurs at about 454 nm, and this wavelength was chosen for the determination of K_c. At this wavelength there was a small absorption due to the donor which was directly subtracted from the total absorbance and the small absorption due to uncomplexed iodine was corrected for by use of eq 1. The standard enthalpy and standard entropy of complex formation were evaluated from a plot of log K_c $vs.$ $1/T$ and the results are listed in Table I.

The charge-transfer band peak of this complex was located at about 285 nm and this wavelength was employed for the K_c determination. The iodine concentration was about 6 × 10^{-5} M and the donor concentration varied from 1.0 × 10^{-2} to 6.0 × 10^{-2} M. The small absorption due to the donor was directly subtracted from the total absorbance and the small absorption due to uncomplexed iodine was corrected for in eq 1. The standard enthalpy and entropy, evaluated from a log K_c $vs.$ $1/T$ plot, are

TABLE I: Thermodynamic Characteristics of the Trioctylphosphine Oxide–Iodine and the Triethoxyphosphine Sulfide–Iodine Complexes

Donor	K_c, mol^{-1} (20°)	$\Delta H°$, kcal/mol	$\Delta S°$, eu
	(a) From Uv Data		
Trioctylphosphine oxide	472 ± 543	−4.4 ± 3.8	−2.9 ± 12.9
Trioctylphosphine sulfide[a]	8500 ± 200	−11.4 ± 0.1	−21 ± 2
Triethoxyphosphine sulfide	34 ± 2	−3.5 ± 0.1	−5 ± 0.5
	(b) From Visible Data		
Triocytlphosphine oxide	592 ± 185	−5.8 ± 5.4	−7.0 ± 18.2
Trioctylphosphine sulfide[a]	8800 ± 400	−11.5 ± 0.5	−21 ± 5
Triethoxyphosphine sulfide	20 ± 2	−2.9 ± 0.2	−4 ± 0.5
Tri-n-butoxyphosphine oxide[b]	21	−2.9	−4

[a] Reference 1. [b] Reference 6.

TABLE II: Spectral Characteristics of the Trioctylphosphine Oxide–Iodine and the Triethoxyphosphine Sulfide–Iodine Complexes

Donor	λ_{max}, nm	ϵ_{max}, M^{-1} cm^{-1}	$\Delta \bar\nu_{1/2}$, cm^{-1}	f	D, D
	(a) Charge-Transfer Band				
Trioctylphosphine oxide	230 ± 1	29,000 ± 6000	6000 ± 150	0.75 ± 0.10	5.9 ± 0.5
Trioctylphosphine[a] sulfide	300 ± 1	36,000 ± 1000	5200 ± 100	0.80 ± 0.03	7.1 ± 0.2
Triethoxyphosphine sulfide	285 ± 1	25,000 ± 1000	4200 ± 100	0.45 ± 0.03	5.2 ± 0.2
	(b) Shifted Visible Iodine Band				
Trioctylphosphine oxide	440 ± 2	1,250 ± 110	4300 ± 100	0.023 ± 0.002	1.5 ± 0.1
Trioctylphosphine sulfide	440 ± 2	2,260 ± 100	4300 ± 100	0.042 ± 0.002	2.0 ± 0.1
Triethoxyphosphine[a] sulfide	455 ± 2	1,520 ± 150	4100 ± 100	0.027 ± 0.002	1.6 ± 0.1
Tri-n-butoxyphosphine[b] oxide	456	1,280	4200	0.023	1.5
n-Heptane, solvent	522 ± 2	897 ± 8	3200 ± 100	0.012 ± 0.001	1.2 ± 0.1

[a] From ref 1. [b] From ref 6.

listed in Table I. Again there is a somewhat large difference between the values obtained from the shifted visible iodine band and those obtained from the charge-transfer band.

The spectral data for the charge-transfer and shifted visible iodine bands, listed in Table II, for the triethoxyphosphine sulfide–iodine complex were obtained by the same method that was discussed previously for the trioctylphosphine oxide–iodine complex. For the shifted visible iodine band the experimental spectral curve resolution resulted in a shift of the absorption maximum from 254 to 255 nm. In the case of the charge-transfer band the correction for overlaping absorption due to the donor and uncomplexed iodine did not result in a change in the absorption maximum wavelength position mainly because the overlaping absorption was small and essentially horizontal.

Discussion

Trioctylphosphine Oxide. From the thermodynamic data in Table I one can see that trioctylphosphine oxide is a substantially weaker donor toward iodine than trioctylphosphine sulfide. These results are consistent with the analogous thermodynamic data for the iodine complexes of the tetramethylthiourea–tetramethylurea[2] and the diethyl sulfide[3]–diethyl ether[4] sulfur atom–oxygen atom donor pairs.

Furthermore, according to the charge-transfer band data in Table II, the weaker oxide complex has a less intense charge-transfer band than the stronger sulfide complex, although the weaker complex has the greater band half-width. Once again these results are in qualitative agreement with the charge-transfer band data for the thiourea–urea and sulfide–ether donor pairs mentioned previously. Also, the weaker oxide complex has its charge-transfer band located at a shorter wavelength than the

stronger sulfide complex again in agreement with the charge-transfer band data of the thiourea–urea and sulfide–ether donor pairs. These experimental results are in general agreement with the predictions of the most commonly accepted theories of molecular complex formation.[5]

In contrast to the consistent agreement discussed in the previous paragraphs the shifted visible iodine band data of Table II show the somewhat surprising experimental result of the coincidence of the wavelength maxima of the shifted visible iodine bands for the trioctylphosphine oxide and sulfide complexes with iodine. This result is in substantial disagreement with the shifted visible iodine band data for the thiourea–urea and sulfide–ether donor pairs. For both of these donor pairs the "blue shift" of the visible iodine band is considerably greater for the stronger sulfur atom donor (see Figure 3, points 3 and 5) than for the weaker oxygen atom donor (Figure 3, points 4 and 6). On the other hand, the shifted visible iodine band intensity data for the trioctylphosphine oxide and sulfide complexes follow the general trend[1,3a] of increasing intensity along with increasing donor strength (see Figure 4).

According to "simple" theory[5] there should be a direct correlation between the strength of complex formation and the magnitude of the "blue shift." And since there is an experimentally significant difference in donor strength between the trioctylphosphine oxide and sulfide–iodine complexes one would expect a corresponding experimentally significant difference in the shifted position of the visible iodine band for these two structurally similar molecular complexes.

Perhaps the solvent may have an influence on the correlation and the effect may not be the same for all complexes.[12] Tamres recent vapor-phase work on the diethyl and dimethyl sulfide–iodine complexes[13] indicates that the visible iodine band is shifted to a greater extent in n-heptane than in the vapor phase. Furthermore, some re-
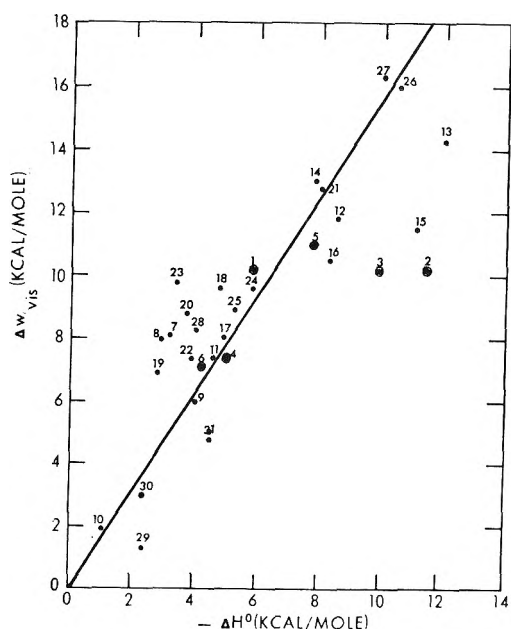
Figure 3. Correlation between the blue shift of the visible I_2 band ($\Delta W_{vis} = h\nu_{comp} - h\nu_{free\ I_2}$) and the standard enthalpy of formation, $-\Delta H°$, for some I_2 complexes. The linear correlation curve is taken from Figure 10-7 of ref 5. The donors are (1) trioctylphosphine oxide (this work); (2) trioctylphosphine sulfide (ref 1); (3) tetramethylthiourea (ref 2); (4) tetramethylurea (ref 2); (5) diethyl sulfide (ref 3a); (6) diethyl ether (ref 4); (7) triethoxyphosphine sulfide (this work); (8) tri-n-butoxyphosphine oxide (ref 6); (9) diethylchlorophosphine sulfide (ref 1); (10), trichlorophosphine sulfide (ref 7); (11) diethyl disulfide (ref 3a); (12) dimethyl selenide (ref 3a); (13) triethylamine (ref 3a); (14) pyridine (ref 3a); (15) selenacyclopentane (ref 16); (16) thiacyclopentane (ref 3b); (17) tetrahydropyran (ref 4); (18) diphenylselenium oxide (ref 17); (19) diphenyl sulfoxide (ref 18); (20) dimethyl sulfoxide (ref 19); (21) triphenylarsine oxide (ref 20); (22) ethyl isothiocyanate (ref 21); (23) N,N-dimethylmethanesulfonamide (ref 22); (24) pyridine N-oxide (ref 23); (25) N-methylbenzaldoxime (ref 23); (26) tribenzylamine N-oxide (ref 23); (27) trimethylamine N-oxide; (28) N,N-dimethylformamide; (29) thiophene (ref 24); (30) 2-methylfuran (ref 24); (31) N-methylpyrrole (ref 24).

cent preliminary vapor-phase results from Tamres laboratory indicate that there is a considerable difference between the shifted visible iodine band position in the vapor phase and in solution (n-heptane) for the diethyl ether–iodine complex.[12] These results would seem to indicate that the effect of solvent on the position of the shifted visible iodine band is greater for the weaker of a structurally similar donor pair.

If the above reasoning is correct then perhaps the exactness of the agreement in the position of the trioctylphosphine oxide and sulfide shifted visible iodine bands is accidental and the "simple" theory may be satisfactory for vapor-phase correlations between donor strength and band position. Using this reasoning the coincidence of the phosphine oxide and sulfide band positions could be explained in the following way. In the vapor phase the visible iodine band of the trioctylphosphine sulfide–iodine complex would be "blue" shifted to a significantly greater extent than that of the weaker trioctylphosphine oxide–iodine complex. The effect of the n-heptane solvent would be to further "blue shift" the visible iodine band of both complexes. However, this solvent effect would be greater for the weaker trioctylphosphine oxide–iodine complex than for the stronger trioctylphosphine sulfide–iodine complex, resulting in an accidental coincidence of absorption maxi-
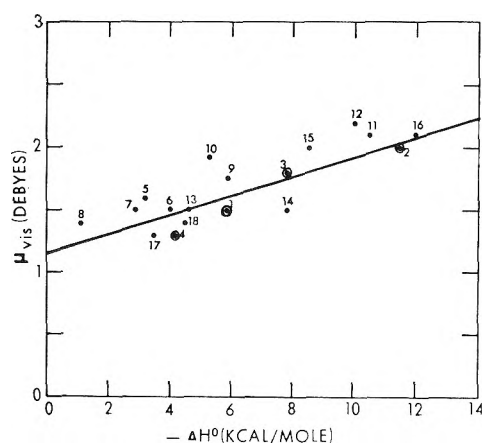
Figure 4. Correlation between the integrated intensity, transition dipole (μ_{vis}), of the shifted visible iodine band, and the standard enthalpy of formation, $-\Delta H°$, for some I_2 complexes. The donors are (1) trioctylphosphine oxide (this work); (2) trioctylphosphine sulfide (ref 1); (3) diethyl sulfide (ref 3a); (4) diethyl ether (ref 4); (5) triethoxyphosphine sulfide (this work); (6) diethylchlorophosphine sulfide (ref 1); (7) tri-n-butoxyphosphine oxide (ref 6); (8) trichlorophosphine sulfide (ref 1); (9) pyridine N-oxide (ref 23); (10) N-methylbenzaldoxime (ref 23); (11) tribenzylamine N-oxide (ref 23); (12) trimethylamine N-oxide (ref 23); (13) diethyl disulfide (ref 3a); (14) pyridine (ref 3a); (15) dimethyl selenide (ref 3a); (16) triethylamine (ref 3a); (17) methanol (ref 25); (18) ethanol (ref 25).

ma for these two iodine complexes. Tamres has pointed out, based on preliminary results, that the dimethyl sulfide– and selenide–iodine complexes (in n-heptane) also seem to have their shifted visible iodine band maxima in the same spectral region ($\sim$437 nm) although the selenide is stronger than the sulfide complex.[12a]

Triethoxyphosphine Sulfide. The data in Table I show that the triethoxyphosphine sulfide–iodine complex is considerably weaker than the trioctylphosphine sulfide–iodine complex which is to be expected because of the greater electron-withdrawing inductive effect of an alkoxy group relative to an alkyl group.[14] Also, a comparison of the charge-transfer band data of Table II show the expected result of the weaker iodine complex having the less intense charge-transfer band with its absorption maximum being located at a shorter wavelength. In addition, the shifted visible iodine band data for these two complexes follow the general trend that the stronger the complex the greater the magnitude of the "blue shift" and the more intense the shifted iodine band (see Figures 3 and 4, respectively).

A comparison of the thermodynamic data, determined from visible spectral data (Table I), for the triethoxyphosphine sulfide–iodine complex with that of the tri-n-butoxyphosphine oxide–iodine complex shows the somewhat surprising result that the molar concentration equilibrium constant and the standard enthalpy change for both complexes are essentially the same, within experimental error. Since one would probably not expect a very significant difference between the inductive effects of the ethoxy and n-butoxy groups on the donor ability of the phosphino and thiophosphino groups one would expect the sulfur atom donor complex to be somewhat stronger than the corresponding oxygen atom donor complex,[15] as demonstrated in the case of the trioctylphosphine sulfide and oxide–iodine complexes. The shift of the visible iodine band (Table II) is essentially the same for these two trialkoxyphosphine sulfide and oxide complexes and the intensity

data are also essentially the same when one considers the possible experimental error. However, since the thermodynamic data indicate comparable complex stability for these two iodine complexes one would most likely expect the observed comparable shifted visible iodine band data.

References and Notes

(1) R. P. Lang, *J. Amer. Chem. Soc.*, **93**, 5047 (1971).
(2) R. P. Lang, *J. Phys. Chem.*, **72**, 2129 (1968).
(3) (a) H. Tsubomura and R. P. Lang, *J. Amer. Chem. Soc.*, **83**, 2085 (1961); (b) M. Tamres and S. Searles, *J. Phys. Chem.*, **66**, 1099 (1962).
(4) (a) M. Brandon, M. Tamres, and S. Searles, *J. Amer. Chem. Soc.*, **82**, 2129 (1960); (b) M. Tamres and M. Brandon, *ibid.* **82**, 2134 (1960).
(5) R. S. Mulliken and W. B. Person, "Molecular Complexes," Wiley, New York, N. Y., 1969.
(6) H. Tsubomura and J. Kliegman, *J. Amer. Chem. Soc.*, **82**, 1314 (1960).
(7) M. Tamres, *J. Phys. Chem.*, **65**, 654 (1961); see eq 25.
(8) (a) A. D. Awtrey and R. E. Connick, *J. Amer. Chem. Soc.*, **73**, 1842 (1951); (b) R. E. Buckles, J. P. Yuk, and A. I. Popov, *ibid.*, **74**, 4379 (1952).
(9) L. E. Orgel and R. S. Mulliken, *J. Amer. Chem. Soc.*, **79**, 4839 (1957).
(10) (a) M. Tamres and J. M. Goodenow, *J. Phys. Chem.*, **71**, 1982 (1967); (b) W. B. Person, *J. Amer. Chem. Soc.*, **87**, 167 (1965).
(11) R. S. Mulliken and W. B. Person, *Annu. Rev. Phys. Chem.*, **13**, 107 (1962).
(12) (a) M. Tamres, private communication. (b) M. Tamres and S. N. Bhat, *J. Amer. Chem. Soc.*, **95**, 2516 (1973).
(13) (a) M. Tamres and S. N. Bhat, *J. Phys. Chem.*, **75**, 1057 (1971); (b) *J. Amer. Chem. Soc.*, **94**, 2577 (1972).
(14) The Taft σ^* substituent values can be used to obtain a quantitative estimate of the relative substituent inductive effect for an alkyl and an alkoxy group (see, for example, W. B. Person, W. C. Golton, and A. I. Popov, *J. Amer. Chem. Soc.*, **85**, 891 (1963)). The Taft σ^* values for an *n*-butyl group (R. W. Taft, Jr., "Steric Effects in Organic Chemistry," M. S. Newman, Ed., Wiley, New York, N. Y., 1956, Chapter 13) and an ethoxy group (T. Gramstad, *Spectrochim. Acta*, **20**, 729 (1964)) are −0.130 and +1.35, respectively. The Taft σ^* value for a chloro group is +2.94 (A. Allerhand and P. v. R. Schleyer, *J. Amer. Chem. Soc.*, **85**, 866 (1963)), which is consistent with the experimental data that indicate trichlorophosphine sulfide forms a weaker complex with iodine than triethoxyphosphine sulfide (ref 1).
(15) T. Gramstad and W. J. Fuglevik, *Acta Chem. Scand.*, **16**, 2368 (1962), have reported standard enthalpy of formation values for iodine complexes (in carbon tetrachloride) with the donors triethoxyphosphine oxide and sulfide of −3.2 and −5.9 kcal/mol, respectively.
(16) J. D. McCullough and A. Brunner, *Inorg. Chem.*, **6**, 1251 (1967).
(17) J. Grundnes and P. Klaeboe, *Acta Chem. Scand.*, **18**, 2022 (1964).
(18) P. Klaeboe, *Acta Chem. Scand.*, **18**, 999 (1964).
(19) P. Klaeboe, *Acta Chem. Scand.*, **18**, 27 (1964).
(20) J. Grundnes, P. Klaeboe, and E. Plahte, "Selected Topics in Structure Chemistry," Universitetsforlaget, Oslo, 1967, pp 265–275.
(21) E. Plahte, J. Grundnes, and P. Klaeboe, *Acta Chem. Scand.*, **19**, 1897 (1965).
(22) H. Mollendal, J. Grundnes, and P. Klaeboe, *Spectrochim. Acta, Sect. A*, **24**, 1669 (1968).
(23) T. Kubota, *J. Amer. Chem. Soc.*, **87**, 458 (1965).
(24) R. P. Lang, *J. Amer. Chem. Soc.*, **84**, 4438 (1962).
(25) L. Julien, Ph.D. Thesis, University of Iowa, 1966.

Studies of Hydrogen Bonding in Carboxylic Acid–Dimethyl Sulfoxide Systems by Nuclear Magnetic Resonance Dilution Shifts

Hideaki Fujiwara

Chemical Research Institute of Non-Aqueous Solutions, Tohoku University, Katahira-2-chrome, Sendai 980, Japan

(Received February 13, 1974)

Nmr dilution shifts have been measured for binary systems of carboxylic acids and dimethyl sulfoxide (DMSO). The acids studied were acetic, propionic, isobutyric, and trifluoroacetic acids. The dilution shifts of OH proton plotted against acid mole fraction showed characteristic *v*-type curves with the highest chemical shifts at the concentration of 0.65~0.75 mole fraction. The curves could be well explained by assuming the formation of a 2(acids):1(DMSO) complex besides the 1:1 complex in the chemical equilibrium. The formation constants of the 2:1 and 1:1 complexes were estimated. In the carboxylic acid–cyclohexane systems, the dilution shifts changed linearly with the acid concentration in 0.1~0.9 mole fractions.

Introduction

Recently dimethyl sulfoxide (DMSO) has come to be well known as a proton acceptable polar solvent. Because of its excellent properties as a solvent for organic and inorganic substances, it has attracted special interests in the field of organic synthesis, macromolecular chemistry, and pharmacology.[1,2] For nmr studies, DMSO which de-

presses exchange rate of OH proton has been effectively used for classifications[3] or measurements of coupling constants[4] of alcohols.

In the present study, the interaction of DMSO with some carboxylic acids was investigated by analyzing the dilution curves of nmr chemical shifts. The carboxylic acids studied were acetic, propionic, isobutyric, and trifluoroacetic acids.
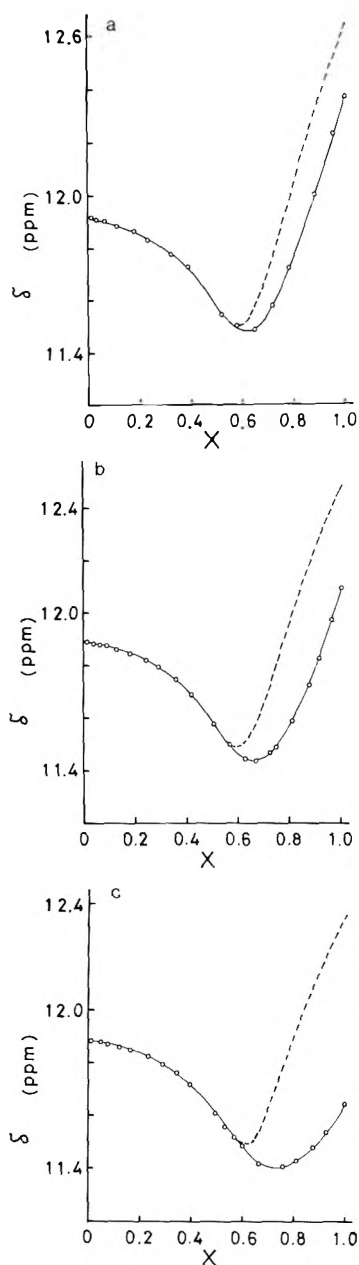
Figure 1. Observed and calculated dilution shift curves for the acid–DMSO systems: a, isobutyric acid; b, propionic acid; c, acetic acid; ---, dilution shift curves calculated; O, experimental points.
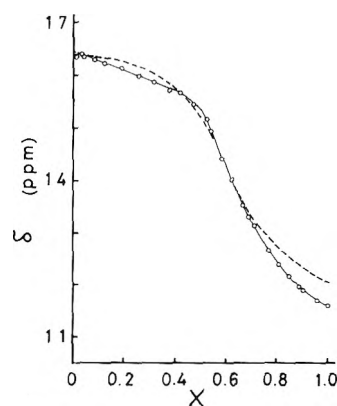

Figure 2. Observed and calculated dilution shift curves for the TFA–DMSO system: ---, dilution shift curve calculated ($K_1 = 500$, $K_2 = 10$, $\delta_{C\alpha} = 13.35$ ppm); O, experimental points.

bon tetrachloride to zero concentration of the acid. Other δ_D values have been obtained by several authors[10-12] from the analysis of the dilution shift curves in consideration of the appropriate equilibria of acid self-associations. However, it is difficult to find the reliable δ_D values of carboxylic acids for the discussion of the present results.

Experimental Section

Since traces of impurities having exchangeable protons, such as water, acids, and bases, give serious errors to the shift curves of OH proton, all procedures for purification of reagents and preparation of solutions were carried out in a completely shielded system.[13]

Research grade DMSO was refluxed over CaH_2 for 24 hr and then fractionally distilled under reduced pressure. The middle cut was stirred with CaH_2 for 1 week in a sealed bottle and then separated by vacuum distillation. To eliminate a trace of ammonia, coming from the reaction of water and nitrogen containing impurities in CaH_2,[14] vacuum distillation was repeated several times and ca. $\frac{1}{20}$ of the DMSO was discarded in each time.

Research grade cyclohexane was allowed to stand over P_2O_5 for 2 weeks with occasional stirring and then fractionally distilled. To check the purity of the solvent, it was mixed with ethanol. The mixture showed the nmr fine structure of OH proton for the wide range of alcohol concentrations. This shows that serious impurities are negligible. Carboxylic acids were dried with the boron tricarboxylates.

Nmr spectra were obtained with a Hitach R-20B high-resolution nmr spectrometer (60 MHz, at 35°). About 10^{-3} mole fraction of TMS was added to each specimen as the internal standard.

Results

The chemical shifts of the OH proton (δ_{OH}) in the systems of carboxylic acid–DMSO plotted against acid mole fraction (X) are shown in Figures 1 and 2 (solid line). The characteristic ν-type patterns are clearly shown in the shift curves of acetic, propionic, and isobutyric acids.

The system trifluoroacetic acid (TFA)–DMSO, however, showed a different curve from those for other acids (Figure 2).

δ_{OH}'s of the acid–cyclohexane systems are shown in Figure 3. In the case of TFA–cyclohexane system, nmr data could not be obtained in the intermediate concentration range, because the two components were immiscible.
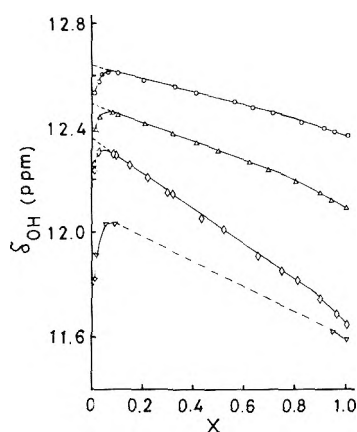
The acetic acid–DMSO system has been studied[5-8] by means of infrared and Raman spectroscopy, cryoscopy, and measurements of viscosities and electric conductivities. Although those studies gave evidences of the presence of a 1:1 complex, the existence of a 2:1 complex was still ambiguous. In some literature[5,8] the 2:1 complex was assumed, but its structure has not been confirmed yet. In the present experiments it was observed that the dilution shift curves of OH proton in the carboxylic acid–DMSO systems plotted against acid mole fraction showed characteristic ν-type patterns. These ν-type curves could be well explained by assuming the formation of a 2:1 complex besides a 1:1 complex.

The OH proton chemical shift of the acetic acid cyclic dimer (δ_D) was first reported by Reeves and Schneider[9] who evaluated it by extrapolating the dilution shift curve of moderately concentrated solution in cyclohexane or car-

Figure 3. Chemical shifts of OH proton in the acid–cyclohexane systems: $\lozenge$, acetic acid; $\triangle$, propionic acid; $\bigcirc$, isobutyric acid; $\triangledown$, trifluoroacetic acid.
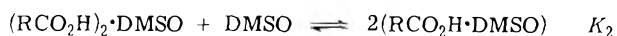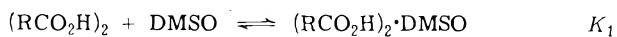
Discussion

Infrared,[15] far infrared,[16] Raman,[17] and X-ray[18] studies have shown that acetic acid consists mostly of cyclic dimers and only partly of chain oligomers in the pure state, and that upon dilution with cyclohexane or n-heptane chain oligomers reduce to cyclic dimers. As the complexes formed between acetic acid and DMSO, two species, viz. 1:1 complex[5-8] and 2(acids):1(DMSO) complex,[5,8] have been proposed.

For simplification chain oligomers are neglected in the present consideration. The presence of acid monomer is also neglected, since the amount of the monomer is usually negligible in pure carboxylic acid and the monomer should be liable, if at all, to form hydrogen bonds with basic DMSO. Assuming the formation of only a 1:1 complex, the following equilibrium might be considered.

$$(RCO_2H)_2 + 2DMSO \rightleftharpoons 2(RCO_2H \cdot DMSO)$$
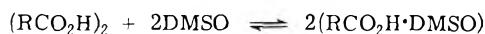
This assumption, however, can not explain the v-type curves in Figure 1, because this equilibrium leads to the monotonous change of the chemical shift of OH proton from the value of cyclic dimer to that of the 1:1 complex with the dilution of the acid. Therefore, the formation of both 1:1 and 2:1 complexes were assumed.

$$(RCO_2H)_2 + DMSO \rightleftharpoons (RCO_2H)_2 \cdot DMSO \qquad K_1$$

$$(RCO_2H)_2 \cdot DMSO + DMSO \rightleftharpoons 2(RCO_2H \cdot DMSO) \qquad K_2$$

Let us suppose that A moles of cyclic dimer, B moles of free DMSO, C_1 moles of 2:1 complex, and C_2 moles of 1:1 complex are produced by mixing totally 1 mol of carboxylic acid and DMSO, $i.e.$, X moles of the acid (in monomer unit) and $(1 - X)$ moles of DMSO, X being the initial mole fraction of the acid. The mole fraction of each species corresponds to A, B, C_1, and C_2 divided by $(A + B + C_1 + C_2)$, and hence two equilibrium constants, K_1 and K_2, are expressed as follows

$$K_1 = C_1(A + B + C_1 + C_2)/(AB) \qquad (1a)$$

$$K_2 = C_2{}^2/(C_1B) \qquad (1b)$$

Since the number of acid or DMSO molecules, enumerated in monomer units, is constant before and after mixing, following two equations should hold

$$X = 2A + 2C_1 + C_2 \qquad (1c)$$

$$1 - X = B + C_1 + C_2 \qquad (1d)$$

The shift of OH proton can be expressed as the weighted sum of the shift in each species, that is

$$\delta_{cald} = (2A\delta_D + 2C_1\delta_{c\alpha} + C_2\delta_{c\beta})/X \qquad (2)$$

where the following abbreviations are used: δ_{cald} = calculated chemical shift of the OH proton; δ_D = chemical shift of the OH proton in the cyclic dimer; $\delta_{c\alpha}$ = chemical shift of the OH proton in the 2:1 complex; and $\delta_{c\beta}$ = chemical shift of the OH proton in the 1:1 complex. From eq 1a–d the following three equations are derived.

$$4[K_1K_2 - (1 + K_1)^2]A^4 - 8(1 -$$
$$3X/2)[(1 + K_1)^2 - K_1K_2]A^3 + \{K_1K_2(1 - 2X)(5 -$$
$$6X) - 4(1 + K_1)[(1 - 3X/2)^2K_1 + 13X^2/4 -$$
$$4X + 1]\}A^2 + (1 - X)[K_1K_2(1 - 2X)^2 + 4X(1 -$$
$$3X/2)(1 + K_1)]A - X^2(1 - X)^2 = 0 \qquad (3)$$

$$C_1 = K_1A[1 + 2(A - X)]/[(1 - K_1)A + 1 - X] \qquad (4)$$

$$C_2 = X - 2(A + C_1) \qquad (5)$$

The estimation of the δ_{cald} value for any value of X from eq 2 requires six variables, A, C_1, C_2, δ_D, $\delta_{c\alpha}$, and $\delta_{c\beta}$. Among these, A, C_1, and C_2 are calculated from eq 3, 4, and 5, respectively, if K_1 and K_2 are given. δ_D and $\delta_{c\beta}$ can be determined experimentally as will be shown later. $\delta_{c\alpha}$, K_1, and K_2 remain as unknown parameters. In the present study, $\delta_{c\alpha}$, K_1, and K_2 values of a given system were determined so as to give the best fit between the calculated and observed dilution shift curves.

The $\delta_{c\beta}$ value was substituted by the value of δ_{OH} at infinite dilution of the acid in DMSO, since the 1:1 complex predominates with decreasing acid concentration. This value can be obtained without much uncertainty, because the change of δ_{OH} upon dilution is small at low concentration of acids as seen in Figure 1.

The δ_D value was evaluated by extrapolating the straight part of the dilution shift curve in cyclohexane (Figure 3) to infinite dilution of the acid, since the straight line may indicate the conversion of the acid chain oligomer to cyclic dimer.[9a]

To obtain the best set of K_1, K_2, and $\delta_{c\alpha}$, $\delta_{c\alpha}$ was calculated by eq 2 using a trial set of K_1 and K_2 so that δ_{cald} equaled δ_{OH} at a point about 0.5 mole fraction of acid, and then the validity of the set of the three parameters was checked for the other δ_{OH}'s.[19]

As a result of the calculation δ_{cald} deviated from δ_{OH} toward the low-field side above 0.6 mole fraction of acids, though it agreed well with δ_{OH} below 0.6 mole fraction. This deviation is relatively small in the case of isobutyric acid (Figure 1a) but it increases in the order of isobutyric, propionic (Figure 1b), and acetic acids (Figure 1c). Such deviation is also observed in the acid–cyclohexane systems (Figure 3), in which δ_{OH} changed from δ_D toward the high-field side with increasing acid concentration, suggesting the formation of chain oligomers.[9] In connection with this the formation of chain oligomers was suggested to be prevented by the increased steric hindrance around the CO_2H group.[20] In fact, the deviation decreases in the order of increased steric hindrance also in the present case. In order to minimize the above deviation, it should be necessary to introduce the equilibrium of the formation of chain oligomers and also the equilibrium of the complex formation of chain oligomers with DMSO. However,
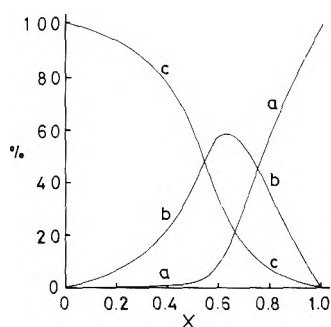
Figure 4. Distribution probability of an acid molecule in the three species for the acetic acid–DMSO system: a, cyclic dimer; b, 2:1 complex; c, 1:1 complex.

the introduction of these equilibria is liable to make the calculation intractable, otherwise increase in the number of parameters may prevent the unequivocal determination of parameters, and so the equilibria were omitted. In practice, K_1, K_2, and $\delta_{c\alpha}$ values were determined by using the values of δ_{OH} in the region below 0.6 mole fraction of the acid.

The calculations are shown in Table I and Figure 4. The distribution curves for the acetic acid–DMSO system in Figure 4 are taken up as a representative case. This figure indicates that the formation of a 2:1 complex having a more shielded OH proton than that in the 1:1 complex or in the cyclic dimer caused the appearance of the ν-type pattern in the dilution shift curve, confirming the validity of the assumption about the presence of both complexes.

The δ_D values shown in Table I were obtained by applying a simple method[9a] to the dilution shift curves for the acids in cyclohexane. Careful attention was paid to otain these reliable data under the same conditions as the DMSO system and to exclude impurities. Although the δ_D values of a few carboxylic acids have been reported by several investigators,[9-12,21,22] there are little reliable data particularly on the acids other than acetic acid because of the uncertainties of the temperature dependence of δ_D[10,12] and the dilution shift of δ_{OH}.[23]

The influence of the δ_D value on the δ_{cald} value examined for the acetic acid–DMSO system showed that the change of ±0.2 ppm in δ_D value results in the change of ±0.005 ppm in δ_{cald} value at the concentration of 0.57 mole fraction of acetic acid, where the contribution of cyclic dimer to the δ_{cald} value is largest in the region used for the calculation. This small influence of δ_D value on δ_{cald} value can be readily seen from Figure 4, which indicates that the distribution probability of the acid molecule in the cyclic dimer is very small at the acid concentrations below 0.6 mole fraction. Thus, the δ_D value adopted in the present study was not strictly determined, but is sufficient to discuss results relating to the carboxylic acid–DMSO systems.

The disappearance of ν-type pattern in the case of TFA (Figure 2) is probably due to the large low-field shift of $\delta_{c\beta}$. As shown in Table I, $\delta_{c\beta}$ of TFA lies at lower field than those of the other acids by ca. 6 ppm, and this low-field shift has probably masked the ν-type pattern.

The values of δ_{cald} for three sets of K_1, K_2, and $\delta_{c\alpha}$ are shown in Table II, which indicates that there are uncertainties in the determination of the three parameters, ca. $\pm20\%$ for K_1 and K_2, and ca. ±0.05 ppm for $\delta_{c\alpha}$. For the precise determination of the three parameters it is necessary to measure δ_{OH} with high accuracy (better than ±0.1

TABLE I: Parameters Obtained Experimentally or by Calculation for Carboxylic Acid–DMSO Systems

	Acetic acid	Propionic acid	Isobutyric acid	TFA
δ_D, ppm	12.36	12.49	12.64	12.03[c]
$\delta_{c\beta}$, ppm	11.88	11.89	11.92	16.44
K_1[b]	100	60	40	d
K_2[b]	9	9	9	d
$\delta_{c\alpha}$, ppm[a]	11.13	11.00	10.87	d

[a] With an accuracy of ca. ±0.05 ppm. [b] With an accuracy of ca. $\pm20\%$. [c] Shift at 0.05 mole fraction of TFA in cyclohexane. [d] Not fully analyzed.

Hz) and is also necessary to carry out the elaborate curve fitting by the use of a computer.

In the case of TFA (Figure 2), the results are not as straightforward as the other acids. A satisfactory agreement between δ_{cald} and δ_{OH} was not obtained for any set of K_1, K_2, and $\delta_{c\alpha}$. Below 0.4 mole fraction of the acid δ_{OH} changed almost linearly with acid concentration, but such linear variation could not be realized by the calculation based on the model mentioned above. Reasons for this deviation can be considered as follows: (a) ionizations of the 1:1 and/or 2:1 complexes take place, such as

$$CF_3CO_2H\text{---}O{=}S\overset{\displaystyle CH_3}{\underset{\displaystyle CH_3}{<}} \rightleftharpoons CF_3CO_2^- + H\text{---}O^+{=}S\overset{\displaystyle CH_2}{\underset{\displaystyle CH_3}{<}}$$
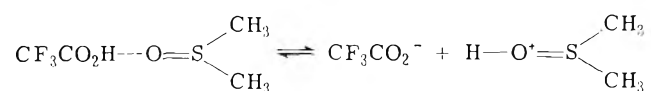
(b) the acid can not be regarded as being only the cyclic dimer. In connection with a, Nawrot and Veis[24] reported from an infrared study that the carboxylate ion is present in the TFA–DMSO system. In connection with b, Murty and Pitzer[25] reported that TFA is reasonably expected to have a better chance than other monocarboxylic acids to form chain oligomers. A similar dilution shift curve was also observed for the TFA-N,N-dimethylacetamide system. These two systems are now concurrently under investigation in detail.

The following two structures have been proposed for the 2:1 complex[5,8]

A

B
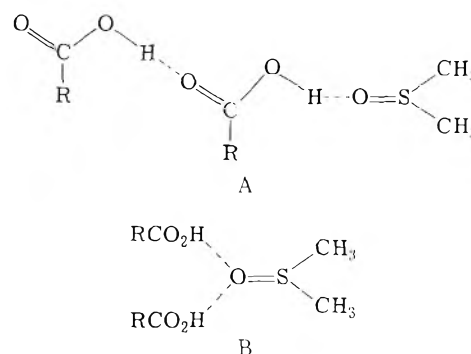
In the case of structure A, $\delta_{c\alpha}$ may be equal to $(\delta_D + \delta_{c\beta})/2$.[26] In the present experiment (Table I), however, $\delta_{c\alpha}$ lies at higher field than $(\delta_D + \delta_{c\beta})/2$ by ca. 1.5 ppm. Therefore, though some authors[5,8] preferred A, A is improbable and B may be presumed. In agreement with this result, it has been reported[27,28] for the other systems that DMSO is able to accept two protons as in the case of B. Also an alternative structure seems to be possible; in the structure one proton is accepted on the oxygen atom and the other on the sulfur atom. The ν-type dilution shift curves were also observed for carboxylic acid-N,N-dimethylacetamide systems and the isobutyric acid–pyraz-

TABLE II: Values of δ_{cald} for Three Sets of K_1, K_2, and $\delta_{c\alpha}$ in the Acetic Acid–DMSO System

X	δ_{OH}	δ_{cald} $K_1 = 120$ $K_2 = 8$ $\delta_{c\alpha} = 11.17$	100 9 11.13	90 10 11.10
0.010	11.88$_0$	11.878	11.878	11.879
0.015	11.88$_0$	11.877	11.877	11.878
0.048	11.87$_7$	11.871	11.871	11.872
0.078	11.86$_7$	11.864	11.865	11.866
0.119	11.85$_7$	11.855	11.856	11.857
0.164	11.84$_5$	11.842	11.844	11.846
0.232	11.82$_0$	11.818	11.821	11.824
0.290	11.79$_2$	11.791	11.795	11.798
0.345	11.76$_0$	11.759	11.763	11.767
0.395	11.71$_8$	11.720	11.724	11.727
0.496	11.60$_8$	11.608	11.608	11.608
0.532	11.55$_3$	11.560	11.559	11.557
0.570	11.51$_5$	11.513	11.513	11.512
0.600	11.48$_0$	11.493	11.497	11.497
		0.0033[a]	0.0032[a]	0.0043[a]

[a] Root mean square deviation from $X = 0.010$ to $X = 0.570$.

ine (typical diacidic base) system. These facts support the assumption that the ν-type dilution shift curve results from the formation of 2:1 complex. Those results will be published later.

Acknowledgments. The author wishes to express his gratitude to Mr. T. Ikenoue, Mr. N. Yoshida, Mr. M. Kumano, Dr. K. Kondo, Dr. Y. Ikegami, and Dr. M. Iwaizumi for their helpful discussions. He is also grateful to Mr. K. Fujieda for helpful advice on accurate nmr measurements.

References and Notes

(1) S. Oae, "Chemistry of Organosulfur Compounds," Kagaku Dojin, Tokyo, 1969.
(2) D. Martin, A. Weise, and H. J. Niclas, *Angew. Chem.*, **79**, 340 (1967).
(3) O. L. Chapman, *J. Amer. Chem. Soc.*, **86**, 1256 (1964).
(4) (a) C. P. Rader, *J. Amer. Chem. Soc.*, **91**, 3248 (1969); (b) P. L. Corio, R. L. Lutledge, and J. R. Zimmerman, *ibid.*, **80**, 3163 (1958); (c) D. E. McGreer and M. M. Mocek, *J. Chem. Educ.*, **40**, 358 (1963).
(5) J. J. Lindberg and C. Majani, *Suomen Kemistilehti B*, **37**, 21 (1964).
(6) M. Haurie and A. Novak, *J. Chim. Phys.*, **64**, 679 (1967).
(7) I. M. Bokhovkin, Yu. I. Bokhovkin, and V. F. Chesnokov, *Zh. Obshch. Khim.*, **39**, 1437 (1969).
(8) I. V. Khazova and V. F. Chesnokov, *Zh. Obshch. Khim.*, **40**, 7 (1970).
(9) (a) L. W. Reeves and W. G. Schneider, *Trans. Faraday Soc.*, **54**, 314 (1958); (b) L. W. Reeves, *ibid.*, **55**, 1684 (1959).
(10) U. Jentschura and E. Lippert, *Ber. Bunsenges. Phys. Chem.*, **75**, 556 (1971).
(11) M. Servanton, J. Biais, and B. Lemanceau, *J. Chim. Phys.*, **67**, 800 (1970).
(12) M. A. Goldman and M. T. Emerson, *J. Phys. Chem.*, **77**, 2295 (1973).
(13) T. Ikenoue, K. Kondo, N. Yoshida, and H. Fujiwara, to be submitted for publication.
(14) "Gmelins Handbuch der Anorganischen Chemie" E. H. Erich Pietsch, Ed., Weinheim/Bergstrasse, sys. No. 28, B (2), 1957, p 276.
(15) M. Haurie and A. Novak, *C. R. Acad. Sci. Ser. B* **264**, 694 (1967).
(16) G. Statz and E. Lippert, *Ber. Bunsenges. Phys. Chem.*, **71**, 673 (1967).
(17) P. Waldstein and L. A. Blatz, *J. Phys. Chem.*, **71**, 2271 (1967).
(18) N. I. Gulivets, A. E. Lutskii, and I. V. Radchenko, *Zh. Strukt. Khim.*, **6**, 27 (1965).
(19) Electronic computer NEAC 2200 Model 500, Computer Center, Tohoku University, was used to solve the biquadratic eq 3 and to obtain δ_{cald}. Equation 3 was solved using modified Newton Raphson method programmed by Y. Abe.
(20) T. Ikenoue, H. Fujiwara, K. Kondo, and N. Yoshida, to be submitted for publication.
(21) U. Jentschura and E. Lippert, *Ber. Bunsenges. Phys. Chem.*, **75**, 782 (1971).
(22) J. C. Davis, Jr., and K. S. Pitzer, *J. Phys. Chem.*, **64**, 886 (1960).
(23) In the acetic acid–carbon tetrachloride system the shift data in ref 12 fairly deviate toward higher field than those in ref 11, as is easily seen by comparing the shift value at 0.2 mole fraction of the acid. Although the dilution shift curve for the acetic acid–cyclohexane system is linear over the wide concentration range in the present work, the dilution shift curve in ref 9a deviates toward the higher field side from the linear line as the concentration of the acid decreases.
(24) C. F. Nawrot and A. Veis, *J. Amer. Chem. Soc.*, **92**, 3903 (1970).
(25) T. S. S. R. Murty and K. S. Pitzer, *J. Phys. Chem.*, **73**, 1426 (1969).
(26) D. Ziessow, U. Jentschura, and E. Lippert, *Ber. Bunsenges. Phys. Chem.*, **75**, 901 (1971).
(27) A. L. McClellan, S. W. Nicksic, and J. C. Guffy, *J. Mol. Spectrosc.*, **11**, 340 (1963).
(28) Reference 1, pp 212 and 221.

Electrolyte Diffusion in Acetonitrile. Harned Conductometric Technique

Terrence A. Renner[1] and Philip A. Lyons*

Yale University, New Haven, Connecticut 06520 (*Received July 13, 1973; Revised Manuscript Received April 16, 1974*)

Diffusion coefficients for solutions of sodium tetraphenylboride in acetonitrile and n-tetrabutylammonium tetraphenylboride in acetonitrile have been determined at 25° using the Harned conductometric technique. In the concentration range below 0.01 M, the data are compared with values predicted by the Debye–Hückel–Onsager–Fuoss theory as well as by the extended theory of Gronwall, La Mer, and Sandved. The electrophoretic effect in acetonitrile is much larger than in aqueous solutions. As a result, the new data provide the most reliable test of the Onsager–Fuoss theory yet possible. Each term in the theory has been separately validated. Precise, internally self-consistent activity coefficients were computed from the diffusion data.

Introduction

Harned's conductometric method has been used successfully to determine diffusion coefficients in many aqueous electrolyte solutions.[2] We propose in this work to extend this study to nonaqueous solutions. The systems NaBPh$_4$–acetonitrile and $(n$-C$_4$H$_9)_4$NBPh$_4$–acetonitrile were used since mobility data are available for these systems[3-6] and also since, below 0.01 M, the electrolytes above display no measurable association to neutral pairs.

The purposes of the work were several. First, it was necessary to discover whether or not precise measurements could be made in the very dilute solutions of theoretical interest. Secondly, it was important to determine whether or not a self-consistent set of activity coefficients could be evaluated from the diffusion data since, if this were possible, such a procedure would often be the method of choice for experimental convenience. Finally, the study should provide a decisive test for the Onsager–Fuoss theory of the electrophoretic effect,[7,8] since the magnitude of the electrophoretic contribution is very large for acetonitrile solutions.

Experimental Section

The Harned method for the determination of electrolyte diffusion coefficients is based on an estimate of the flow of electrolyte in a rectangular parallelepiped by measurements of the electrical resistance of the solution at different levels in the cell. Except for the use of all-glass cells, the procedure followed was substantially that which has already been well described.[2a,9-11]

Fisher ACS Certified acetonitrile was refluxed over calcium hydride in a dry nitrogen atmosphere for 1 day and then distilled. In the middle fraction of the distillate which was retained, there was no chromatographic evidence of any water. Fisher ACS Certified sodium tetraphenylboride was recrystallized once from a mixture of acetone and toluene.[12] The product needles decomposed at 280°. Tetrabutylammonium tetraphenylboride (hereafter, TBA-TPB) was prepared metathetically from reagent grade tetrabutylammonium bromide and sodium tetraphenylboride. This product was twice recrystallized from a 2:1 acetone–water mixture.[6] The purified crystals melted at 232.5° and began to decompose at about 236°.

All of the sliding surfaces of the diffusion cells were lubricated with Apiezon M grease which had been subjected to acetonitrile extraction for 1 week to remove soluble

components. At no time during or after the diffusion experiments was there any evidence of solution contamination by Apiezon M residue.

In the process of restricted diffusion, the solution of Fick's second law

$$\partial c / \partial t = D(\partial^2 c / \partial x^2) \qquad (1)$$

leads, for times ≥ 48 hr, to the expression

$$\ln (K_b{}^* - kK_t{}^*) = -\pi^2 Dt / A^2 + \text{constant} \qquad (2)$$

In (2), A is the cell height, $K_b{}^*$ and $K_t{}^*$ are the reciprocals of the resistances measured at the bottom and top electrode pairs (at $A/6$ and $5A/6$, respectively), and k is the ratio, k_t/k_b, of the cell constants of the electrode pairs. Measurement of the conductance difference between the electrode pairs as a function of time permits a determination of the diffusion coefficient, D, from a plot of $\ln (K_b{}^* - kK_t{}^*)$ against time.

Results and Discussion

Experimental data were fit to eq 2 by least squares to give the slope $(-\pi^2 D/A^2)$ and hence D. Typical plots for each system are shown in Figure 1.

Measured diffusion coefficients are summarized in Table I. They may be compared with values calculated from the Onsager–Fuoss expression

$$D = (D^0 + \Delta_1 + \Delta_2)(1 + \text{d} \ln y_\pm/\text{d} \ln c) \qquad (3)$$

D^0 is the Nernst limiting value for the diffusion coefficient as c approaches zero, c is the molar concentration, $y_\pm$ is the mean ionic activity coefficient on the molar scale, and Δ_1 and Δ_2 are the Onsager–Fuoss electrophoretic terms for symmetrical electrolytes[8]

$$\Delta_1 = -(kT/6\pi\eta)(l_2{}^0 - l_1{}^0)^2(\kappa/(1 + \kappa a)) \qquad (4)$$

$$\Delta_2 = (e^2/12\pi\eta\epsilon a^2)\phi_2(\kappa a) \qquad (5)$$

where

$$\phi_2(\kappa a) = (\kappa a)^2 [\exp(\kappa a)/(1 + \kappa a)^2] Ei(2\kappa a) \qquad (6)$$

and

$$Ei(2\kappa a) = Ei(x) = \int_x^\infty \exp(-t) \, \text{d}t/t = -0.5772 -$$
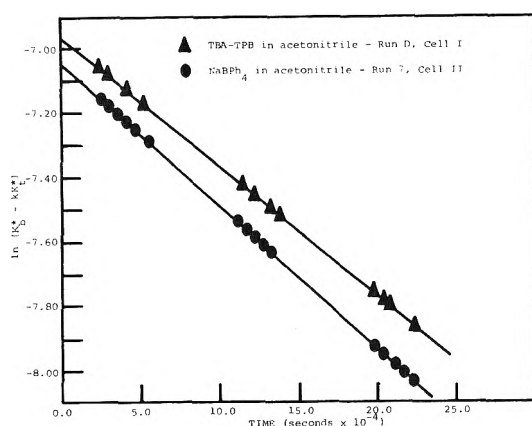
$$\ln x + x - \frac{x^2}{2^2} + \ldots \qquad (7)$$

Figure 1. Typical plots of ln $(K_b{}^* - kK_t{}^*)$ vs. time for Harned diffusion runs.

Figure 2. Diffusion coefficients for NaBPh$_4$ in acetonitrile at 25°.

TABLE I: Determination of the Experimental Diffusion Coefficients by the Conductometric Method[a]

NaBPh$_4$			TBA-TPB		
10^3c, M	10^5D_{expt}, cm²/sec	$y_\pm$ (eq 11)	10^3c, M	10^5D_{expt}, cm²/sec	$y_\pm$ (eq 11)
1.886	1.6710	0.861	1.901	1.5037	0.860
2.281	1.6621	0.849	2.467	1.5042	0.844
2.417	1.6625	0.845	3.125	1.4844	0.828
3.667	1.6426	0.817	4.017	1.4809	0.811
4.119	1.6433	0.809	5.032	1.4800	0.794
4.354	1.6388	0.805	6.004	1.4742	0.780
4.871	1.6356	0.796	6.911	1.4710	0.768
5.377	1.6360	0.789			
5.706	1.6260	0.784			
8.534	1.6182	0.751			

[a] NaBPh$_4$ in acetonitrile at 25°; $D^0 = 1.7662 \times 10^{-5}$ cm²/sec. TBA-TPB in acetonitrile at 25°; $D^0 = 1.5894 \times 10^{-5}$ cm²/sec.

TABLE II: Auxiliary Constants and Parameters for Theoretical Computation of Diffusion and Activity Coefficients

	Description of constant or parameter	NaBPh$_4$	TBA-TPB
ϵ	dielectric constant of acetonitrile	36.0	36.0
η	viscosity of acetonitrile, P	0.003412	0.003412
$\lambda_1{}^0$	limiting conductance of cation, ohm^{-1} cm² equiv^{-1}	77.3	61.75
$\lambda_2{}^0$	limiting conductance of anion, ohm^{-1} cm² equiv^{-1}	58.1	58.1
S_f	DH theoretical limiting slope for activity coefficient	1.6409	1.6409
B	activity B coefficient, M^{-1}	-0.1095	-0.3130
$D'/c^{1/2}$	limiting value as c goes to zero	-1.8892	-1.8892
a	DH ion-size parameter 10^8, cm	5.15	5.18
a'	GLS ion-size parameter sum of individual ionic radii 10^8, cm	5.15	8.94

$$\kappa^2 = \{(4\pi Ne^2)/(1000\epsilon kT)\} \sum_i c_i z_i{}^2 \quad (8)$$

Other terms are defined and listed in Table II.

The thermodynamic correction, $(1 + d \ln y_\pm/d \ln c)$, was computed from an extended form of the Debye-

Figure 3. Diffusion coefficients for TBA-TPB in acetonitrile at 25°.

Hückel theory[13].

$$\log y_\pm = -S_f c^{1/2}/(1 + \kappa a) +$$

$$Bc - \log \frac{d + 0.001c(\nu M_1 - M_2)}{d_0} \quad (9)$$

where M_1 and M_2 are the molecular weights of solvent and solute, respectively. The same thermodynamic term was also calculated from a different extended form due to Gronwall, La Mer, and Sandved.[14] Diffusion coefficients computed using the different thermodynamic corrections are included in Figures 2 and 3 as are values obtained by omitting the electrophoretic terms from eq 3.

The (extended) Debye-Hückel theory incorporates an empirical correction for short-range ion-solvent interaction in the form of the Bc term of (9). The ion-size parameter, a, used in computing activity coefficients from the DH expression is derived from the conductance data of Kay, Hales, and Cunningham[3] for NaBPh$_4$; for TBA-TPB, the value of "a" is taken from the conductance data of Fuoss and Brown.[6] In the GLS theory, no provision is made for interactions other than coulombic attraction and repulsion. The only adjustable parameter is the ion size, a'. They recommended using the sum of the ionic radii in the activity coefficient expression which they derived.[14] For the sodium ion,[15] $r^+ = 0.95$ Å. For the tetraphenylboride ion, the ionic radius, r^-, was determined from a molecular model according to the method suggested by Grunwald;[16] thus, $r^- = 4.20$ Å. There seems to be some disagreement in the literature in assigning ionic radii to tetraalkylam-
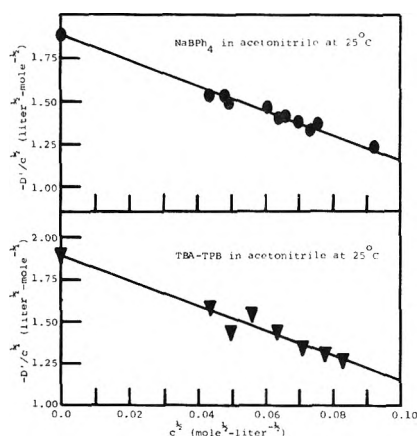
Figure 4. $D'/c^{1/2}$ vs. $c^{1/2}$ for evaluation of activity coefficients from Harned diffusion data.

monium ions, which may coil when the hydrocarbon chains become long. We have selected a value of $r^+ = 4.74$ Å for the tetrabutylammonium ion, which is taken from data of Fuoss and Tuan.[5] Hence, for all GLS theory calculations, the thermodynamic correction terms were evaluated with $a'(\text{NaBPh}_4) = 5.15$ Å and $a'(\text{TBA–TPB}) = 8.94$ Å. Regardless of the exact choice of a' for either salt in the GLS development, the importance of including the electrophoretic effect in computations of the diffusion coefficient is still evident from Figures 2 and 3.

The empirical constant, B, in eq 9 was determined from the diffusion data using a method proposed by Harned.[2b] Rearranging eq 3 to the form

$$D' = (D/(D^0 + \Delta_1 + \Delta_2) - 1.0) = c(\text{d} \ln y_\pm/\text{d}c) \quad (10)$$

and integrating after a change of variable gives the expression

$$\ln y_\pm = \int_0^c (2D'/c^{1/2}) \, \text{d}c^{1/2} \quad (11)$$

Plots of $D'/c^{1/2}$ against $c^{1/2}$ are given in Figure 4. Linear least-squares analyses of these plots, subject to the constraint

$$\lim_{c \to 0} D'/c^{1/2} = 02.303S_f/2 \quad (12)$$

yield analytical expressions for $D'/c^{1/2}$, which can be numerically integrated to determine $\ln y_\pm$ from eq 11. See Table I.

To obtain a value of the empirical constant, B, an averaging procedure was employed. Equations 9 and 10 were combined to give

$$D' + 1.1514S_f c^{1/2}/(1 + \kappa a)^2 + c\Psi(d) = 2.303Bc \quad (13)$$

$\Psi(d)$ is the derivative with respect to concentration of the final density term in eq 9. Individual values of B were calculated from eq 13 for pairs of experimental points (D',c). The average of these values was used in eq 9 to yield a working expression for $\ln y_\pm$.

It is evident from Table II that the value of B in each system studied was quite small and negative. Averaged B values resulted in a fit of activity coefficients to about $\pm 0.15\%$. At the lowest concentrations, the Bc term in eq 9 is obviously negligible; but, even at 0.01 M, Bc contributes only -0.001 to log $y_\pm$ for NaBPh$_4$ and -0.003 for TBA–TPB.

While the work of Harned and coworkers had established without reasonable doubt that the electrophoretic

TABLE III: Electrophoretic Terms for Diffusion Equation

$c \times 10^3$, M	$10^7 \Delta_1$	$10^6 \Delta_2$
NaBPh$_4$ in Acetonitrile at 25°		
1.886	−0.2448	0.2588
2.281	−0.2665	0.2931
2.417	−0.2735	0.3042
3.667	−0.3286	0.3951
4.119	−0.3455	0.4238
4.354	−0.3538	0.4380
4.871	−0.3712	0.4679
5.377	−0.3871	0.4955
5.706	−0.3969	0.5125
8.534	−0.4688	0.6388
9.999	−0.4998	0.6933

$c \times 10^3$, M	$10^8 \Delta_1$	$10^6 \Delta_2$
TBA–TPB in Acetonitrile at 25°		
1.901	−0.0920	0.2591
2.467	−0.1034	0.3070
3.125	−0.1147	0.3564
4.017	−0.1280	0.4155
5.032	−0.1409	0.4745
6.004	−0.1518	0.5248
6.911	−0.1610	0.5674
9.999	−0.1871	0.6894

theory of Onsager and Fuoss was correct both in sign and in order of magnitude, it must be conceded that the intrinsic error in the experiments (about $\pm 0.2\%$) was sizable compared with the electrophoretic contribution. As an example, one finds a variation of only 0.8% in the quantity $D/(1 + \text{d} \ln y_\pm/\text{d} \ln c)$ over the concentration range 0–0.01 M for aqueous KCl, the result quoted most often.[8] Guggenheim[17] had also commented on the fact that the variation in the same quantity for NaCl solutions is of the same magnitude as the scatter in the data,[18] implying that the experimental data did not constitute compelling evidence for the validity of the theory.

Happily, the electrophoretic contributions are much larger for acetonitrile solutions than for aqueous systems. Thus the residual variation in $D/(1 + \text{d} \ln y_\pm/\text{d} \ln c)$ from 0–0.01 M was 3.6% for NaBPh$_4$ and 4.2% for TBA–TPB. The striking deviations from experiments which are observed from omission of the electrophoretic terms in theoretical computations of diffusion coefficients are displayed in Figures 2 and 3. These figures include some additional diffusion coefficients measured by the Gouy optical method. All results lie on the same curve for a given salt. The internal consistency lends some confidence to the procedure employed for the calculation of the values of B in each system.

For the case of TBA–TPB, the first term, Δ_1, in the Onsager–Fuoss theory is negligible compared with Δ_2. This is due to the fact that the tetrabutylammonium ion and the tetraphenylboride ion have nearly the same limiting ionic mobilities, λ_i^0, in acetonitrile; and, since Δ_1 is proportional to $(t_2^0 - t_1^0)^2$ where $t_i^0 = \lambda_i^0/\Lambda^0$, this first electrophoretic term is a very small fraction of Δ_2. For TBA–TPB the electrophoretic effect is due then essentially to the Δ_2 term.

For solutions of NaBPh$_4$ in acetonitrile, Δ_1 makes a larger relative contribution. Table III lists Δ_1 and Δ_2 for both systems. In the range of expected theoretical applicability, i.e., less than 0.01 M, the Bc term, although included for completeness, could well be eliminated from (9) without significant effect on diffusion coefficients calculated using the Debye–Hückel activity coefficient ex-

pression. It should be pointed out that the activity coefficients evaluated from diffusion data were only used to obtain the empirical parameter, B. One would furthermore expect that the simple DH activity coefficient treatment, with the effect of ion size included, would adequately describe the thermodynamic behavior of these systems in the dilute solution region which is of interest here; and indeed, in the absence of any activity data for the systems studied, such as assumption must be made.

The agreement of theory with experiment is excellent, ±0.1% for NaBPh4 and ±0.2% for TBA–TPB; at the same time, the estimated error in our experimental data is ±0.15%. It would appear that the validity of the Onsager–Fuoss electrophoretic theory has been established term by term, and only in the very unlikely event that the Debye–Hückel theory for activity coefficients of dilute electrolyte solutions is invalid would such a conclusion be unduly optimistic.

References and Notes

(1) Ph.D. Thesis, Yale University, 1973.
(2) (a) H. S. Harned and D. M. French *Ann. N. Y. Acad. Sci.*, **46**, 267 (1945); (b) H. S. Harned, *Discuss. Faraday Soc.*, **24**, 7 (1957).
(3) R. L. Kay, B. J. Hales, and G. P. Cunningham, *J. Phys. Chem.*, **71**, 3925 (1967).
(4) R. L. Kay and D. F. Evans, *J. Phys. Chem.*, **70**, 2325 (1966).
(5) R. M. Fuoss and D. F. Tuan, *J. Phys. Chem.*, **67**, 1343 (1963).
(6) R. M. Fuoss and A. M. Brown, *J. Phys. Chem.*, **64**, 1341 (1960).
(7) L. Onsager and R. M. Fuoss, *J. Phys. Chem.*, **26**, 2689 (1932).
(8) R. A. Robinson and R. H. Stokes "Electrolyte Solutions," 2nd ed, Butterworths, London, 1959, Chapter 11.
(9) M. Blander, Dissertation, Yale University, 1953.
(10) R. M. Hudson, Dissertation, Yale University, 1950.
(11) C. A. Blake, Dissertation, Yale University, 1950.
(12) J. F. Skinner and R. M. Fuoss, *J. Phys. Chem.*, **68**, 1882 (1964).
(13) P. Debye and E. Hückel, *Phys. Z.*, **24**, 185 (1923).
(14) T. H. Gronwall, V. K. La Mer, and K. Sandved, *Phys. Z.*, **29**, 358 (1928).
(15) L. Pauling, "The Nature of the Chemical Bond," Cornell University Press, Ithaca, N. Y., 1940, Chapter X.
(16) E. Grunwald, "Electrolytes," B. Pesce, Ed., Pergamon Press, New York, N. Y., 1962, p 74.
(17) E. A. Guggenheim, *Trans. Faraday Soc.*, **50**, 1048 (1954).
(18) H. S. Harned and C. L. Hildreth, *J. Amer. Chem. Soc.*, **73**, 650 (1951).

Dielectric Properties of Liquid Sulfur in the Ring–Chain Transition Region[1a]

M. E. Baur* and D. A. Horsma

Department of Chemistry, University of California, Los Angeles, California 90024[1b] (*Received September 20, 1973; Revised Manuscript Received March 1, 1974*)

The dielectric constant of liquid sulfur has been determined to within a precision of ±0.0001 over the temperature range 134–206° at frequencies up to 10 kHz. The data reveal some interesting new features not noted in previous less precise investigations. The liquid below the ring–chain transition at 159°, assumed to consist entirely of S_8 rings, exhibits a temperature-dependent molar polarization [P]. This behavior is explained by postulating the existence of both crown and chair conformers of the S_8 ring, with the latter having either a dipole moment or enhanced polarizability relative to the crown. The parameters which must be associated with the chair conformer appear reasonable. Above the transition, [P] increases proportionally to W, the total concentration of S_8 units incorporated in chains. This is taken to imply a similarity in conformational flexibility and symmetry between the high-temperature S_8 rings and S_8 units in the (infinite) chain. The increase of [P] with W is interpreted in terms of an increment in the isotropic temperature-independent polarizability of S_8 units when converted from ring to chain. This increment is attributed to a slight increase in π-electron bonding in the chain. Extrapolation of [P] to the transition temperature indicates a finite discontinuity at that point. This anomaly is accounted for qualitatively by treating the ring–chain transition from the standpoint of fluctuation theory. No significant dependence of dielectric constant on frequency was found.

I. Introduction

The liquid sulfur system possesses the unusual feature of a thermodynamic transition between two distinct fluid modifications; below $T_c = 159°$, a liquid of relatively low viscosity consisting in the main of S_8 rings, and above this temperature a highly viscous material in which conversion of a significant fraction of the material to polymeric chains $(S_8)_x$ has occurred.[2a] The onset of the transition is marked by sharp changes in both equilibrium and nonequilibrium properties.[2b,3] Analysis of the transition in terms of a simple chemical equilibrium model[4,5] leads to excellent agreement of predicted degree of polymerization with experiment, leaving no doubt as to the central role of the ring–chain conversion in producing the transition.

Although this equilibrium polymerization theory is undoubtedly correct and self-consistent as far as it goes, it represents an analysis at a thermodynamic level and

would not be expected to account in depth for phenomena connected, e.g., with fluctuations near the transition. The sulfur transition has some tantalizing similarities to λ-type transitions in other systems; the constant pressure heat capacity has a λ form near T_c[2] and the density of liquid sulfur is reported to have an apparently logarithmic singularity at the transition.[6] Such anomalies are difficult of precise characterization because of the considerable experimental problems and of assuring that equilibrium has been reached when significant amounts of polymer are present. In addition, much of the available experimental data on liquid sulfur are old and of restricted precision. The analysis of the dielectric behavior of liquid sulfur, for example, rests almost exclusively on the work of Curtis[7] of some 40 years ago. However, dielectric properties would be expected to be quite sensitive to gross changes in internal molecular structure such as those believed to be present in sulfur and it is therefore important to have as precise information on such properties as possible. Accordingly it seemed to us worthwhile to examine and reassess the dielectric behavior of sulfur as a function of temperature through the transition region, using a wider frequency range than did Curtis and making use of the more powerful instrumentation now available.

This report summarizes the results of this investigation. We have determined the static dielectric constant of liquid sulfur in the temperature range from 134 to 206°, at frequencies up to 10 kHz, with a precision of one part in 10^5. The main aspect of Curtis' results is confirmed, but a number of interesting new features appear. In particular, the low-temperature ring form of liquid sulfur is found to have a definite temperature dependence, which we believe is attributable to the presence of a small concentration of the weakly polar chair form of S_8 ring; moreover there is clear evidence for a dielectric anomaly at the ring–chain transition, with both a discontinuity in slope of the curve of molar polarization [P] vs. T and a small but definite jump in [P] at T_c.

After summarizing the experimental procedure in section 2 below, we present our data in section 3 and an interpretation and analysis in light of present understanding of the sulfur system in section 4.

2. Experimental Procedure

Material. J. T. Baker sublimed sulfur powder was used without further purification.

Measurements. A dielectric cell was constructed for use with high-temperature sulfur using anodized aluminum with boron nitride as insulating material. Examination of the cell after use indicated no attack by sulfur. The cell incorporated the usual design features of a three terminal measuring device.[8] Boron nitride spacers were used to insulate the inner and outer measuring electrodes from the central guard electrode in such a way as to minimize the lead capacitances. The volume of the cell was approximately 20 cm^3.

The capacitance of the cell was measured with a General Radio Type 1615A capacitance bridge. A General Radio Type 1311A audio oscillator supplied the input signal to the bridge and a General Radio Type 1232A tuned amplifier and null detector was used to null the output signal from the bridge. The capacitance of the empty cell was found to be $C_0(t) = [12.032 + 1.20 \times 10^{-3}(t - 120)]$ pF over the temperature range 120–280°. The overall sensitivity of the capacitance measuring assembly at the temperatures employed was 0.001 pF and measurements were

typically reproducible to within this increment. Measurements were carried out over the temperature range 134–206°. Temperature was measured by a thermocouple to better than 0.1°.

Care was taken to obtain equilibrium values for the dielectric constant, especially in the high viscosity region above 159°, by repeating measurements at a given temperature at 1-hr intervals until constancy was obtained. It was not, however, possible to obtain good quality data closer than 8° to the transition from the high-temperature side, because of electrical noise in the sample.

3. Results

The capacitance C of the loaded cell at temperature T was measured and after correcting for cell capacitance C_0 the dielectric constant ϵ was determined in the usual way.[8] Determinations were carried out at frequencies of 1, 2, 5 and 10 kHz; as variation of ϵ with frequency was negligible throughout the temperature range of interest, only 1- and 10-kHz data are reported here.

In Table I below we report the measured values of ϵ at 1 and 10 kHz as a function of temperature. The densities d listed are those given by Kellas;[9] we have averaged Kellas' determinations, series II and III. For theoretical interpretation the quantity of principal interest is the molar polarization [P] where

$$[P] = \frac{\epsilon - 1}{\epsilon + 2} \frac{M}{d} \qquad (1)$$

M is the molecular weight. In this work we have adopted a uniform normalization of all data to the S_8 ring as the standard, so $M = 256.53$ g/mol. To conform with other usage in the field,[10] we list not [P] but $[P]/M = (\epsilon - 1)/(\epsilon + 2)(1/d)$, but continue to term this the molar polarization. Values are given for [P] at both 1 and 10 kHz. The variation of [P] with T is shown in Figure 1.

The following features of these results should be noted. Curtis[7] quoted a constant value of [P] for liquid sulfur in the temperature range 118–158° of 0.2528 ± 0.0008 cm^3/g. This is in agreement within experimental error with our value of 0.25344 ± 0.00002 for the 1-kHz determination at 134°. We have, however, clear indication of an increase with temperature of [P] below T_c, not detectable by Curtis because of his lower precision. The increase of [P] with T above T_c parallels that of Curtis. The extrapolation of our high-temperature data back to T_c, however, does not join smoothly to the low-temperature branch. There appears to be a gap $\Delta = 0.00052$ cm^3/g = 0.133 cm^3/mol between the two branches at T_c. The variation in [P] with frequency, though outside experimental error, is only on the order of 0.0001 cm^3/g, indicating that no dielectric loss mechanism of importance is present over the temperature range studied.

4. Interpretation and Discussion

We base our analysis of the dielectric data for liquid sulfur on the Clausius–Mosotti equation.[10] For a mixture of species labeled with index i

$$[P] = \frac{\epsilon - 1}{\epsilon + 2} \frac{1}{d} = \frac{4\pi}{3} \frac{N_{Av}}{10^3} \sum_i M_i \left(\alpha_i + \frac{\mu_i^2}{3kT} \right) \qquad (2)$$

where M_i is the concentration of species i in moles/kg, and α_i and μ_i are the polarizability and permanent dipole moment, respectively, of species i. Below the transition point the concentration of polymer is negligibly small and can be ignored, so that only the properties of the S_8 ring
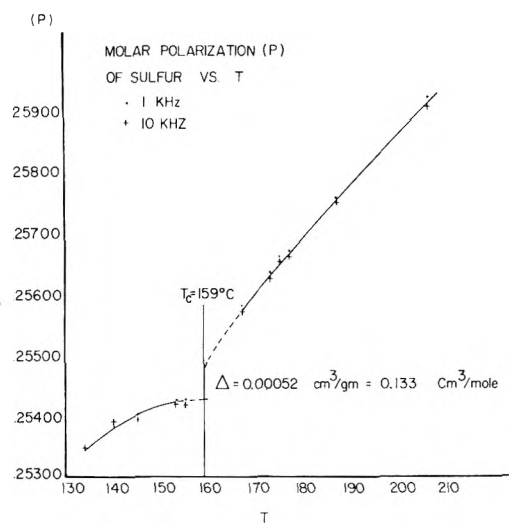
Figure 1. Molar polarization $[P] = (\epsilon - 1)/(\epsilon + 2)(1/d)$ in cm^3/g of liquid sulfur vs. T. The solid curve for temperature range 134–159° is obtained using eq 9. The extrapolation to 159° from the high-temperature side is obtained from Figure 2.
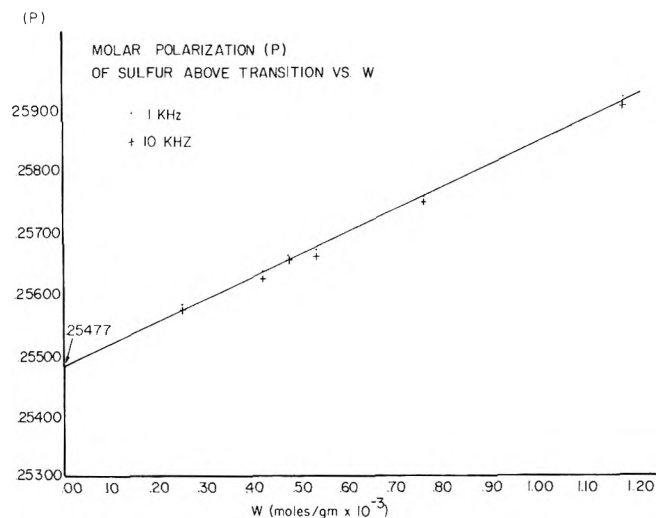

Figure 2. Molar polarization $[P]$ in cm^3/g vs. W, the total concentration of S_8 incorporated in polymer. The slope is 3.68 cm^3/mol.

need be considered. Above the transition, liquid sulfur is a mixture of S_8 rings, whose concentration (moles/kg) we denote as M, and of polymer species $(S_8)_x$, whose concentrations we denote as $M_j{}^*$. The total concentration of polymer is $N = \Sigma_{j=1} M_j{}^*$, the total concentration of S_8 units taken up in polymer is $W = \Sigma_{j=1} jM_j{}^*$, and the number-average degree of polymerization is $P = W/N$. M_0 = total concentration of S_8 units = 3.8982 mol/kg. According to the equilibrium polymerization theory,[5] N is less than 10^{-9} mol/kg below the transition, and ranges from 10^{-6} mol/kg just above to about 10^{-5} mol/kg at 206°. However, average molecular weight is large and in the temperature region studied in the present work, a significant fraction of S_8 units are taken up in polymer. No effects of finite polymer size are to be anticipated; in particular, no effects due to radical chain ends will be observed even though they presumably manifest an enhanced polarizability and a permanent dipole moment. Thus we represent the polymer chain $(S_8)_j$ in relation 2 by an effective polarizability α_j where

$$\alpha_j = j\alpha_1 \tag{3}$$

i.e., the polarizabilities of the chains are proportional to numbers of S_8 residues with a scale factor α_1. Note that α_1 is not taken as the polarizability of the $(S_8)_1$ species, i.e., the open diradical $S_8{}^*$ chain. The letter is surely different from α_1, but this is unimportant since the concentration $M_1{}^*$ of this species is less than 3×10^{-10} mol/kg. Inserting (3) in (2) yields

$$\frac{\epsilon - 1}{\epsilon + 2} \frac{1}{d} = \frac{4\pi}{3} \frac{N_{Av}}{10^3} \left[M\left(\alpha_r + \frac{\mu^2}{3kT}\right) + \sum_{j=1} M_j{}^*(j\alpha_1) \right] =$$

$$\frac{4\pi}{3} \frac{N_{Av}}{10^3} \left[M\left(\alpha_r + \frac{\mu^2}{3kT}\right) + W\alpha_1 \right] =$$

$$\frac{4\pi}{3} \frac{N_{Av}}{10^3} \left[(M_0 - W)\left(\alpha_r + \frac{\mu^2}{3kT}\right) + W\alpha_1 \right] =$$

$$\frac{4\pi}{3} \frac{N_{Av}}{10^3} \left[M_0\left(\alpha_r + \frac{\mu^2}{3kT}\right) + \right.$$

$$\left. W\left(\alpha_1 - \left[\alpha_r + \frac{\mu^2}{3kT}\right]\right)\right] \tag{4}$$

where the term $M[\alpha_r + (\mu^2/3kT)]$ refers to the ring. If α_r and α_1 are temperature independent and μ, the dipole associated with the ring, is small, relation 4 predicts a simple proportionality of the molar polarization $[P] = (\epsilon - 1)/(\epsilon + 2)(1/d)$ to W, with slope $(4\pi/3)(N_{Av}/10^3)(\alpha_1 - \alpha_r)$. The plot of $[P]$ vs. W for the high-temperature phase in Figure 2 gives a curve linear to within experimental error, with slope 3.68 cm^3/mol. The extrapolation to $W = 0$ in Figure 2 is represented by the dashed portion of the curve of $[P]$ vs. T for the high-temperature phase in Figure 1.

The assumption that the rings have only a temperature-independent polarizability α_r is, however, in conflict with the observation that $[P]$ below the transition depends on temperature. Since this dependence is not of $1/T$ form, it cannot be attributed to a simple permanent dipole moment in the ground state of the ring. Moreover, the geometry of the ring in the ground state is that of a crown, with D_{4d} symmetry,[11] for which no permanent dipole moment is possible.

According to X-ray data,[12] the crown form of S_8 ring has S–S bond length 2.05 Å and an S–S–S bond angle of 108°. Inspection of molecular models shows that there is one other possible geometry of the ring preserving these distances and angles; this might be termed the chair form, in which one S atom is rotated through an angle of 72° relative to the S atoms to which it is joined. The chair form has a mirror plane as only element of symmetry and hence will exhibit a permanent dipole moment. The analysis of ring and chain conformer states of sulfur by Semlyen[13] indicates that the chair form would not be prohibitively strained. Although its energy is certainly greater than that of the crown, this effect would be partially compensated by entropic effects. Accordingly it is reasonable to postulate the presence in liquid sulfur below the transition of an appreciable concentration of rings in the chair conformation. To be sure, infrared data[14] for the liquid at 120° are consistent with the presence of only the crown form. However, a Raman investigation at 190°[15] showed deviations from prediction based upon the latter, detailed interpretation being rendered difficult due to the presence of polymer.

Consider the effect on dielectric properties below 159° of

TABLE I: Dielectric Constant, Density, and Molar Polarization of Sulfur

T, °K	T, °C	ϵ(1 kHz)	ϵ(10 kHz)	d,[a] g/cm³	$[P]$(1 kHz), cm³/g	$[P]$(10 kHz), cm³/g
407	134	3.4991	3.4996	1.7931	0.25344	0.25346
413	140	3.4934	3.4946	1.7882	0.25383	0.25390
418	145	3.4870	3.4851	1.7843	0.25402	0.25391
426	153	3.4743	3.4730	1.7778	0.25424	0.25417
428	155	3.4702	3.4688	1.7761	0.25424	0.25416
440	167	3.4866	3.4849	1.7719	0.25578	0.25569
446	173	3.4912	3.4893	1.7700	0.25631	0.25620
448	175	3.4942	3.4924	1.7693	0.25658	0.25648
450	177	3.4933	3.4915	1.7685	0.25666	0.25655
460	187	3.4953	3.4939	1.7633	0.25752	0.25744
479	206	3.4976	3.4952	1.7533	0.25911	0.25898

[a] Reference 9.

the presence of an equilibrium

$$(S_8)_r \;\rightleftharpoons\; (S_8)_h \tag{5}$$

where r denotes crown, and h chair, conformers. Let μ_h be the dipole moment of the chair. In general we should allow for a difference in scalar electric polarizability α between crown and chair, but as this difference will be very small we neglect it. We expect then that the contribution of the S_8 rings to the electric properties of the liquid will take the form of a temperature-dependent effective polarizability

$$\alpha(S_8)_{eff} \;=\; \alpha_r \;+\; \frac{\mu_h^2}{3kT}\,\frac{g\,\exp(-\Delta/kT)}{1 + g\,\exp(-\Delta/kT)} \tag{6}$$

where g is a symmetry factor for the chair conformer and Δ is the energy of the chair relative to the crown. The effective polarizability in eq 6 has a maximum at a temperature T_m given by

$$\Delta/kT_m \;=\; 1 \;+\; g\,\exp(-\Delta/kT_m) \tag{7}$$

From Figure 1, the effective polarizability of the S_8 rings below the transition approaches a maximum at about 160°. With $g = 4$, eq 7 is satisfied by $\Delta/kT_m = 1.72$, or $\Delta \approx 1.5$ kcal/mol if $T_m = 433$°K. We then find μ_h from

$$[P](160°) - [P](134°) \;=\; \frac{4\pi}{3}\,\frac{N_{Av}}{M}\,\frac{\mu_h^2}{3k}\{[4\,\exp(-\Delta/kT)/$$

$$(1 + 4\,\exp(-\Delta/kT))](160°) -$$

$$[4\,\exp(-\Delta/kT)/(1 + 4\,\exp(-\Delta/kT))](134°)\} \tag{8}$$

This yields $\mu_h = 2.8$ D; the solid curve indicated in Figure 1 is that predicted by eq 8 with this choice of parameters. For comparison, cyclohexane has a reported dipole moment over the temperature range 35–105° of 0.6 D[16] in the gas phase; this dipole can only be due to admixture of the boat form with the nonpolar chair form. α_r for the S_8 ring is found to be 1.0×10^{-23} cm³/mol; we take this as a lower limit for α_r with 2.0×10^{-23} cm/mol as an upper limit. Other explanations for the observed temperature dependence of dielectric constant below 159°, invoking other ring species than S_8, could be devised, and we do not claim our work to be proof of the presence of the S_8 chair conformer. Nevertheless the analysis above appears the simplest possible and gives good agreement with experiment, with a reasonable choice of parameters.

The mixture of rings and chains above the transition exhibits a molar polarization depending on temperature only through its proportionality to W, the concentration of S_8 taken up in chains. The slope in the plot of $[P]$ vs. W, Figure 2, reflects the increment in the temperature-inde-

pendent part of the S_8 unit upon incorporation in the chain; there is evidently no net effect of this incorporation on configurational factors involved in any intrinsic temperature dependence of the total effective polarizability. This observation is consistent with the picture of the sulfur polymer as a rigid, tightly coiled structure[17] having local geometry closely similar to that of the rings. The slope 3.68 cm³/mol obtained from Figure 2 leads to a value 1.5×10^{-24} cm³ per S_8 unit for the polarizability increment $\alpha_1 - \alpha_r$ in eq 4, representing an increase of 5–15% in S_8 polarizability upon inclusion in the polymer. Without attempting to elaborate upon the point, we note that a slight increase in the π-bonding character in S–S bonds upon conversion to the chain form could account for this; for example, the molar bond refraction increases from 1.3 cm³ for C–C to 4.2 cm³ for C=C.[18]

A final question concerns the discontinuity in molar polarization at the transition temperature, evident in Figure 1. This anomaly is too large to be associated with the reported density discontinuity at the transition,[6] and the latter has in any case the wrong sign, the high-temperature liquid having the smaller density. Nor is it reasonable to associate the anomaly with some specific feature of the transition, having the character of a critical fluctuation, e.g., since the effect is evidently that of a change in the base line of $[P]$ as a function of T. We believe that the explanation lies in the fact that polarization fluctuations are coupled to composition fluctuations in a system containing interconvertible species of different polarizability.[19] In particular, the dielectric constant and the mean square polarization fluctuation per unit volume, $\overline{m^2}$ are related by[20]

$$\frac{(\epsilon - 1)(3\epsilon + 1)}{3\epsilon} \;=\; \frac{4\pi}{3kT}\,\overline{m^2} \tag{9}$$

To first order $\overline{m^2}$ is proportional to $\overline{\alpha^2}$, the mean square polarizability of an S_8 segment. In the high-temperature fluid, in which a segment can be either in the ring or chain state, $\overline{\alpha^2}$ differs from $\bar{\alpha}^2$ and in fact

$$\overline{\alpha^2} - \bar{\alpha}^2 \;=\; \frac{W(M_0 - W)}{M_0^2}(\alpha_1 - \alpha_r)^2 \tag{10}$$

Moreover, it can be shown that to a first approximation

$$\Delta[P] \;=\; \frac{4\pi}{3}\,M_0 N_{Av}\,\frac{(\overline{\alpha^2} - \bar{\alpha}^2)}{\bar{\alpha}} \tag{11}$$

where $\Delta[P]$ is the increment in polar polarization due to the inclusion of composition fluctuations. Combination of eq 10 and 11, taking the value for $(\alpha_1 - \alpha_r)$ found above,

the estimate 1.5×10^{-23} cm^3 for $\bar{\alpha}$, and setting $W(M_0 - W)$ equal to its average value $M_0^2/6$, then yields $\Delta[P] = 2.4 \times 10^{-4}$ cm^3/g for comparison with the experimental jump in $[P]$ at the transition of 5.2×10^{-4} cm^3/g. This order-of-magnitude agreement with the theoretical estimate lends some confidence to the explanation advanced. If it is correct, the sulfur system would appear to be the first system in which the effect of composition fluctuation on dielectric properties has been directly observed.

Summary

The careful examination of the dielectric properties of liquid sulfur reveals new phenomena calling for refinement of the interpretation of the physical properties of this system. In particular the low-temperature phase, which we have assumed to consist entirely of S_8 rings, exhibits a temperature-dependent molar polarization; the high-temperature phase, consisting of a complex mixture of rings and chains, exhibits a molar polarization increasing proportional to W; and extrapolation of the molar polarization to the transition temperature indicates a discontinuity at that point. The temperature dependence of the dielectric properties of the low-temperature phase can be interpreted in terms of a postulated polar S_8 ring conformer, whose predicted properties are reasonable. The strict proportionality of molar polarization to W in the high-temperature phase raises some interesting questions on relative symmetry and conformational flexibility of S_8 units in ring and chain. Further study of this matter is certainly desirable. Results of a simple fluctuation analysis are consistent with the magnitude of the discontinuity in molar polarization at the transition. Finally, no evidence was found for any dependence of static dielectric constant on frequency up to 10 kHz.

The interpretation of our results involves many uncertainties. We have made heavy use of the Clausius-Mosotti equation, the validity of which in assessing effects as delicate as those considered in this work may be questioned. We have not attempted to take into account species other than the S_8 ring and the $(S_8)_x$ chain, though other ring species, at least, are known to be present.[2a] It is evident that many points remain to be clarified before full understanding of the physical properties of liquid sulfur is attained.

References and Notes

(1) (a) Supported in part by the Public Health Service, National Institutes of Health under Grant No. GM 11125-03. (b) Contribution No. 3216.
(2) (a) J. A. Poulis and C. H. Massen in "Elemental Sulfur," B. Meyer, Ed., Interscience, New York, N. Y., 1965, p 109; (b) E. D. West, J. Amer. Chem. Soc., 81, 29 (1959).
(3) W. J. MacKnight and A. V. Tobolsky in ref 1, p 95.
(4) G. Gee, Trans. Faraday Soc., 48, 515 (1952).
(5) A. V. Tobolsky, J. Polym. Sci., 25, 220 (1957); A. V. Tobolsky and A. Eisenberg, J. Amer. Chem. Soc., 81, 780 (1959); 82, 289 (1960).
(6) G. E. Sauer and L. B. Borst, Science, 158, 1567 (1967).
(7) J. Curtis, J. Chem. Phys., 1, 160 (1933).
(8) C. P. Smyth, "Dielectric Behavior and Structure," McGraw-Hill, New York, N. Y., 1955, Chapter VI.
(9) A. M. Kellas, J. Chem. Soc., 113, 903 (1918).
(10) J. F. Böttcher, "Theory of Electric Polarisation," Elsevier, New York, N. Y., 1952.
(11) H. L. Strauss and J. A. Greenhouse in ref 2a, p 241.
(12) A. S. Cooper, W. L. Bond, and S. C. Abrahams, Acta. Crystallogr., 14, 1008 (1961).
(13) J. A. Semlyen, Trans. Faraday Soc., 63, 743 (1967). We are indebted to the referee for calling our attention to this paper.
(14) Reference 8, Chapter XI.
(15) H. Gerding and R. Westrik, Recl. Trav. Chim. Pays-Bas, 62, 68 (1943).
(16) M. Kubo, Sci. Papers Inst. Phys.-Chem. Res. (Tokyo), 32, 26 (1937); A. L. McClellan, "Tables of Experimental Dipole Moments," W. A. Freeman, San Francisco, Calif., 1963, p 212.
(17) M. Schmidt, Osterr. Chem. Z., 64, 236 (1963).
(18) M. Davies, "Electrical and Optical Aspects of Molecular Behavior," Pergamon, New York, N. Y., 1965, p 20.
(19) M. E. Baur, manuscript in preparation.
(20) H. Fröhlich, "Theory of Dielectrics," Oxford University Press, London, 1949, Chapter II.

Pressure Dependence of Viscosity and Nuclear Relaxation Time in Water and Deuterium Oxide[1]

D. E. O'Reilly

Argonne National Laboratory, Argonne, Illinois 60439   (Received February 7, 1974)

The pressure dependence of viscosity and nuclear relaxation times in water and deuterium oxide may be readily explained in terms of a new model for water that has been formulated recently. Effective values of the deuteron quadrupolar coupling constant in D_2O are given.

Water is unusual among liquids as evidenced by the fact that, at low temperatures and pressures, the coefficient of viscosity (η) *decreases* with increase in pressure.

Likewise, the nuclear relaxation time (T_1) of deuterium in D_2O and the proton in H_2O *increase* with increase in pressure. A quantitative explanation of these effects has been
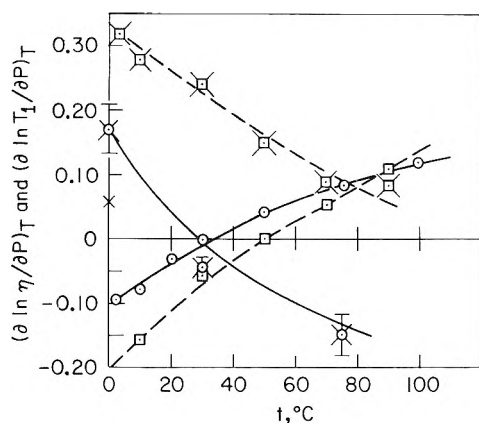
Figure 1. $(\partial \ln \eta/\partial P)_T$ for H_2O (-$\odot$-, ref 3a) and for D_2O (- - $\boxdot$- -, ref 3c); $(\partial \ln T_1/\partial P)_T$ for H_2O (-$\otimes$-, ref 3b) and for D_2O (- -$\boxtimes$- -, ref 3c).

proposed in recent communications[2] with the aid of a model which is based on the ice VII and ice Ic structures. It may easily be shown (from eq 6, ref 2a) that the pressure coefficients of T_1 and η are related as follows

$$\left(\frac{\partial \ln T_1}{\partial P}\right)_T = -\left(\frac{\partial \ln \eta}{\partial P}\right)_T +$$

$$\frac{\langle\theta^2\rangle e^{-\langle\theta^2\rangle}}{1 - e^{-\langle\theta^2\rangle}}\left(\frac{\partial \ln \langle\theta^2\rangle}{\partial P}\right)_T + \frac{1}{RT}\left(\frac{\partial w}{\partial P}\right)_T \quad (1)$$

where $\langle\theta^2\rangle$ is the mean square angle of rotation of a water molecule during a hard collision and w is the mean work required to form a vacancy in water. Equation 1 is written with the approximation that the water molecule is considered to be a spherical top molecule. In addition, it was shown[2b] that the pressure coefficient of η is given by

$$\left(\frac{\partial \ln \eta}{\partial P}\right)_T = \left(\frac{1}{RT} - \frac{1}{\Delta E}\right)\left(\frac{\partial \Delta E}{\partial P}\right)_T +$$

$$\frac{1}{RT}\left(\frac{\partial w}{\partial P}\right)_T + (\partial \ln \langle\theta^2\rangle^{1/2}/\partial P)_T \quad (2)$$

where ΔE is the mean rotational energy barrier for molecular reorientation.[2b,c] For deuterium oxide, the term $-2(\partial \ln Q/\partial P)_T$ must be added to the right-hand side of eq 1 where Q is the effective quadrupolar coupling constant of deuterium in liquid deuterium oxide.

Experimental[3] values of the pressure coefficients $(\partial \ln \eta/\partial P)_T$ and $(\partial \ln T_1/\partial P)_T$ for liquid H_2O and D_2O are shown in Figure 1 over the temperature range 0-100°. Water and deuterium oxide exhibit differences, particularly with regard to $(\partial \ln T_1/\partial P)_T$. Small differences in the energy parameters[2b,c] ϵ_0 and ϵ_1, the equilibrium constant[2b,c] K, and $(\partial w/\partial P)_T$ between H_2O and D_2O can reasonably account for the difference between $(\partial \ln \eta/\partial P)_T$ for H_2O and D_2O shown in Figure 1. However the differ-

ence between $(\partial \ln T_1/\partial P)_T$ for H_2O and D_2O (Figure 1) is considerably larger and the variation of Q with pressure and the intermolecular contribution to the proton in H_2O must be taken into account.

The variation of Q with pressure is readily estimated from the following semiempirical equation[4]

$$Q = 310 - (572/R^3) \quad (3)$$

where Q is in kHz and R is the H- - -O hydrogen bond length in Ångstrom units. From eq 3 and the compressibility[2a] of H_2O we obtain $(\partial \ln Q/\partial P)_T = -0.031$ kbar^{-1} at 0°. The fraction of intact hydrogen bonds increases slightly with increase in pressure,[5] but this is a small effect and will be neglected. Using the approximation[2b] for protons in H_2O that $(T_1)_{inter}^{-1} \simeq \frac{1}{2}(T_1)_{intra}^{-1}$, the difference between $(\partial \ln T_1/\partial P)_T$ for H_2O and D_2O is accounted for accurately by eq 1 with $(\partial \ln \langle\theta^2\rangle^{1/2}/\partial P)_T = -0.021$ kbar^{-1} (10°) where we have used the result[2b,c] that $\langle\theta^2\rangle = 1.1$ which was assumed to be the same for H_2O and D_2O. That is, the root mean square angle of rotation upon a hard collision decreases slightly with increase in pressure. The magnitude of the coefficient $(\partial \ln \langle\theta^2\rangle^{1/2}/\partial P)_T$ given above appears to be a reasonable value.

In the interpretation of the temperature and pressure dependence of the relaxation times of deuterium and oxygen-17 in water the variation of Q with the fraction of hydrogen bonds that are intact (f) as well as the change of Q with the mean hydrogen bond length must be taken into account. Denoting the quadrupolar coupling constants for the deuteron in a ruptured and intact hydrogen bond by Q_M and Q_{HB}, respectively, the effective value of Q is given by $Q = fQ_{HB} + (1 - f)Q_M$. In the present model the effective value of Q for deuterium in D_2O at 0° is 237 kHz and at 100° $Q = 245$ kHz; in the calculation we have placed $Q_M = 318$ kHz[6] and $Q_{HB} = 213$ kHz[7] and used values of f recently reported[5] (at 0° $f = 0.774$; at 100° $f = 0.694$).

The behavior of water with temperature and pressure can be explained readily with the aid of the quasilattice model with reasonable values of the parameters that occur in the model and that are consistent with molecular dynamics calculations[8] on water.

References and Notes

(1) Based on work performed under the auspices of the U. S. Atomic Energy Commission.
(2) (a) D. E. O'Reilly, Phys. Rev. A, **7**, 1659 (1973); (b) D. E. O'Reilly, E. M. Peterson, and C. E. Scheie, Chem. Phys. Lett., in press; (c) D. E. O'Reilly, J. Chem. Phys., **60**, 1607 (1974).
(3) (a) K. E. Bett and J. B. Cappi, Nature (London), **207**, 620 (1965); (b) H. G. Hertz and C. Radle, Z. Phys. Chem. (Frankfurt am Main), **68**, 324 (1969); (c) Y. Lee and J. Jonas, J. Chem. Phys., **57**, 4233 (1972).
(4) G. Soda and T. Chiba, J. Chem. Phys., **50**, 439 (1969).
(5) D. E. O'Reilly, J. Chem. Phys., in press.
(6) P. Thaddeus, L. C. Kirsher, and T. H. Loubser, J. Chem. Phys., **40**, 257 (1964).
(7) P. Waldstein, S. W. Rabideau, and J. A. Jackson, J. Chem. Phys., **41**, 3407 (1964).
(8) (a) F. H. Stillinger and A. Rahman, J. Chem. Phys., **57**, 1281 (1972); (b) A. Rahman and F. H. Stillinger, ibid., **55**, 336 (1971).

Relaxation Kinetics of Micelle Formation[1]

Alan H. Colen[2]

Department of Chemistry, Kalamazoo College, Kalamazoo, Michigan 49001 and the Molecular Biochemistry Research Laboratory, Veterans Administration Hospital, Kansas City, Missouri 64128   (Received January 9, 1974)

The relaxation time associated with a slow, rate-determining step in a general mechanism for micelle formation is expressed as a function of free surfactant concentration. The predictions of this treatment are shown to fit data in the literature on the formation of dodecylpyridinium iodide micelles over a wider concentration range than the linear concentration dependence originally proposed. In addition, when a plot of the reciprocal of the relaxation time against total surfactant concentration possesses a maximum, the slow step involves aggregates smaller than the full micelle. Finally, the model presented in this paper resolves reported discrepancies between chemical relaxation and nmr observations.

Introduction

Before the introduction of relaxation methods[3,4] for the observation of fast reactions in solution, a large body of data necessary to the study of the kinetics of micelle formation was inaccessible to experiment.[5,6] In 1966, however, Kresheck, *et al.*,[6] demonstrated that the temperature jump method could be used to obtain information about rate processes associated with dodecylpyridinium iodide (DPI) micelle dissociation.

In these experiments, two relaxation processes were noted, one too rapid to study quantitatively, interpreted as the formation of DPI molecule pairs, and a slower one attributed to dissociation of DPI molecules from micelles. The reciprocal of the slow relaxation time gave a linear plot against DPI concentration above the critical micelle concentration (cmc) with negative deviations from linearity at high concentrations (see Figure 1). Using the first two terms of a power series expansion of the rate equation, an expression was derived which gave a linear concentration dependence for the reciprocal of the relaxation time for the mechanism

$$(n - 1)A = A_{n-1} \quad \text{(rapid equilibrium)}$$

$$A + A_{n-1} \rightleftharpoons A_n \quad \text{(slow)}$$
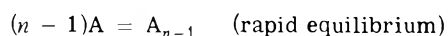
where A represents a surfactant molecule and A_n is a micelle containing n molecules. It was suggested that the deviations from linearity at high concentrations result from interactions between micelles. More recent temperature-jump and pressure-jump studies have given similar results for other micelle systems.[7-10] Employing the model described above, all investigators have computed rate constants of the order of 100 sec^{-1} or smaller for the dissociation of detergent molecules from micelles.

Nmr experiments on micelle systems[11-13] have given single bands which shift with micelle concentration above the cmc but show no exchange broadening, thus leading to the conclusion[14] that residence times in aqueous and micellar environments are too short to measure under the experimental conditions. Muller[14] shows, on the basis of these observations, that the rate constant for the dissociation of surfactant molecules from micelles must be greater than 4.5×10^5 sec^{-1}, over three orders of magnitude greater than the largest dissociation rate constant calculated from temperature-jump measurements but in agreement with the results of esr[15] and ultrasonic absorption[16] measurements. He proposes that the relaxation time observed by temperature jump is associated with many steps, not just a single one, and he presents an approximate calculation of the half-life for the dissociation of the entire micelle as might be observed in stopped-flow dilution studies, noting that in this way the nmr observations and temperature-jump results appear less divergent. He did not obtain an expression for the concentration dependence of the slow relaxation time. It should be noted that one recent stopped-flow study[17] gave a dissociation rate 7 times faster than the temperature-jump result for small micelles,[9] whereas a second, using an indicator dye, gave identical results for stopped-flow[18] and pressure-jump[10] experiments.

It is the purpose of the present paper to introduce a more general form of the mechanism for micelle formation proposed by Kresheck, *et al.*,[6] eliminating any assumption as to which step in the aggregation process possesses the observed relaxation time, to show that deviations from linearity are a general feature of all such mechanisms and do not require additional explanation, to discuss the significance of maxima which may appear in plots of the reciprocal of the relaxation time against concentration, and finally, to demonstrate that although the model presented here is still an over-simplification, it resolves the discrepancy between temperature-jump and nmr results.
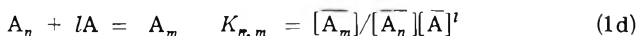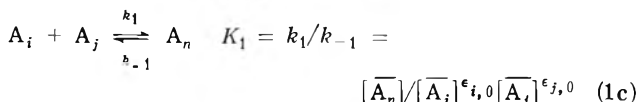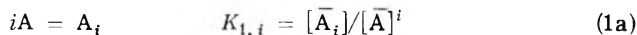
Extended Mechanism

The basic assumption which will be made in the presentation of the generalized mechanism is that there exists, in the spectrum of relaxation times observed in the study of micelle formation, one distinct relaxation time, well separated from the rest, which is the longest and which may be associated with a single bimolecular or unimolecular step in the aggregation process.

The first part of this assumption, that there is a distinct relaxation time which will be called the longest, is based on the experimental evidence presented in all chemical relaxation studies reported to date.[6-10] It is this particular relaxation time that will be treated below.

The second part arises from the fact that simultaneous termolecular and higher order collisions are relatively low probability events and should not contribute significantly to the reaction kinetics. It can be argued, of course, as has

been demonstrated in many other cases,[3,4,19-22] that the normal mode of reaction resulting in the longest relaxation time is not necessarily associated with a single reaction step, but with several. A good example of this phenomenon would be a mechanism in which a steady state is established for one or several reaction intermediates.[19,20] On the other hand, an extended sequence of steps does not in general produce a single distinct relaxation time, but a spectrum as demonstrated in experimental and theoretical studies of the helix-coil transition.[23] In that case, a single relaxation time would be observed theoretically only when there is a concerted transition with only two states possible for each molecule: helix or coil. Since we know that average micelle size grows with detergent concentration,[24-26] a two state model, involving only monomer and micelle of fixed size is highly unrealistic. The grounds, then, for association of the longest relaxation time with a single step are those of simplicity, to keep the equations manageable, and of conservatism, because no evidence to the contrary has been produced. The basic conclusions of the present treatment will still be valid should a more complex mechanism be indicated in the future.

In the general mechanism, consistent with the assumption above, all steps in the aggregation process equilibrate much more rapidly then a single slowest or rate-controlling step. These rapid steps can then be written as equilibria relating the concentrations of monomer and micelle in solution to those of reactants and products, respectively, in the slow step. The slow step is that in which an aggregate A_i containing i units of the monomer A reacts with an aggregate A_j containing j units to form the aggregate A_n where $n = i + j$.

$$iA = A_i \qquad K_{1,i} = [\overline{A_i}]/[\overline{A}]^i \qquad (1a)$$

$$jA = A_j \qquad K_{1,j} = [\overline{A_j}]/[\overline{A}]^j \qquad (1b)$$

$$A_i + A_j \underset{k_{-1}}{\overset{k_1}{\rightleftharpoons}} A_n \qquad K_1 = k_1/k_{-1} =$$
$$[\overline{A_n}]/[\overline{A_i}]^{\epsilon_{i,0}}[\overline{A_j}]^{\epsilon_{j,0}} \qquad (1c)$$

$$A_n + lA = A_m \qquad K_{n,m} = [\overline{A_m}]/[\overline{A_n}][\overline{A}]^l \qquad (1d)$$

where $[A_r]$ represents the equilibrium concentration of $r$mers, $K_{r,s}$ is the equilibrium constant for the formation of $s$mers from $r$mers, k_1, k_{-1}, and K_1 are the forward and reverse rate constants and the equilibrium constant, respectively, for the slow step, and the subscript m represents the number of monomer units in the largest aggregate. The number m is considered to be constant for simplicity in the present treatment although the size of micelles is concentration dependent.[24-26] Thus, the results obtained here represent an approximate average over the distribution of micellar species.

$\epsilon_{q,r}$ is the complement of the Kroenecker delta

$$\epsilon_{q,r} = 1 - \delta_{q,r} = \begin{cases} 0 \text{ if } q = r \\ 1 \text{ if } q \neq r \end{cases} \qquad (2)$$

The $\epsilon_{i,0}$ and $\epsilon_{j,0}$ factors render the equations valid for a unimolecular rate controlling step (either $i = 0$ or $j = 0$, with $K_{1,0} = 0$). The relaxation rate equation for the slow step is[27]

$$\frac{d(\delta[A_n] + \delta[A_m])}{dt} = k_1\{\epsilon_{j,0}[\overline{A_i}]^{\epsilon_{i,0}}\delta[A_j] +$$
$$\epsilon_{i,0}[\overline{A_j}]^{\epsilon_{j,0}}\delta[A_i]\} - k_{-1}\delta[A_n] \qquad (3)$$

where $\delta[A_r]$ represents a small deviation of $r$mer concentration from its equilibrium value $[\overline{A_r}]$

$$\delta[A_r] = [A_r] - [\overline{A_r}] \qquad (4)$$

Mass balance requires that

$$\delta[A] + \epsilon_{i,1}i\delta[A_i] + \epsilon_{j,1}j\delta[A_j] + n\delta[A_n] +$$
$$m\delta[A_m] = 0 \qquad (5)$$

where $\epsilon_{i,1}$ and $\epsilon_{j,1}$, defined in eq 2, allow for the possibility that either A_i or A_j, respectively, is really the monomer A.

Writing the expressions for the equilibrium constants (eq 1a, 1b, and 1d) in differential form (i.e., in terms of small deviations of concentrations from their equilibrium values)

$$\delta[A_i] = iK_{1,i}[\overline{A}]^{i-1}\delta[A] \qquad (6a)$$

$$\delta[A_j] = jK_{1,j}[\overline{A}]^{j-1}\delta[A] \qquad (6b)$$

$$\delta[A_m] = K_{n,m}(l[\overline{A_n}][\overline{A}]^{l-1}\delta[A] + [\overline{A}]^l\delta[A_n]) \qquad (6c)$$

and combining these with eq 5 in order to express the rate expression (eq 3) as a function of $(\delta[A_n] + \delta[A_m])$ yields a simple linear differential equation of the form

$$\frac{d(\delta[A_n] + \delta[A_m])}{dt} = -\frac{1}{\tau}(\delta[A_n] + \delta[A_m]) \qquad (7)$$

Thus, the reciprocal of the longest relaxation time τ is given by

$$\frac{1}{\tau} = k_{-1}\frac{B}{C} + k_1\frac{D[\overline{A}]^{n-1}\{n + E[\overline{A}]^l\}}{C} \qquad (8)$$

where

$$B = 1 + \epsilon_{i,1}i^2K_{1,i}[\overline{A}]^{i-1} + \epsilon_{j,1}j^2K_{1,j}[\overline{A}]^{j-1} +$$
$$lmK_{1,i}^{\epsilon_{i,0}}K_{1,j}^{\epsilon_{j,0}}K_1K_{n,m}[\overline{A}]^{m-1}$$

$$C = \{1 + \epsilon_{i,1}i^2K_{1,i}[\overline{A}]^{i-1} + \epsilon_{j,1}j^2K_{1,j}[\overline{A}]^{j-1}\}\{1 +$$
$$K_{n,m}[\overline{A}]^l\} + l^2K_{1,i}^{\epsilon_{i,0}}K_{1,j}^{\epsilon_{j,0}}K_1K_{n,m}[\overline{A}]^{m-1}$$

$$D = jK_{1,j}K_{1,i}^{\epsilon_{i,0}} + iK_{1,i}K_{1,j}^{\epsilon_{j,0}}$$

$$E = mK_{n,m}$$

For the purposes of comparison with data, it will be necessary to plot $1/\tau$ vs. $[A]_0$, where $[A]_0$ is the total (or formal) surfactant concentration, related to $[\overline{A}]$ by the equation

$$[A]_0 = [\overline{A}] + \epsilon_{i,1}iK_{1,i}[\overline{A}]^i + \epsilon_{j,1}jK_{1,j}[\overline{A}]^j +$$
$$nK_{1,i}K_{1,j}K_1[\overline{A}]^n + mK_{1,i}K_{1,j}K_1K_{n,m}[\overline{A}]^m \qquad (9)$$

In the theoretical curves to be presented later in the paper, $1/\tau$ and $[A]_0$ are computed as a function of $[\overline{A}]$ using eq 8 and 9, respectively, and then $1/\tau$ is plotted against $[A]_0$ using values computed for each value of $[\overline{A}]$.

Concentration Dependence of the Slow Relaxation Time

Since the general expression for the relaxation time (eq 8) is quite complex, it will be instructive to focus on two special cases.

Case I. $K_{n,m} = 0$. In this case, the concentration dependence of the relaxation time is given by

$$\frac{1}{\tau} = k_{-1} +$$

$$k_1 \frac{n^2 K_{1,i} K_{1,j} [\bar{A}]^{n-1}}{1 + \epsilon_{i,1} i^2 K_{1,i} [\bar{A}]^{i-1} + \epsilon_{j,1} j^2 K_{1,j} [\bar{A}]^{j-1}} \quad (10)$$

The model treated by Krescheck, *et al.*,[6] in which the rate-determining step is the reaction of *i*mer with monomer to form the micelle A_n belongs to this category, with $i > 1$ and $j = 1$, $K_{1,j} = K_{1,1} = 1$, $\epsilon_{i,1} = \epsilon_{j,0} = \epsilon_{i,0} = 1$, and $\epsilon_{j,1} = 0$. Here the reciprocal of the relaxation time becomes

$$\frac{1}{\tau} = k_{-1} + k_1 \frac{n^2 K_{1,i} [\bar{A}]^{n-1}}{1 + i^2 K_{1,i} [\bar{A}]^{i-1}} \quad (11)$$

The concentration dependent term in the denominator of the fraction in eq 11 did not appear in their work[6] because the derivation of the equivalent expression in that paper was accomplished by dropping high order terms in a power series expansion yielding a solution which is valid only when $i^2 K_{1,i} [\bar{A}]^{i-1} \ll 1$, a condition which, as Muller[14] pointed out, may cease to hold at high surfactant concentrations. The authors[6] noted that the expression they obtained in this approximation was identical in form with the one which would arise precisely from the highly unrealistic mechanism in which the observed relaxation time is associated with an n-molecular collision to form $n$mer. Their data are shown in Figure 1, plotted along with a solid line representing their fit to the data and a dashed line, plotted according to eq 11, with $n = i + 1 = 87$, $k_{-1} = 47$ sec^{-1}, $k_1 = 2.5 \times 10^6$ M^{-1} sec^{-1}, and $K_{1,i} = 10^{186}$ $M^{-85.28}$ It can be seen that the present treatment fits adequately the high concentration deviations from linearity without added assumptions about interactions between micelles. It might be added that one would expect a plot of $1/\tau$ *vs.* $[A]_0$ to level off at sufficiently high $[A]_0$ not only because, under these conditions, eq 11 becomes

$$\frac{1}{\tau} = k_{-1} + k_1 \frac{n^2}{i^2} [\bar{A}] \quad (12)$$

and $[\bar{A}]$ is virtually constant,[6] but simply because the concentrations of monomer, *i*mer, and micelle are all increasing very slowly compared to $[A]_0$. Plots of $[\bar{A}]$, $[\bar{A}_i]$, and $[\bar{A}_n]$ are given as a function of $[A]_0$ in Figure 2.

As discussed above, when $j = 1$ in this case $(K_{n,m} = 0)$, the rate-limiting step is the dissociation of monomer from the micelle. In addition, in this case, if $j = 0$, the rate-limiting step is an isomerization of the micelle, and if $i > 1$ and $j > 1$, the slow step involves the combination of sub-micellar aggregates to form the micelle. All of these models obey eq 10, which predicts that $1/\tau$ will be a monotonically increasing function of $[\bar{A}]$. (This property follows simply from the fact that $n = i + j$.) It should be noted also that the case $l = 0$, $K_{n,m} > 0$ is functionally identical with that treated above.

Case II. $j = 1$ or 0, $l > 0$, $K_{n,m} > 0$. This is the case in which the rate-determining step involves $n$mer smaller
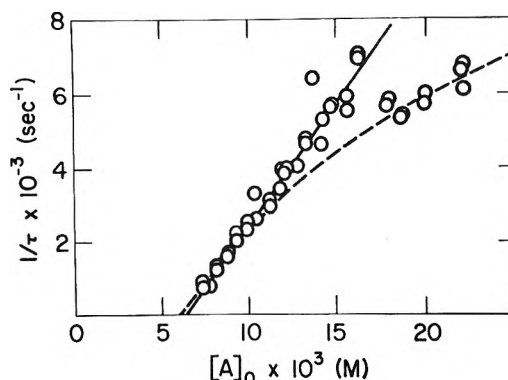
Figure 1. Plot of the reciprocal of the relaxation time observed in temperature jump studies performed on dodecylpyridinium iodide micelles against surfactant concentration. The data points and the solid line are taken from ref 6. The dashed line is a theoretical curve plotted according to eq 11.
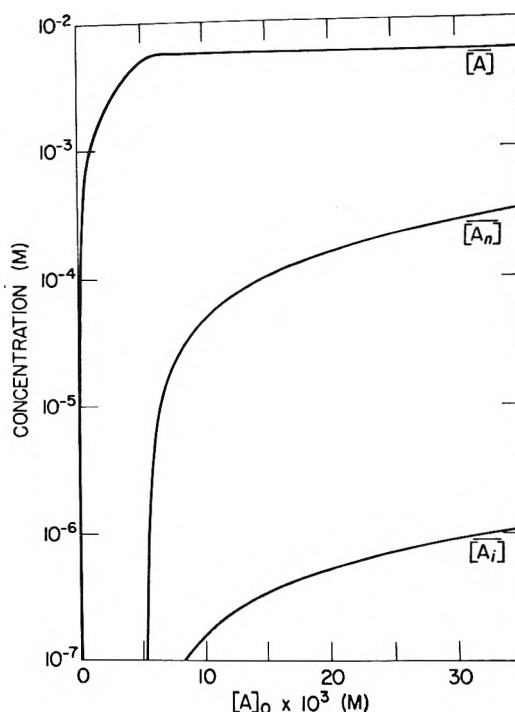
Figure 2. Semilogarithmic plots of monomer, *i*mer, and *n*mer concentrations as a function of surfactant concentration, corresponding to the theoretical curve in Figure 1.

than the micelle. In this case, eq 8 becomes

$$\frac{1}{\tau} =$$

$$k_{-1} \frac{1 + i^2 K_{1,i} [\bar{A}]^{i-1} + lm K_{1,i} K_1 K_{n,m} [\bar{A}]^{m-1}}{\{1 + i^2 K_{1,i} [\bar{A}]^{i-1}\}\{1 + K_{n,m} [\bar{A}]^l\} + l^2 K_{1,i} K_1 K_{n,m} [\bar{A}]^{m-1}} +$$

$$k_1 \frac{n K_{1,i} [\bar{A}]^{n-1} \{n + m K_{n,m} [A]^l\}}{\{1 + i^2 K_{1,i} [\bar{A}]^{i-1}\}\{1 + K_{n,m} [\bar{A}]^l\} + l^2 K_{1,i} K_1 K_{n,m} [\bar{A}]^{m-1}} \quad (13)$$

This expression will also fit the data of Kresheck, *et al.*,[6] although the number of constants in eq 13, coupled with the limitations to experimental accuracy preclude the de-
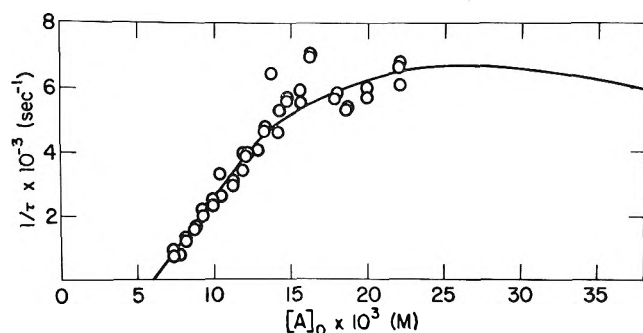
Figure 3. The reciprocal of the relaxation time *vs.* surfactant concentration plotted according to eq 13 for a case in which a maximum is observed. The constants used for the theoretical curve are $i = 43$, $n = 44$, $m = 87$, $k_{-1} = 94$ sec^{-1}, $k_1 = 2 \times 10^7$ M^{-1} sec^{-1}, $K_{1,i} = 10^{89}$ M^{-42}, and $K_{n,m} = 2.1 \times 10^{93}$ M^{-43}. The data of Kresheck, *et al.*,[6] are presented for comparison.

termination of a unique fit. Unlike the previous case, it can be shown that for many values of the constants this expression possesses a maximum. Such a case is given in Figure 3. The corresponding concentration plots resemble those of Figure 2, with no maxima or minima or other singular features and will not be shown here. When both i and j are greater than 1, the dependence, which possesses an extra term in the denominator, can also have a maximum.

On the basis of this analysis, a maximum is diagnostic when it is observed. If a system possesses a peak in the plot of $1/\tau$ against $[A]_0$, the slow, or rate-determining step must involve aggregates smaller than the micelle, both as reactants and as products. Conversely, a failure to observe such a maximum is inconclusive.

For the purposes of this paper only the data of Kresheck, *et al.*,[6] which show significant negative high concentration deviations from linearity, have been treated. Other investigators have reported either no significant deviations from linearity[7,8,10] or a low concentration foot (a positive deviation from linearity) in the vicinity of the cmc.[9] Both types of behavior may be simulated readily by the equations developed here.

This paper treats only the longest relaxation time for a mechanism for micelle formation. Development of the equations for the shorter relaxation times, which must also exist for such a mechanism, requires the inclusion of greater mechanistic detail than is appropriate at this time. Evidence for such faster relaxation processes has been reported in temperature-jump,[6] ultrasonic absorption,[16] esr,[15] and nmr[11-13] experiments.

Relation between Nmr and Chemical Relaxation Results

A final point to be discussed is the relation between the results of nmr and chemical relaxation experiments. The linear mechanism presented here for the chemical relaxation results involves rapid exchange of detergent molecules between solvent and aggregates at all states of aggregation coupled to one slow step at a particular state of aggregation. Since the slow step is not observed in nmr experiments, it must not itself produce a change in the magnetic environment of the nuclei under study. In addition, before and after the slow step the exchange rate must be high, with all detergent molecules free to dissociate from and associate with the micelle.

The mechanism of Kresheck, *et al.*,[6] and all similar

mechanisms in which the last step is rate limiting (*i.e.*, all cases mentioned under case I) are ruled out because a fraction of the detergent molecules would undergo slow exchange with solvent and this slow exchange would be detected by nmr. Muller[14] has also pointed out that for large micelles, the affinity for surfactant molecules is relatively constant at high states of aggregation and thus the initial dissociation steps for a micelle should be similar in rate, with no single one considerably slower than the rest. The rate-limiting step, therefore, occurs at an earlier stage in micelle formation than originally proposed.[6] It probably involves a minor rearrangement of micelle, counterion, and solvent structure either to facilitate further growth or to incorporate submicellar aggregates, without any major change in the net electromagnetic environment of chemical groups within each aggregate. As with macromolecules, very subtle changes in the free energy of micelles can have an appreciable effect on micelle stability. For the model presented here, then, the nmr and chemical relaxation results produce a consistent picture.

In conclusion, any mechanism which fits the data available will have to incorporate rapid exchange of detergent molecules between micelle and solvent, coupled to a slow step or concerted combination of steps which affect the stability of the micelle without rendering a substantial fraction of the detergent molecules inaccessible to rapid exchange.

References and Notes

(1) Supported in part by a grant from the Sloan Foundation at Kalamazoo College.
(2) Address correspondence to the author at Molecular Biochemistry Research Laboratory, Veterans Administration Hospital, 4801 Linwood Blvd., Kansas City, Mo. 64128.
(3) M. Eigen, *Z. Elektrochem.*, **64**, 115 (1960).
(4) M. Eigen and L. De Maeyer in "Technique of Organic Chemistry," Vol. VIII, A. Weissberger, Ed., Interscience, New York, N. Y., 1963.
(5) P. Mukerjee and K. J. Mysels, *J. Amer. Chem. Soc.*, **77**, 2937 (1955).
(6) G. C. Kresheck, E. Hamori, G. Davenport, and H. A. Scheraga, *J. Amer. Chem. Soc.*, **88**, 246 (1966).
(7) B. C. Bennion, L. K. J. Tong, L. P. Holmes, and E. M. Eyring, *J. Phys. Chem.*, **73**, 3288 (1969).
(8) B. C. Bennion and E. M. Eyring, *J. Colloid Interface Sci.*, **32**, 286 (1970).
(9) J. Lang and E. M. Eyring, *J. Polym. Sci. A-2*, **10**, 89 (1972).
(10) K. Takeda and T. Yasunaga, *J. Colloid Interface Sci.*, **40**, 127 (1972).
(11) H. Inoue and T. Nakagawa, *J. Phys. Chem.*, **70**, 1108 (1966).
(12) N. Muller and F. E. Platko, *J. Phys. Chem.*, **75**, 547 (1971).
(13) A. T. Florence and R. T. Parfitt, *J. Phys. Chem.*, **75**, 3554 (1971).
(14) N. Muller, *J. Phys. Chem.*, **76**, 3017 (1972).
(15) N. M. Atherton and S. J. Strach, *J. Chem. Soc., Faraday Trans. 2*, **68**, 374 (1972).
(16) E. Graber and R. Zana, *Kolloid-Z. Z. Polym.*, **238**, 479 (1970).
(17) J. Lang, J. J. Auborn, and E. M. Eyring, *J. Colloid Interface Sci.*, **41**, 484 (1972).
(18) T. Yasunaga, K. Takeda, and S. Harada, *J. Colloid Interface Sci.*, **42**, 457 (1973).
(19) G. G. Hammes and R. A. Alberty, *J. Colloid Interface Sci.*, **82**, 1564 (1960).
(20) R. A. Alberty, G. Yagil, W. F. Diven, and M. T. Takahashi, *Acta Chem. Scand.*, **17**, 534 (1963).
(21) G. W. Castellan, *Z. Elektrochem.*, **67**, 898 (1963).
(22) G. W. Czerlinski, "Chemical Relaxation," Marcel Dekker, New York, N. Y., 1966.
(23) G. Schwarz, *J. Theor. Biol.*, **36**, 569 (1972).
(24) C. P. J. Hoeve and C. J. Benson, *J. Phys. Chem.*, **60**, 1149 (1957).
(25) D. C. Poland and H. A. Scheraga, *J. Phys. Chem.*, **69**, 2431 (1965).
(26) P. Mukerjee, *J. Phys. Chem.*, **76**, 565 (1972).

(27) For the mechanism presented here, each aggregate A_n produced or lost through the slow step (1c) simply increases or decreases the sum $(\delta[A_n] + \delta[A_m])$ since A_n and A_m are assumed to be in rapid equilibrium. Thus the normal reaction coordinate for the slow step is $(\delta[A_n] + \delta[A_m])$. This fact may be verified by deriving the expression for $1/\tau_{slow}$ and the corresponding normal coordinate as follows: assume only steps 1a and 1b are in rapid equilibrium, write the rate expressions for $\delta[A_n]$ and $\delta[A_m]$ independently, and solve the resuling 2×2 matrix equation. When the expressions obtained are taken in the limit in which step 1d equilibrates much more rapidly than step 1c, the results are identical with those reported here.

(28) The value of n used in the present calculations was chosen arbitrarily by dividing the reported molecular weight of the micelle, 32,700 at the critical micelle concentration [H. C. Parreira, *An. Acad. Brasil. Cienc.*, **32**, 207 (1960)], by the molecular weight of monomer.

Journal of Chemical and Engineering Data

JULY 1974, Vol. 19, No. 3

TABLE OF CONTENTS

■ Supplementary material for this paper is available separately, in photocopy or microfiche form. Ordering
information is given in the paper.

Molecular Sieve Zeolites

ADVANCES IN CHEMISTRY SERIES No. 101 and 102
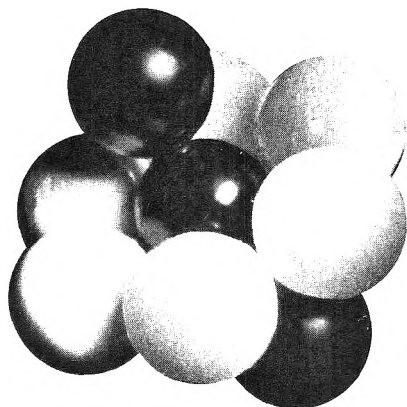
Seventy-seven papers from a symposium co-sponsored by the Divisions of Colloid and Surface Chemistry, Petroleum Chemistry, and Physical Chemistry of the American Chemical Society and Worcester Polytechnic Institute, Edith M. Flanigen and Leonard B. Sand, co-chairmen.

Do you need a group of substances that can remove radioactive isotopes from nuclear wastes, remove ammonia from secondary sewage effluents, remove sulfur dioxide from waste gases, foster formation of actinides, or disrupt bacterial cells? These and many other possibilities are available through research on molecular sieve zeolites. For example, they are used for separating hydrogen isotopes . . . solubilizing enzymes . . . carrying active catalysts in curing of plastics . . . transporting soil nutrients in fertilizers . . . filtering tars from cigarette smoke.

"Molecular Sieve Zeolites" reports recent advances in this rapidly developing field. Volume I offers 41 papers devoted to the synthesis, structure, mineralogy, and modification of sieve zeolites. These are followed in Volume II by 36 papers discussing sorption and catalysts.

Volume I: 526 pages with index   Cloth   (1971) $16.00
Volume II: 459 pages with index   Cloth   (1971) $16.00
No. 101 and 102 ordered together $30.00

Postpaid in U.S. and Canada; plus 40 cents elsewhere.
Set of L.C. cards with library orders upon request.

Other books in the ADVANCES IN CHEMISTRY series on colloid chemistry include:

No. 95 Cellulases and Their Applications
Twenty-five papers stress the practical application of cellulolytic systems in biochemistry, animal nutrition, textiles, forest product utilization. Topics include new mechanisms for cellulose degradation, the cellulase complex, structure and morphology of cellulase, a commercial enzyme process and wood-derived products as nutritional sources.
470 pages with index   Cloth   (1969) $14.50

No. 87 Interaction of Liquids at Solid Substrates
Twelve papers survey recent research on solid/liquid interaction, including work on "coupling agents," adhesion of polymers, organic/inorganic interfaces, ultrasonic impedometry. Four more papers are concerned with heparinized surfaces at the blood/material interface.
212 pages with index   Cloth   (1968) $9.50

No. 84 Molecular Association in Biological and Related Systems
Nineteen articles survey and report new work on molecular association in fat digestion, in soap systems, in membrane constituents, and in mixed monolayers. Other topics include bile salt micelles, lipid monolayers and membranes, and a definitive review of biological membrane structure.
308 pages with index   Cloth   (1968) $10.50

No. 79 Adsorption from Aqueous Solution
Fifteen papers discuss thermodynamic and kinetic aspects of adsorption phenomena and the results of studies on a variety of adsorbate-adsorbent systems.
212 pages with index   Cloth   (1968) $10.00

No. 63 Ordered Fluids and Liquid Crystals
Twenty-two studies on characterization, properties, and occurrence of these phenomena in many substances such as tristearin, *p*-azoxyanisole, mono- and di-hydric alcohols, phospholipids, and polypeptides.
332 pages with index   Cloth   (1967) $11.50

No. 43 Contact Angle, Wettability, and Adhesion
Surface chemistry studies. Relation of equilibrium contact angle to liquid and solid constitution, contact angle as a thermodynamic property, surface energy estimation from contact angle. Contact angle hysteresis, relationship between wetting and adhesion.
389 pages with index   Cloth   (1964) $10.50

No. 33 Solid Surfaces and the Gas-Solid Interface
Thirty-seven papers from the Kendall Award Symposium honoring Stephen Brunauer. Theory and techniques for studying surface phenomena.
381 pages with index   Cloth   (1961) $12.00

Order from: **Special Issues Sales**
       American Chemical Society, 1155 16th Street, N.W., Washington, D.C. 20036